# DETECTION AND IDENTIFICATION OF MECHANISMS AND TRENDS OF SEA-ICE DRIFT VARIABILITY IN THE SOUTHERN OCEAN

by

Wayne de Jager


Department of Oceanography
University of Cape Town
South Africa

Supervised by Professor Marcello Vichi

A dissertation submitted to the University of Cape Town in accordance with the requirements for award of the degree of Doctor of Philosophy in the Faculty of Science.

Word Count: 54 510

# Abstract

Antarctic sea ice regulates global climate processes by mediating exchanges of heat, momentum, and mass between the Southern Ocean and atmosphere. However, the logistical constraints of acquiring *in situ* sea-ice observations is challenging. Inferring sea-ice properties, such as concentration and motion, from satellite observations helps to address these data gaps, but the retrieval algorithms carry some limitations that complicate data acquisition. Temporal resolution limits are particularly pronounced when studying the effect of transient weather phenomena, such as polar and extra-tropical cyclones, which are major drivers of short-term sea-ice variability.

This thesis presents a systematic investigation into the weather-induced rotation dynamics in Antarctic sea ice, with a focus on the feasibility of quantifying hourly-to-daily sea-ice concentration and drift variability. A new algorithmic approach that is sensitive to the detection of rotational sea-ice drift features from satellite data at spatial and temporal scales comparable to that of polar weather is proposed, yielding a novel index for assessing interannual dynamical trends. Comparing selected 48-hour satellite ice motion products in the Atlantic Sector between 2013–2020 indicates good agreement in detecting anticyclonic rotation but discrepancies for cyclonic rotation. Cyclonic rotation is shown to be more intense than anticyclonic rotation, with the mean intensity of the 95th percentile of cyclonic features shown to be 1.5–2.0 times larger than their anticyclonic counterparts. Cyclonic rotation is also associated with greater variability and observational uncertainties, suggesting that the cyclones engender more heterogenous motion compared to high-pressure systems but also reduce the capacity of satellite products to accurately detect this motion. The analysis was expanded from 1991–2020 over the entire Southern Ocean using the latest generation 24-hour satellite sea-ice drift product. Results demonstrate that sea-ice rotation has become more correlated with atmospheric rotation at daily timescales, suggesting an increasing responsiveness of sea ice to weather forcing over the past three decades. Notably, the increased correlation between ice and atmospheric rotational dynamics is evidenced despite no discernible trends in the atmospheric forcing, pointing to a plausible role of the ocean in modifying the rheology of pack-ice. While the Southern Annular Mode was considered, it does not directly explain the strengthened coupling. Uniquely, sea ice in the Weddell Sea experienced a sharp decline in the intensity of its cyclonic and

anticyclonic components from 2002 onwards, which may instantiate that large synoptic systems are not the primary driver of ice rotation in this region.

To further address the temporal resolution limitations associated with daily-averaged satellite products, this thesis also explored a novel method for deriving sub-daily sea-ice type and motion observation from passive microwave swath data. The ECICE algorithm was directly applied to AMSR-2 Level-1B footprint data to produce sub-daily young (YI), first year (FYI) and multiyear (MYI) sea-ice concentration (SIC) observations. Results indicate ice-type classification was inconsistent, primarily because the radiometric signature of YI overlaps considerably with that of FYI and MYI. The use of motion vectors derived from the same swath data revealed a significant sea-ice response to weather forcing in just ~9 hours, which cannot be resolved by traditional daily-averaged products. The role of ice advection, melt, and growth contributions to SIC variability was calculated, but two major challenges arose: (i) coverage limitations associated with the drift retrieval algorithm caused unrealistic melt and growth estimates in the marginal ice zone (MIZ); and (ii) SIC saturation in the mobilized ice interior yielded minimal SIC changes despite a significant and widespread drift response. Ultimately, an assessment of drift products against dedicated observational experiments is recommended to evaluate product performance, especially in the MIZ, before swath-based retrieval techniques can be improved and systematically implemented.

# Author's Declaration

I declare that the work in this dissertation was carried out in accordance with the requirements of the University of Cape Town's Regulations and Code of Practice for Research Degree Programmes and that it has not been submitted for any other academic award. Except where indicated by specific reference in the text, the work is the candidate's own work. Work done in collaboration with, or with the assistance of, others, is indicated as such. Any views expressed in the dissertation are those of the author.

Signed by candidate

Wayne de Jager
10/02/2025

# Acknowledgements

This thesis funded by the **National Research Foundation of South Africa** (via the South African National Antarctic Programme, project no. 118745) and from the European Union's Horizon 2020 research and innovation programme under grant agreement No 101003826 via the **CRiceS project**. I would like to express my gratitude to these programmes for financially supporting me through my early career training at the University of Cape Town.

To **Professor Marcello Vichi**, your mentorship has been invaluable, not only in improving the quality of my work but also in deepening my appreciation for science. Thank you for challenging me to think critically and broaden my knowledge. I am especially grateful for your belief in my abilities and for granting me the freedom and independence to pursue my own ideas. Your dedication of time – into our papers, meetings and this thesis – is extremely appreciated. It is a privilege to learn from you as an aspiring scientist. I also sincerely appreciate the opportunities to travel and learn abroad, particularly on the S.A. Agulhas II. These experiences are cherished personal memories for which I will always be grateful.

A special thank you to **Dr. Christian Melsheimer** and **Dr. Gunnar Spreen** for hosting me at the University of Bremen, Germany, and for generously sharing your expertise in satellite data acquisition techniques. The knowledge and insights I gained during my time with you were instrumental in shaping the analysis presented in Chapter 5 of this thesis.

To my colleagues in the Department of Oceanography – **Cashifa**, **Isabelle**, **Rutger**, **Dayna** and **Magata** – thank you for creating a friendly and helpful work environment.

On a personal note, I am forever grateful to my parents, **Brian** and **Nikki**, for their unwavering support. From my very first day of school to the final stages of this PhD, I have relied on your constant love, encouragement and guidance. You instilled in me curiosity, perseverance, discipline, and resilience – values that have shaped my academic journey. Thank you for the sacrifices you have made to give me the opportunities to pursue my passions; if anyone deserves their names on the certificate, it's you.

To **Dion** and **Rene**, your example led the way into university, always acting as role models by providing guidance and reminding me of the bigger picture when I followed.

**Granny** and **Choppie**, your love, encouragement, and endless enthusiasm for my studies have meant the world to me. Thank you for always sending consistent support and optimism my way.

**Samantha**, your emotional support, energy, patience, and unwavering belief in me kept me motivated during the stressful times of a challenging year. Thank you for always reminding me to step back, breathe, and order an iced coffee.

To my Cape Town family – **Saif**, **Phillip**, **Natasha**, **Farhaan**, **Kirti**, **Chad** and **Alvin** – your kindness, guidance and support have made for such a positive university experience. Thank you all for helping me maintain balance between work and life. And to my friends around the world – **Daimon**, **Eric**, **Ross**, **Nathan**, **Jason**, **Sejal** and **Guy** – thank you for being part of my academic journey and personal support group, no matter the time difference. I am grateful to all of you for your friendship.

# Table of contents

# List of Figures

# List of Tables

# Acronyms

| | | | |
|---|---|---|---|
| **ACC** | Antarctic Circumpolar Current | **ECMWF** | European Centre for Medium-Range Weather Forecasts |
| **AMSR-2** | Advanced Microwave Scanning Radiometer 2 | **ENSO** | El Niño-Southern Oscillation |
| **ASCAT** | Advanced Scatterometer | **ERA-5** | 5$^{th}$ Generation ECMWF Reanalysis |
| **CMCC** | Continuous Maximum Cross Correlation | **FYI** | First Year Ice |
| **CoV** | Coefficient of Variation | **GPS** | Global Positioning System |
| **DJF** | December, January, February | **GR** | Gradient Ratio |
| **EKE** | Eddy Kinetic Energy | **HP** | High Pressure |
| **ECICE** | Environment Canada's Ice Concentration Extractor | **LP** | Low Pressure |

**MAM** March, April, May

**MCC** Maximum Cross Correlation

**MIZ** Marginal Ice Zone

**MLD** Mixed Layer Depth

**MSLP** Mean Sea Level Pressure

**MYI** Multiyear Ice

**NSIDC** National Snow and Ice Data Center

**S2S** Swath-to-Swath

**SAM** Southern Annular Mode

**SIC** Sea-Ice Concentration

**SIE** Sea-Ice Extent

**SoD** Stage of Development

**SST** Sea Surface Temperature

**SSM/I** Special Sensor Microwave Imager

**SSMIS** Special Sensor and Microwave Imager/Sounder

**YI** Young Ice

# Chapter 1 : Introduction

## 1.1 Problem statement

Vast landscapes of sea ice form in the polar oceans, with the Arctic and Southern Oceans experiencing strong seasonal sea-ice cycles characterized by equatorward expansion in winter and poleward retreat in summer. Sea ice plays a critical role in regulating Earth's climate by modulating heat, chemical, and momentum exchanges between the ocean surface and the atmosphere (McPhee, 2016). As the impacts of human-induced climate change become increasingly apparent (Lynas et al., 2021), the ability to accurately model sea ice in global climate systems is essential for improving predictions of future climate scenarios. Understanding sea-ice variability at regional and daily scales is a key requirement for improved model parameterization, necessitating detailed knowledge of the atmospheric and oceanic processes that drive ice formation, melt, and advection.

Sea-ice models typically incorporate thermodynamic (ice formation and melt) and dynamic processes (ice advection and deformation). While models provide valuable simulations of sea-ice behaviour, they must be supplemented by observations for validation, calibration, and initial conditions. However, acquiring i*n situ* data over the vast Antarctic sea-ice landscape – consistently exceeding a 17 million km² winter extent (Parkinson, 2019) – is logistically impractical. This challenge is amplified when research objectives require high temporal resolution data, such as hourly or daily measurements. In this context, satellite remote sensing has become indispensable, offering large-scale observations of sea-ice concentration, motion, thickness, albedo and more. However, these observations are derived from electromagnetic radiation emitted or reflected from Earth's surface, meaning that ice properties are inferred rather than directly measured. Consequently, sea-ice observations can be derived using several differing algorithms, each designed to process satellite radiances into useful variables such as concentration and motion. This leads to algorithm-specific strengths and limitations. For research focusing on daily sea-ice variability, careful consideration of the design and suitability of these processing algorithms are therefore essential.

One of the most significant drivers of short-term sea-ice variability in the Antarctic are polar and extra-tropical cyclones. These synoptic-scale weather systems, with radii ranging from 500 to 2,000 km and lifetimes of 1 to 3 days, bring intense cyclonic winds and warm, moist air over the sea-ice landscape (Vichi et al., 2019; Z. Wang et al., 2014). Cyclones can substantially influence sea-ice drift and concentration; for example, Turner et al. (2017) and Z. Wang et al. (2019) highlighted their contribution to the unprecedented decrease in ice cover between 2014–2016 by causing ice to move northward and melt at the warmer lower latitudes. This phenomenon is likely to grow in influence as extratropical cyclones shift poleward and polar storms intensify (Chang, 2017; Tamarin-Brodsky & Kaspi, 2017). Furthermore, recent studies indicate a significant decline in the Antarctic sea-ice extent trend since 2014 (Fogt et al., 2022; Hobbs et al., 2024; Purich & Doddridge, 2023), a decline that models failed to predict, highlighting a knowledge gap in our understanding of sea-ice variability. It is therefore necessary to consider the effect that local weather systems have on ice dynamics and to evaluate whether these phenomena influence the overall Antarctic sea ice drift over time, but their transient nature and abundance complicate systematic observational studies. While opportunistic *in situ* measurements under a polar cyclone revealed pronounced sea-ice drift variability near the ice edge, single-location datasets are insufficient for broader spatial and temporal analysis. Satellite observations offer the only feasible means of systematically observing cyclone-driven sea-ice variability across the entire Southern Ocean. While dynamic and thermodynamic processes together alter the sea-ice landscape, distinguishing their relative contribution from satellite data is still a challenge (e.g. Aue et al., 2023; Aue & Rinke, 2023; Clancy et al., 2022; Stevens & Heil, 2011).

This thesis addresses the aforementioned challenges by examining the influence of synoptic-scale weather systems on Antarctic sea ice. More specifically, sea-ice motion driven by polar weather is analysed, with a heightened focus on the link between sea-ice and surface wind rotation dynamics at short-term timescales. Additionally, the suitability of current satellite data acquisition techniques for detecting sub-daily to daily concentration and drift variability is assessed, and a new framework of sea-ice retrieval processing steps is explored with the aim to maximise scientific value from historical satellite records.

## 1.2 Background in Antarctic Sea Ice

Sea ice is frozen seawater that grows and melts at the ocean surface. Unlike icebergs, glaciers, or ice shelve – which form from fresh water on land – sea ice forms directly on the ocean's surface when the temperature drops to the freezing point of seawater at approximately -1.8°C, dependent on salinity content. Its coverage is a transient feature that expands and contracts each year, with its presence primarily dictated by seasonal and regional ocean temperatures and atmospheric conditions. Sea ice which forms and melts within a single seasonal cycle is termed 'young' or 'first year' ice, while ice that survives a melting season is termed 'multiyear' ice (WMO, 2014). These ice type distinctions are useful for describing longer-term changes to the seasonal ice coverage, as these vast landscapes advance equatorward in freezing periods of the winter months and then retreat poleward in the proceeding melting periods of the summer months. While the presence of sea ice is locationally limited to the Arctic, Antarctic and some marginal seas, it contributes greatly to the global climate system through interactions with solar radiation, atmospheric processes and ocean circulation (Budikova, 2009; Massom & Stammerjohn, 2010). The ice insulates the ocean from the atmosphere by regulating the heat and chemical exchange between adjacent water and air masses, which subsequently influences local weather and ultimately affects climate feedback processes (Vancoppenolle et al., 2013; Vihma, 2014). Because of its high albedo, sea ice reflects a significant portion of incoming solar radiation back into space, contributing to the cooling of the polar regions which helps to moderate global temperatures. As the ice melts and exposes the darker ocean surface, less sunlight is reflected, leading to increased absorption of heat by the ocean. This phenomenon is known as the *ice-albedo feedback* (Perovich et al., 2011). Sea ice also plays a role in the global ocean's *thermohaline circulation*, a term used to describe a large-scale ocean current engendered by density differences between different water masses that in turn redistribute heat and nutrients around the world (Clark et al., 2002; Toggweiler & Key, 2003). The formation of sea ice expels salt, thus increasing the density of the surrounding surface water. These dense waters then sink and flow equatorward, driving these deep ocean currents (Yang & Neelin, 1993, 1997). Furthermore, the carbon cycle is also influenced by sea ice. During the formation of sea ice, gases such as carbon dioxide are exchanged between the ocean and atmosphere, while biological productivity is also related to the distribution of sea ice through the buffering of nutrients further supporting phytoplankton

communities (Arrigo et al., 1995; Vancoppenolle et al., 2013). Sea-ice processes further modulate the sink for greenhouse gases through the absorption of carbon dioxide from the atmosphere (Mongwe et al., 2024).

The Antarctic and Arctic sea-ice landscapes exhibit significant differences driven by a complex interplay of oceanic, atmospheric, and geographical factors over extreme seasonal cycles (Maksym, 2019). In the Arctic, sea ice forms within a semi-enclosed ocean surrounded by North America, Eurasia, and Greenland. This geographical configuration, illustrated in Figure 1.1a, limits the outward movement of sea ice during the freezing period as it expands from the central Arctic Ocean towards surrounding coastlines. As a result, Arctic sea ice comprises both first-year ice and multiyear ice, with multiyear ice typically concentrated at higher latitudes. Multiyear ice – having survived one or more summer melt seasons (June to September in the Northern Hemisphere) – tends to be thicker (approximately 2-4 meters) and exhibits a smoother, weathered surface due to prolonged exposure to environmental processes (Comiso, 2012). This ice also forms densely packed, cohesive fields known as *consolidated* ice fields. In contrast, Antarctica consists of a landmass encircled by the open Southern Ocean, where the absence of surrounding land barriers allows sea ice to drift more freely (Figure 1.1b). This mobility, combined with the influence of intense storms and large ocean swells, results in a highly variable sea-ice cover characterized by loosely packed ice floes spread over a larger area, referred to as *unconsolidated* ice fields (Alberello et al., 2020; Vichi, 2022). Unlike in the Arctic, most of the Antarctic sea ice does not survive the melting season (December to February in the Southern Hemisphere). Consequently, the sea ice is predominantly composed of thinner, young and first-year ice that forms and melts within a single seasonal cycle (Melsheimer et al., 2023). The annual cycle of Antarctic sea ice demonstrates dramatic expansion and retreat, growing to ~18 million square kilometres ($km^2$) during the austral winter and contracting to ~3 million $km^2$ in summer (Parkinson, 2019). By comparison, Arctic sea ice fluctuates between ~4 and ~15 million $km^2$ (Parkinson, 2022). Superimposed on these pronounced seasonal cycles are significant regional and interannual variations, driven by both natural processes and anthropogenic influences. Notably, the Arctic has experienced a consistent decline in sea-ice extent over the past four decades, strongly linked to regional warming. In contrast, the Antarctic sea-ice extent has shown a more complex and variable pattern, with alternating periods of both expansion and contraction and a sudden decrease in recent years (Maksym, 2019; Parkinson

& DiGirolamo, 2021; Serreze & Meier, 2019). A summary of the key differences between these two regions is presented in Table 1.1.

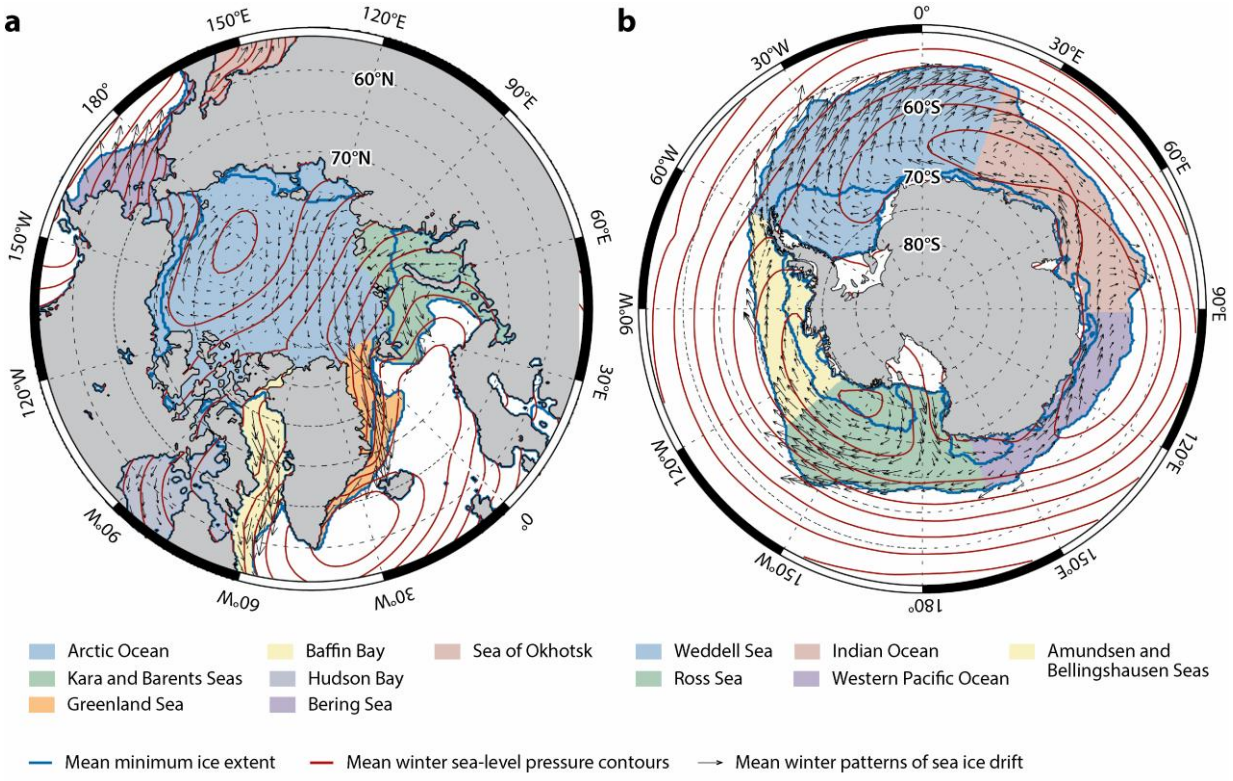


**Figure 1.1: Geographic setting of (a) Arctic and (b) Antarctic sea ice. The average maximum sea ice extents for 1979–2016 (March in the Arctic, September in the Antarctic) are indicated by the coloured ocean areas. The blue lines indicate the mean minimum ice extents (September in the Arctic, February in the Antarctic). The black arrows indicate the mean winter patterns of sea ice drift, and the red lines show the mean winter sea-level pressure contours (2-hPa intervals) (January–March in the Arctic, July–September in the Antarctic). Different colours indicate different traditional regions or sectors chosen to examine trends and variability (Cavalieri & Parkinson, 2008; Parkinson & Cavalieri, 2008). Sea ice drift patterns are driven largely by climatological highs and low pressures, which drive prevailing winds. Much of the variability in the ice cover is then driven by atmospheric variability. Source: Maksym (2019).**

**Table 1.1: Key differences between Arctic and Antarctic sea-ice characteristics, based on satellite and *in situ* observational records and modelling studies.**

| | Arctic | Antarctic |
|---|---|---|
| **Observed Trends (since 1979)** | Significant decline in both extent and thickness over the past four decades. (Kwok, 2018; Parkinson, 2022) | Extreme interannual and regional extent variability. Thickness trends unclear. (Kurtz & Markus, 2012; Mangatane & Vichi, 2025; Parkinson, 2019) |
| **Recent Anomalies** | Record low extents in recent years. Projections of ice-free summers in coming decades. (Parkinson, 2022; Shen et al., 2023) | Record low extents in recent years suggesting potential shifts in sea ice behaviour away from extreme interannual variability. (Fogt et al., 2022; Purich & Doddridge, 2023) |
| **Geographic Layout** | Landlocked ocean surrounded by continents, leading to confined sea ice. | Continent surrounded by open ocean, allowing sea ice to expand freely. |
| **Seasonal Variability** | Maximum extent in March (~15 million km²); minimum in September (~4 million km²). (Parkinson, 2022) | Maximum extent in September (~18 million km²); minimum in February (~3 million km²). (Parkinson, 2019) |
| **Atmospheric Influences** | High and low pressure dipole drives circulation patterns that favour thick ice persistence. (Watanabe et al., 2006) | Westerly winds impart a northerly Ekman drift to the ice causing northward seasonal expansion. (Raphael et al., 2016) |
| **Ocean Influences** | Fresh, buoyant surface waters drive insulates surface from warmer deep water, promoting ice growth. (Steele & Boyd, 1998) | Weakly stratified upper ocean drives higher ocean heat flux which limits ice thickening. (Martinson & Iannuzzi, 2013) |
| **Ice Type Composition** | Typically, thick and consolidated with substantial multiyear ice coverage. (Kwok et al., 2009) | Typically, thin and mobile/unconsolidated. Seasonal ice types dominate. Significant pancake ice coverage, prone to rafting. (Alberello et al., 2019; Roach et al., 2018) |
| **Model Representation** | Overall decline represented well but regional variability missed. (Massonnet et al., 2012) | Fail to show extreme interannual and regional variability, even in high-resolution model attempts. (Notz et al., 2016; Roach et al., 2020) |

## 1.3 Drivers of Sea-Ice Variability

To further develop our understanding of the Antarctic sea ice landscape, it is necessary to understand the various scales of variability that influence its behaviour and properties. Here, *sea-ice properties* refer to a wide range of variables that describe characteristics of the ice including, but not limited to, its thickness, age, motion, temperature, salinity, etc. The terms *temporal* and *spatial variability* are used to describe the variations in the ice landscape over time and location, respectively. More specifically, Antarctic sea ice variability occurs across a wide spectrum of temporal scales, including short-term weather events (hours-days), seasonal and interannual fluctuations (months-years), and long-term climatic trends (decades-centauries). Spatially, scales of variability can range from microscopic changes in the ice crystallization processes to global climate impacting sea-ice extent trends. The range of scales of selected atmospheric phenomena is depicted in Figure 1.2, each of which play a role in modifying the sea-ice conditions. Distinguishing these scales helps to disentangle and identify complex interactions between the sea ice, atmosphere, and ocean and how sea-ice properties change because of these interactions. Ultimately, the combination of these environmental processes at different scale manifests into the overall sea ice variability that is observed. Short-term variability in Antarctic sea ice is heavily influenced by weather events (Alberello et al., 2020; P. Uotila et al., 2011; Vichi et al., 2019), which in this context, describe synoptical-scale atmospheric phenomena that span hundreds to thousands of kilometres and occur at timescales ranging from hours to several days (Figure 1.2). The transient nature of these weather systems introduces significant wind and temperature variability on daily timescales, which is especially important to its overall distribution at daily timescales. Polar and extra-tropical cyclones, for instance, can be several hundred kilometres in diameter and persist for one to five days, generating strong winds that move the underlying sea ice and transport warm, moist air along its' trajectories. These effects can be seen over vast areas of the Southern Ocean, although their most intense impacts are often concentrated in the vicinity of the cyclone's central core (Vichi et al., 2019). Phenomena such as katabatic winds - a term used to describe downslope winds that blow off the Antarctic ice sheet - can influence sea ice formation and movement along the coastal regions, redistributing the sea-ice cover in these locations (P. Holland & Kwok, 2012). While short in duration, weather events can have widespread and long-lasting effects on sea ice distribution. In some

cases, from the Arctic region, the effects of these events can propagate over time, as changes in sea ice cover influence ocean circulation and weather patterns, creating feedback loops that extend the influence of a short-term event (Aue et al., 2023). The response of sea-ice to dynamic and thermodynamic processes associated with cyclones is further discussed in Section 1.3.1.1.

Antarctic sea ice displays a dramatic seasonal cycle, expanding in winter and retreating in summer. This is one of the most extreme seasonal changes observed in any natural environment, with sea ice extent varying by ~15 million $km^2$ over the course of a year (Parkinson, 2019). During the austral winter (June to September), sea ice grows rapidly due to colder temperatures, advancing northward to a latitude of 55°S to 60°S. As summer approaches (December to February), increased solar radiation and warmer temperatures lead to a sharp retreat to the continent's coastline or a latitude of 70°S to 75°S (Vichi, 2022). This seasonal variability is primarily driven by changes in solar energy input and air temperature, though ocean currents, wind patterns and topographical features also a role in sea-ice distribution. Furthermore, an asymmetry in the regional distribution of sea ice is notable, with the Weddell and Ross Seas retaining ice in summer due to their higher latitudes and favourable ocean circulation patters, while ice in the Amundsen and Bellingshausen Seas melts almost completely due to warmer waters and ice export (Kumar et al., 2021; Kwok et al., 2017). Interannual variability in Antarctic sea ice refers to changes in sea ice distribution from year to year. This variability is influenced by large-scale atmospheric and oceanic processes, which result in significant differences in sea ice behaviour across different regions of the Southern Ocean. Unlike seasonal variability, which follows a predictable annual cycle of ice expansion and contraction, interannual variability is less regular and is often driven by complex climate and ocean interactions. Large scale climate modes and structures – such as the Southern Annular Mode (SAM), El Niño-Southern Oscillation (ENSO) or localized low-pressure anomalies – demonstrate correlations with sea-ice distribution, but do not fully explain observed interannual fluctuations (Coggins & McDonald, 2015; Doddridge & Marshall, 2017; Pezza et al., 2012). Furthermore, these fluctuations are not uniform across the Southern Ocean, with some regions experiencing increases in ice cover while others see declines, depending on the localized impacts of changing wind patterns, ocean currents and sea surface temperatures (SST). Oceanic variability – such as changes in the strength of the Antarctic Circumpolar Current (ACC), sea surface temperature (SST), salinity-driven stratification, Ekman pumping, etc – can also affect the

melting and freezing rates of sea ice, influencing its distribution. These processes that will be discussed explicitly in Section 1.3.2.

On longer timescales, decadal and multi-decadal variability in Antarctic sea ice is often linked to broader climatic trends, such as global warming and its associated changes in oceanic and atmospheric circulation patterns (P. Holland & Kwok, 2012; Meehl et al., 2019). Despite the global trend of an overall warming, Antarctic sea ice has shown a more complex and less consistent response compared to the clear decline in Arctic sea ice. Between 1979 and the mid-2010s, Antarctic sea ice extent showed a slight increase, confounding expectations from climate models. However, in recent years, a sharp decrease in sea ice extent has been observed, raising questions about the underlying drivers of these decadal trends, and so long-term observations and accurately represented sea-ice processes in climate models are essential to disentangle its natural variability from anthropogenic forcing (Fogt et al., 2022; Hobbs et al., 2024; Purich & Doddridge, 2023). Research into Antarctic sea ice variability also extends to centennial and millennial scales – typically through the study of paleoclimate records such as ice cores and sedimentary deposits – which helps place current trends within a broader context of different climate scenarios.

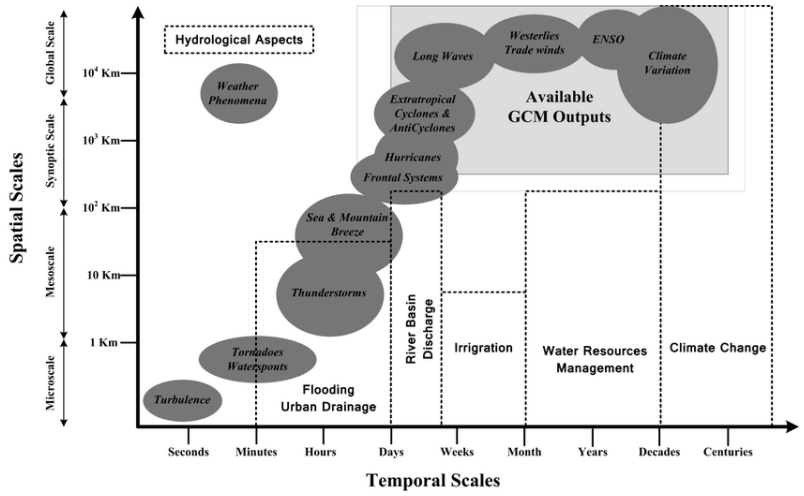


**Figure 1.2: The spatial (y-axis) and temporal (x-axis) scales associated with various atmospheric phenomenon that effect sea-ice variability. The range of atmospheric phenomena typically resolve by Global Climate Models (GCM) is indicated with the shaded rectangle. Source: Adapted by Tavakolifar et al. (2017) from Nese & Grenci (2020).**

### 1.3.1 Atmospheric Contributions to Sea Ice Variability

The interaction between atmospheric forces and sea ice is complex, with the atmosphere playing a major role both short-term changes through phenomena like polar and extra-tropical cyclones, as well as long-term variability through large-scale climate patterns like the SAM and ENSO (Matear et al., 2015). On shorter timescales (days-weeks), atmospheric phenomena like cyclones, frontal systems, and katabatic winds can cause rapid changes in sea ice concentration, thickness, and distribution. The effects of these short-term variations are superimposed on the seasonal and interannual variability. On interannual to decadal timescales, variability in sea ice is linked to broader atmospheric circulation patterns, such as the SAM and the El Niño-Southern Oscillation (ENSO). These large-scale climate modes influence the strength and position of the westerly winds and atmospheric pressure systems, which in turn affect sea ice formation and advection more directly (P. Holland & Kwok, 2012; Kwok et al., 2017; Kwok & Comiso, 2002). Over decades, shifts in these patterns can lead to noticeable trends in sea-ice extent and variability, and so to fully understand ice variability, it is necessary to examine how atmospheric drivers operate and interact with sea ice across these different timescales.

#### 1.3.1.1 Cyclones and Short-Term Variability

Polar and extra-tropical cyclones are intense low-pressure systems that develop around Antarctica, predominantly during the austral winter (Grieger et al., 2018). These dynamic weather systems typically persist for several days but can last over a week, significantly influencing short-term variability in Antarctic sea ice. As cyclones traverse the Southern Ocean, their strong, cyclonically rotating winds induce widespread impacts on the underlying sea-ice field, often spanning hundreds of kilometres (Vichi et al., 2019). The primary mechanism through which cyclones affect sea ice is wind stress, which describes the frictional drag forces generated by strong cyclonic winds that engender motion into the underlying ice field, especially closer to the centre of the cyclone where wind speeds are highest. The intensity of this ice drift depends on the strength and duration of the cyclone, as well as the ice conditions prior to its arrival (Aue et al., 2023). This can cause a redistribution of the sea-ice field, whereby individual floes can be pushed tightly together (termed *convergence*) or spread further apart (termed *divergence*). The convergence and

divergence of floes plays a key role in determining the overall thickness of the field (and subsequently, the sea-ice volume) through both dynamic and thermodynamic mechanisms (Worby et al., 1996). In cases of convergence, individual floes become more tightly packed and causing the ice floes to interlock and fuse into consolidated pack-ice (Auclair et al., 2022). In highly dynamic regions – such as the marginal ice zone (MIZ) – large ocean swells combined with other unknown factors can cause rafting (floes overriding each other) or ridging (repeated bumping of adjacent floes causes ice piling along floe perimeter) as illustrated in Figure 1.3. Both rafting and ridging are mechanisms of dynamic thickening (Audh et al., 2023; Doble et al., 2003; Lange et al., 1989), although the latter is more common in the Arctic where coastline constraints contribute additional pressure forces (Damsgaard et al., 2021; Maksym, 2019). In cases of divergence, cyclones can disperse ice and create open water areas within the ice pack (e.g. leads or polynyas). This exposes the surface ocean to the cold, overlying air which quickly freezes over, thus leading to the formation of thin, new ice (Heorton et al., 2017; Willmes et al., 2023). Consequently, this promotes horizontal expansion but impedes vertical thickening. Thermodynamic processes induced by cyclones further compound their impact. Cyclones often transport warm, moist air from lower latitudes to the polar regions, elevating surface temperatures which promotes ice melt before and during the storm events, decreasing local ice cover. Proceeding this, the post-storm cold, dry air leads to rapid refreezing and increased ice cover (Aue & Rinke, 2023; P. Uotila et al., 2011; Vichi et al., 2019). The repetitive and transient nature of cyclones therefore subject the underlying ice field to alternating phases of melting and freezing conditions, each of which modify the material structure of the ice and its larger-scale composition (Paul et al., 2023). These modifications in turn effect the behaviour of the ice to subsequent cyclones – which is discussed further in Section 1.5.2 (Aue et al., 2023). In some cases, cyclones can also approach from higher latitudes and draw cold, dry air from the Antarctic interior, promoting ice formation (Aue et al., 2023; Clancy et al., 2022; Koyama et al., 2017). Ultimately, while dynamic forcings primarily drive the sea-ice distribution over daily timescales, the combined mechanical and thermodynamic processes associated with cyclones determine its behaviour and distribution.

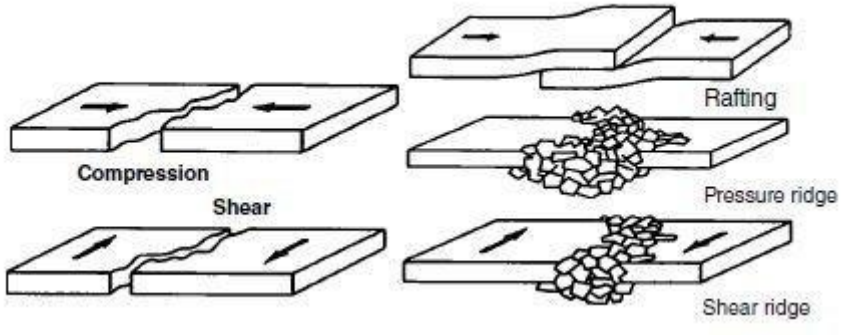


**Figure 1.3: The dynamics of a sea-ice field govern the interactions between adjacent floes. Converging floes creates compression forces, causing rafting (floes overriding each other) or ridging (repeated bumping of adjacent floes causes ice piling along floe perimeter). Floes in contact moving parallel to one another create shear forces, also causing ridging. Source: Shokr & Sinha (2015).**

The frequent passage of cyclones introduces additional complexity. Thin ice – being more susceptible to deformation (Leppäranta, 2005; Rampal et al., 2009; Spreen et al., 2011) – is more easily broken and redistributed by subsequent cyclones. This susceptibility establishes a potential feedback mechanism: cyclone-induced thinning or thickening affects the vulnerability of the ice to future cyclonic activity, a phenomenon demonstrated by Aue et al. (2023). The cumulative influence of successive cyclones is therefore significant as a means for short-term weather-driven changes to contribute to longer-term sea-ice variability. This feedback has important implications for sea-ice models, which would thus require more detailed memory of past ice conditions to accurately simulate future states. Cyclones primarily originate from cyclogenesis regions in the Atlantic and Pacific sectors of the Southern Ocean, migrating eastward (Grieger et al., 2018; Wei & Qin, 2016). The sea-ice cover is thus exposed to frequent and repeated cyclonic events, each inducing cycles of melting, freezing, and advection. The typical cyclone conditions are depicted in Figure 1.4, whereby it is shown that the leading and trailing fronts carry warm northerly and cold southerly winds, respectively, exposing the underlying sea-ice to vastly different conditions over just 3-5 days. While individual cyclone impacts on sea ice have been documented (Alberello et al., 2020; Aue et al., 2023; P. Uotila et al., 2011; Vichi et al., 2019), the cumulative effects of repeated exposure remain poorly understood. Limited availability of *in situ* data at appropriate spatial and temporal scales poses a

significant challenge, and current large-scale climate models lack sufficient resolution to fully resolve smaller-scale interactions. Consequently, we currently rely heavily on satellite retrieval methods to detect and quantify this sea-ice variability.

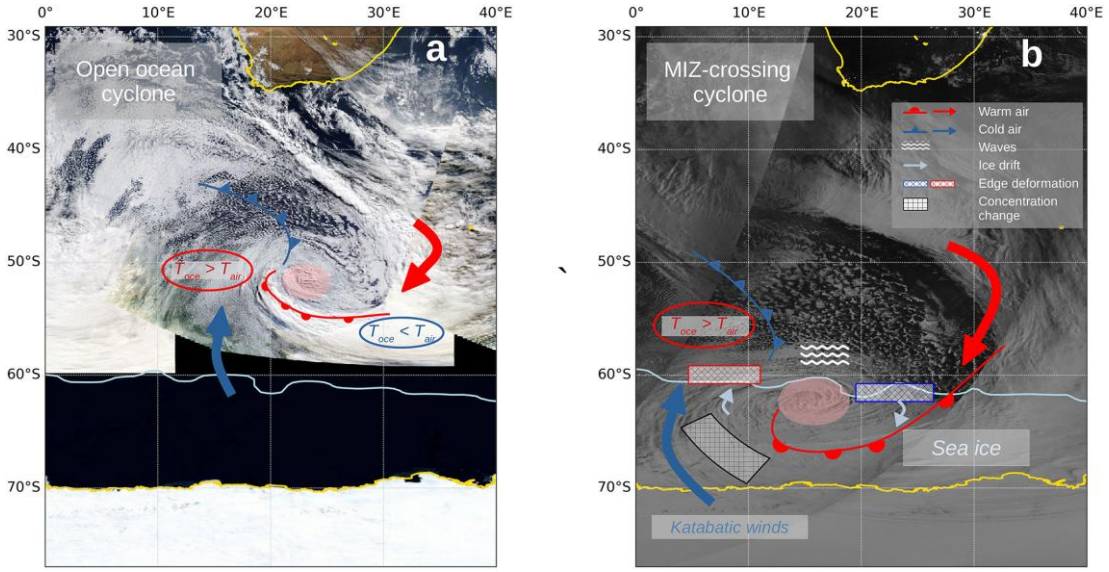


**Figure 1.4: Schematic of a polar cyclone (a) on the open ocean (from Moderate Resolution Imaging Spectroradiometer, MODIS-Terra true colour mosaic, 02 July 2017) and (b) when crossing the MIZ (from Visible Infrared Imaging Radiometer Suite, VIIRS nighttime imagery of Cyclone 1, 03 July 2017). The light blue contour is the daily 15% sea ice concentration as assimilated in ERA5. The location of the arrows, fronts, and warm core (the red elliptic region) with respect to the depicted storms is illustrative of their main features. The open-ocean case (a) presents air-sea interactions showing the expected relationship between the air temperature (Tair) and the ocean temperature (Toce); this is not shown for the sea ice case (b) due to the less known interactions between air and sea ice under extreme events. MIZ = marginal ice zone. Source: Vichi et al. (2019).**

### 1.3.1.2 The Southern Annular Mode and Interannual Variability

The Southern Annular Mode (SAM) is the dominant mode of climate variability in the Southern Hemisphere, characterized by shifts in the position and intensity of the westerly winds that encircle Antarctica (Fogt & Marshall, 2020). These winds form a belt of strong atmospheric circulation, commonly referred to as the polar vortex, which undergoes periodic contraction and relaxation around the Southern

Ocean. These fluctuations drive contrasting atmospheric conditions and are termed *positive* and *negative* SAM phases. In the positive phase of SAM, the westerly winds intensify and the polar vortex contracts towards Antarctica. Conversely, during the negative phase of SAM, the westerly winds weaken and shift northward. Although SAM represents a naturally occurring pattern of climate variability, it also responds to anthropogenic influences. Notably, increasing concentrations of greenhouse gases and ozone depletion over the South Pole have been linked to a more positive SAM phase in recent decades (King et al., 2023; Thompson et al., 2011). The SAM is the leading mode of variability over the Southern Ocean, and it operates across a wide range of temporal scales, from daily to decadal, making it a critical driver of variability in the Southern Ocean (Baldwin & Dunkerton, 2001; Kidson, 1999). Changes in the strength and position of the SAM-induced winds are closely associated with observed variations in sea-ice extent and concentration (P. Holland & Kwok, 2012; Kwok & Comiso, 2002). Generally, during the positive phase of SAM, stronger westerly winds enhance northward Ekman drift, promoting the expansion of sea-ice cover (Doddridge & Marshall, 2017; Hall & Visbeck, 2002). However, the spatial response of sea ice is highly complex and regionally variable (Matear et al., 2015). While stronger winds can drive sea ice northward, differential responses to warm and cold air transport as well as local wind dynamics complicate the relationship between SAM and sea-ice distribution. For instance, regional studies have demonstrated that while certain areas experience increased ice extent, others may see reductions, depending on atmospheric circulation patterns and oceanic feedbacks (Hobbs et al., 2016; Lefebvre et al., 2004).

The influence of SAM on sea-ice variability is further modulated by interactions with other large-scale climate modes like the El Niño-Southern Oscillation (ENSO) and the Amundsen Sea Low (ASL). ENSO, a dominant driver of interannual global climate variability, affects Antarctic atmospheric circulation patterns and thereby sea-ice extent, which can amplify or mitigate the SAM's effect on sea ice variability. For example, the combined influence of a SAM+ and La Niña conditions can enhance cyclone activity in certain regions, directly impacting sea-ice dynamics through short-term changes in wind stress and thermodynamic processes, as described in Section 1.3.1.1 (Pezza et al., 2012; Stammerjohn et al., 2008). This specific case is illustrated in Figure 1.5, whereby SAM+ and La Niña phases align and facilitate the zonal asymmetry in the sea-ice distribution. Furthermore, studies highlight a teleconnection between ENSO events and Antarctic sea-level pressure anomalies that can influence regional sea-ice distribution

(Turner, 2004; Yeung et al., 2019). The Amundsen Sea Low, for example, is a quasi-stationary low pressure system that affects climate in West Antarctica and is amplified during periods of SAM+ and La Niña, consequently intensifying polar jets and cyclonic activity around Antarctica (Clem et al., 2016, 2017; Coggins & McDonald, 2015), while the seasonality of the SAM–ENSO teleconnection introduces additional complexity to their combined influence on Antarctic sea-ice variability.

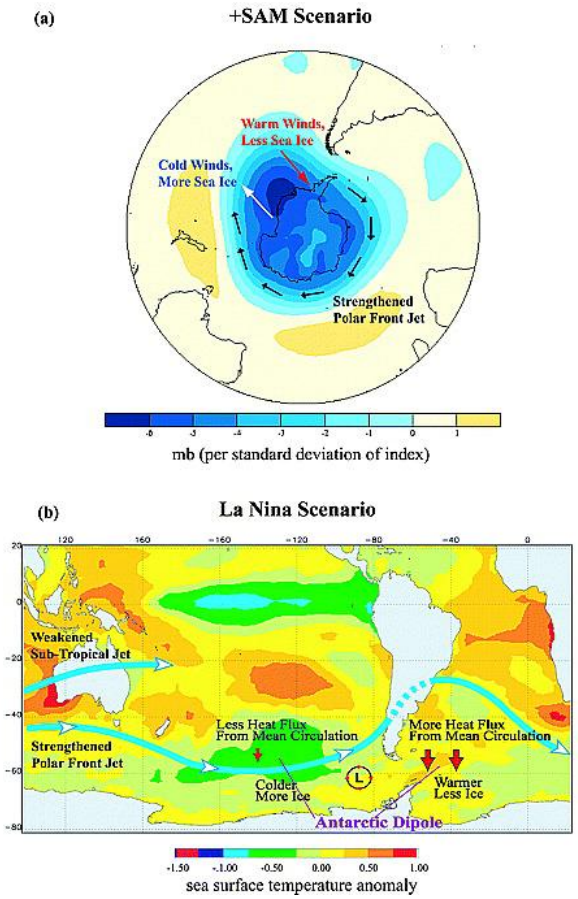


**Figure 1.5: Schematic depiction of the high-latitude ice-atmosphere response to (a) SAM+ and (b) La Niña. The base image in panel a is from T. Mitchell (http://www.jisao.washington.edu/sam) and shows the regression of SLP anomalies onto a SAM-derived index. The arrows schematically depict wind anomalies during a SAM+ scenario. The image in panel b is adapted from Yuan (2004), with the base map showing a La Niña composite of sea surface temperature anomalies. Source: Stammerjohn et al. (2008).**

### 1.3.2 Ocean Contributions to Sea Ice Variability

The ocean beneath the ice exerts a significant influence on sea-ice variability through surface currents, sea surface temperature (SST), waves, and vertical mixing. Like atmospheric processes, oceanic forces drive sea-ice variability through both dynamic and thermodynamic mechanisms (McPhee, 2016). Despite its critical role, our understanding of oceanic contributions to Antarctic sea-ice variability remains limited due to the challenges of obtaining direct observations beneath the ice. The presence of sea ice hinders the deployment of conventional oceanographic instruments and complicates the use of remote sensing techniques. Recent technological advances, including autonomous underwater vehicles and ice-tethered profilers, have partially mitigated these challenges by facilitating data collection beneath the ice. However, these technologies are still in their infancy, providing only sparse and localized observations. Furthermore, remote sensing observations are limited to the surface and cannot penetrate sea ice, meaning ocean data is mostly inferred from sea-ice conditions. Ocean reanalysis datasets offer an alternative by combining sparse observations with model dynamics, but their reliability beneath sea ice remains constrained by limited input data, coarse resolution, and uncertainties in model parameterizations (Storto et al., 2019; P. Uotila et al., 2019). These limitations are particularly pronounced in regions with thick ice cover or strong stratification, where assimilation constraints are weakest. Consequently, coupled ocean-ice modelling remains a key approach for estimating ocean properties and investigating their role in sea-ice variability. (Pellichero et al., 2017; Wilson et al., 2019).

A pronounced vertical temperature gradient characterizes much of the Southern Ocean, with the Mixed Layer Depth (MLD) emerging as a critical oceanographic feature influencing Antarctic sea-ice variability. The MLD refers to the uppermost layer of the ocean where temperature, salinity, and density are relatively homogeneous due to turbulent mixing driven by wind stress, wave activity, and buoyancy forcing (such as surface cooling or freshwater input). Variations in freshwater input – for example, from sea-ice melt or increased precipitation – can freshen the surface ocean and enhance stratification (Hellmer, 2004). This stratification inhibits vertical mixing, resulting in a shallower MLD and limiting the upward transport of oceanic heat, thereby promoting sea-ice growth. In contrast, processes such as brine rejection during ice formation can deepen the MLD, enhancing vertical mixing and increasing the heat flux to the surface.

These dynamics can accelerate the melting of ice and delay freeze-up. Wind forcing also plays a role, whereby strong winds can deepen the MLD through wind-driven turbulence and Ekman pumping, potentially drawing warm Circumpolar Deep Water (CDW) toward the surface (Callahan, 1972; Greene et al., 2017; Morrison et al., 2020). These processes operate over weekly to seasonal timescales and are central to both the seasonal cycle and interannual variability of Antarctic sea ice. Regional differences in sea-ice extent across the Southern Ocean are partially attributable to spatial heterogeneity in MLD and upper-ocean heat content. For instance, the recent sharp decline in Antarctic sea-ice extent since 2014 has been strongly linked to regional ocean warming (Meehl et al., 2019; Purich & Doddridge, 2023). Among the most affected regions are the Amundsen and Bellingshausen Seas, which have experienced substantial sea-ice loss in conjunction with warming surface ocean conditions (P. Holland et al., 2010; Naughten et al., 2022). While other regions such as the eastern Weddell Sea and eastern Ross Sea have also shown declining trends, the magnitude of these changes has been comparatively smaller (Meehl et al., 2019).

Large-scale oceanic circulatory systems also play a role in controlling sea-ice distribution in the Southern Ocean. The eastward-flowing Antarctic Circumpolar Current (ACC) acts as both a thermal and dynamic barrier, limiting the northward expansion of sea ice (Figure 1.6). The ACC interacts with the Subantarctic Front (SAF) and the Polar Front (PF), regions characterized by sharp temperature and salinity gradients, which inhibit the poleward movement of warm subtropical waters (Orsi et al., 1995). This interaction effectively insulates Antarctica, confining sea ice primarily to latitudes south of approximately 60°S. Any shift in the position or strength of the ACC, often driven by changes in wind patterns, can have a direct impact on the sea ice distribution. For instance, when the ACC intensifies or shifts poleward, the resulting increase in warm water upwelling can further reduce sea ice cover, particularly along the margins (Fyfe et al., 2007). Conversely, a weakening of the ACC allows colder waters to extend farther north, fostering sea-ice expansion. Ocean gyres further influence Antarctic sea-ice dynamics extent on seasonal to decadal timescales (Neme et al., 2021). Cyclonic gyres, such as those in the Weddell and Ross Seas (Figure 1.6), trap cold water and sea ice, promoting the formation and maintenance of thick, consolidated ice (Kumar et al., 2021). In contrast, regions outside the influence of these gyres, including the Amundsen and Bellingshausen Seas, are more susceptible to northward ice export (Kwok et al., 2017).

Towards the ocean margin, the large Southern Ocean waves significantly influence sea-ice variability on shorter timescales, particularly within the marginal ice zone (MIZ), but also beyond and into the ice interior (Massom et al., 2018). This dynamic region is highly sensitive to wave action, with wave energy and influence diminishing as waves propagate deeper into the pack-ice (Alberello et al., 2020; Kohout et al., 2014, 2020). Waves – primarily driven by wind stress – can form locally from nearby storms or travel long distances as low-frequency swells. When large waves reach the MIZ, they can fracture sea ice, enhancing melting and creating conditions that accelerate further ice loss (Alberello et al., 2021; Passerotti et al., 2022). Wave-sea ice interactions operate on timescales of seconds, making them a key driver of the highly variable nature of sea ice along the ice edge. Tides also play a role in modulating sea-ice dynamics, particularly in coastal polynyas and adjacent to ice shelves. Tidal currents enhance turbulent mixing within the ocean beneath ice shelves, leading to increased basal melting (Hausmann et al., 2020; Padman et al., 2018).

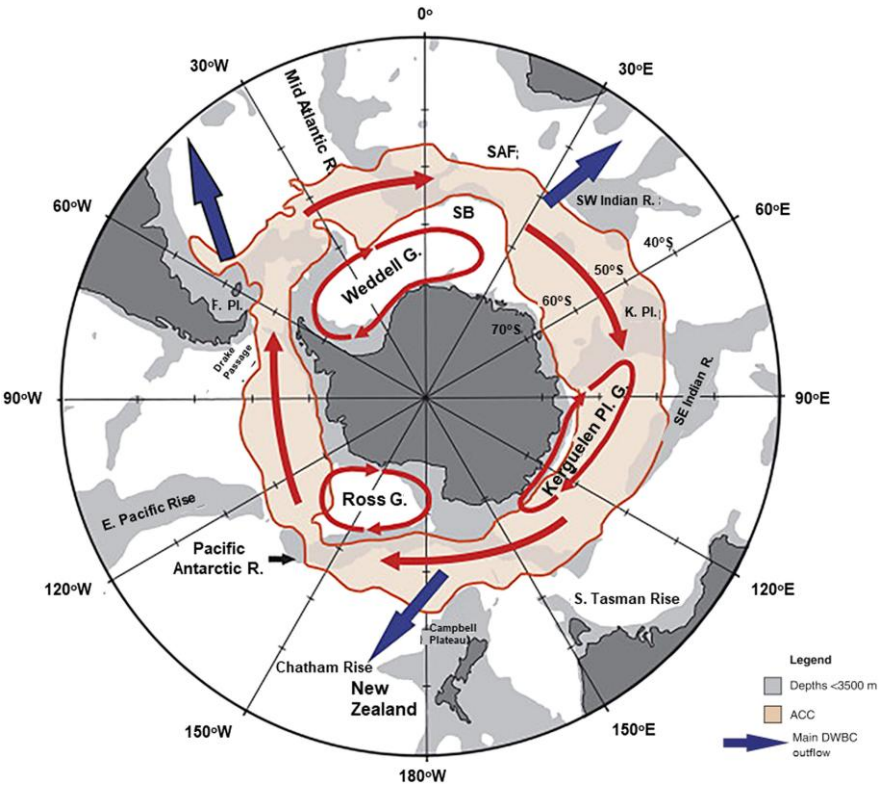


**Figure 1.6: The main oceanographic features of the Southern Ocean: (i) the Antarctic Circumpolar Current (ACC) south of the Subantarctic Front (SAF) and southern limit of Upper Circumpolar Deep Water or southern boundary (SB); (ii) the Ross, Weddell, and Kerguelen Plateau gyres; and (iii) the main exit locations of deep western boundary currents (DWBC) from the Southern Ocean (blue arrows). Bathymetric elevations are annotated as R = ridge; K. Pl. = Kerguelen Plateau; F. Pl. = Falkland/Malvinas Plateau; and G. = gyre. Source: Vernet et al. (2019). Reprinted from Carter et al. (2008) with permission from Elsevier.**

## 1.4 Sea-Ice Distribution from Space

Sea-ice concentration (SIC) is a fundamental parameter used to describe the proportion of the ocean surface covered by sea ice. It is expressed as a percentage, where 100% indicates a fully ice-covered region and 0% denotes open water. SIC is a quantifiable measure of ice coverage and so is useful for understanding the variability of Antarctic sea ice. It informs the spatial distribution of sea ice at any given time and is useful in monitoring seasonal and interannual variability, assessing long-term trends, and evaluating the

role of sea ice in the global climate system. Additionally, SIC is widely used in operational applications, such as polar forecasting and navigation. SIC is primarily measured using passive microwave (PM) satellite remote sensing methods, which enable daily, large-scale observations of polar regions (e.g. Comiso et al., 1984; Shokr et al., 2008; Spreen et al., 2008; Swift & Cavalieri, 1985). Other methods, such as synthetic aperture radar (SAR) or optical and infrared sensors, are also employed to refine SIC estimates (Sandven et al., 2023). *In situ* measurements are necessary for validating these satellite-derived estimates, improving detection algorithms, and addressing uncertainties. Additional details of deriving SIC from PM data are discussed in Sections 1.4.1 and 2.1.2.

Because remote sensing methods have enabled large-scale data coverage of the polar landscapes at daily timescales, SIC has traditionally been used to derive a host of sea-ice distribution metrics. Sea-ice extent (SIE) is a widely used metric derived from SIC, representing the total area of ocean with SIC exceeding a specific threshold, typically 15% (WMO, 2014). This 15% threshold defines the boundary where sea ice can be reliably detected by passive microwave satellite sensors (Comiso & Zwally, 1984) and has rationally been used to define the ice edge – and subsequently the perimeter of the sea-ice extent. This threshold was originally proposed by validation studies showing it best matches satellite passive microwave observations (Cavalieri, 1991). It also avoids distortions from post-processing filters used to remove weather-related noise which may inadvertently exclude low-concentration ice (e.g. Partington, 2000). However, the accuracy of the 15% threshold can vary depending on ice conditions near the edge, which often consists of fragmented, thin floes and open water. Different passive microwave sensors and retrieval algorithms may over- or underestimate concentrations in such cases, ultimately yielding different SIE estimates (Comiso & Steffen, 2001; Meier & Stewart, 2019). These factors must be considered when comparing sea-ice extent across different satellite products. Notably, it is therefore a metric based on the constraints of detection rather than having specific physical meaning or presence, and does not capture information regarding the thickness, floe properties or the consolidation state of the ice cover. SIE treats all grid cells with >15% SIC equally, regardless of their actual concentration. In contrast, sea-ice area (SIA) accounts for the actual ice coverage within each grid cell by summing fractional concentrations (WMO, 2014). While SIA provides a more precise measure of ice-covered surface, it is more sensitive to retrieval inaccuracies in satellite algorithms. Consequently, SIE is favoured for large-scale trend analysis due to its stability and simplicity,

particularly in climate and ecosystem modelling as an attempt to describe a complex distribution of sea ice as a simplified parameter. A large portion of the total sea-ice cover in the Southern Ocean – compared to ice coverage in the Arctic – is the Marginal Ice Zone (MIZ). This is a highly dynamic region with considerable spatial and temporal variability over just hourly or daily timescales (WMO, 2014). This region represents the transitional interface between consolidated sea ice and the open ocean, and its distribution holds considerable climatic and ecological importance. However, defining the MIZ is complex, as different approaches emphasize distinct physical properties. A widely used method defines the MIZ as the region where sea-ice concentration (SIC) lies between 15% and 80%, capturing the gradual transition from dense pack ice to open water. This threshold-based definition is prevalent due to its practical advantages, particularly its compatibility with global-scale observations derived from passive microwave satellite sensors. Alternative SIC-based definitions have also been proposed, whereby the statistical spread of SIC values over space and time are considered, rather than the threshold values based on retrieval limitations (Vichi, 2022). These retrieval limitations are discussed further in Section 1.4. Alternatively, some definitions are based on wave–ice interactions, identifying the MIZ as the region where ocean waves propagate into and attenuate within the ice, exerting significant influence on sea-ice dynamics through processes such as breakup and collision-induced stress (Williams et al., 2013). From a remote sensing perspective, wave activity in sea ice has been estimated using Synthetic Aperture Radar (SAR) imagery (Ardhuin et al., 2017; Stopa et al., 2018) and satellite altimetry (Brouwer et al., 2022; C. Horvat et al., 2020), enabling estimates of MIZ distribution based on wave–ice coupling. Another approach delineates the MIZ by floe type and size distribution, identifying it as the zone where mechanical interactions among ice floes are shaped by wave-induced fragmentation. This perspective is particularly useful for describing regions dominated by pancake ice – small (2.3–4.0 m), elliptical ice floes that form in mechanically active environments (Alberello et al., 2019; Wadhams et al., 2018). Pancake formation begins when grease and frazil ice consolidates into nearly circular ice floes under the influence of wave action. These floes cement and raft over one another, leading to the development of thicker, more resilient ice structures (Paul et al., 2021). Pancake ice is often considered a precursor to consolidated ice formation in the MIZ as it allows increased heat loss from the ocean to the atmosphere due to the heterogenous surface (Doble et al., 2003; Doble & Wadhams, 2006; Roach et al., 2018). This accelerates ice growth and thus ultimately influences

the evolution of the sea-ice landscape. Recognizing the limitations of any single criterion, a multifaceted approach that incorporates sea-ice concentration, wave activity, and floe size distribution may be necessary to provide a more comprehensive characterization of the MIZ, capturing its role in climate interactions, sea-ice mechanics, and associated ecological processes (Dumont, 2022).

Atmospheric weather events, such as polar and extra-tropical cyclones, influence SIC on daily timescales by generating strong winds that compress or disperse sea ice, leading to localized increases or decreases in SIC (Vichi et al., 2019). This potentially causes short-term fluctuations in SIE without significant changes in overall ice volume. Oceanic processes primarily affect SIC on longer timescales (seasonal to interannual) through mechanisms such as surface currents and sea surface temperature (SST) variability (Meehl et al., 2019). A more in-depth look of these interactions was detailed in Sections 1.3.1 and 1.3.2, but overall, Antarctic sea ice is characterized by the highly variable SIE depicted in Figure 1.7. Between 1978 and 2016, it exhibited a slight overall increase, with significant regional and seasonal variability. However, since 2016, a sharp decline has been observed, culminating in record-low SIE in 2023 and 2024 (Gilbert & Holmes, 2024). This abrupt change has raised questions about the roles of atmospheric and oceanic drivers, and whether anthropogenic forces superimposed on natural climate variability may have yielded a new sea-ice state characterized by a gradual decline rather than extreme variability (Fogt et al., 2022; Hobbs et al., 2024; Purich & Doddridge, 2023). In contrast, Arctic sea ice has experienced a consistent and dramatic decline over the satellite era, with summer minimum SIE decreasing by approximately 10% per decade (Comiso et al., 2008; Parkinson & Comiso, 2013; Stroeve & Notz, 2018). Arctic ice is also thinning, transitioning to a younger, more seasonal ice cover (Kacimi & Kwok, 2022; Kwok, 2018). Understanding Antarctic sea ice, with its highly seasonal and dynamic characteristics, may provide insights into the future evolution of Arctic sea ice.

Sea-ice type is a subdivision of SIC that provides more detailed information about the ice cover. Different sea ice types are classified based on age, thickness, physical properties and stage of development (WMO). Albeit subjective, this classification provides critical insights into sea-ice dynamics, as different types have distinct impacts on climate and ecosystems. For instance, multi-year ice is thicker, more deformed, and typically supports higher snow cover, whereas first-year ice is thinner, rougher and more vulnerable to

melting. In the Arctic, multi-year ice has declined significantly, at approximately $13 \pm 2\%$ per decade (IPCC, 2023), reflecting a shift toward a less stable, first-year-dominated regime. The Antarctic, in contrast, is predominantly composed of seasonal first-year and young ice, with limited evidence of significant trends in ice type (Melsheimer et al., 2023). Notably, the ice-type separation is possible because radiometric data are sensitive to the differing properties for the ice types, yielding a pathway to distinguishing ice-type via remote sensing techniques. These techniques are further detail in Section 2.1.2, and an in-depth analysis of a modified sea-ice type retrieval algorithm using passive microwave data is presented in Chapter 5.

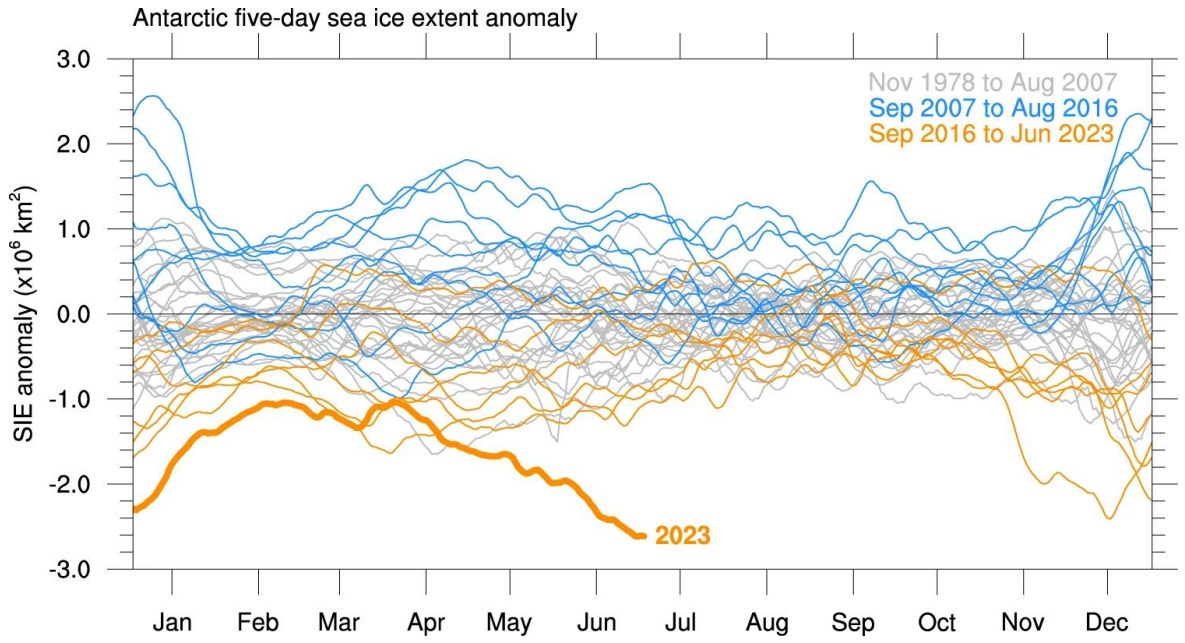


**Figure 1.7: Antarctic five-day sea ice extent anomalies for each year from the National Snow and Ice Data Center. Sea ice extent anomalies are calculated relative to the 1979–2022 climatology. Anomalies are coloured by period: November 1978 to August 2007 (grey), September 2007 to August 2016 (blue), and September 2016 to June 2023 (orange). January to June 2023 is shown in bold orange, with the largest negative areal extent anomaly of the satellite era observed during June 2023. Source: Purich & Doddridge (2023).**

## 1.5 Sea-Ice Motion in Response to External Forcing

### 1.5.1 Sea Ice Advection

Sea-ice advection or drift refers to the horizontal movement of sea ice driven by environmental forces. This process significantly influences the variability of sea ice across the Southern Ocean, making it necessary to understand the dynamics governing ice drift. The primary factors influencing sea-ice motion include wind stress, ocean currents, rheological properties, sea surface gradients, inertial oscillations, and the Coriolis effect (Martinson & Wamser, 1990; McPhee, 1988; Womack et al., 2024). Among these, wind stress is the dominant driver, accounting for approximately 40% of the variance in ice drift (P. Holland & Kwok, 2012; Kwok et al., 2017; J. Uotila et al., 2000; Vihma et al., 1996). Friction transfers momentum from wind and water to the ice, while kinetic energy is dissipated through internal ice stressors such as compression and tensile stress. The balance between the external and internal stressors determines the ice *deformation* – the term describing changes in the shape and arrangement of the ice cover, which will be discussed further in the following Section 1.5.2. The *Coriolis effect* – resulting from Earth's rotation – deflects ice motion to the left in the Southern Hemisphere by an angle typically ranging from 0° to 45°, relative to the driving force (Ekman, 1905; Leppäranta, 2005; Thorndike & Colony, 1982). Consequently, anticlockwise rotation (in the Southern Hemisphere) will establish a zone of convergence as ice is deflected inwards, squeezing it together into a thicker and more consolidated floes. Conversely, clockwise rotation will deflect ice outwards, spreading ice apart and promoting an unconsolidated composition of heterogenous ice types (Kwok, 2015; Kwok & Cunningham, 2012). Wind-stress associated with synoptic weather systems (e.g. cyclones, high pressure cells) engender rotational motion in the underlying sea-ice field at daily timescales (de Jager & Vichi, 2022; Vichi et al., 2019). In the Southern Ocean, the cyclonic rotation associated with the Weddell and Ross Seas gyres promote sea-ice divergence in these regions and facilitate its northward export into warmer regions (Drinkwater & Liu, 1999; Vernet et al., 2019), explaining why summer sea-ice distribution – and consequently the multiyear ice distribution – is primarily limited to the coastal zones in the Weddell and Ross Seas (Melsheimer et al., 2023; Vichi, 2022). The Coriolis effect also influences sea-ice advection in the form of inertial oscillations, which describe the loop-

like drift trajectories of moving ice occurring at semi-diurnal timescales. These oscillations are seasonally dependent with a greater influence in melting conditions (Womack et al., 2024), and decay over a few days due to frictional damping and internal stresses (Doble & Wadhams, 2006; Gimbert et al., 2012; Heil et al., 2009; Kottmeier & Sellmann, 1996).

Sea-ice drift variability is governed by a combination of dynamic (advection and deformation) and thermodynamic processes (ice formation and melt). The relative importance of these processes changes seasonally: dynamic processes dominate during the freezing months, while thermodynamic processes are more influential during melting (Schroeter et al., 2017, 2018). More specifically, the advective component of sea-ice distribution variability can be described by the momentum equation:

$$m\frac{\partial u}{\partial v} = \nabla \cdot \sigma + \tau_a + \tau_o - Cmk \times u - mg\nabla \mathrm{H} \tag{1.1}$$

where $m$ is the mass of the ice and $\tau_a$ and $\tau_o$ are atmospheric and ocean forcing, respectively. Sea ice strength and rheology are considered in the internal ice stresses term σ. The final two terms quantify the Coriolis Effect and the gravitational acceleration associated with sea the surface height, respectively (Golden et al., 2020), although these contributions are relatively minor over shorter timescales relative to external forcing. The momentum equation (Equation 1.1) indicates that both external forcing and the energy dissipation associated with internal stresses effect the motion of the sea-ice. As discussed in Section 1.3.1, wind forcing is the primarily mechanisms of redistribution, and a common rule-of-thumb is that Antarctic sea ice generally drifts at 1-4% of the speed of the overlying wind stress – the $\tau_a$ term in Equation 1.1 – although faster speeds have been reported in free drift conditions (Alberello et al., 2020; Womack et al., 2022). This is about 50% faster than Arctic sea ice, a discrepancy mostly due to the thinner and less compact nature of Antarctic sea ice (Kottmeier et al., 1992; Kwok et al., 2017; Leppäranta, 2005), as thicker ice drifts more slowly and responds less to wind forcing (Fukamachi et al., 2011). Other rheological properties such as floe size and concentration – represented by the σ term in Equation 1.1 – also influence sea-ice resistance to mechanical forcing, (Heil et al., 2011). Thus, while wind stress is the primary driver of sea-ice dynamics, the feedback interactions between its deformation and mobility means that the

thermodynamic processes governing its rheology must also be considered and will be further discussed in Section 1.5.2.

Antarctic sea-ice drift patterns are closely linked to broader climate dynamics, as trends in ice drift, export, and circulation patterns are associated with atmospheric circulation changes, dense water formation, and sea-ice coverage variability (Kwok et al., 2017). Large-scale drift anomalies are driven by seasonality and modes of climate variability, including the Southern Oscillation and the Southern Annular Mode as introduced in Section 1.3.1, primarily through modulation of westerly wind intensity during different phases of their superposition (Kwok et al., 2016; Stammerjohn et al., 2008; Yuan & Li, 2008). Trends in the position of the ice edge – typically defined as the 15% sea-ice concentration contour – correlate with meridional wind variability on monthly timescales and synoptic weather events on daily timescales (Kwok et al., 2017; Vichi et al., 2019). This meridional transport of ice is responsible for the zonal asymmetry of sea-ice coverage around Antarctica. Three persistent cyclonic drift patterns are governed by the location and strength of atmospheric low-pressure cells in the Amundsen, Riiser-Larsen, and Davis Seas (illustrate with the red "+" symbols in Figure 1.8). Seasonal sea-level pressures at the three centres are interlinked, suggesting circumpolar teleconnections in the atmosphere and consequently somewhat synchronised variability in their associated wind-driven drift patterns (Kwok et al., 2017).

Measuring sea-ice drift involves satellite remote sensing, numerical modelling, and *in situ* data collection, which is central to the focus of this thesis. Satellites offer broad and regular spatial coverage but limited resolution for sub-grid scale processes. Furthermore, systematic estimates of large-scale drift dynamics usually rely on automated digital image processing techniques rather than direct tracking, consequently introducing retrieval error and method biases (Lavergne et al., 2010). Discussion on satellite drift retrieval is detailed further in the following Section 2.1.1. Drifting buoys equipped with GPS or Argos transmitters provide high-resolution *in situ* position data for calibration and validation of satellite observations and models, though deployment costs and logistical challenges restrict expanding their use substantially (Rabault et al., 2020; Womack et al., 2024). Numerical models simulate ice dynamics and offer predictive capabilities but are limited by uncertainties in parameterizations and an incomplete understanding of rheological processes, and often fail to simulate the heterogeneity and intermittency in sea ice deformation

(Girard et al., 2009). Combining these approaches yields the most comprehensive assessment into sea-ice drift, emphasizing the need for continued advancements in observational methods and modelling techniques to enhance our understanding of Antarctic sea-ice dynamics.

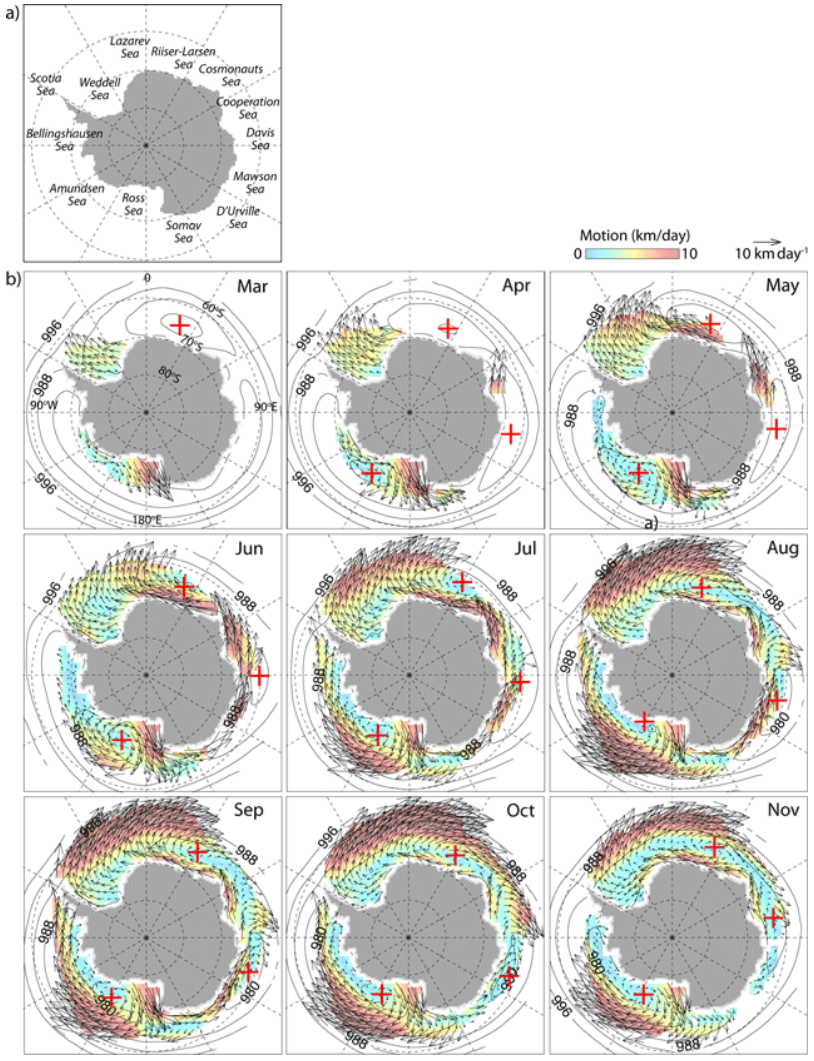


**Figure 1.8: Ice motion of the 34-year record (1982–2015). (a) Names and locations of the marginal seas. (b) Mean monthly (March through November) ice drift. Contours are isobars (interval: 4 hPa) from ERA-Interim sea-level pressure fields. Drift estimates are shown on a 200-km grid to reduce density of vectors within each plot; every other vector is displayed. Red crosses show the centres of the three atmospheric lows in the monthly mean fields. Source Kwok et al. (2017).**

### 1.5.2 Sea Ice Rheology

Sea-ice rheology is the study of the mechanical properties of sea ice, describing how it moves, deforms, and responds to external forces. Understanding rheology is necessary for examining sea-ice motion variability and the mechanisms linking it to oceanic and atmospheric influences. External forces, primarily from wind stress and ocean currents, impart friction onto the sea-ice field, modifying its horizontal momentum and internal stresses (Feltham, 2008). Internal stresses arise from the material properties of the sea-ice, including its temperature, salinity, porosity, molecular and crystalline structure, and more. These properties determine its overall resistance to compressive (squeezing), tensile (stretching), and shear (sliding) forces, as well as interactions between heterogenous ice types such as large floes, pancakes and interstitial grease ice (Hutchings et al., 2011; Paul et al., 2023; Shokr & Sinha, 2015). Internal stresses are fundamental to sea-ice dynamics as they counterbalance external forcing and govern deformation (Equation 1.1). Sea-ice deformation is not static but instead evolves over time under varying external forces and determines how the sea ice responds to subsequent environmental conditions. Convergent deformation, driven by compressive forces from winds, surface currents, or ocean swells, increases ice collisions at multiple spatial scales, resulting in thicker features like pressure ridges and rafted ice – as discussed in Section 1.3.1.1 with Figure 1.3 (Heorton et al., 2018; Shokr & Sinha, 2015). This thickened ice becomes more resistant to further deformation. Conversely, divergence can drive the formation of leads, which describe the openings within the sea-ice field which promote ocean-atmosphere heat and mass exchange. Shear deformation occurs when ice slides past each other, which can create cracks in consolidated floes that promote its breakup. Deformation is quantitatively described by strain rates, which measure the rate of change in the shape of a material, including divergence (expansion or contraction), shear strain (lateral motion or twisting), and rotation (Feltham, 2008). Internal stresses and resulting deformations dissipate kinetic energy, establishing an energy balance with external forces (Bouillon & Rampal, 2015). This dissipation is a key component in sea-ice dynamics and influences the accuracy of numerical models that simulate momentum transfer. Improved representation of these mechanisms is a key milestone towards the development of improved sea ice forecasting (Hunke et al., 2011).

In the Antarctic, intense weather systems like polar and extra-tropical cyclones significantly alter the sea-ice surface heterogeneity and ultimately its rheology over short timescales by subjecting the ice to strong winds, waves, and warm, moist air masses (Kohout et al., 2014; Vichi et al., 2019). As indicated by the momentum equation (Equation 1.1) in Section 1.3.3, the rheological properties of the sea-ice field are important for understanding its motion, as small-scale changes in ice's material properties can have large-scale impacts on overall ice dynamics. Much of the observed variability in Antarctic sea ice is rooted in the rheological differences between various types of ice. Practically, sea-ice deformation can be measured using ice-tethered buoys (Hutchings et al., 2011; Itkin et al., 2017; Rampal et al., 2008; Womack et al., 2022) and high-resolution satellite imagery (Kwok et al., 1990). However, limitations in *in situ* data coverage and satellite spatial resolution make it challenging to determine mechanical properties over large regions. Traditional assumptions about sea-ice mechanics often rely on sea-ice concentration variability, where higher concentration is associated with thicker, more resistant ice due to enhanced ridging and rafting (Auclair et al., 2022; Lange & Eicken, 1991; Worby et al., 2013). However, dynamic drift has been observed deep within the pack-ice, contradicting earlier assumptions that interior regions represent consolidated and relatively immobile ice (Alberello et al., 2020). Thicker ice supports higher internal stresses, providing greater mechanical resistance, while thinner ice is weaker and more prone to deformation (Leppäranta, 2005; Wilchinsky & Feltham, 2004) and so pack-ice mostly constitutes a complex mosaic of heterogenous ice types rather than thick, uniform ice cover. Air temperature also affects ice strength: warmer temperatures soften the ice, increasing its susceptibility to internal stresses, whereas colder temperatures make it more rigid and resilient (Heorton et al., 2017). The pack-ice zone, characterized by thick, continuous ice floes extending tens-to-hundreds of kilometres, is typically located between the landfast ice and the MIZ. Large, consolidated floes exhibit greater inertia and reduced variability. In contrast, MIZ experiences direct oceanic and atmospheric forcing, making it more dynamic and variable (Vichi, 2022). The MIZ comprises smaller, thinner, and unconsolidated floes, often including pancake ice formed from frequent collisions and breakups (Alberello et al., 2020; Doble et al., 2003). Mechanical differences between these zones affect their response to external forces, and observing these distinctions is required for interpreting sea-ice behaviour and improving predictive models.

## 1.6 Satellite Observation and Modelling of Sea Ice

Quantifying sea-ice properties is essential for understanding the processes governing its variability and predicting future trends in response to changing environmental conditions. Although *in situ* data collection provides reliable measurements across a wide range of sea-ice properties, its role is limited by logistical challenges fieldwork and so are inherently sparse and localized which restricts their spatial and temporal coverage. This limitation is emphasized as spatial and temporal scales grow and shrink, respectively (Giles et al., 2011). To overcome these limitations, satellite-based observations and modelling have become key tools for supplementing *in situ* samples and addressing data gaps. Satellites equipped with specialized instruments – such as passive microwave sensors, radar, and optical imagers – provide continuous, large-scale observations of sea-ice properties and allow for the monitoring of sea-ice variability at daily timescales. However, remote sensing alone cannot fully capture this variability, as only surface properties with a recognizable radiometric appearance can be detected. Sea-ice models complement observations by simulating physical processes, including ice formation, melting, and interactions with atmospheric and oceanic forces. Models facilitate the study of sea-ice variability across a range of timescales – from daily weather-induced fluctuations to multidecadal projections under different climate scenarios – while enabling the testing of hypotheses about underlying mechanisms. Nonetheless, modelling efforts are challenged by uncertainties in parameterizations, input data, and the representation of complex processes like ice rheology, floe advection, environmental interactions, and unresolved sub-grid-scale variability (Hunke et al., 2011).

The synergy between remote sensing and modelling is crucial for advancing our understanding of sea-ice dynamics. Satellite-derived data improve model accuracy, while models offer a framework for interpreting observations and forecasting future changes. Robust observational datasets are required for testing model simulations, yet challenges persist in measuring sea-ice variability at relevant temporal and spatial scales. Short-term weather events, such as cyclones, induce rapid changes in sea ice, necessitating high-resolution satellite data to supplement ice-models that aim to resolve atmospheric and oceanic related processes. Conversely, assessing long-term trends in sea-ice extent and thickness requires sustained, multi-decadal observations to validate model predictions.

### 1.6.1 Remote Sensing using Passive Microwave

Remote sensing is a powerful method of data acquisition for monitoring Antarctic sea ice variability, involving the use of sensors mounted onto satellites which orbit the Earth and continuously scan its surface. As vast and frequent sampling of the Antarctic sea-ice landscape is not logistically plausible, measurements from space has become one of the most effective applications of Earth observation data. Various retrieval methods utilizing satellite-derived data have allowed us to gather over 50 years of systematic and robust estimates of certain sea-ice properties, including three *Essential Climate Variables* (ECV). An Essential Climate Variable describes a key parameter for understanding of the global climate system and its changes, defined by the Global Climate Observing System (GCOS). These variables cover atmospheric, oceanic, and terrestrial domains and are identified as necessary for observing based on their significance in climate processes and feasibility of their measurement (Teresa et al., 2019). Concentration, thickness and motion are the three Essential Climate Variables associated with sea-ice measurements from space (Lavergne et al., 2022).

One of the most widely used remote sensing techniques for measuring sea ice is the use of passive microwave sensors. Here, *passive* informs that these sensors detect naturally emitted microwave radiation from the Earth's surface, and *microwave* informs the frequency range of the radiation being measured. The radiation emitted by sea ice and water differs because of the contrast in their dielectric properties, which refers to the ability of a material to store and transmit electromagnetic energy, which ultimately influences how much microwave radiation is emitted or reflected by the surface (Meier, 2019). In the context of sea-ice research, passive microwave sensors typically operate in the 19 to 37 GHz range, although some retrieval algorithms designed for specific use cases will utilize frequencies beyond this range. The data collected by passive microwave sensors are processed to derive a variable known as *brightness temperature*. Brightness temperature ($T_b$) is a measure of the microwave radiation emitted by the surface area which is related to the physical temperature and the radiative properties (Comiso et al., 2011), and can be defined as:

Here, $T_{physical}$ is the physical temperature of the surface and ε is the emissivity – a function of the electromagnetic properties of the surface, the radiation frequency and the polarization. $T_b$ is therefore not a direct measurement of physical temperature of the surface but rather a measure of the emitted energy, which is proportional to its temperature. For sea-ice applications, brightness temperature data is sensitive to the temperature difference between sea ice and open water because the ice emits more energy than the water, thus enabling the discrimination of these surface types in satellite imagery (Meier, 2019). This information is then processed using various retrieval algorithms, which interpret the brightness temperature data to produce maps of sea ice (Cavalieri et al., 1984; Comiso, 1983; Lavergne & Down, 2023; Shokr et al., 2008). These maps can then be used to study sea ice variability over time and space.

One of the key advantages of passive microwave sensors is their ability to operate in all weather conditions, including during cloud cover (Comiso, 1983). This is especially important in the Antarctic, where regular cloudy conditions mean that traditional optical sensors cannot measure the surface. Additionally, passive microwave sensors do not rely on sunlight, thus they can collect data during the long polar nights and ensure continuous monitoring of sea ice throughout the year (Meier, 2019; Swift & Cavalieri, 1985). Another major benefit of passive microwave sensors is their large *footprint*, which refers to the area on the Earth's surface that a sensor can observe from any given location. Notably, brightness temperature measurements from space are therefore not a point-based measurement, but rather the average radiance emitted over the footprint's surface area. A generalized schematic of the satellite scanning processes is shown in Figure 1.9. A broad strip of surface measurements is generated along the orbital track, termed a *swath*, which is composed of sequential footprints recorded as the satellite moves along its orbital track. Depending on the specific sensor, this footprint can range from 3 to 50 kilometres, allowing for broad coverage of the Arctic and Southern Oceans. This large spatial coverage makes passive microwave data a good candidate for monitoring daily sea ice variability at regional to global scales, although it comes at the cost of spatial resolution. While passive microwave sensors can excel at providing an overview of sea ice behaviour across the entire Antarctic region, the coarse resolution can make it impossible to resolve small-scale features such as narrow leads, cracks in the ice, floes size or the detailed structure of the marginal ice zone. As highlighted in Section 1.5.2, these finer details are necessary to understand localized sea ice dynamics better. Modern passive microwave sensors have a spatial resolution of 3.125 km (JAXA, 2012),

which typically limits their use to larger-scale regional sea-ice analysis and demonstrates a limitation of current passive microwave data acquisition methods. Additionally, passive microwave sensors are less effective at detecting ice thickness, which is a key parameter for understanding sea ice variability (Kaleschke et al., 2012). While passive microwave data can provide some indirect information about sea ice thickness through the detection of surface roughness or snow cover, other technologies such as radar and laser altimetry are better suited for direct thickness measurements (Zwally et al., 2008).

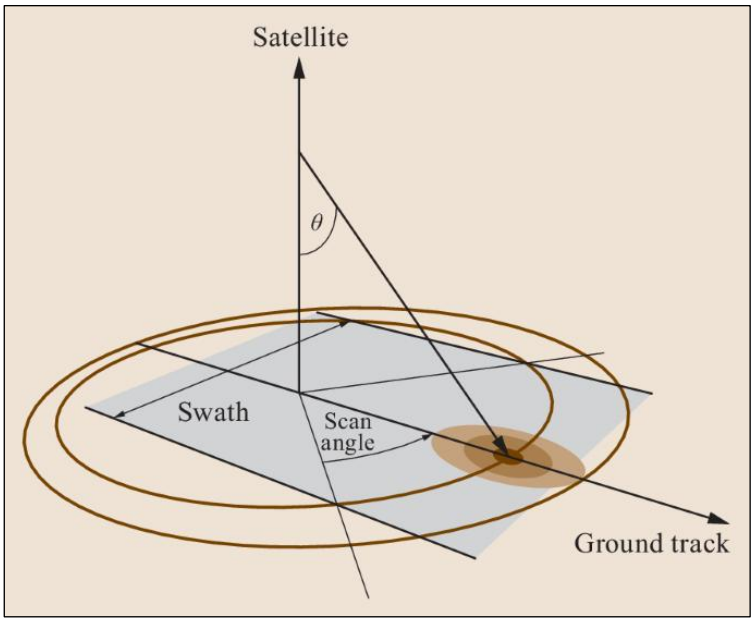


**Figure 1.9: Generalized schematic of satellite data acquisition using conical scans. The scan angle dictates the width of the swath (blue area) which is based on a row of adjacent footprint scans (brown shaded area) along the ground track. Angle Θ indicates the scanning incidence angle, typically 50-55° for passive microwave scanners. Source: Crewell et al. (2021).**

### 1.6.2 Sea-Ice Modelling

Sea-ice modelling involves the application of mathematical and computational techniques to simulate the physical properties, dynamics, and thermodynamics of sea ice. These models are essential tools for testing current scientific understanding of sea-ice behaviour and interactions, as well as for simulating historical and future scenarios. These models are designed to simulate the physical processes that affect sea ice formation, movement, and melting, which in turn play a role in regional and global climate and ocean dynamics. As discussed in Section 1.3, sea ice can be studied at varying spatial and temporal scales, depending on the research objective. Global Climate Models (GCMs) typically employ parameterizations to approximate small-scale processes while resolving large-scale atmospheric and oceanic circulation patterns and heat fluxes. *Parameterization* refers to describing complex physical systems using simplified functions based on independent variables, which allows for the efficient use of computational resources. This method is particularly important in large-scale modelling where the direct resolution of all physical mechanisms, if known, is computationally prohibitive. Furthermore, parameterizations enable the integration of different models, a necessity for streamlined collaboration between independent research groups. GCMs generally operate at relatively low spatial resolution, focusing on long-term variability and trends. Early sea-ice models – constrained by limited computing power – often represented sea ice as either stationary or freely drifting fields of uniform thickness that did not participate in thermodynamic or chemical exchanges (Hibler & Bryan, 1987). However, thermal conduction at the ocean-air interface influences vertical temperature gradients in both, in addition to sea-ice growth and melt. Consequently, modern models incorporate dynamic and thermodynamic sea-ice properties – such as concentration and thickness – for more comprehensive simulations (Holmes et al., 2022; Notz, 2020). This coupling improves the representation of critical processes that depend on ice coverage and volume, like ice-albedo feedback, heat and gas exchanges, ice transport, and ocean stratification.

Operational and regional forecasting models prioritize short-term predictions, spanning days to weeks, and often employ higher spatial resolution to resolve finer-scale processes. These include polynyas, snow cover variations, floe interactions, wave attenuation, etc. Such models have practical applications beyond research, for example, in producing sea-ice distribution charts to support maritime navigation. The

increased detail simulated by these models is computationally demanding and therefore typically focus on shorter timescales. They also serve to refine parameterizations used in broader-scale GCMs. This is visualized by Figure 1.10, illustrating that adjacent cells in the model exchange information between them (through horizontal and vertical exchanges) but smaller scale processes within each cell are not resolved. Balancing computational efficiency with the need to represent smaller scale processes remains a significant challenge in model design, often meaning that sub-grid processes are relevant but not explicitly resolved. While parameterizations help manage computational demands, they inevitably simplify physical representations, potentially reducing model accuracy (Notz, 2014). Data assimilation – the integration of observational data into models – improves predictive capabilities, but observational data itself remains a critical bottleneck (Kimmritz et al., 2018; Stark et al., 2008). *In situ* data collection is logistically challenging and costly in polar regions, while satellite-derived observations often rely on indirect inferences from radiometric measurements of sea ice. This limitation underscores the ongoing need for robust data to validate and calibrate models. However, there remains substantial uncertainty in climate model simulations of Antarctic sea ice, particularly in reproducing observed long-term trends and interannual and regional variability (Notz, 2014; Roach et al., 2020). Discrepancies between model outputs and satellite observations are often attributed to limitations in parameterizations, biases in atmospheric or oceanic forcing, and the underrepresentation of critical processes such as sea-ice dynamics, melt pond evolution, and ice-ocean-atmosphere coupling (Bracegirdle et al., 2015; M. Holland et al., 2017; Li et al., 2023; Massonnet et al., 2011; Notz, 2015). In this thesis, the observational analysis presented offers insights that can help constrain and improve these models, particularly by identifying patterns of variability and mechanisms that are currently misrepresented or unresolved.

Despite these challenges, sea-ice models offer two major advantages over direct sampling or remote sensing alone. First, they provide diagnostic tools that isolate and examine the mechanisms driving sea-ice variability. Second, they enable predictive modelling of complex, interactive systems. As the impacts of high-latitude climate change become increasingly evident (e.g. Hahn et al., 2021; M. Holland & Bitz, 2003; Smith et al., 2019), the importance of sea-ice modelling in climate research continues to grow. Advancing the representation of sea-ice processes and their interactions within climate models remains crucial. Although this thesis does not explicitly focus on the modelling of sea ice, the motivation of this research

that will be presented in the next section is related and twofold: (a) to characterize aspects of sea-ice variability that are inadequately represented or unresolved in current sea-ice models and (b) to extract valuable insights from satellite observations that can aid and supplement the sea-ice modelling community's efforts.

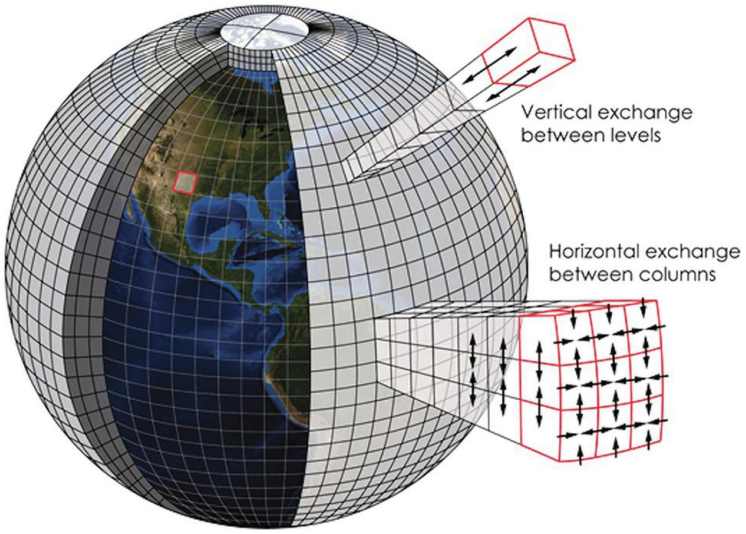


**Figure 1.10: A generalized schematic depicting the spatial resolution of a Global Climate Model (GCM). Adjacent cells exchange information through vertical and horizontal exchanges, but sub-grid scale processes are represented as parameterized function rather than being resolved explicitly by the model. Source: Kotamarthi et al. (2021).**

## 1.7 Research Aims and Thesis Outline

### 1.7.1 Research aims

To achieve the overarching goal of examining the influence of synoptic systems on Antarctic sea-ice dynamics and thermodynamics, and improving satellite monitoring techniques, this thesis focuses on the following objectives:

I. Evaluate the capability of selected satellite-derived sea-ice motion products to capture rotational dynamics in Antarctic sea ice driven by synoptic-scale weather systems.
II. Quantify and compare the relative intensity of sea-ice rotation induced by cyclones versus high-pressure systems, assessing detection uncertainties associated with satellite retrievals.
III. Conduct a long-term analysis of sea-ice rotation dynamics, identifying trends, interannual variability, and regional differences.
IV. Correlate long-term sea-ice rotation dynamics with overlying wind stresses to evaluate the efficiency of rotational wind forcing on sea ice.
V. Assess the advantages and limitations of using swath-based satellite retrieval techniques for estimating rotational drift and concentration changes at sub-daily timescales.
VI. Decompose sub-daily variability in satellite-derived sea-ice concentration into dynamic and thermodynamic components using swath-based ice motion data.

### 1.7.2 Thesis outline

This thesis is presented as six chapters, which constitutes the following:

**Chapter 1**: Provides a broad overview of Antarctic sea ice, its variability, and the environmental factors that influence it, including atmospheric and oceanic processes. This chapter also introduces key information about remote sensing techniques used to monitor sea-ice variability and the associated challenges.

**Chapter 2**: Describes the primary datasets used in this research, including satellite-derived sea-ice concentration and motion products, and atmospheric reanalysis data. Expanding on Chapter 1, it presents a detailed technical explanation of retrieval techniques to highlight their benefits and limitations, providing necessary context for interpreting results in subsequent Chapters 3 and 4 and understanding the value of the modified retrieval approach presented in Chapter 5.

**Chapter 3**: Compares selected satellite-derived sea-ice motion products to evaluate their ability to detect rotational features driven by cyclones and high-pressure systems. The chapter quantifies the intensity of sea-ice rotation induced by these weather systems and examines the uncertainties associated with the ice

motion retrieval. Results are based on a 48-hour motion product due to the unavailability of the 24-hour product used in Chapter 4 at the time of analysis. This chapter incorporates the published study: De Jager, W. & Vichi, M. (2022). Rotational drift in Antarctic sea ice: Pronounced cyclonic features and differences between data products. *Cryosphere*, *16*(3). https://doi.org/10.5194/tc-16-925-2022. The results and discussion are taken verbatim, while introduction and methodology sections are adapted to avoid redundancy with Chapters 1 and 2.

**Chapter 4**: Analyses 30 years (1991-2020) of sea-ice rotation dynamics, assessing long-term trends and interannual variability. Regional differences are explored, and ice dynamics are compared with overlying atmospheric wind stress to assess the effectiveness of air-to-ice rotational forcing. This chapter incorporates a study accepted for publication in the *Journal of Geophysical Research: Oceans*: De Jager, W. & Vichi, M. (2025). Increased Rotational Coupling Between Antarctic Sea Ice and the Atmosphere Over the Last 30 Years (DOI not yet available at the time of thesis submission). The results and discussion are taken verbatim, while introduction and methodology sections are adapted to avoid redundancy with Chapters 1 and 2.

**Chapter 5**: Explores the potential of swath-based retrieval methods for high-frequency sea-ice concentration estimates. An existing algorithm is modified to operate on satellite footprint data, enabling sub-daily observations. The combination of swath-based ice motion and concentration products allows decomposition of dynamic and thermodynamic processes. A case study demonstrates the improved temporal resolution's benefits. Limitations and future development opportunities are discussed.

**Chapter 6**: Synthesizes the findings from Chapters 3, 4, and 5 within the broader context presented in Chapter 1. The chapter revisits the research objectives outlined in Section 1.7.1, evaluating how each has been addressed by the analyses. It also discusses limitations associated with the data sources and methodologies used and provides recommendations for future research directions to advance understanding and monitoring of short-term Antarctic sea-ice dynamics.

---

# Chapter 2 : Materials and Methods

Chapter 2 serves as a foundational component of this thesis, providing the technical and methodological context for the analyses presented in Chapters 3, 4, and 5. This chapter bridges the understanding of weather impacts on sea ice with the technical methods used to acquire observational data on these interactions. It introduces the primary datasets central to this research – specifically, satellite-derived and atmospheric reanalysis data – and examines what information can be reasonably inferred within the constraints of these data acquisition techniques. A detailed examination of satellite-derived sea-ice drift and concentration retrieval algorithms is conducted to assess their suitability for capturing short-term variability at sub-daily to daily timescales. This evaluation is necessary for determining the feasibility of describing large-scale sea-ice rotation dynamics from satellite observations. As Chapters 3 and 4 investigate the atmosphere's role in driving rotation within the sea-ice field, a comprehensive understanding of the satellite datasets is required for interpreting the robustness of observed variability and trends. Furthermore, this technical exploration establishes the current capabilities and limitations of satellite-based sea-ice monitoring and lays the groundwork for the modified retrieval algorithm developed in Chapter 5. By elaborating on these details, Chapter 2 contextualizes the advancements presented in this thesis. It connects the technical intricacies of satellite datasets with the overarching scientific objective of advancing our understanding of short-term sea-ice dynamics.

## 2.1 Sea-Ice Brightness Temperature from Spaceborne Radiometers

Reliable brightness temperature measurements of sea-ice date back to NASA Nimbus 5 spacecraft launched in 1972, which was equipped with the Electrically Scanning Microwave Radiometer (ESMR). The ESMR measured the natural radiation emitted by Earth's surface and atmosphere at the 37 GHz frequency channel (Parkinson et al., 1999; Wilheit, 1972). Here, a *frequency channel* describes the narrow band of frequencies within the electromagnetic spectrum that are being measured, while other frequencies lying outside of that band are filtered out. As technology developed, proceeding missions launched spacecraft that carried more advanced sensors. This included the implementation of *polarization filters* – a

component of the sensor that selectively measures the orientation of electromagnetic waves – and developing instruments that could measure multiple frequency channels simultaneously. In polar research applications, satellites typically follow a polar orbit, a term used to describe a high-latitude orbital track which allows for the collection of measurements close to the Earth's poles. This particular orbital track is necessary for gathering a high density of data from high-latitude regions like the Arctic and Antarctic, with satellites generally flying at altitudes of around 700 to 850 kilometres above the Earth's surface, completing approximately 14 orbits per day. This frequent coverage of vast areas of the sea-ice landscape makes the polar orbit a good choice for satellite missions with cryosphere-orientated research objectives. The spatial resolution at which these radiometers can resolve surface measurements is proportional to the size of the instrument's antenna reflector and inversely proportional to the radiation frequency channel being selected for. Older radiometers (e.g. SSM/I and SSMIS) were equipped with reflectors 0.6 m in diameter, while more modern sensors utilize 1.6-2.0 m diameter reflectors (e.g. AMSR-E and AMSR-2), with the upper limit of the reflector's size restricted by the logistical challenges involved in launching the payload into space. Modern radiometers can resolve to ~50 km at lower frequencies (6.93 GHz) and ~4 km at higher frequencies (89.0 GHz) (Hori et al., 2010; Imaoka et al., 2010; Kawanishi et al., 2003). The discrepancies in the spatial resolutions at different frequencies is an important consideration when deriving sea-ice properties, as many derived parameters use a combination of measurements from multiple frequency channels. This means that deriving the desired sea-ice parameter often requires a spatial interpolation step in the data processing chain, and thus the spatial resolution of the derived parameter is often limited to the resolution of its coarsest constituent. Radiometers scan in a conical scanning scheme, meaning that the radiometer's antenna rotates around the vertical axis of the satellite, tracing out a circular or conical pattern on the surface termed a footprint – as illustrated by Figure 1.9 in Section 1.4.1. The *incidence angle*, labelled as $\Theta$ in Figure 1.9, of approximately 50° is used, which describes the angle between the sensor's line of sight and the portion of the surface being observed. This specific angle maximises the contrast in brightness temperature between sea ice and open water due to their differing emissivity properties. At around 50-55°, the emissivity of sea ice remains relatively high, while that of open water is significantly lower, resulting in a pronounced distinction in the observed microwave signal (Kern et al., 2020).

### 2.1.1 Sea-Ice Drift from Space

Satellite-derived sea-ice drift can be estimated by detecting and tracking ice cover features across consecutive microwave radiometer images (e.g. Kwok et al., 1998; Lavergne et al., 2010). This is done by systematically selecting a spatial feature in an initial gridded brightness temperature image and then by identifying that same feature in a subsequent image. In this context, an *ice feature* describes a specific assortment of values in a gridded field of brightness temperature measurements – although the application of this approach is not limited brightness temperature and can be applied to a range of gridded scalar quantities, having been first used to compute sea surface velocities from infrared observations (Emery et al., 1986). Locating the start and end locations of the ice feature from one image to the next thus yields its relative displacement. For sea-ice drift, the identification and detection steps of the processing chain are automated using the *Maximum Cross Correlation* (MCC) technique. The MCC technique describes a digital image processing algorithm whereby a matrix of scalar quantities is defined in the initial image (reference block) and then compared against all possible matrices in the subsequent image (candidate blocks). The candidate block which yields the largest cross correlation to the reference block is assumed to represent the same feature, yielding the change in location of the block, and thus its displacement between images can be inferred. This process is systematically repeated over the entire image to generate a map of displacement vectors over the entire sea-ice extent. The size of the reference block is an important parameter, as it must be large enough such that it can be found in the subsequent image, but small enough as to resolve the desired details of the ice dynamics. The spatial resolution of the drift data is therefore inherently constrained by the resolution of the passive microwave image and is typically 5-10 times coarser depending on the size of reference block chosen. This technique has shown to be a robust way to monitor large-scale sea-ice motion patterns using low resolution passive microwave data (e.g. P. Holland & Kwok, 2012; Kwok et al., 2017; Matear et al., 2015), meaning that it has a major benefit of being able to be retroactively applied onto historical passive microwave datasets – a valuable benefit for climatological studies. However, some significant limitations exist. As the MCC technique is essentially a feature-tracking method across a discretized time dimension, it is required that the radiometric appearance of the ice feature persists between subsequent images. In other words, the algorithm attempts to find a matching pair of

matrices between two images (reference and candidate blocks), but if the ice has experienced a change that effects its radiometric appearance within the observation window (e.g. melting, freezing, deformation, precipitation, etc), then the resultant feature would not be recognizable in the subsequent brightness temperature image, yielding an erroneous displacement vector. As a result, the MCC typically performs poorly in the MIZ due to the rapid dynamic and thermodynamic changes associated with sea ice in this region. Additionally, further uncertainty is introduced when generating the daily brightness temperature maps on which the algorithm is applied. Here, independent swath measurements are binned, averaged and sewn together to generate one full coverage map. This causes the spatial blurring of an ice field in motion, while also creating temporal ambiguity of the measurement's timestamp (Kwok et al., 1998).

The MCC technique is susceptible to *quantization noise* (Lavergne et al., 2010). Quantization noise describes the difference between the actual signal and the quantized signal, caused by the discretized approximation of an ice field that exists in continuous space. So, as ice moves along its continuous plane on the ocean's surface, the feature may fall at the intersections of the gridded, discretized plane in the subsequent image. The discretized quantification of the ice feature will thus appear different between the two images, increasing the uncertainty associated with pairing the reference and candidate blocks. Figure 2.1 is an idealized diagram illustrating the quantization noise in the context of sea-ice concentration measurements from space. Here, the ice feature (red rectangle) is moving left-to-right along a continuous plane, where columns $t_0$ and $t_1$ represent the location of the ice feature in the initial and subsequent images, respectively. $Row_A$ shows the real-world feature in the continuous plane, while $Row_B$ demonstrates the appearance of the feature in the discretized, digital domain determined by its radiometric appearance. Here it is shown that the appearance of the feature is dependent by its location relative to the grid intersections on the discretized domain, thus making identifying the same feature in image $t_1$ challenging. This error is particularly prominent when the ice displacement is small relative to the spatial resolution of the image, as the feature is more likely to fall at the intersections of the discretized plane and appear distorted.

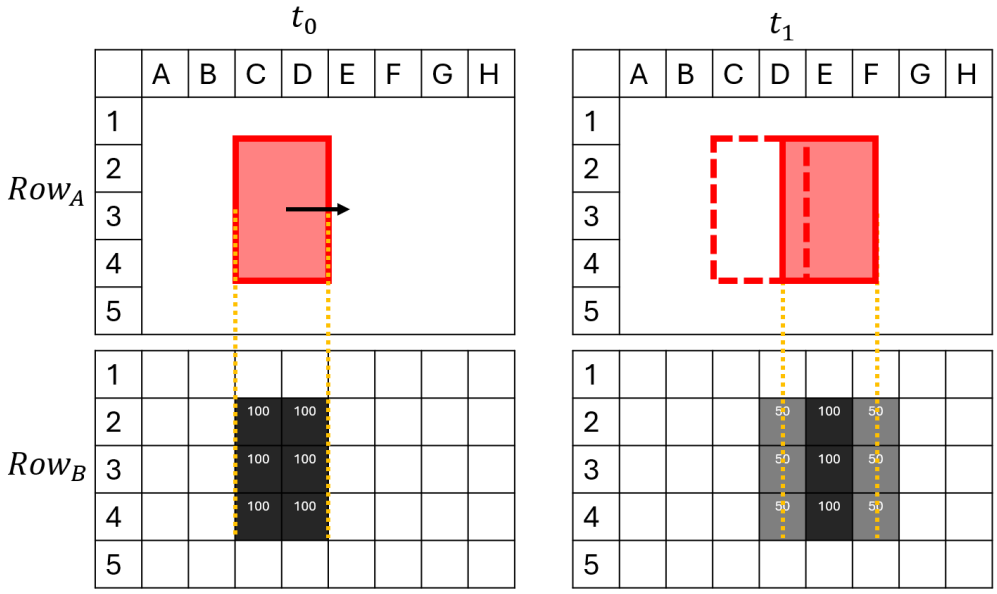


**Figure 2.1: An idealized diagram illustrating the quantization noise associated with detecting an ice floe using a gridded brightness temperature measurement over the whole domain. $Row_A$ represents the real-world ice floe in continuous space, indicated by the red rectangle. Between time $t_0$ and $t_1$, the floe has moved towards the right, and the change in location is indicated with the dashed (location at $t_0$) and solid (location at $t_0$) rectangles. $Row_B$ represents the discretized radiometric appearance of the floe at $t_0$ and $t_1$.**

With the aim to reduce the quantization noise limitation of the MCC method, Lavergne et al. (2010) introduced a modified version termed the *Continuous Maximum Cross Correlation* technique (CMCC). This involved the computation of virtual, discretised domains that utilize a grid shifted infinitesimally small along each axis of the original grid. The MCC method utilizes a singular domain comprising of a limited number of candidate blocks. This domain can be described by:

$$D = \langle x_i;\ y_j \rangle \tag{2.1}$$

Where domain $D$ is the $xy$-coordinate system overlying the continuous plane, and $ij$ represent the discretized grid point intersections at which we have a brightness temperature measurement. Meanwhile, the CMCC algorithm generates $n$-number of domains:

$$D_n = \langle x_i + \delta x;\ y_j + \delta y \rangle \tag{2.2}$$

Where $\delta x$ and $\delta y$ described the infinitesimally small shifts of $xy$-coordinate system from the original domain $D$. The brightness temperature measurements corresponding to the original domain $D$ are then spatially interpolated onto every virtual domain $D_n$ using a bilinear interpolation scheme weighted against the distance from the original grid points. This has the effect of mimicking a continuous spatial plane while still using discretised brightness temperature measurements, ultimately reducing the quantization noise. In practice, computational resource limitations means that small but finite $\delta x$ and $\delta y$ increments are used, and the weighted interpolation scheme chosen introduces its own uncertainty. However, validation reports indicate that the additional steps applied in the CMCC processing algorithm has reduced the uncertainty of brightness temperature derived ice drift estimates when compared against ice-tethered buoys, especially for slower moving ice fields (Lavergne et al., 2010).

Throughout this thesis, the satellite derived ice motion estimates used in the analysis were derived using the CMCC technique applied onto brightness temperature measurements, publicly distributed by the European Organisation for Exploitation of Meteorological Satellites (EUMETSAT) Ocean and Sea Ice Satellite Application Facility (OSI SAF) within their low resolution sea ice drift product range. Here, a *product* refers to a type of dataset generated from satellite observations and processed for end-user applications. These datasets are transformed through processing algorithms, calibration steps and quality controls, making them useful to a broad range of operational and scientific applications. In this thesis, three unique sea-ice drift products are utilized in the proceeding chapters: OSI-405, OSI-455 and S2S, which are used for analysis presented in Chapters 3, 4 and 5 respectively. OSI-405 provides global ice displacement estimates at 62.5 km spatial and 48 hr temporal resolution – meaning that all satellite swath observation within a 48 hour window were sewn together, binned and averaged to create a single brightness temperature map on which the CMCC algorithm is applied. OSI-455 is a more recently released product which provides ice displacement estimates at 62.5 km spatial and 24 hr temporal resolution, however it was not available when the analysis in Chapter 3 was performed. In austral winter months (April – September), both OSI-405 and OSI-455 deploy the CMCC drift retrieval algorithm – which performs well in freezing conditions (RMSE of ~3km and a bias of only a few hundred meters) – while OSI-455 switches to a free-drift model

in summer months (November – February) due to the aforementioned limitations of the CMCC algorithm in highly dynamic conditions. This free-drift model derives ice drift from the momentum equation (Equation 1), where only wind and ocean forces are considered, and internal ice stresses are ignored. Spring (October) and autumn (March) datasets combine a weighted average of CMCC and free-model methods. Finally, the S2S product provides localized ice drift at 75 km spatial resolution and sub-daily frequency by applying the CMCC algorithm onto the area of overlap between two satellite swaths. Further analysis of S2S and its potential applications are presented in Section 5.2.2.

### 2.1.2 Sea-Ice Concentration from Space

Sea-ice concentration (SIC) estimates are derived empirically from satellite brightness temperature ($T_b$) observations. As discussed in Section 1.4.1, brightness temperature is a metric quantifying the radiation emitted by a surface, but notably, represents the energy radiated over an area of surface instead of at a point. This is an important distinction because the observed $T_b$ value thus describes the mean intensity of radiation emitted over a heterogenous area of ice. In practice, this means that a single $T_b$ measurement represents the combined radiation emitted from the ice and water within the area of the radiometer's scanning footprint. Therefore, $T_b$ is a function of the intensity of radiation emitted by the ice, water and their respective area coverage, and written by Meier (2019) as:

$$T_b = C_{ice}T_{b,ice} + C_{water}T_{b,water} \tag{2.3}$$

Where $T_b$ is the brightness temperature measurement of an area of surface at a given frequency and polarization, $C_{water}$ and $C_{ice}$ describe the area fraction covered by water and sea ice (i.e. concentration), and $T_{b,\,water}$ and $T_{b,\,ice}$ is the intensity of radiation emitted by each surface type. Isolating $C_{ice}$ by rearrangement yields:

$$C_{ice} = \frac{T_b - T_{b,water}}{T_{b,ice} - T_{b,water}} \tag{2.4}$$

Thus, $C_{ice}$ can be determined with known $T_{b,\,water}$ and $T_{b,\,ice}$ terms. In idealistic conditions, $T_{b,\,water}$ and $T_{b,\,ice}$ can be obtained by manual inspection of 100% or 0% sea-ice concentration locations – termed *tie points*. Tie points are used in most sea-ice concentration retrieval algorithms and are necessary input parameters

to calibrate the full range of possible brightness temperature values. However, variation in the radiometric appearance of different ice and water properties and atmospheric conditions means this approach can be limited as the scattering of observations around the tie points means that the subsequently derived concentration values can sometimes fall outside of the 0-100% range, which has no physical meaning. The use of different frequency channels and polarization filters can be incorporated to the algorithm to derive a more robust $C_{ice}$ estimate. An example of this includes the Bootstrap retrieval algorithm (Comiso, 1986), whereby a linear interpolation between cluster points in the 37 vs 19 GHz relationship is utilized to derived $C_{ice}$ (depicted in Figure 2.2). Another commonly incorporated method is the use of gradient and polarization ratios, whereby spectral gradient information from the 19V, 37V and 37H channels is computed, such as in the NASA Team and ECICE retrieval algorithms (Cavalieri et al., 1984; Shokr et al., 2008). These frequency channels are widely used because they are effective at distinguishing ice from water and radiate through cloud cover (Comiso, 1986). The gradient ration (GR) and polarization ratio (PR) are defined as:

$$GR = \frac{T_{b(37V)} - T_{b(19V)}}{T_{b(37V)} + T_{b(19V)}} \qquad (2.5)$$

$$PR = \frac{T_{b(19V)} - T_{b(19H)}}{T_{b(19V)} + T_{b(19H)}} \qquad (2.6)$$

The gradient (Equation 2.5) and polarization (Equation 2.6) ratios populate the scatterplot shown in Figure 2.3, which illustrates the cluster analysis performed to extract a fractional $C_{ice}$ value. Here it is shown that incorporating multiple frequency and polarization channels (Figure 2.2) – as well as their derived variables such as the GR and PR (Figure 2.3) – can potentially solve for multiple surface types. This forms the basis of satellite-derived ice-type estimates, whereby sea ice is further categorized into multiple types based on their radiometric properties. Chapter 5 will explore this in more detail, using brightness temperature data retrieved from a modern radiometer (AMSR-2) to estimate sea-ice concentration and type at a spatial resolution of 6.25 km in the Southern Ocean. The chapter includes a comprehensive discussion of the polarization filters, frequency channels, processing algorithms, and the associated advantages and limitations of these choices.

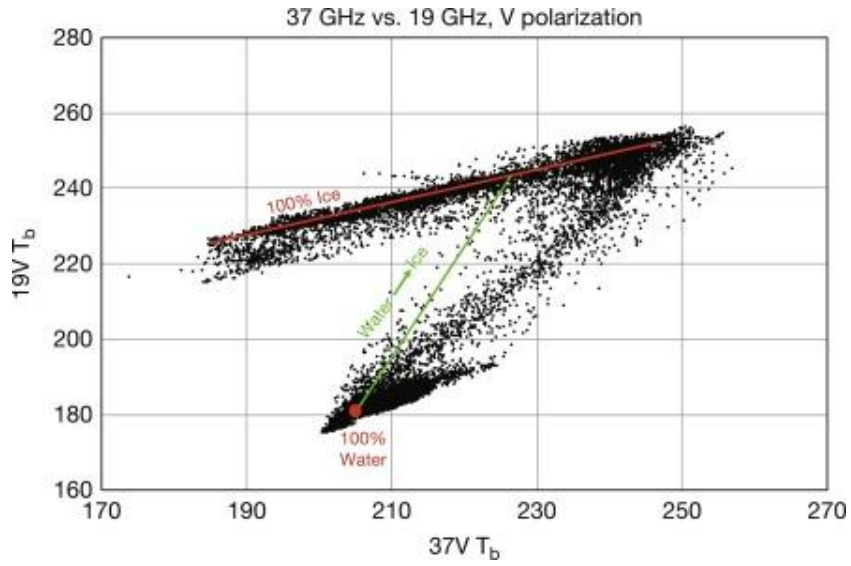


**Figure 2.2: Example distribution of 19V versus 37V GHz brightness temperature values from the F18 SSMI/S sensor on 19 March 2018. This distribution forms the basis of the Bootstrap algorithm. Figure source: Meier (2019). Data source: Maslanik & Stroeve (1999).**

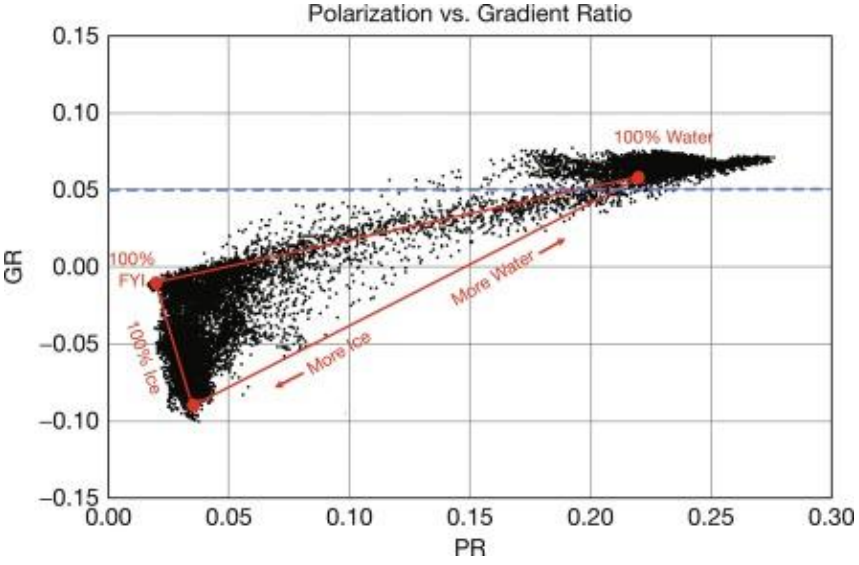


**Figure 2.3: Example polarization ratio versus gradient ratio values from the F18 SSMI/S sensor on 19 March 2018. The distribution forms the basis for the NASA Team algorithm. Figure source: Meier (2019). Data source: Maslanik & Stroeve (1999).**

## 2.2 Sea-ice Vorticity

As initially discussed in Section 1.3.1.1, weather events such as cyclones and high pressure systems are major drivers of Antarctic sea-ice drift variability. These synoptic features are characterized by their strong cyclonic and anticyclonic winds, respectively, and typically follow an eastward trajectory (Grieger et al., 2018). When these rotating weather systems traverse over the sea-ice, frictional forces engender rotational motion into the ice field. Figure 2.4 depicts an example of this response, whereby the clockwise-rotating polar cyclone imparts clockwise rotation in the ice throughout its cover, including in the interior pack-ice zone. Using a gridded field of ice-displacement observations to estimate the mean velocity, the rotational motion exemplified in Figure 2.4 can be quantified by its *vorticity* (or *curl*).

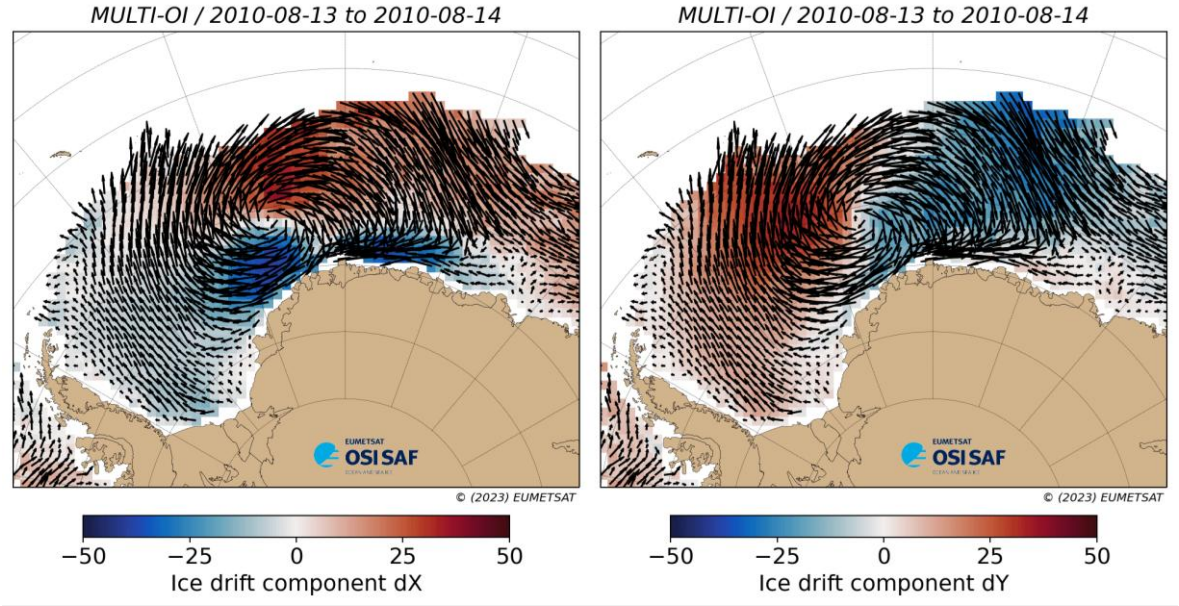


**Figure 2.4: The rotational motion observed in Antarctic sea ice in response to a polar cyclone situated over the ice. Sea-ice drift estimates were computed using the CMCC algorithm (Section 2.1.1) applied to satellite brightness temperature observations averaged over the 24-hour period between noon 13th-14th August 2010. Black vector arrows indicate cyclonic motion, and the colour maps show the displacement (units: km) in the x and y directions, respectively. Source: Lavergne & Down (2023).**

Vorticity is commonly used in fluid dynamics to describe the tendency of a fluid to rotate around a point and is a key quantity in understanding the dynamics of cyclones, atmospheric circulation, currents and ocean gyres. Mathematically, the vorticity ($\vec{\omega}$) is defined as the curl of the velocity vector field ($\vec{V}$):

$$\vec{\omega} = \nabla \times \vec{V} \tag{2.7}$$

where $\vec{\omega}$ describes the intensity of rotation ($\vec{\omega}$ = 0 indicates no rotation; units of seconds$^{-1}$), and its sign denotes the direction of rotation. In a *xyz*-Cartesian coordinate system with a velocity field $\vec{V} = \langle u|v|z\rangle$, Equation 2.7 expands into:

$$\vec{\omega} = \left\langle \frac{\delta w}{\delta y} - \frac{\delta v}{\delta z} \middle| \frac{\delta u}{\delta z} - \frac{\delta w}{\delta x} \middle| \frac{\delta v}{\delta x} - \frac{\delta u}{\delta y} \right\rangle \tag{2.8}$$

For sea-ice, however, floes are constrained to horizontal advection over the ocean's surface and so there is no vertical motion – yielding a vector field of $\vec{V} = \langle u|v|0\rangle$. This reduces vorticity into a scalar value acting perpendicular to the *xy*-plane:

$$\omega_z = \langle \frac{\delta v}{\delta x} - \frac{\delta u}{\delta y} \rangle \tag{2.9}$$

In practice, gridded displacement vectors from the OSI-405, OSI-455 and S2S ice displacement satellite products were used in Chapters 3 and 4 to compute the vorticity of the sea-ice field. The $u$ and $v$ components of the ice velocity were calculated from these displacement vectors for every grid cell $C_{i,j}$ and the relative vorticity ($\zeta_{i,j}$) was calculated using a centered-in-space scheme as:

$$\omega_z \cong \zeta_{i,j} = \frac{\delta v_{i,j}}{\delta x} - \frac{\delta u_{i,j}}{\delta y} \cong \frac{v_{i+1,j} - v_{i-1,j}}{2\Delta L} - \frac{u_{i,j+1} - u_{i,j-1}}{2\Delta L} \tag{2.10}$$

where $u$ and $v$ are the zonal and meridional sea-ice velocity components, respectively (units: meters seconds$^{-1}$), and $\Delta L$ is the spatial resolution of the drift product used. The relative vorticity for every grid cell $C_{i,j}$ was computed using the *u* and *v* components from adjacent cells (i.e. $C_{i+1,j}$, $C_{i-1,j}$, $C_{i,j+1}$ and $C_{i,j-1}$), meaning the vorticity for any given cell could only be computed if its neighbouring grid cells had a displacement vector. Consequently, no vorticity estimate could be computed along the ocean or continent margins. Low-quality displacement vector estimates were excluded from the analysis – defined as non-

nominal quality flagged estimates in the product metadata – and thus no vorticity value was computed for those cells or for their neighbouring cells. Furthermore, the propagation of uncertainties from the satellite ice-displacement estimates must be considered. Following the methods described in Section 2.4 of Dierking et al. (2020), we assume that the position error and uncertainty in the timing of the measurements are negligible, and therefore the uncertainty in vorticity of a square cell can be estimated by:

$$\sigma_{vort}^2 = \frac{2\sigma_{tr}^2}{L^2 \Delta T^2} \tag{2.11}$$

where $\sigma_{tr}^2$ is the tracking error of the drift vector and $\Delta T$ is the time interval between two sequential brightness temperature images. The uncertainty associated with the sea-ice vorticity estimates is further explored in Chapter 3, whereby the feasibility of quantifying sea-ice rotation with satellite drift products is analysed.

## 2.3 Atmospheric Reanalysis Data

Atmospheric reanalysis is a method used to create a comprehensive, consistent, and long-term record of the atmospheric condition by combining historical observational data with a numerical weather prediction model. Reanalysis data provides an estimate of the state of the atmosphere at any given time, filling in gaps where observations are sparse or unavailable, and produces a gridded dataset of atmospheric variables across multiple vertical levels at regular time intervals. Throughout this thesis, atmospheric variables were sourced from the European Centre for Medium-Range Weather Forecasts' (ECMWF) ERA-5 reanalysis product (Hersbach et al., 2023)., which provided the surface winds, vorticity, and mean sea level pressure (MSLP) conditions on a 0.25° spatial resolution grid at hourly intervals. Opportunistic *in situ* validations indicate that ERA-5 appropriately characterizes wind conditions at scales associated with polar cyclones in the Antarctic MIZ (Vichi et al., 2019), while reanalysis products compared against independently sourced sea-ice parameters suggests that ERA-5 correlates well with long-term winter sea-ice trends (Hobbs et al., 2020).

# Chapter 3 : Rotational Drift in Antarctic Sea Ice: Pronounced Cyclonic Features and Differences Between Data Products

This chapter is adapted from de Jager & Vichi (2022). The Results (Section 3.3) and Discussion (Section 3.4) are taken verbatim from the publication, while the Introduction (Section 3.1) and Materials and Methods (Section 3.2) have been modified as to streamline its integration into the thesis and avoid repetition and redundancy with Chapters 1 and 2.

## 3.1 Introduction

As broadly discussed in Chapter 1, sea ice plays a major role in ocean and atmosphere interactions, and therefore its coverage is a key component of the Southern Ocean and ultimately the global climate system (Mayewski et al., 2009). Antarctic sea ice extent (SIE) is characterized by high temporal and spatial variability (Section 1.4), with a key driver of this variability attributed to regional wind stress (Kottmeier et al., 1992; Matear et al., 2015; Vihma et al., 1996). As noted in Section 1.3.1.2, the El Niño Southern Oscillation (ENSO) and the Southern Annular Mode (SAM) have also been shown to influence sea-ice variability (Goosse et al., 2009; Pezza et al., 2012; Thompson & Solomon, 2002; Yuan, 2004). However, the degree of relative influence of these larger scale atmospheric modes is debated (Schroeter et al., 2017), and it is becoming increasingly argued that sea-ice distribution trends – especially in the Atlantic Sector – are primarily driven by local weather events rather than larger scale atmospheric features (Kwok et al., 2017; Matear et al., 2015). Section 1.3.11 outlines the overall effect of local weather on sea ice, while Section 1.5.1 specifically details the mechanisms in which ice motion is engendered by atmospheric forcing. It has been suggested that the unprecedented decrease in the SIE between 2014–2016 was partially the result of intense atmospheric cyclones injecting large scale momentum into the underlying sea ice, causing the ice to drift northward and melt at the warmer lower latitudes (Turner et al., 2017; Z. Wang et al., 2019). This phenomenon is likely to grow in influence as extratropical cyclones shift poleward and polar storms intensify (Chang, 2017; Tamarin-Brodsky & Kaspi, 2017). It is therefore necessary to consider

the effect that local weather systems have on ice dynamics and to evaluate whether these phenomena influence the overall Antarctic sea-ice dynamics over time.

Sea-ice products derived from satellite passive microwave observations can be used to help quantify the rotational motion associated with cyclones and high pressure (HP) systems – through the data acquisition techniques describe in Section 2.1.1. At present, changes in rotational features in the Antarctic sea-ice cover have not yet been quantified. Therefore, this chapter proposes a method for the detection and quantification of rotational drift in Antarctic sea ice at temporal and spatial scales similar to that of local weather events. This was done by computing the sea-ice vorticity using satellite ice drift estimates – through the process described in Section 2.2 – which quantified sea-ice rotation within circular domains. This analysis focused on the Atlantic Sector, as the region is more directly affected by weather variability (Matear et al., 2015). This chapter proposes a measure of rotational drift in sea ice which could be used as a potential index with which interannual dynamical trends can be examined. This approach forms the basis with which the long-term rotational trends presented in Chapter 4 are evaluated. Here, six ice motion products are selected, each of which are subject to different methodological constraints associated with the feature-tracking algorithm – details of which are discussed in Section 2.1.1. While a validation of the vorticity estimates is not included due to the sparsity of *in situ* data, a comparison between the relative performance of the selected drift products is shown.

## 3.2 Materials and Methods

Six different products from the EUMETSAT OSI SAF low resolution sea-ice drift product range (named OSI-405) were used in this chapter. At the time this analysis was performed, the 24-hour OSI-455 product was not yet available, and so the OSI-405 product range was used because its spatial coverage spans over the entire Antarctic sea ice landscape with a comparably intermediate temporal resolution of 48 hours, although the 62.5 km spatial resolution is coarse. The selected OSI-405 products compared were the multi-sensor merged, Advanced Microwave Scanning Radiometer 2 (AMSR-2), Advanced Scatterometer (ASCAT), Special Sensor Microwave Imager (SSM/I) and two Special Sensor and Microwave Imager/Sounder (SSMIS) products. The OSI-405 processing starts from daily maps of brightness

temperature or backscatter observations aggregated from swath observation. Details regarding the derivation of brightness temperature from passive microwave satellite data is discussed in Sections 1.6.1 and 2.1. Satellite observations were sourced from the following sensors: the AMSR-2 on Japan Aerospace Exploration Agency (JAXA) platform GCOM-W1; the SSM/I on the Defence Metalogical Satellite Program (DMSP) platform F15, the SSMIS on DMSP platforms F17 and F18 and the backscatter data from the ASCAT sensor on EUMETSAT platform MetOp-A. A Laplacian filter was applied to these daily maps to enhance specific ice features in the image. Because brightness temperature retrieval algorithms perform relatively poorly in areas with low sea-ice presence (<15% SIC), an ice-edge mask was also applied. Displacement vectors are then computed from two daily images approximately 48 hours apart using the CMCC feature-tracking method described in Section 2.1.1. The temporal range of these single-sensor products in the Southern Hemisphere are as follows: The AMSR-2 product is available from September 2015 to present; the ASCAT from March 2013 to present; the SSM/I from March 2013 to September 2015; the SSMIS-F17 from September 2015 to April 2018; and the SSMIS-F18 from August 2018 to present. For this analysis, motion vectors derived from the SSM/I and SSMIS instruments are grouped to provide a continuous dataset of measurements since 2013. This group will be analysed as a single product and referred to as the SSMI/S product. The multi-sensor merged product implements a two-step process, firstly by using a weighted average of all valid single-sensor data at a particular grid point – where the weighting of each single-sensor product is inversely proportional to the error of that product – and secondly by interpolating surrounding vectors for grid points where no data is available from any single-sensor product. Due to the limitations of measuring sea-ice drift in melting conditions and during periods of insufficient ice cover (Sumata et al., 2015), only the months of June-October were considered, and our analysis focused on the Atlantic Sector of the Southern Ocean, spanning the area between 65° W and 50° E.

Sea-ice vorticity features were systematically identified using a detection algorithm applied to the single-sensor products (AMSR-2, ASCAT and SSMI/S family) and the merged product (code made available in de Jager (2022)). The first step of this process was the computation of the vorticity field – and its associated uncertainty – following the method outlined in Section 2.2. Vector displacement uncertainties are included in all OSI-405 products from 1st June 2017. Low-quality flagged drift estimates (i.e., assigned flag values 0-19) were rejected, while only those flagged with a good quality index (i.e., flag values 20-30) were

considered. Nominal quality estimates (i.e., flag value of 30) have the lowest retrieval uncertainty and were measured independently of their neighbours, while flag values 20-29 included drift estimates that required a correction or interpolation scheme from neighbouring locations and therefore have a larger uncertainty. Rejection quality flags correspond to locations where no valid drift estimate could be made, and therefore no vorticity values are computed at those grid points or their adjacent neighbours. The 20-30 range of flag values was chosen for this analysis due to the availability of the corresponding uncertainty, and so while some non-nominal drift vectors may be of degraded quality, this potential error could be quantified.

In the second step of the process, the detection algorithm generates virtual circular subdomains $D_r$ of radius $r$ centred at every grid point in our vorticity field. Each of these subdomains represent a vorticity feature, which can partially overlap one another in space. We define the feature intensity as the mean of all vorticity estimates contained within its circumference, and the feature variability as the standard deviation of all vorticity estimates contained within its circumference. Therefore, a negative mean intensity feature represents a circular area of sea ice dominated by cyclonic rotation, while a positive mean intensity feature represents an area dominated by anticyclonic rotation. A minimum pixel validity threshold of $T$ is applied to every subdomain $D_r$, ensuring that each classified feature has an adequate number of valid vorticity values within its circumference. Subdomains that fail to meet the minimum pixel validity threshold are ignored, thus reducing the algorithm's susceptibility to classifying small regions of intense vorticity at the ice edge or coastline as features. This process is repeated independently per product with varying $r$ (500, 450 and 400 km) and $T$ (90, 85 and 80 %) parameter values, meaning that all identified features contain 180-220 valid vorticity values within their circumference, depending on the choice of $r$. The choice of 500, 450 and 400 km radius features was oriented towards capturing the effect of large-scale synoptic features on the underlying sea ice, which are of the order of 1000 km, and therefore the 62.5 km grid resolution of OSI-405 is fine enough to capture meso-α (200–1000 km) to synoptic (>1000 km) scale rotational features. All permutations of varying parameter values radius $r$ and threshold $T$ produced similar results, indicating that the presented results are robust to the choice of free parameters. Results shown in Section 3.3 used $r$ = 450 km and $T$ = 90 %.

## 3.3 Results

### 3.3.1 Case Study Analysis

Two case studies were considered in this analysis to highlight the usefulness of quantifying synoptic scale rotational features in the sea ice, and to assess the vorticity feature detection algorithm and its associated uncertainty described in Section 3.2. These examples have been selected based on known synoptic events observed during the winter expeditions of the SA Agulhas 2 in the region. Case Study 1 (Section 3.3.1.1) considers an explosive polar storm which formed over the open ocean and propagated south-east over the MIZ and ice interior. Case Study 2 (Section 3.3.1.2) considers a stationary high-pressure cell persisting over the ice interior in the eastern Weddell Sea. These maps illustrate some of the features of the vorticity fields obtained from the available products and the overall functioning of the detection algorithm. An in-depth analysis of the resulting vorticity values and the relative uncertainties is given in Sections 3.3.2 and 3.3.3 in which we will refer to these case studies for comparison.

#### 3.3.1.1 Case Study 1: Explosive Polar Storm Traversing Over the Sea Ice

There existed an explosive atmospheric cyclone moving from the MIZ to over the ice interior between 2-5 July 2017. This cyclone was chosen for a case study as its effects on the underlying sea ice has been well documented with both satellite and *in situ* data (Vichi et al., 2019). Figure 3.1 shows the vorticity field between midday 3 July and midday 5 July according to each of the four products, with the masking due to rejected drift estimates indicated by the dotted hatching. Overlain mean sea level pressure (MSLP) contours indicate that cyclonic structure in the atmosphere persisted over the ice interior during this 48 hr period, with the mean position of its core located at approximately 65°S and 21°E. According to the merged product, the cyclonic vorticity feature in the sea-ice field is consistent with the structure of the atmospheric cyclone over the same period. This is evidenced by the large region of negative vorticity in the sea-ice field (blue) underneath the overlying atmospheric cyclone (Figure 3.1d). The magenta ring shown in Figure 3.1 represents the location of the most intense cyclonic ice drift feature detected using the merged product, with its 450 km radius centred at 65.7° S and 20.6° E (mean vorticity: $-1.13 \times 10^{-3} \pm 0.90 \times 10^{-6}$ $s^{-1}$).

Conversely, none of the single-sensor ice drift products detect this intense feature underneath the atmospheric cyclone (Figure 3.1a, b and c), although they all capture some negative vorticity in the region. In addition to the area of ice beneath the atmospheric cyclone, the wider vorticity field is also associated with the cyclonic and anticyclonic curvature of the isobars. All four products detect positive vorticity beneath the elongated high-pressure ridge over the Weddell Sea, separating two smaller regions of negative vorticity at the ice edge (approximately 62°S and 30°W) and continental coastline (approximately 77°S and 15°W), each of which lie below a pressure trough. All products have some rejected drift estimates at the MIZ, while the single-sensor products have far more in the ice interior, which results in a patchier vorticity field, especially when it is negative. All four products instead detect a similar vorticity field in the Weddell Sea region, suggesting that good quality drift estimates are more in agreement under anticyclonic drift conditions.

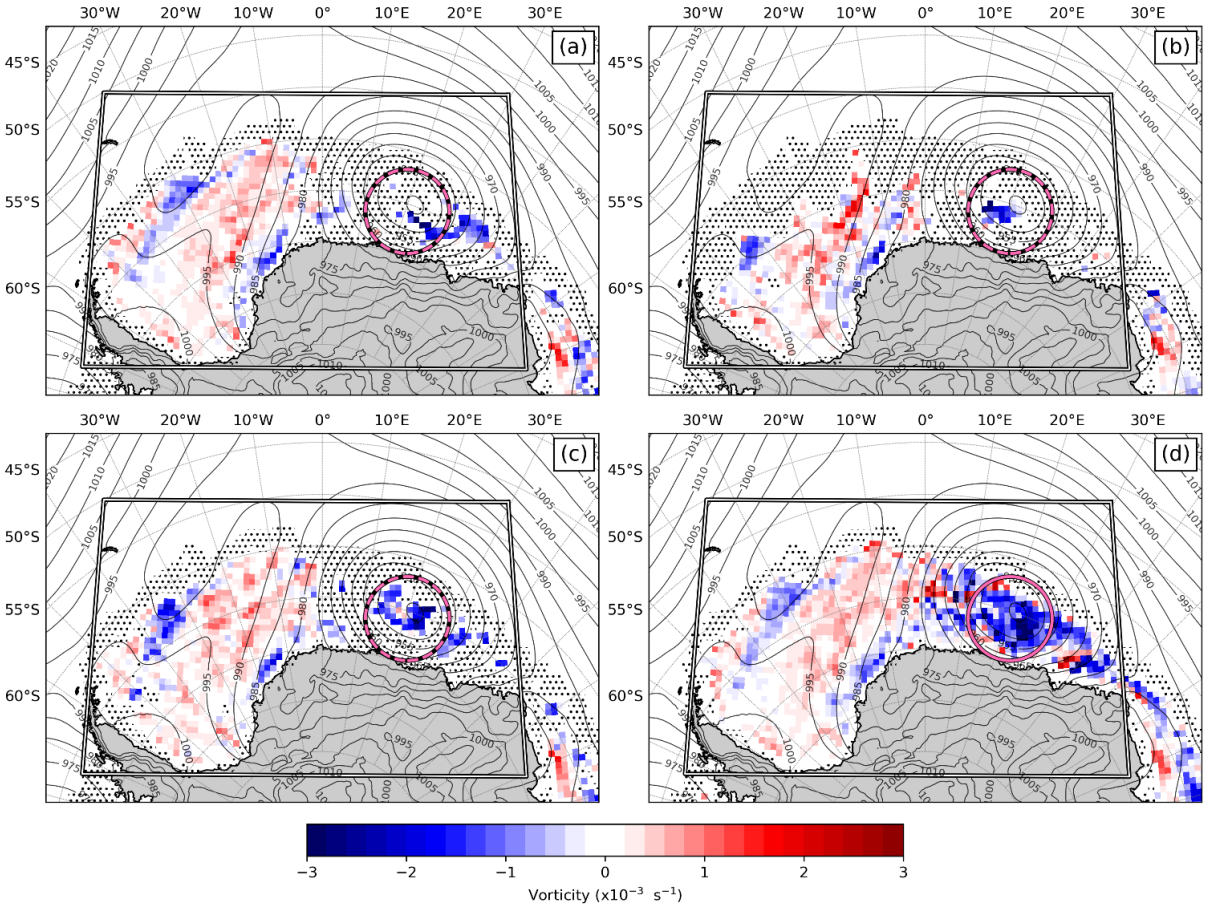


**Figure 3.1: The sea-ice vorticity field for Case Study 1 between 3 July 2017, 12:00:00 – 5 July 2017, 12:00:00 (UTC) computed using the (a) AMSR-2, (b) ASCAT, (c) SSMI/S and (d) merged ice drift products from EUMETSAT OSI SAF. Overlying contours show the 48 hr mean sea level pressure (MSLP) computed from hourly ECMWF-ERA5 reanalysis data over the same period. Ice drift estimates that were not considered in the vorticity computation due to their rejection flag status are shown with dotted hatching, and the rectangular box marks the area boundaries over which the algorithm applied (as described in Section 3.2). The magenta ring shows the location of the most intense cyclonic feature detected by the merged product over this 48 hr period, while the dashed rings indicate that the corresponding features did not meet the pixel validity threshold requirement using the AMSR-2, ASCAT and SSMI/S products.**

### 3.3.1.2 Case Study 2: High-Pressure Cell Persisting Over the Eastern Weddell Sea

Figure 3.2 shows the sea-ice vorticity field from approximately midday 21 July to midday 23 July 2019. During this period, ERA-5 reanalysis data indicates that a strong high-pressure cell was persistent over the eastern Weddell Sea, with the average position of its core between located at 67.2°S and 18.9°W. The green ring represents the location of the most intense anticyclonic ice drift feature detected using the merged product, with its 450 km radius centred at 66.5°S and 19.8°W (mean vorticity: $0.63 \times 10^{-3} \pm 0.37 \times 10^{-6}$ $s^{-1}$, Figure 3.2). The passive-microwave based single-sensor products detect similar vorticity fields over the same area, with the AMSR-2 and SSMI/S products measuring $0.63 \times 10^{-3} \pm 0.36 \times 10^{-6}$ $s^{-1}$ (Figure 3.2a) and $0.64 \times 10^{-3} \pm 0.72 \times 10^{-6}$ $s^{-1}$ (Figure 3.2c) respectively. The active microwave based ASCAT product fails to detect this feature due to the insufficient number of valid vorticity points (Figure 3.2b). Again, the vorticity fields detected by all four products show a strong correlation with the curvature of the overlying isobars across the entire rectangular region, much like that shown in Case Study 1 (Figure 3.1). This is particularly visible in Figure 3.2 along the negative-to-positive vorticity gradient from the western-to-eastern Weddell Sea, where the parallel isobars lie perpendicular to the vorticity gradient, suggesting the atmospheric pressure gradients control the underlying vorticity field. A region of negative vorticity is also detected near the eastern boundary of the rectangular region which mimics the curvature of the overlying low-pressure cell deflecting eastwards. Similarly to Case Study 1, all three single-sensor products have a higher frequency of rejected drift estimates compared to the merged product (Figure 3.2).

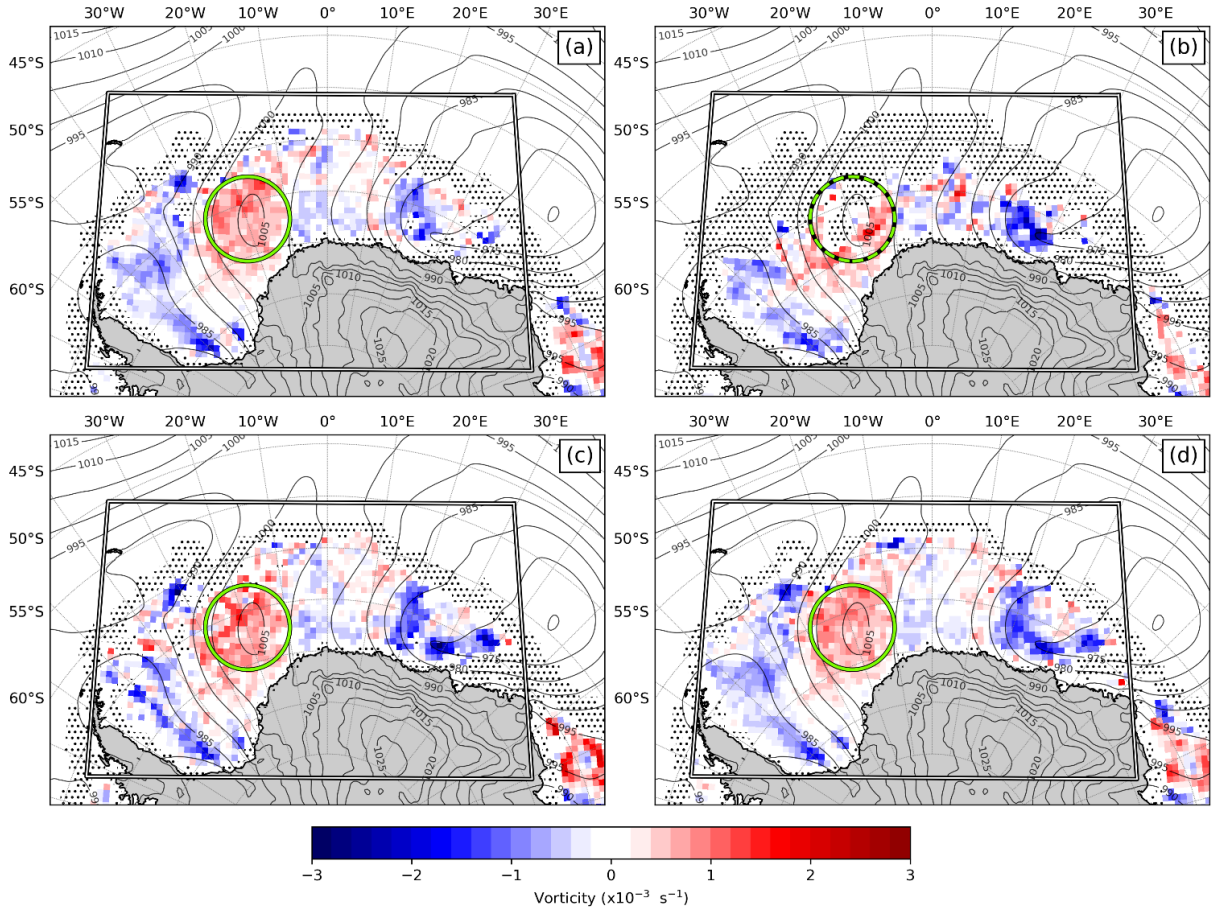


**Figure 3.2: The sea-ice vorticity field for Case Study 2 between 21 July 2019, 12:00:00 – 23 July 2019, 12:00:00 (UTC) computed using the (a) AMSR-2, (b) ASCAT, (c) SSMI/S and (d) merged ice drift products from EUMETSAT OSI SAF. Overlying contours show the 48 hr mean sea level pressure (MSLP) computed from hourly ECMWF-ERA5 reanalysis data over the same period. Ice drift estimates that were not considered in the vorticity computation due to their rejection flag status are shown with dotted hatching, and the rectangular box marks the area boundaries over which the algorithm applied (as described in Section 3.2). The green ring shows the location of the most intense anticyclonic feature detected by the merged product over this 48 hr period, while the dashed ring indicates that the corresponding feature did not meet the pixel validity threshold requirement using the ASCAT product.**

### 3.3.2 Analysis of Uncertainties and Comparison of Detected Features in the Drift Products

Figure 3.3 shows the distribution of feature intensity relative to its uncertainty for both cyclonic and anticyclonic features. This analysis was done using years 2017-2020 due to the availability of drift uncertainty estimates in the OSI-405 product. The intensity of rotational features (~$10^{-3}$ $s^{-1}$) is approximately 3 orders of magnitude larger than its associated uncertainty (~$10^{-6}$ $s^{-1}$ mostly due to the large $L^2$ and $\Delta T^2$ terms in the denominator of Equation 2.11 in Section 2.2. The SSMI/S product shows the largest mean uncertainty for both cyclonic and anticyclonic features, while uncertainties are smallest using the AMSR-2 product (Table 3.1). Despite differences between the three single-sensor products, each of them shows near identical estimates of the mean uncertainty of cyclonic features relative to that of anticyclonic features. Conversely, the merged product shows a larger mean uncertainty for cyclonic features (0.48 ×$10^{-6}$ $s^{-1}$) than anticyclonic features (0.41 ×$10^{-6}$ $s^{-1}$), suggesting that cyclonic drift estimates are noisier than that of anticyclonic ones. Single-sensor derived products show a small range of uncertainties for both cyclonic and anticyclonic features, as indicated by the flatness of scattering in Figure 3.3a-f. This is also shown statistically in Table 3.1, where the standard deviation of the uncertainty spread is approximately 0.04 ×$10^{-6}$ $s^{-1}$ for all three single-sensor products. This is because the tracking error ($\sigma_{tr}^2$) term in Equation 2.11 (Section 2.2) is mostly spatially uniform, although there is some variation introduced into the uncertainty field by the non-nominal quality flagged drift estimates and relatively small deviations in the time interval (ΔT). Conversely, the merged product (Figure 3.3g and h) shows a far greater standard deviation of uncertainties; 0.15 ×$10^{-6}$ $s^{-1}$ and 0.10 ×$10^{-6}$ $s^{-1}$ for cyclonic and anticyclonic features, respectively. This result is intuitive as the merged product is created using a combination of the single-sensor products and its uncertainty is computed using a Gaussian error propagation function based on the uncertainties of its constituents, and thus the resultant uncertainty of the merged product is expectedly more variable than that of the single-sensor products. The features detected in Case Studies 1 (Figure 3.1) and 2 (Figure 3.2) are shown with magenta and green diamond markers respectively in Figure 3.3. The cyclonic vorticity feature detected by the merged product in Case 1 (Figure 3.1d) had both an intensity and variability measured beyond the 95$^{th}$ percentiles relative to the other cyclonic features detected from 2017-

2020 (dashed lines in Figure 3.3h). The anticyclonic feature detected in Case 2 (Figure 3.2a, c and d) is measured beyond the 95$^{th}$ percentile of intensity - but near average uncertainty - relative to the other anticyclonic features detected between 2017-2020, according to the AMSR-2 (Figure 3.3a), SSMI/S (Figure 3.3e) and merged (Figure 3.3g) products.

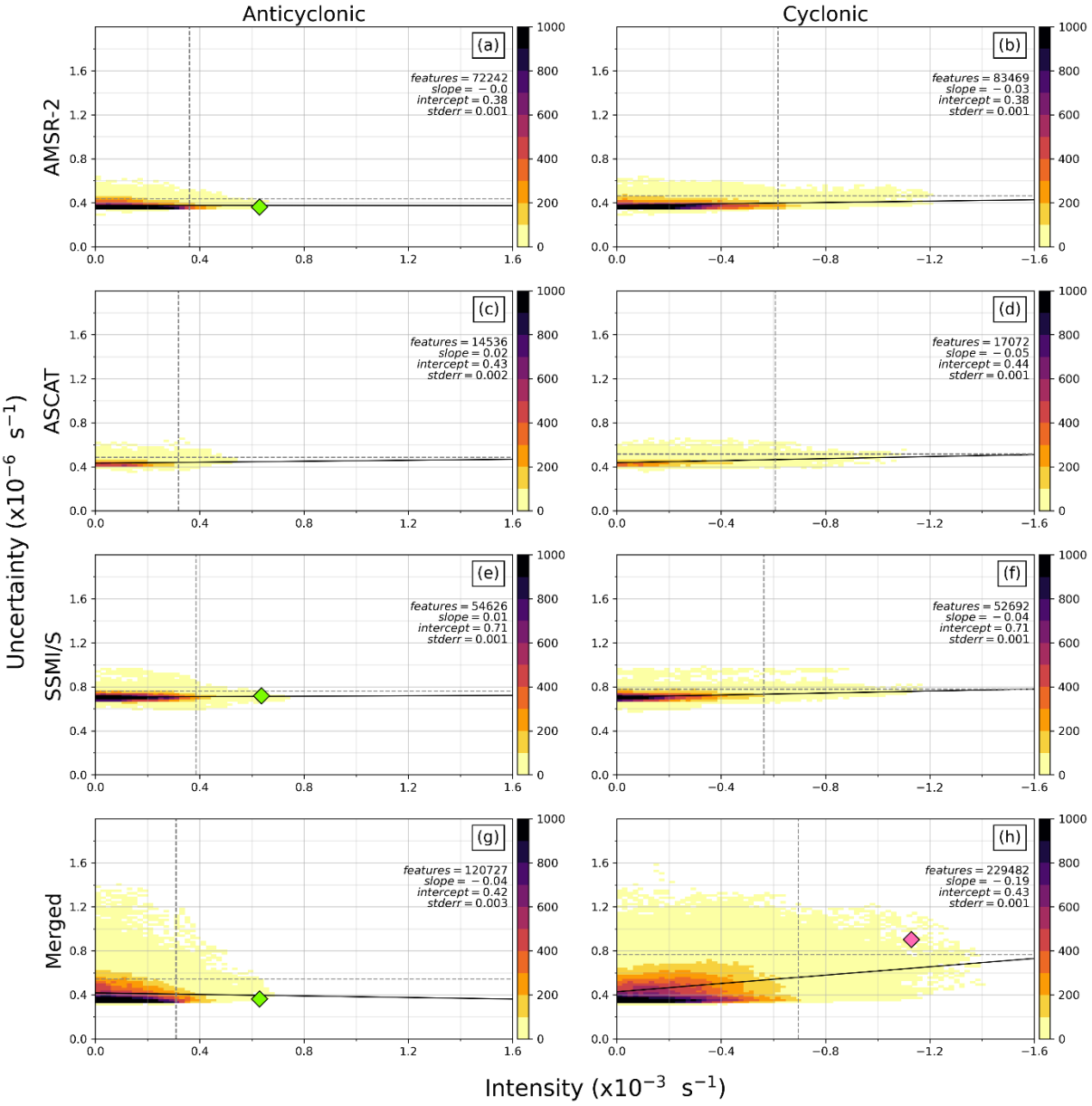


**Figure 3.3: A two-dimensional histogram of the intensity and uncertainty of vorticity of all features detected between 2017-2020. Anticyclonic and cyclonic features are shown in the left and right columns respectively, while each product is shown in a different row. Panels (a) and (b) show features detected using the AMSR-2 product; panels (c) and (d) using the ASCAT product; panels (e) and (f) using the SSMI/S product; and panels (g) and (h) using the merged product. The lines-of-best-fit are**

**shown with a black solid line, along with its slope, intercept, standard error, and the number of features detected. The vertical and horizontal dashed lines represent the 95th percentiles of the intensity and uncertainty respectively. The colormap indicates the number of features detected in each bin. The anticyclonic feature described in Case Study 2 (Section 3.3.1.2) is shown with a green diamond marker, and the cyclonic feature described in Case Study 1 (Section 3.3.1.1) is shown with a magenta diamond marker. Note the relative scaling order of magnitude between variables, and the reverted x-axis for cyclonic features to aid comparison. The gradients of the lines-of-best-fit reported in Section 3.3.2 have been computed using the absolute values of the x-axis to simplify the comparison between the cyclonic and anticyclonic distributions.**

**Table 3.1: The mean and standard deviation of the uncertainty and variability of vorticity of all features detected between 2017-2020 (Format: Mean ± STD). Note the relative scale of units of the uncertainty estimates relative to that of the variability.**

| **Uncertainty** ($\times 10^{-6}\ s^{-1}$) | **AMSR-2** | **ASCAT** | **SSMI/S** | **Merged** |
|---|---|---|---|---|
| **Anticyclonic** | $0.39 \pm 0.04$ | $0.44 \pm 0.03$ | $0.71 \pm 0.03$ | $0.39 \pm 0.01$ |
| **Cyclonic** | $0.39 \pm 0.03$ | $0.45 \pm 0.04$ | $0.72 \pm 0.04$ | $0.48 \pm 0.15$ |
| **Variability** ($\times 10^{-3}\ s^{-1}$) | | | | |
| **Anticyclonic** | $0.33 \pm 0.11$ | $0.38 \pm 0.09$ | $0.38 \pm 0.10$ | $0.39 \pm 0.17$ |
| **Cyclonic** | $0.42 \pm 0.14$ | $0.47 \pm 0.13$ | $0.46 \pm 0.13$ | $0.55 \pm 023$ |

The relationship between the feature intensity and its associated variability within the search radius (Figure 3.4) indicated that they are of the same order of magnitude. Here it can be seen that the scale of standard deviation is far more comparable to the feature intensity. It is shown that the mean variability is larger for cyclonic features than anticyclonic features in all four products, of which the largest spread is noted using the merged product (Table 3.1). Additionally, all four products agree that the variability of cyclonic features

is proportional to its intensity – as visualized by the gradient of the black lines-of-best-fit in Figure 3.4b, d, f, and h – indicating that the highest intensity cyclonic features are also the most variable. The merged product has the largest slope of 0.44 for cyclonic features (Figure 3.4h), and the single-sensor AMSR-2 (Figure 3.4b), ASCAT (Figure 3.4d) and SSMI/S (Figure 3.4f) products have smaller slopes of 0.31, 0.33 and 0.34 respectively. No obvious relationship between intensity and associated variability is seen for anticyclonic features, with the single-sensor AMSR-2 (Figure 3.4a), ASCAT (Figure 3.4c) and SSMI/S (Figure 3.4e) products all showing a slope of approximately 0.01. The merged product has an inversely proportional slope of -0.10 (Figure 3.4g), indicating that intense anticyclonic features are more homogenous. The features detected in Case Studies 1 (Figure 3.1) and 2 (Figure 3.2) are shown in Figure 3.4 with magenta and green diamond markers respectively. The cyclonic vorticity feature detected by the merged product in Case 1 lies close to the regression line, with its intensity and variability both measured beyond the 95$^{th}$ percentiles relative to the other cyclonic features detected in the same period (dashed lines in Figure 3.4h). This is aligned with the atmospheric event that was reported to be an explosive cyclone (Vichi et al., 2019). Much like the uncertainty distribution shown in Figure 3.3, the AMSR-2 (Figure 3.4a), SSMI/S (Figure 3.4e) and merged (Figure 3.4g) products detected the anticyclonic feature described in Case 2 with an intensity measured beyond the 95th percentile but near-average variability relative to the other anticyclonic features.

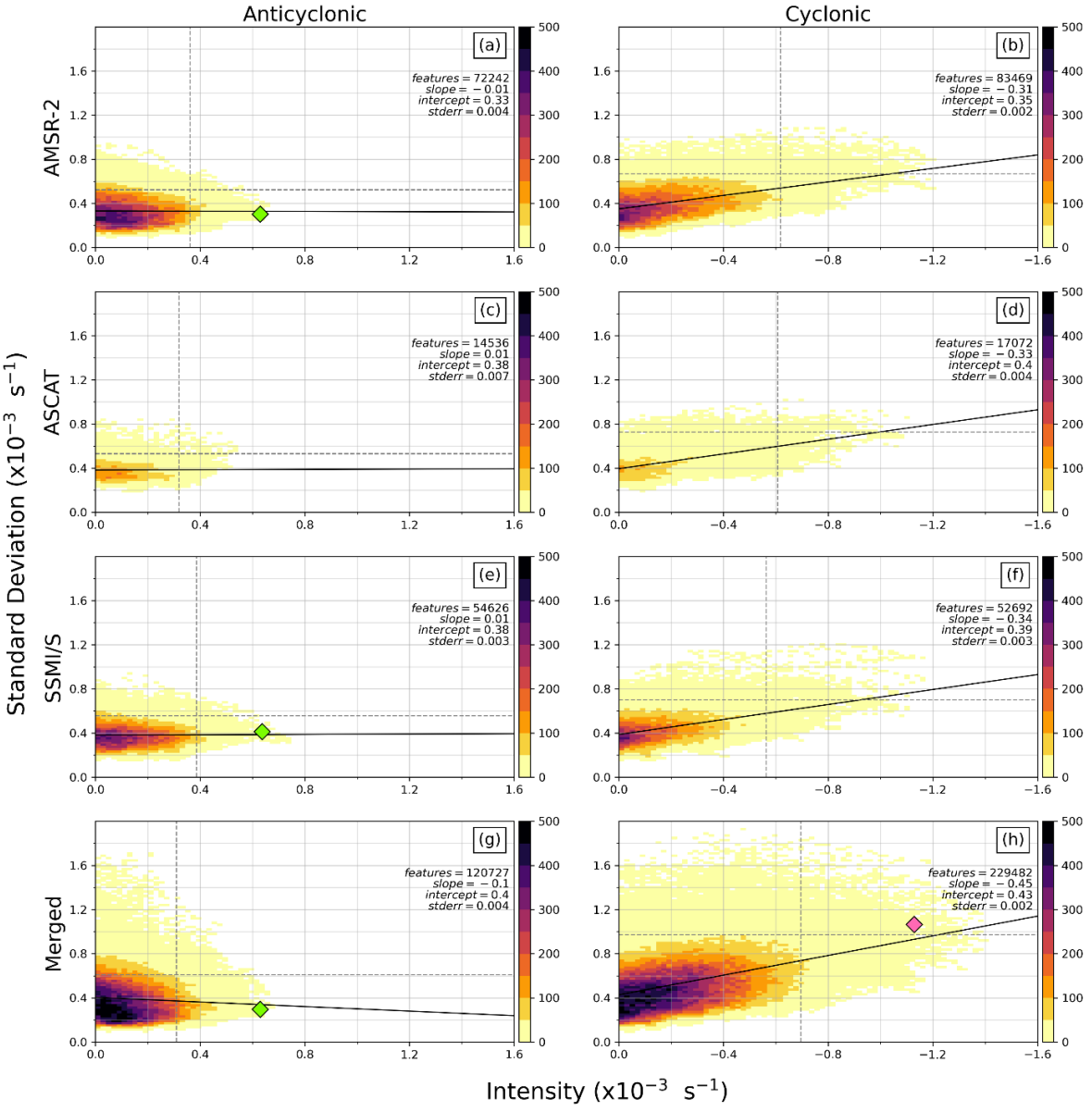


**Figure 3.4: A two-dimensional histogram of the intensity and standard deviation of vorticity of all features detected between 2017–2020. Anticyclonic and cyclonic features are shown in the left and right columns respectively, while each product is shown in a different row. Panels (a) and (b) show features detected using the AMSR-2 product; panels (c) and (d) using the ASCAT product; panels (e) and (f) using the SSMI/S product family; and panels (g) and (h) using the merged product. The**

**lines-of-best-fit are shown with a black solid line, along with its slope, intercept, standard error, and the number of features detected. The vertical and horizontal dashed lines represent the 95$^{th}$ percentiles of the intensity and standard deviation respectively. The colormap indicates the number of features detected in each bin. The anticyclonic feature described in Case Study 2 (Section 3.3.1.2) is shown with a green diamond marker, and the cyclonic feature described in Case Study 1 (Section 3.3.1.1) is shown with a magenta diamond marker. Note the relative scaling order of magnitude between variables, and the reverted x-axis for cyclonic features to aid comparison. The gradients of the lines-of-best-fit reported in Section 3.3.2 have been computed using the absolute values of the x-axis to simplify the comparison between the cyclonic and anticyclonic distributions.**

The disagreement between cyclonic and anticyclonic features is further highlighted in Figure 3.5, which shows the intensity distribution of anticyclonic (Figure 3.5a) and cyclonic (Figure 3.5b) features. Justified by our vorticity uncertainty analysis between 2017–2020, we have assumed that the negligible importance of this uncertainty can be retroactively applied to earlier years, and so Figure 3.5 is representative of all features detected from 2016-2020 between 1$^{st}$ June to 31$^{st}$ October. We have chosen this temporal range to maximise the use of available data for which all four products overlap in time. It must be noted that no SSMI/S ice drift estimates in June and July of 2018 are available, due to the gap in the transition period from the SSMIS-F17 and -F18 platforms. Results show that the intensities of cyclonic features (Figure 3.5b) are higher than that of anticyclonic features (Figure 3.5a), as indicated by the heavier tail of the gaussian curve estimate of the cyclonic distribution. A total of 311 308 anticyclonic features were detected over this period, with the most being returned by the merged product (144 491), followed by the passive-microwave based AMSR-2 (84 171) and SSMI/S (64 263) products and the active-microwave based ASCAT (18 383) product. The number of cyclonic features returned was similar in the single-sensor AMSR-2 (105 889), SSMI/S (66 111) and ASCAT (21 991) products, while the merged product detected approximately twice as many cyclonic features (295 484) as anticyclonic features. A total of 489 475 cyclonic features were returned by all four products, 57 % more relative to the total number of anticyclonic features detected.

Inter-product comparisons indicate that there is little difference in the intensity of anticyclonic features (Figure 3.5a) – as shown by the similarity of overlapping curve estimates – with only the ASCAT product (blue line) deviating slightly from the other distributions with a higher frequency of low-intensity features detected (between 0 and $-0.2\times10^{-3}$ $s^{-1}$). Conversely, the cyclonic distribution curves show a larger

discrepancy between products (Figure 3.5b), particularly the merged product (yellow line), which shows a disproportionately small frequency of low-intensity features (between 0 and $-0.2\times10^{-3}$ $s^{-1}$) and high frequency of intermediate-intensity features (between $-0.25\times10^{-3}$ and $-0.6\times10^{-3}$ $s^{-1}$). If the quality flag restriction is relaxed to include all the available data in the OSI-405 product datasets, the difference between the cyclonic distributions is enhanced, with the merged product showing a much-extended tail of high intensity cyclones (not shown). This indicates that the extent of disagreement between products is dependent on the choice of quality flags used. Due to the large number of low-intensity features detected, the differences between products in detecting high-intensity features is less clear. Therefore, the most intense cyclonic and anticyclonic features for each product were compared. Here, we define the major events as those features above the 95$^{th}$ percentile (vertical dashed lines in Figure 3.5a and b). Similar thresholds are shown for major anticyclones in the SSMI/S ($0.37\times10^{-3}$ $s^{-1}$), AMSR-2 ($0.36\times10^{-3}$ $s^{-1}$) and merged ($0.35\times10^{-3}$ $s^{-1}$) products, with the ASCAT ($0.32\times10^{-3}$ $s^{-1}$) product again deviating slightly from the others (Figure 3.5a). For cyclonic features, the merged product ($-0.69\times10^{-3}$ $s^{-1}$) had the most intense threshold, followed by the AMSR-2 ($-0.63\times10^{-3}$ $s^{-1}$), ASCAT ($-0.62\times10^{-3}$ $s^{-1}$) and SSMI/S ($-0.54\times10^{-3}$ $s^{-1}$) products (Figure 3.5b). The 95$^{th}$ percentile intensity threshold was therefore 1.5–2.0 times larger for cyclonic features than for anticyclonic features.

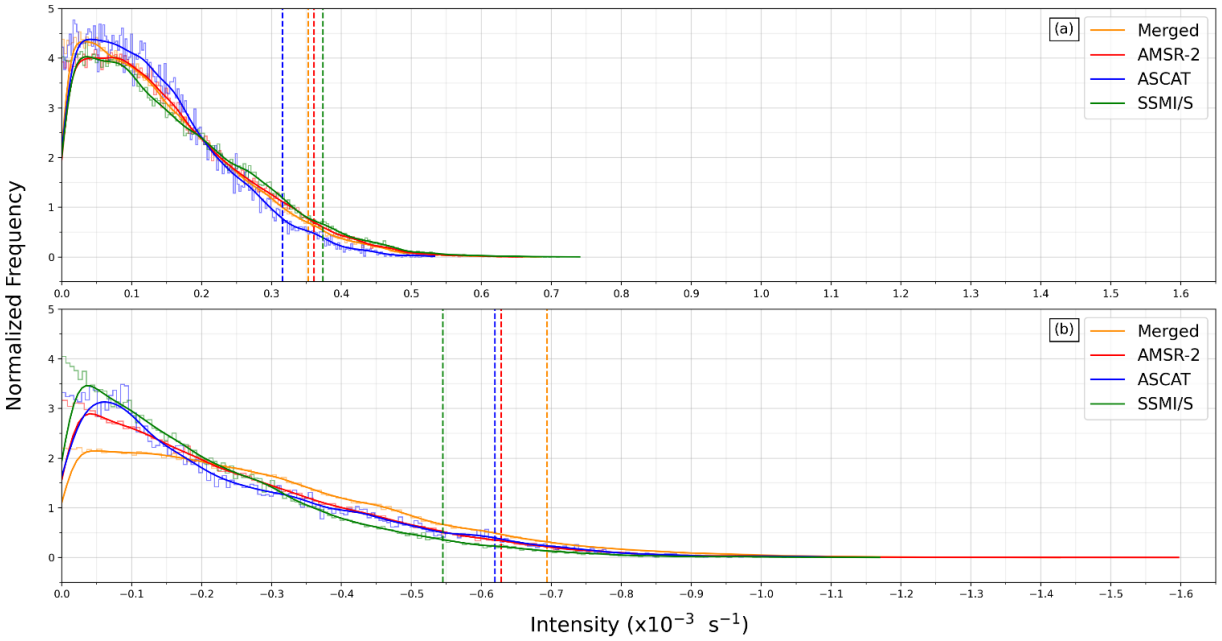


**Figure 3.5: The normalized frequency distribution of (a) anticyclonic vorticity features and (b) cyclonic vorticity features from 2016-2020 (note the reverted x axis for comparison). Lighter shaded lines show a stepped histogram of 200 bins, while the darker shaded curve represents a kernel-density estimate using Gaussian kernels. Vertical dashed lines indicate the intensity threshold of the 95$^{th}$ percentile.**

**Table 3.2: Summary of key difference between detected Cyclonic and Anticyclonic features based on the algorithmic criteria outlined in Section 3.2.**

| | Cyclonic Features | Anticyclonic Features |
|---|---|---|
| **Direction of Rotation in the Southern Hemisphere** | Clockwise | Anticlockwise |
| **Overlying Weather conditions** | Stormy; heavy cloud cover; snow. | Clear and fair |
| **Features Detected** | 489 475 | 311 308 |
| **Intensity of 95$^{th}$ percentile (x10$^{-3}$ s$^{-1}$)** | 0.5 – 0.7 (clockwise) | 0.3 – 0.4 (anticlockwise) |
| **Satellite Product Detection uncertainty (x10$^{-6}$ s$^{-1}$)** | 0.4 – 0.7 | 0.4 – 0.7 |
| **Satellite Product Detection Variability (x10$^{-3}$ s$^{-1}$)** | 0.42 – 0.55; Proportional to intensity | 0.33 – 0.39; Independent of intensity |
| **Spatial Field Composition** | Heterogeneous | Homogeneous |
| **Satellite Product Detection Discrepancy** | High | Low |
| **Interannual Variability (2013-2020)** | Intensified abruptly from 2014-2017 | No obvious change |

### 3.3.3 Year-to-Year Variability

The previous analysis of uncertainties indicated that the difference between the products in the number and intensity of the detected features is robust. A further analysis of the interannual variability of major events was conducted, to assess the presence of year-to-year differences during the period of data availability. The temporal range of analysis was extended to the period 2013-2020, as 2013 is the earliest year of available data in the Southern Hemisphere. However - upon defining the 95$^{th}$ percentile intensity thresholds like that shown in Figure 3.5 - it was noticed that no cyclonic feature exceeded this threshold in 2013 or 2014 for any product. This was also the case at the 90$^{th}$ percentile. It is therefore noteworthy that a strict, consistent intensity threshold applied to all years does not allow us to discern the relative dynamical changes earlier than 2015. For this reason, we have defined the 95$^{th}$ percentile threshold for each year independently. This means that the results presented in Figure 3.6 show the interannual intensity distribution of the major cyclonic and anticyclonic features based on each year's distribution. The mean, standard deviation, and

intensity threshold of the 95$^{th}$ percentile for each year is also provided to show how different the years are and to justify the choice of this diagnostics (Table 3.3). Note that the AMSR-2 drift product is only available from September 2015, and no SSMI/S ice drift estimates were available in June and July of 2018. There is no obvious interannual trend seen in anticyclonic intensity between 2013–2020 (Figure 3.6a, c, e and g), visually indicated by the box-and-whisker rectangles remaining relatively constant in all four products and with few outlier features detected. This is further supported by the relatively small variability in the mean intensity and standard deviation between years (Table 3.3). Conversely, a clear cyclonic interannual trend is evident, characterized by relatively low-intensity features in 2013 and 2014, followed by an abrupt increase in intensity from 2015–2017 (Figure 3.6b, d, f and h). From 2014–2017, the mean of the 95th percentile of cyclones increased by a factor of 2.8, 2.6 and 1.7 for the ASCAT, SSMI/S and merged products respectively (Table 3.3). Much like the cyclonic variability-to-intensity relationship described earlier (Figure 3.4b, d, f and h), it is again evident that the standard deviation increases with the intensity from 2014–2017 for each available product (Table 3.3). All four products indicate a relatively high frequency of cyclonic outlier features – representing features which were more intense than the annual upper bound ($> |Q3| + 1.5 \times |IQR|$) – with SSMI/S product showing a larger frequency of outliers in 2015 (Figure 3.6).

**Table 3.3: The mean, standard deviation, and intensity threshold of the 95$^{th}$ percentile of all rotational features detected between 2013–2020 (Format: Mean ± STD (Threshold)); Units in $\times 10^{-3}\ s^{-1}$). For comparison, the 95$^{th}$ percentile of all anticyclonic (cyclonic) features from 2016–2020 is 0.36 (-0.63) for the AMSR-2; 0.32 (-0.62) for the ASCAT; 0.37 (-0.54) for the SSMI/S; and 0.35 (-0.69) for the merged product as illustrated by the vertical lines in Figure 3.5.**

| Anticyclonic | 2013 | 2014 | 2015 | 2016 | 2017 | 2018 | 2019 | 2020 |
|---|---|---|---|---|---|---|---|---|
| **AMSR-2** | - | - | 0.43±0.07 (0.37) | 0.29±0.04 (0.24) | 0.41±0.05 (0.36) | 0.36±0.05 (0.31) | 0.48±0.06 (0.41) | 0.43±0.03 (0.38) |
| **ASCAT** | 0.33±0.05 (0.29) | 0.38±0.05 (0.33) | 0.40±0.09 (0.30) | 0.28±0.03 (0.25) | 0.38±0.03 (0.35) | 0.31±0.03 (0.27) | 0.39±0.04 (0.34) | 0.41±0.05 (0.33) |
| **SSMI/S** | 0.27±0.04 (0.22) | 0.33±0.06 0.27) | 0.45±0.07 (0.37) | 0.31±0.05 0.26) | 0.43±0.04 (0.39) | 0.34±0.04 (0.30) | 0.50±0.06 (0.42) | 0.42±0.04 (0.37) |
| **Merged** | 0.33±0.05 (0.27) | 0.35±0.06 (0.29) | 0.43±0.06 (-0.36) | 0.35±0.05 (0.29) | 0.43±0.06 (0.36) | 0.37±0.05 (0.31) | 0.46±0.06 (0.38) | 0.41±0.03 (0.36) |
| **Cyclonic** | **2013** | **2014** | **2015** | **2016** | **2017** | **2018** | **2019** | **2020** |
| **AMSR-2** | - | - | -0.81±0.15 (-0.65) | -0.80±0.18 (-0.63) | -0.82±0.11 (-0.70) | -0.68±0.11 (-0.58 | -0.69±0.12 (-0.56) | -0.73±0.11 (-0.61) |
| **ASCAT** | -0.29±0.04 (-0.25) | -0.29±0.03 (-0.26) | -0.56±0.07 (-0.45) | -0.76±0.11 (-0.65) | -0.82±0.12 (-0.66) | -0.68±0.09 (-0.57) | -0.72±0.10 (-0.61) | -0.66±0.07 (-0.57) |
| **SSMI/S** | -0.39±0.05 (-0.37) | -0.45±0.08 (-0.35) | -0.42±0.11 (-0.34) | -0.58±0.10 (-0.47) | -0.77±0.12 (-0.63) | -0.60±0.10 (-0.49) | -0.66±0.13 (-0.54) | -0.68±0.09 (-0.58) |
| **Merged** | -0.46±0.06 (-0.39) | -0.49±0.06 (-0.41) | -0.76±0.16 (-0.60) | -0.83±0.13 (-0.69) | -0.85±0.10 (-0.72) | -0.83±0.14 (-0.68) | -0.86±0.15 (-0.68) | -0.82±0.11 (-0.69) |

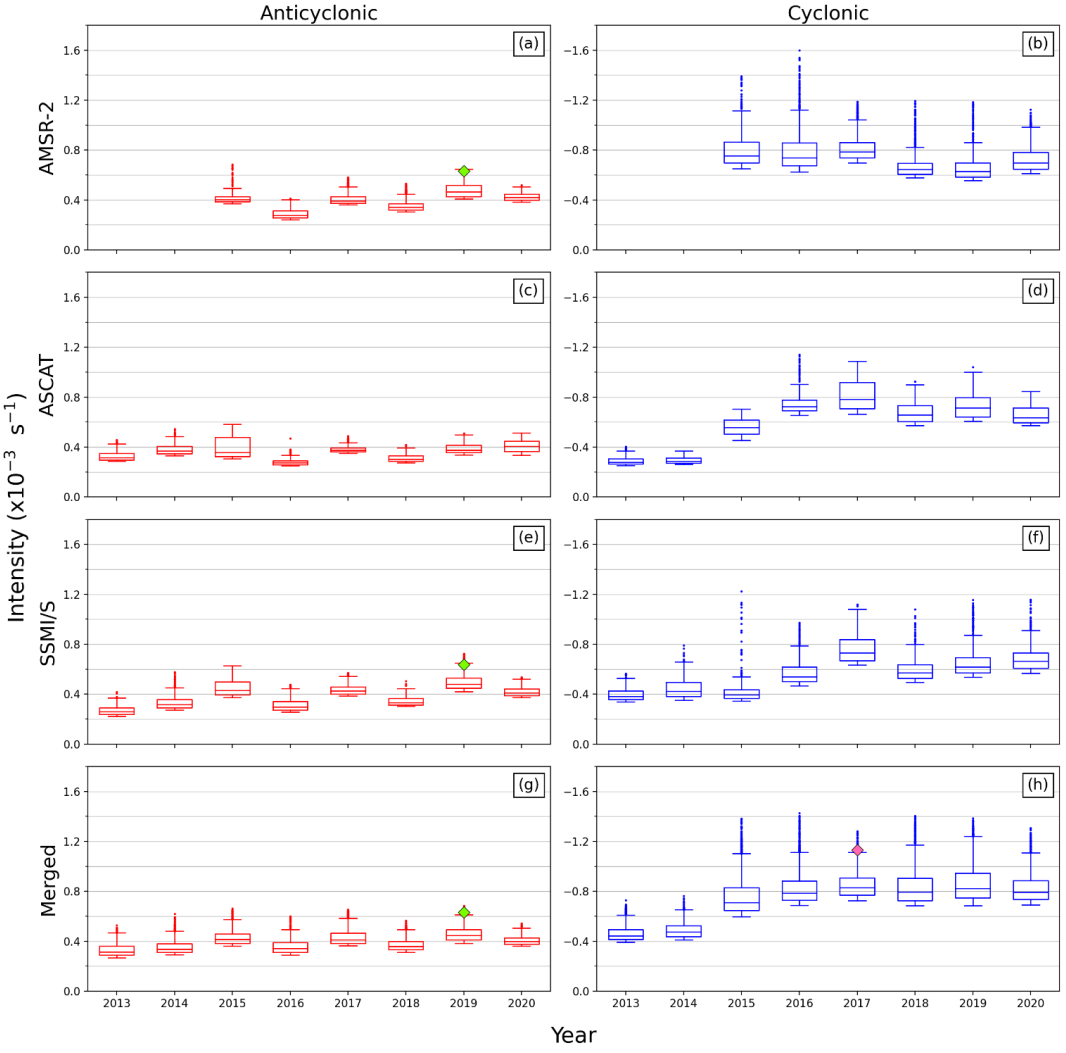


**Figure 3.6: The interannual distribution of the 95$^{th}$ percentile of features detected between 2013-2020. Cyclonic and anticyclonic features are represented with blue and red box-and-whisker plots respectively. Panels (a) and (b) show features detected using the AMSR-2 product; panels (c) and (d) using the ASCAT product; panels (e) and (f) using the SSMI/S product family; and panels (g) and (h) using the merged product. The box-and-whisker rectangles indicate the interquartile range (IQR), with the median line separating the upper (Q3) and lower (Q1) quartiles. Outlier features are shown as dots and represent features of which their intensity exceeds the upper bound (> |Q3| + 1.5 × |IQR|) or lower bound (< |Q1| - 1.5 × |IQR|). The anticyclonic feature described in Case Study 2 (Section 3.3.1.2) is shown with a green diamond marker, and the cyclonic feature described in Case Study 1 (Section 3.3.1.1) is shown with a magenta diamond marker.**

## 3.4 Discussion and Conclusions

This analysis presents a new method to automatically detect and quantify rotational drift in Antarctic sea ice using the EUMETSAT OSI SAF low resolution 48 hour sea-ice drift product range. To our knowledge, this methodological process is the first attempt to quantify synoptic scale vorticity features in sea ice using remote sensing techniques, with the aim to establish an indicator of rotational drift in the sea ice field by which to detect current and future changes in the ice dynamics. Four products are used in this study, focusing on the Atlantic sector of the Southern Ocean: three single sensor derived products and one merged product. Rotational features found in the sea ice may originate from both oceanic and atmospheric drivers, and while some initial studies may indicate that sub-mesoscale oceanic processes under the ice may be concurrent drivers (Stössel et al., 2018; S. Swart et al., 2020), there is larger evidence of the role played by atmospheric cyclones in driving sea-ice motion (Vichi et al. (2019) and references therein). The case studies presented (Section 3.3.1) indicate that the vorticity field of the sea ice is strongly linked to the cyclonic and anticyclonic curvature of isobars, both in cases of extreme weather events and mild atmospheric conditions. There is no apparent evidence of oceanic drivers effecting ice rotation in this region at these spatial and temporal scales, suggesting that the detected vorticity field is dominated by weather at daily – or even sub-daily – timescales. This aligns with existing literature that sea-ice variability in the Atlantic Sector of the Southern Ocean is primarily driven by local atmospheric conditions (Kwok et al., 2017; Matear et al., 2015).

Our method is therefore oriented towards capturing sea-ice rotational features at the scales of the synoptic weather, assuming that the underlying sea-ice field would be affected at similar spatial scales. For this reason, our detection algorithm identifies circular ice drift features with a radius of 450 km ± 50 km – which is the scale of atmospheric weather and about 6-7 times the spatial resolution of the products – and quantifies the characteristics of the vorticity field within this circumference. Two case studies are presented to highlight the type of vorticity fields found in the Atlantic region and their association with atmospheric features. Case Study 1 considers an intense cyclone traversing over the sea ice (Figure 3.1), while Case Study 2 considers a persisting high-pressure cell over the ice interior (Figure 3.2). These examples underline the different quality of the drift retrieval between products, which ultimately leads to a difference

in the coverage of the computed vorticity field and in the detection of features. The resulting vorticity is sensitive to the choice of quality flags used. Unsurprisingly, the merged product has the best coverage in the case of cyclones and anticyclones. This is because the merged product processes drift estimates from multiple sensors and is therefore more likely to have a good quality-flagged drift estimate at each grid point. The better coverage of good quality-flagged drift estimates from the AMSR-2 product means that its resultant vorticity field has better coverage than the SSMI/S product, despite both being passive-microwave based, while the coverage of the active-microwave based ASCAT product is considerably worse than the other three products.

This difference in coverage manifests into different vorticity fields, and so we observe a large discrepancy between products in the intensity of detected cyclonic and anticyclonic features, and major differences in the intensity distribution of cyclones. This result is robust and significant with respect to the uncertainties in the estimation of the vorticity features as demonstrated in Section 3.3.2. The vorticity is three orders of magnitude greater than its associated uncertainty. However, it was also shown that variability in vorticity within the feature radius is of a comparable scale to its intensity (Figure 3.4). The variability of the cyclonic features shows a tendency to increase with an increase in cyclonic intensity, while no such relationship is apparent for anticyclonic features. The small spread of uncertainty shown by single sensor products in Figure 3.3 contrasts with their higher spread of spatial variability shown in Figure 3.4. This, together with the high signal-to-noise ratio, suggests that the large variability detected is not a symptom of the drift uncertainty. It is also necessary to consider that the search radius of the feature detection algorithm described in Section 3.2 can be affected by contiguous cyclonic and anticyclonic features in the sea ice. Such condition would have a neutralizing effect on the value of its mean vorticity, and so these kinds of features should be represented in the low-intensity portions of Figure 3.3, Figure 3.4 and Figure 3.5. Assuming a random distribution of these features, we expect them to be highly heterogenous; however, only the variability of anticyclonic features detected by the merged product show higher heterogeneity in the low-intensity features (Figure 3.4g). None of the products report low-intensity cyclonic features with high variability (Figure 3.4b, d, f, and h). We thus conclude that close, dipole-like features in the vorticity field are relatively uncommon, or that they are spatially more extended, and it is thus unlikely that two opposing rotation features are equally captured in the same 450 km search radius.

The merged product displays the largest variability for both cyclonic and anticyclonic features because it combines the drift estimates from the other independent products. Our analysis of a few case studies gives some hints that the better coverage of the merged product increases the detection of rotational drift in the ice compared to the single-sensor products. The merged product has the most intense 95$^{th}$ percentile threshold for cyclonic features and the smallest proportion of low-intensity cyclonic features (Figure 3.5b). This is counterintuitive as it is expected that the merged product would show intermediate level results relative to its constituents, like that shown by the merged product in the anticyclonic distribution (Figure 3.5a). It also shows the greatest increase in variability relative to cyclonic intensity (Figure 3.4h) – illustrated by the steepest slope of its line-of-best-fit – suggesting that the higher variability detected in the merged product is linked to a larger intensity estimate. The better coverage of the merged product seemingly makes it a good candidate for synoptic scale vorticity analysis; however, we speculate that the large variability introduced by the merging process may also cause an artificial intensification of cyclonic rotation. This is because the more extreme gradients between adjacent drift vectors in a heterogenous drift-field are manifesting into an exaggerated vorticity field. However, in the absence of independent observations that would corroborate our findings, we are unable to fully identify whether this is an artefact or a feature.

The main outcome of our analysis is that all products detect a larger proportion of high intensity cyclonic features – as indicated by the heavier tail of the cyclone distribution (Figure 3.5a) relative to that of the anticyclones (Figure 3.5a) – while the mean intensity of major cyclonic events is 1.5-2.0 times larger relative to major anticyclonic events between 2016-2020. Starting from the consideration that previous studies indicate that weather primarily drives sea-ice drift in the region (see Sections 1.3.1 and 1.5.1), this suggests that atmospheric cyclones may inject more rotational momentum into the underlying sea ice than anticyclones. Furthermore, the Weddell Sea is dominated by a climatological low-pressure cell – termed the Weddell Low – which is the result of the frequent passing of cyclones through this region caused by intense cyclogenesis in the Atlantic Sector (Grieger et al., 2018; Simmonds et al., 2003; Wei & Qin, 2016) or low pressure features crossing the Drake Passage to the east (Gonzalez et al., 2018). Since it has been shown that the ice vorticity field is primarily weather driven, this dominance of cyclonic rotation in the atmosphere likely contributes to the more frequent and intense cyclonic vorticity features detected in the

sea ice. However, there may be other factors that could lead to a higher proportion of cyclones in sea-ice drift. The feature-tracking method of drift retrieval may be susceptible to inaccuracies under conditions of rapid dynamic and thermodynamic changes in sea-ice properties, such as in the event of a strong cyclone traversing the sea ice where the motion field has strong temporal gradients. This may explain the larger disagreement between products in the distribution of cyclonic features (Figure 3.5b) than that of anticyclonic features (Figure 3.5a). It is therefore necessary to consider that rapidly moving ice floes under the effect of polar storms may be blurring the rotational drift we are attempting to estimate over a 48 h period, causing a larger discrepancy between products and contributing to the large spatial variability observed in cyclonic features. It is thus difficult to discern whether the dominance of cyclonic rotation in the ice – both in frequency of events and their intensity – is due to (i) the dominance of cyclonic rotation in the overlying atmosphere; (ii) atmospheric cyclones being more effective at engendering rotational motion in the underlying sea ice than anticyclones; (iii) the feature tracking method of drift retrieval being overly sensitive to the conditions under an atmospheric cyclone; (vi) the 48 hr resolution of the satellite drift products is sufficiently long enough for the cyclone to strengthen, weaken or traverse relatively far; or (v) any combination of the aforementioned considerations.

Despite the differences between products, our results give a consistent indication that anticyclones are less intense than cyclones, and that there is a change in the intensity of the latter after 2015. This gives us confidence in the method and allowed us to perform a provisional analysis of the interannual variations in the most intense cyclonic and anticyclonic features from 2013-2020. We are cognisant that this period is too short to detect any climatic signal, and therefore this analysis is meant to demonstrate the use of this methodology to detect possible trends in the future. The results show that major anticyclonic events have remained relatively constant from 2013-2020 according to the merged, ASCAT and SSMI/S products. The AMSR-2 detected the same uniformity since its derived drift product became available in September 2015. Conversely, a substantial change in the interannual distribution of major cyclonic events is evident, where all available products detected an abrupt increase in their intensity from 2014-2017. This increase coincides with the record decline in the Antarctic sea-ice extent observed from late winter 2015 (Parkinson, 2019; Turner et al., 2017). Furthermore, there is also an increase in the number of outlier features per year from 2015 onwards, suggesting that the most intense cyclonic features may have been intensifying further in the

last years on record. Among other causes that involve atmospheric and oceanic components (Blanchard-Wrigglesworth et al., 2021; Meehl et al., 2019; Stuecker et al., 2017; G. Wang et al., 2019), it has been argued that an intensification in polar storms in 2016 contributed to the anomalously quickened SIE decline from 2015, as the overlying winds of these synoptic features induced changes in the sea-ice dynamics (Z. Wang et al., 2019).

Our results show that sea ice in the Atlantic Sector was more susceptible to cyclonic rotational features after 2015, which can be interpreted as a response to an increased incidence of polar and extra-tropical cyclones. If the sea ice was thinner and more prone to free-drift motion in general, then we would expect both an increase in cyclonic and anticyclonic rotation, but instead, only an increase in the intensity of cyclonic features is detected. This indicates that the increased incidences of polar storms are likely injecting more momentum into the underlying sea ice, however the extent of which is difficult to quantify given the disagreement between satellite products. Prior to performing further analysis of drift variability and longer-term trends linked to polar atmosphere variability, further validation of the vorticity metric with *in situ* experiments is required to better discern the differences between products. We therefore argue for the need of a concerted experiment to increase the number of observations of sea-ice drift in Antarctic sea ice to assess the quality of the products and their use to quantify rotational features. While some buoy data are available, there are much less than in the Arctic (Rabault et al., 2023). Their sparse distribution relative to the vast extent of Antarctic sea ice presents significant challenges for validating satellite-derived drift products, particularly at daily timescales. Lavergne & Down (2023) highlight this issue, demonstrating that root mean square errors (RMSEs) for Antarctic sea-ice drift are larger – ranging from 3 to 4 km – compared to approximately 2.1-2.6 km for the Arctic. This discrepancy is partly due to the limited availability of buoy data for validation in the Southern Hemisphere. Additionally, some buoys are deployed on the ocean surface rather than being attached to sea ice, which can lead to erroneous drift measurements when buoys drift away from the ice field. (Womack, Alberello, De Vos, et al., 2024a). A better validation and understanding of these features will enable us to confidently use rotational drift of sea ice as a potential derived index to detect climatic trends.

# Chapter 4 : Increased Rotational Coupling Between Antarctic Sea Ice and the Atmosphere Over the Last 30 Years

This chapter is adapted from a paper accepted for publication in the Journal of Geophysical Research: Oceans: de Jager, W. & Vichi, M. (2025). Increased Rotational Coupling Between Antarctic Sea Ice and the Atmosphere Over the Last 30 Years. *Journal of Geophysical Research: Oceans*. The Results (Section 4.3) and Discussion (Section 4.4) are taken verbatim from the publication, while the Introduction (Section 4.1) and Materials and Methods (Section 4.2) have been modified as to streamline its integration into the thesis and avoid repetition and redundancy with Chapters 1, 2 and 3.

## 4.1 Introduction

At a global scale, Antarctic sea-ice extent (SIE) had seen a variable but increasing trend between 1979 – 2014, but this was followed by an abrupt decline in 2016 and 2017 with sustained low SIE in proceeding years and subsequent minima in 2022 and 2023 (Fogt et al., 2022; Parkinson, 2019; Turner et al., 2017). This decline suggests a possible regime shift in the Antarctic sea ice system (Fogt et al., 2022; Hobbs et al., 2024; Purich & Doddridge, 2023), with numerous recent studies attributing the significant ice-extent loss to the combination of warmer ocean surface temperatures, strengthened northerly winds and the passage of quasi-stationary cyclones traversing the Southern Ocean (e.g. Blanchard-Wrigglesworth et al., 2021; Gilbert & Holmes, 2024; Jena et al., 2024; Meehl et al., 2019; Purich & Doddridge, 2023; Teske et al., 2024; Zhang et al., 2022). Medium-term atmospheric modes such as the El Niño–Southern Oscillation (ENSO) and the Southern Annular Mode (SAM) have been linked to regional sea-ice concentration (SIC) variability, but do not yet fully explain decadal trends or the recent SIE decline (Pezza et al., 2012; Polvani et al., 2021; Stammerjohn et al., 2008; J. Wang et al., 2023). Recent literature suggests that the influence of these larger-scale processes may be overestimated (Kohyama & Hartmann, 2016; Schroeter et al., 2017), and rather that synoptic-scale weather events may contribute more to the observed sea-ice variability, both

at sub-daily timescales but also as an accumulated effect on longer-term trends (Kwok et al., 2017; Matear et al., 2015; P. Uotila et al., 2011; Vichi et al., 2019).

Originating primarily from regions of cyclogenesis in the Atlantic and Pacific Sectors of the Southern Ocean, cyclones typically move eastwards, transporting warm, moist air and intense winds along their trajectory (Grieger et al., 2018; Wei & Qin, 2016). The underlying sea-ice is therefore exposed to this conveyor belt of intense cyclones, causing melting and refreezing, break-up, and momentum changes at different phases of the cyclone passage (Section 1.3.1). As discussed in Section 1.5.2, these processes change the material properties of the sea-ice, effecting its rheology and therefore its response to subsequent cyclones. While these effects have been well observed in specific cases (Alberello et al., 2020; Aue et al., 2023; P. Uotila et al., 2011; Vichi et al., 2019), the cumulative effect of the frequent and repetitive exposure to these storms do not entirely explain the observed SIC variability (Hepworth et al., 2022). As discussed in Chapter 1, observing and simulating these changes is challenging – due to logistical constraints on *in situ* sampling and the insufficient representation of these processes in models – meaning that we currently rely heavily on satellite retrieval methods to detect and quantify sea-ice variability. Traditionally, sea-ice concentration (SIC) is a widespread means quantify its distribution (see Section 1.4), but its inability to distinguish unconsolidated ice floes from pack-ice or disentangle dynamic and thermodynamic contributions to changes in SIC limits its usefulness. Notably, this limitation is a key motivate for the analysis presented in Chapter 5. Aue et al. (2023) attempts to disentangle dynamic and thermodynamic effects in a simulated case study whereby Arctic sea ice is exposed to three subsequent polar cyclones, concluding that the relative contribution of dynamic and thermodynamic processes is dependent on the length of time between subsequent cyclones. More specifically, it is shown that momentum transfer from atmospheric forcing is the dominant driver of SIC variability in cases where the sea ice is exposed to two or more cyclones within a 2-week window. Repeating this analysis in the Southern Ocean is challenging, as it is unclear how well current Antarctic sea-ice models resolve the advection of sea-ice from synoptic-scale cyclones at daily resolutions. However, as noted in Section 1.2, Antarctic sea ice is typically younger, thinner, and less constrained by coastlines, ultimately resulting in a more mobile sea-ice field compared to the Arctic (Alberello et al., 2020; Kwok et al., 2017). It therefore stands to reason that Antarctic sea ice

may be even more responsive to atmosphere-to-ice momentum transfer, and that dynamic contributions to SIC variability may be the dominant factor at the sub-seasonal scale.

While it is commonly acknowledged that polar weather does drive motion into the underlying sea ice, not much focus has been given to the transfer of cyclonic and anticyclonic momentum from atmospheric vortices into the sea-ice field. Vichi et al. (2019) described the rotation pattern that an extreme polar cyclone drove into the ice field but did not quantify the resulting rotation. Their study showed that throughout the ice interior, large-scale eddies are apparent in regions of 100% SIC, thus suggesting that pack-ice is to some extent mobile at the daily scale and therefore susceptible to rotational forcing. The results of Chapter 3 (Section 3.3) supported this; whereby various remote sensing products revealed weather-induced ice eddies throughout the ice extent (de Jager & Vichi, 2022). However, the short data record prevented any comment on potential long-term trends. Other studies of sea-ice kinematics in the Southern Ocean also showed evidence of rapidly moving, unconsolidated ice floes far into the pack-ice (Alberello et al., 2020) and commented on the strong correlation between sea-ice rotation and the atmospheric surface pressure as previously suggested by J. Uotila et al. (2000).

This Chapter investigates the dynamics of daily rotational coupling between Antarctic sea ice and the overlying atmosphere – here defined as the responsiveness of sea ice to surface wind forcing – at meso-α (200-1000 km) to synoptic (>1000 km) scales, which can be resolved by satellite-derived drift products satellite drift products (Section 2.1.1) and atmospheric reanalysis (Section 2.3). Firstly, two case studies are presented in Section 4.3.1 that substantiate the efficacy of atmospheric reanalysis and satellite-derived sea-ice displacement vectors in aptly characterizing rotational features. These case studies reveal a minimal temporal lag (< 9 hours) from atmospheric impetus to sea ice responsiveness. Furthermore, Section 4.3.2 reveals the 30 year trend in the sea-ice and atmospheric rotation dynamics and its correlation to the SAM, underscoring the complexities of the atmospheric-to-ice momentum transfer process. In Section 4.3.3, we calculated linear correlation coefficients that highlight the spatial and temporal link between atmospheric and sea-ice rotational fields. Notably, our analysis found a progressive strengthening trend in the coupling between the atmosphere and sea ice from 1991–2020 (Section 4.3.3) and counterintuitive evidence of a diminishing rotational intensity in the Weddell Sea (Section 4.3.4).

## 4.2 Materials and Methods

The analysis employed three distinct climate data products. Surface wind components and mean sea level pressure (MSLP) from ERA-5 were used (see Section 2.3) to represent atmospheric dynamics. The recently released OSI-455 product provided daily-average ice drift vectors (Lavergne & Down, 2023), whereby these 24 hour drift datasets were derived from the temporally averaged brightness temperature swaths (see Section 1.4.1) using the CMCC drift retrieval algorithm described in Section 2.1.1. An experimental swath-to-swath ice displacement product (S2S) is also used in two case studies (Section 4.3.1), whereby ice displacement vectors are computed in the area of overlap between individual swaths (Lavergne et al., 2021). This swath-based retrieval method offers precise timestamps of drift observations at sub-daily timescales, but at the cost of limited spatial coverage. Extensive analysis exploring the potential applications of the S2S product is presented in Chapter 5.

To quantify the rotation of the sea-ice field, OSI-455 and S2S displacement vectors were used to compute the sea-ice vorticity following the method described in Section 2.2, while ERA-5 surface wind components yielded hourly atmospheric vorticity. The daily-average atmospheric vorticity was then computed, temporally aligned with each day's respective sea-ice vorticity (cantered at midnight; 12h00 to 11h00). Atmospheric vorticity was also spatially interpolated onto a 75 km EASE-2 grid projection, matching that of the sea-ice drift datasets. Daily atmospheric vorticity fields were masked against corresponding ice vorticity coverage, yielding a pair of spatially coherent vorticity fields every 24 hours (code made available by de Jager (2024)). This methodology was applied daily from April to November between 1991 and 2020, as these months had sufficiently large enough sea-ice extent (SIE). The Southern Ocean region was partitioned into five sectors Figure 4.1: Weddell Sea (WS), King Haakon (KH), East Antarctica (EA), Ross Sea (RS), and Amundsen Bellingshausen (AB), each revealing a regionally distinct link between sea-ice concentration (SIC) variability and atmospheric circulation modes (Raphael & Hobbs, 2014).

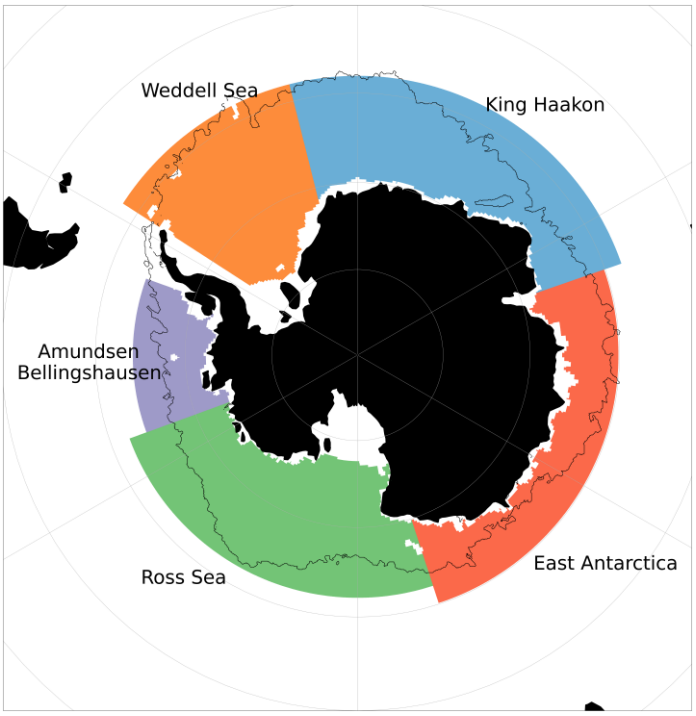


**Figure 4.1: The five sectors constituting the Southern Ocean sea-ice landscape as defined by Raphael & Hobbs (2014), namely the Weddell Sea, King Haakon, East Antarctica, Ross Sea, and Amundsen Bellingshausen sectors. For demonstrative purposes, the ice-edge on the arbitrarily chosen day of July 24, 2019, is shown.**

## 4.3 Results

### 4.3.1 The Response of Sea Ice to Atmospheric Rotation at the Synoptic Scale

Both the swath-derived and daily sea-ice drift estimates were employed to evaluate and quantify their spatial correlation with an atmospheric dipole in terms of vorticity. Figure 4.2 displays two example case studies: one in the Weddell Sea sector (Example 1; panels a-d), and another in the Ross Sea sector (Example 2; panels e-h). The sea-ice vorticity field in the Weddell Sea over a 9.88-hour period was computed from swath-based displacement estimates within the region of overlap between ascending and descending PM AMSR-2 swaths at 16:57:39 on 26 July and 02:50:45 on July 27, 2019, respectively (Figure 4.2a). This

overlap covers a substantial portion of the ice-covered Weddell Sea sector, revealing a distinctive cyclonic rotation on the western half and anticyclonic rotation on the eastern half. Figure 4.2b displays the average ERA-5 Mean Sea Level Pressure (MSLP) and vorticity fields over an overlapping 10-hour observation window (17:00:00 on 26 July to 03:00:00 on July 27). ERA-5 reanalysis data indicates the development of a low-pressure (LP) system over the western Weddell Sea, the core of which is located near the Antarctic Peninsula and had an average pressure of 970.36 hPa over this period. The atmospheric vorticity field follows the LP system, displaying extreme cyclonic rotation in and around the core (Figure 4.2b). Simultaneously, a subtropical high-pressure (HP) system north of the sea-ice edge developed an elongated ridge protruding southward over the ice forming a synoptic scale dipole with the LP core across the Weddell Sea. Spatially, atmospheric rotation in the western and eastern Weddell Sea sector is divided into cyclonic and anticyclonic features, respectively, with diminishing intensity towards the dipole's midpoint, where MSLP contours become squeezed and parallel, and rotation is approximately zero (Figure 4.2b). The sea-ice vorticity field aligns clearly with the atmospheric surface-level vorticity with a magnitude ratio of approximately 100:1. The daily averaged sea-ice and atmospheric vorticity fields are shown (Figure 4.2c, d). Sea-ice drift estimates were derived from temporally averaged swath measurements from 12:00:00 on July 26 to 12:00:00 on July 27 (Figure 4.2c), with hourly ERA-5 pressure and vorticity fields averaged over the same 24-hours period (Figure 4.2d). The general structure of the LP core and HP ridge is still evident in the daily products, although with some blurring of feature details. Pressure contours and atmospheric vorticity show a weaker LP core and less defined HP ridge. Similarly, the cyclonic and anticyclonic features in the sea ice are also less defined in the daily product – particularly at the dipole midpoint – as evidenced by the more heterogeneous vorticity field (Figure 4.2c). However, despite some blurring of detail, it is evident that the daily drift product captures the rotation features well and suggests that the dynamic coupling between the ice and atmosphere persists at daily timescales. After spatially masking the ERA-5 vorticity field against the ice coverage, a linear correlation between the two daily vorticity fields yielded a 0.60 Pearson coefficient. This demonstrates the quantitative similarity of atmospheric and ice rotational patterns alongside the qualitative coherence displayed in panels c and d.

Example 2 provides similar insights from a different region. Here, the sub-daily ice vorticity field was computed over a 15.78-hour window – using swaths at 09:13 on July 23 and 00:52 on July 24, 2019,

overlapping in the Ross Sea. During this period, a LP core (approximately 965 hPa) was located over the Amundsen Bellingshausen sectors – as evidenced by ERA-5 pressure contours (Figure 4.2e, f) – with the cyclone's trailing front persisting over the eastern Ross Sea. Simultaneously, a large HP system existed north of the Ross Sea. The interaction between these two systems – as well as the coastal atmospheric dynamics in the region – resulted in anticlockwise rotation in the central Ross Sea, neighboured by two adjacent cyclonic features. Much like in the Weddell Sea example, both the swath-based and daily drift estimates show strong spatial conformity between ice and atmospheric rotational dynamics. However, in this case there is less difference because both products produce similar levels of detail and field heterogeneity. We notice that the sub-daily temporal window of 15.78 hours is closer to that of the daily product, and therefore a more similar level of blurring is expected, with any minor deviations explained by the temporal window difference and the variation in start and end timestamps. In this case, the linear correlation between atmospheric and ice vorticity produced a coefficient of 0.53 in the Ross Sea sector.

These case studies contribute the following key points that are relevant for the analysis presented in the next sections: (a) a visual demonstration of spatial scales and rotational characteristics in both the atmosphere and sea ice. (b) There can be minimal temporal lag, in the order of 10 hours, between atmospheric forcing and ice drift response. This temporal alignment justifies a 24-hour field similarity correlation method to quantify the coupling between the ice and atmosphere. Lastly, (c) despite the blurring some feature detail, the daily average sea-ice displacement product effectively characterizes weather-driven rotational dynamics in the ice.

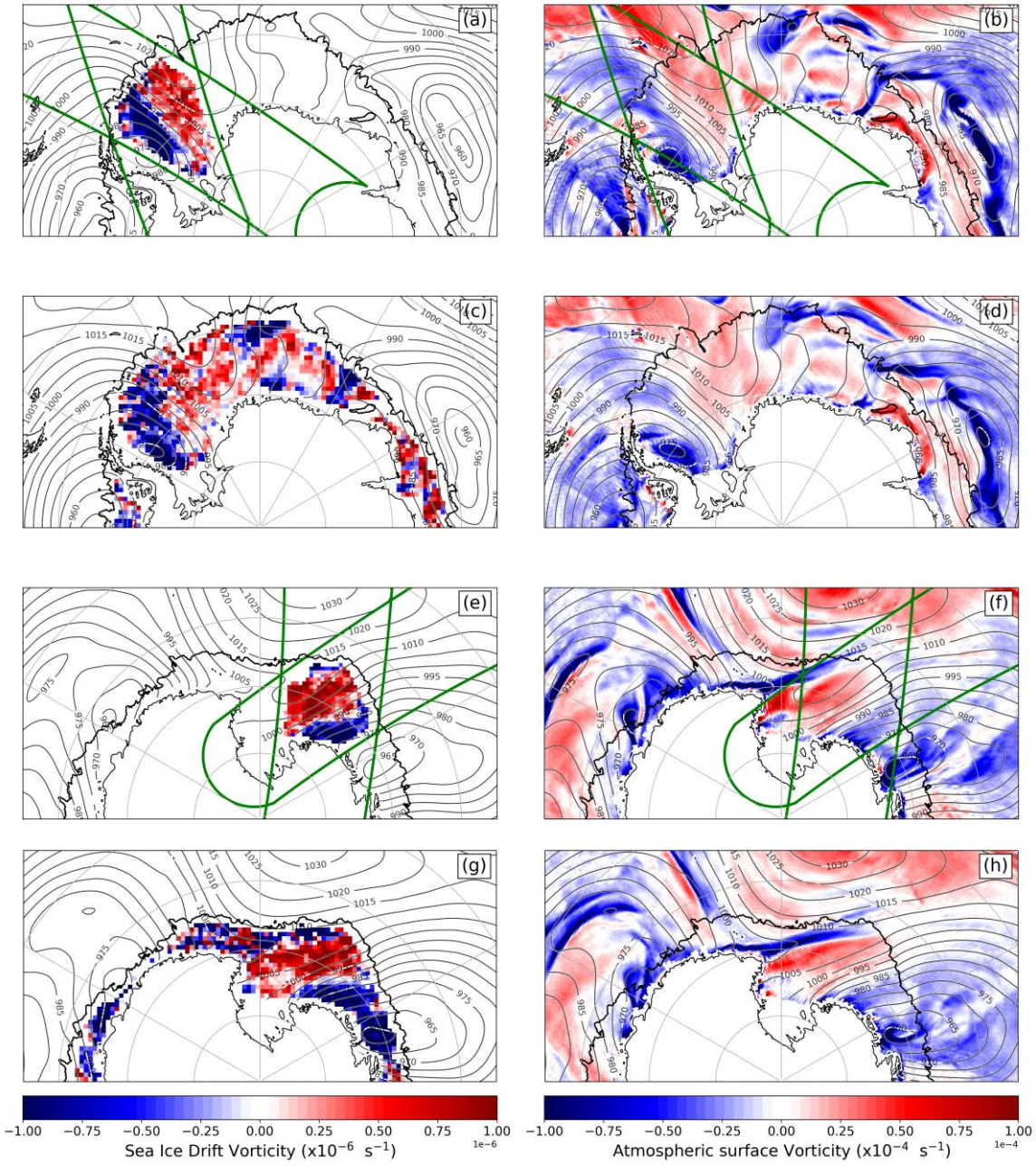


**Figure 4.2: Example 1 – Weddell Sea: (a) the sea-ice vorticity field over an 9.88 hr period from 26 July 2019, 16:57 to 27 July 2019, 02:50 (UTC). (b) A 10-hr average of hourly ERA-5 surface-level vorticity over a period closest in time to the satellite swaths. (c) Sea-ice vorticity computed from the**

**daily drift product on 27 July (midday to midday, backwards-in-time averaging scheme). (d) A 24-hr average of hourly ERA-5 surface-level vorticity. Overlying black contour lines show the mean sea level pressure over the same temporal window as the panel's vorticity field. Example 2 – Ross Sea: (e) the ice vorticity field over a 15.78 hr period from 23 July 2019, 09:13 to 24 July 2019, 00:52. (f) A 16-hr average of ERA-5 vorticity. (g) Ice vorticity computed from the daily drift product on 24 July. (h) The 24-hr average of ERA-5 vorticity over the same window. The green polygons indicate the scanning footprint of the two overlapping satellite PM swaths used for computing the sub-daily drift.**

## 4.3.2 Atmosphere-Ice Vorticity Coupling Between 1991–2020

The case studies in Section 4.3.1 demonstrated that sea-ice and atmospheric rotation patterns are closely aligned in both space and time. Building on these findings, the analysis was expanded to the full OSI-455 daily sea-ice drift dataset (1991–2020) and compared with surface atmospheric reanalysis. The Southern Annular Mode (SAM), a key atmospheric circulation pattern, is characterized by variations in the westerly winds encircling Antarctica (Fogt & Marshall, 2020). Given its significant influence on atmospheric turbulence, storm tracks, and daily sea-level pressure (Baldwin, 2001; Marshall, 2003), it is reasonable to hypothesize that SAM may also affect sea-ice vorticity. To explore this potential connection, we assessed the relationship between atmospheric turbulence, the SAM index, and sea-ice vorticity.

### 4.3.2.1 Interannual Variability of Winter Atmospheric and Sea-Ice Vorticity

Figure 4.3a and Figure 4.3b demonstrate the annual fluctuations in the mean atmospheric and sea-ice vorticity, respectively. These annual means are computed using the months April – September because the CMCC drift retrieval method typically performs well in freeze-up conditions as distinguishable features in the brightness temperature field persist over 24 hours. No discernible trend emerges in the atmosphere nor ice in any sector over the 30-year period, a notable point in the context of the recent asymmetric trend in the SAM index. The magnitude of vorticity in the sea ice ($x10^{-7}$ $s^{-1}$) is shown to be approximately two orders smaller than that of the atmosphere ($x10^{-5}$ $s^{-1}$), a difference consistent with the results described in Section 4.3.1 (Figure 4.2). Our results imply a consistent dominance of cyclonic rotation throughout – denoted by negative vorticity – in both the atmosphere (Figure 4.3a) and ice (Figure 4.3b), and further corroborated by the 30-year means indicated with dashed lines and described in Table 4.1. Atmospheric

mean states reveal regionally distinct vorticity regimes (Figure 4.3a and Table 4.1), as the East Antarctica sector consistently exhibits the most extreme rotation ($-1.45 \times 10^{-5}$ $s^{-1}$) over the 30-year timeseries, while the Weddell Sector displays the weakest rotation in most years ($-0.36 \times 10^{-5}$ $s^{-1}$). In the sea ice (Figure 4.3b and Table 4.1), the Weddell Sea again demonstrates the weakest rotation ($-0.86 \times 10^{-7}$ $s^{-1}$), much like its atmospheric counterpart. However, the disproportionately intense regime observed in the atmosphere in the East Antarctic sector is not found in the sea ice. Instead, the Amundsen-Bellingshausen sector is the most intense ($-1.99 \times 10^{-7}$ $s^{-1}$). Sector discrepancies are further characterized by their year-to-year fluctuations. We calculated the coefficient of variation (CoV) of each timeseries to quantify this interannual variability. The CoV is a standardized measure of dispersion - equal to the standard deviation of the timeseries divided by its mean - and therefore allows for the comparison of variability across the two timeseries of differing scales. Table 4.1 indicates that the Weddell Sea exhibited the highest CoV in the atmosphere (33.6%) and similarly high in the ice (29.1%), suggesting that the sector is characterized by the largest interannual variability in both fields. Similar atmosphere and ice CoV values are also demonstrated in the Ross Sea (both ~15%) and Amundsen Bellingshausen (both ~20%) but to a lesser magnitude than that of the Weddell Sea. Conversely, the King Haakon and East Antarctica sectors each show a large discrepancy between atmospheric and sea-ice variability, with low atmospheric and high ice CoV values, respectively (Table 4.1).

To address the inherent seasonal variability in the atmosphere and sea-ice vorticity fields, a monthly climatology was computed for months April – September. To avoid introducing any supervised bias into our analysis, we chose to use the full 1991-2020 record to compute the climatology, as there are no suggestions in existing literature to justify the use of a subset of years. Subsequently, monthly anomalies were derived for both the ice and atmospheric vorticity fields. This analysis was repeated for all five sectors, although only the Weddell Sea results are shown for demonstration purposes (Figure 4.3c, d), once again with a 1:100 scaling factor between variables. Blue bars denote months with heightened cyclonic rotation, while red bars signify increased anticyclonic rotation. Notably, while each of the monthly anomaly timeseries exhibits no overt trend over the 30-year period, the relative magnitude and sign of the monthly anomalies in both vorticity fields demonstrate remarkable similarity. Linear correlation of these anomalies yielded a coefficient of approximately 0.93 between the two timeseries, affirming a robust link between

atmospheric and sea-ice rotation anomalies in the Weddell Sea sector. This implies that any departure from the monthly climatological mean in the atmosphere is likely to result in a commensurate anomaly in the underlying sea ice. A similarly strong correlation is also demonstrated in the Ross Sea (0.89) while the King Haakon (0.69), East Antarctica (0.66) and Amundsen Bellingshausen (0.65) sectors showed more moderate but still notable similarities. Sector-wise comparisons reveal a notably higher correlation in the Weddell and Ross Sea sectors, which can be attributed to their extensive ice extent throughout the year. This can be explained by the limitations of the ice drift product in highly dynamics regions, which results in lower quality measurements in and around the MIZ. The ratio of the number of measurements taken near the MIZ relative to the total number of measurements is therefore important. The Weddell and Ross Sea sectors have a higher proportion of drift measurements in the ice interior, yielding a more robust mean vorticity calculation that is less sensitive to the poorer quality estimates near the MIZ. Conversely, the other sectors have a narrow ice interior and long coastal perimeter, resulting in a lower number of good measurements in the sector. Although this ratio varies across sectors, it remained relatively consistent for each month throughout the study period, with no discernible trend, confirming that the results are not an artefact of product performance.

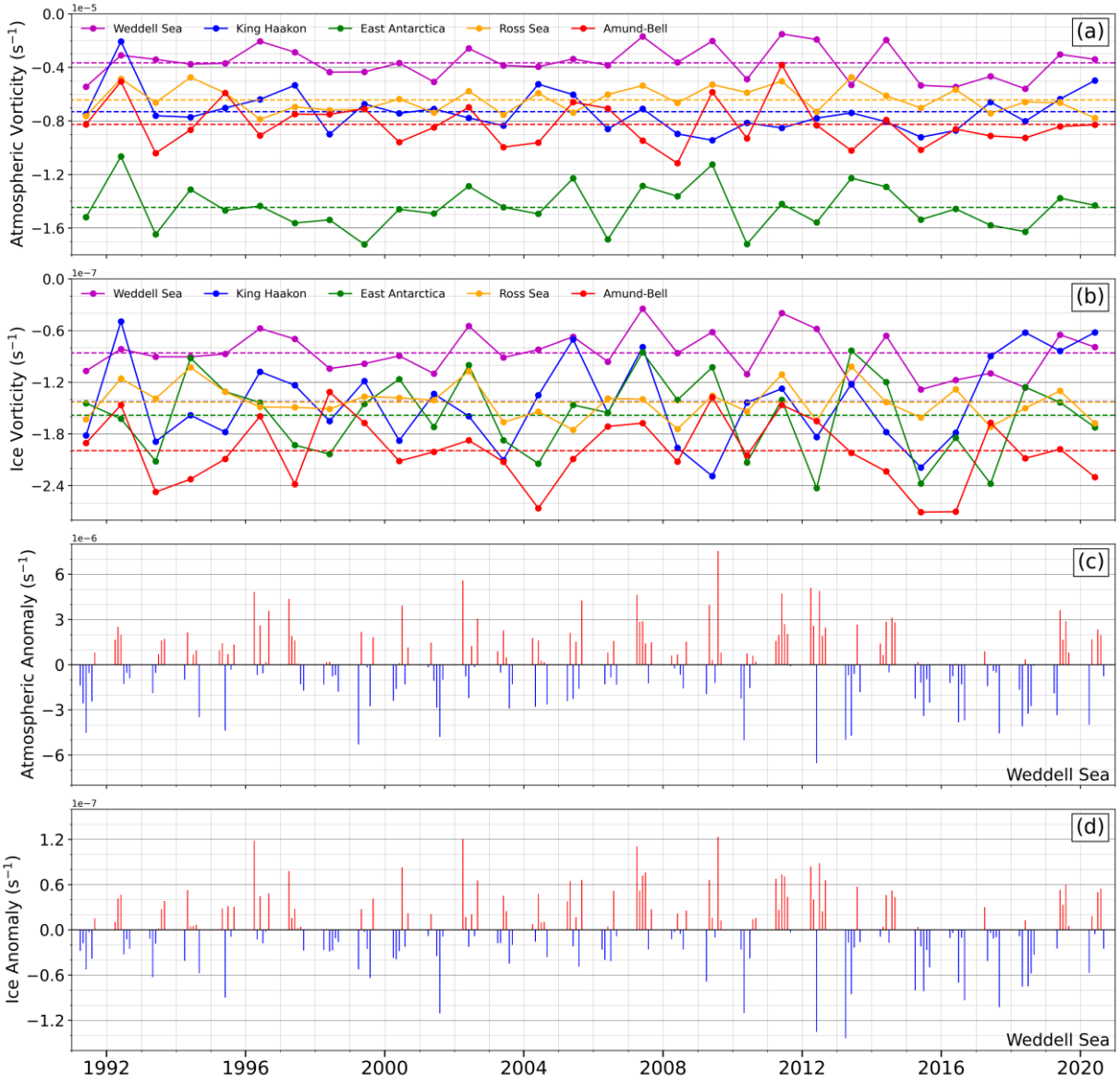


**Figure 4.3: The mean vorticity of the (a) atmosphere and (b) sea ice for each year between 1991-2020, calculated from daily vorticity fields in April-September (note the different order of magnitude). Dashed lines indicate the 30-year mean for each of the five sectors shown in Figure 4.1. Note that the yellow dashed line (Ross Sea) overlaps the blue dashed line (King Haakon) in panel b. The monthly anomalies with respect to their seasonal means in the (c) atmosphere and (d) sea ice for months April-September in the Weddell Sea.**

**Table 4.1: The 1991-2020 mean vorticity ($s^{-1}$) and coefficient of variation (%) in the atmosphere and sea ice. The coefficient of variation is equal to the standard deviation of the timeseries divided by its mean. These values are computed using months April-September. Mean vorticity values correspond to dashed lines shown in Figure 4.3a and Figure 4.3b, while the coefficient of variation describes the interannual fluctuations about the dashed line.**

| | Atmosphere | | Sea Ice | |
|---|---|---|---|---|
| | **Mean vorticity ($x10^{-5}$ $s^{-1}$)** | **Coefficient of variation (%)** | **Mean vorticity ($x10^{-7}$ $s^{-1}$)** | **Coefficient of variation (%)** |
| **Weddell Sea** | -0.36 | 33.6 | -0.86 | 29.1 |
| **King Haakon** | -0.73 | 21.0 | -1.42 | 35.3 |
| **East Antarctica** | -1.45 | 11.5 | -1.58 | 29.4 |
| **Ross Sea** | -0.64 | 15.0 | -1.43 | 14.6 |
| **Amundsen Bellingshausen** | -0.83 | 20.4 | -1.99 | 19.3 |

### 4.3.2.2 The Role of the Southern Annular Mode on Winter Sea-Ice Rotation

Figure 4.4a illustrates the interannual variability of the SAM index as the mean of winter months (June, July and August) standardized over 1957-2022. The monthly indices are defined based on Marshall (2003). The winter index shows a statistically non-significant increasing trend, contrasting with the increasing trend observed in summer months (Fogt & Marshall, 2020; N. Swart & Fyfe, 2012). The trend is also not significant with reference to the 1991-2020 subset period over which atmospheric and sea-ice vorticity was assessed (Section 4.3.2.1). We then computed the daily eddy kinetic energy (EKE) using ERA-5 surface wind components, whereby the EKE is defined as the difference of the daily wind components from their monthly mean (Figure 4.4b). EKE climatological composites were computed, labelled as $EKE_{SAM+}$ and $EKE_{SAM-}$, each representing the surface-level turbulence during months measuring positive and negative SAM indices, respectively. Figure 4.4b and Figure 4.4c assesses the King Haakon sector, chosen because

it demonstrated the most extreme discrepancy between SAM+ and SAM- conditions in terms of monthly mean EKE. Figure 4.4b displays the seasonality of the $EKE_{SAM+}$ and $EKE_{SAM-}$ composites, which indicates that both exhibit a rapid increase in autumn and a plateauing through winter, a period coinciding in time with the sea-ice freeze-up period (April – September). The EKE then gradually diminishes through spring before reaching a minimum in summer. It can therefore be reasoned that the rotational energy associated with surface winds is greatest in winter. The largest difference between the composites is distinguishable in the summer months (DJF) despite some overlap of the standard deviations, and it diminishes through autumn (MAM) and seemingly becomes negligible in winter (JJA). This aligns with the knowledge that the effect of SAM oscillations is primarily a summer phenomenon. Linear regression statistics between the monthly ice vorticity and corresponding SAM index are displayed in Figure 4.4c. Here, $R^2$ (blue bars) quantify the variance in ice vorticity that can be explained by variability in the SAM index, and the Pearson Coefficients (black lines) indicate the sign of the relationship. Correlations were statistically significant in months May – November (p-value < 0.05), although it is necessary to note that ice displacement estimates in October and November are weighted against a free-drift wind-model. Results indicate that the SAM index explains about 16-51% of the variance observed in ice vorticity with an inversely proportional relationship, indicating that a higher SAM index is linked to intensified cyclonic rotation (and vice versa). The analysis was repeated in the other four sectors (not shown), whereby the East Antarctica sector was comparable to the King Haakon, while the other three showed significant but weaker correlations. The same analysis was applied to the atmospheric vorticity (not shown), whereby similar results were found, further evidencing the strong correlation between atmospheric and sea-ice vorticity at monthly scales.

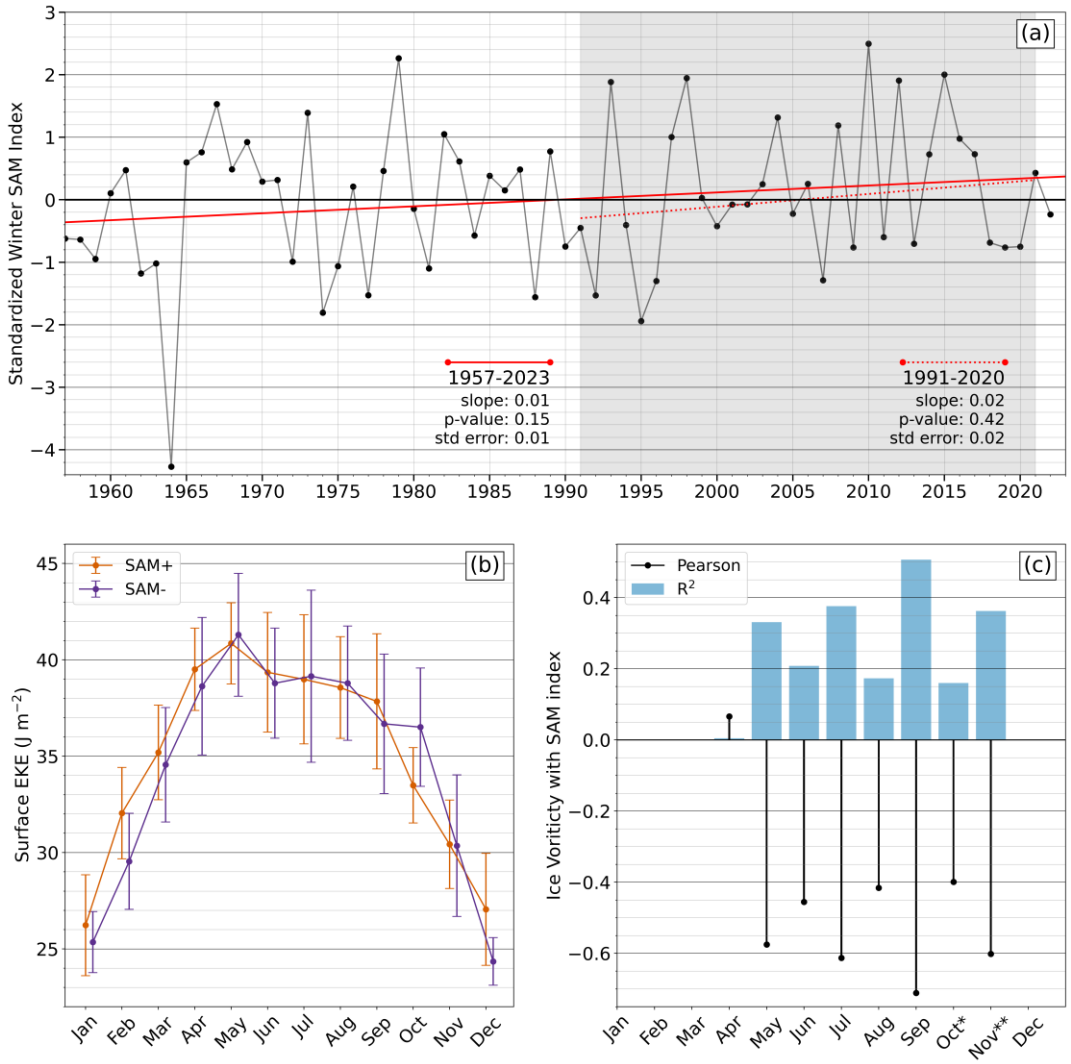


**Figure 4.4: (a) The standardized winter mean SAM index (June, July and August). The grey area indicates the subset period of 1991-2020. Regression lines computed over 1957-2022 (solid line) and 1991-2020 (dashed line) are shown in red with statistics reported in units per year. (b) The mean seasonality of the eddy kinetic energy (units J $m^{-2}$) at the surface between 1991-2020 in the King Haakon sector. Monthly climatologies are generated using ERA-5 surface wind components during positive SAM phases (SAM+; orange) and negative SAM phases (SAM-; magenta). (c) The variance ($R^2$; blue bars) and correlation (Pearson; black lines) in the monthly sea-ice vorticity explained by the SAM index in the King Haakon sector. Note that October and November sea-ice drift estimates are derived from free drift wind-modelled data (denoted with *).**

### 4.3.3 Temporal Evolution of Atmosphere-Ice Vorticity Field Similarity

The similarity of spatial data between the atmospheric and sea-ice vorticity was quantified. The cell-to-cell linear correlation was calculated between daily vorticity fields, meaning that every vorticity estimate in the ice was compared against the corresponding estimate in the overlying atmosphere. As we have demonstrated that any potential temporal lag that exists between atmospheric forcing and sea-ice response is less than ~10hrs (Section 4.3.1), a cell-to-cell linear correlation method preserves both spatial and temporal information, rendering the resultant coefficient an estimate of the spatial similarity between daily scalar fields over the course of a month. A comprehensive systematic correlation at daily intervals over 30 years of winter data was then conducted to generate the presented results discussed in the chapter. Figure 4.5a presents the monthly climatological mean correlation coefficient for the years 1991–2020. Note that the months of October and November obtained from the inclusion of the free-drift model in the ice drift product are also considered, as monthly anomalies are independently computed and thus their interannual variability is represented against their own climatology. Their inclusions in this seasonality analysis (Figure 4.5a) demonstrate the theoretical coefficients expected in an idealized case whereby ice rotation dynamics are exclusively wind driven, providing a contrast to the satellite-derived drift in winter months. Furthermore, to ensure sufficient ice cover, only days with 25 or more nominal ice vorticity values in the sector were considered.

Results of the seasonality analysis provide the climatology of the monthly mean correlation coefficients and associated dispersion. Mean values were then used to calculate the monthly anomalies over the 30-year period within the context of a seasonal signal. All five sectors displayed positive correlations between atmosphere and sea-ice rotation dynamics, with means ranging from 0.32 to 0.92. To discern any coincidental correlation arising from randomness, this analysis was repeated with a shuffled series of cell values (not shown). The low correlation (-0.05 to 0.05) between these shuffled series indicated that the observed correlations reported here are unlikely to be artifacts of randomness. In the April-September period, the Weddell, Ross, and Amundsen Bellingshausen sectors exhibit minimal seasonal variation. The Ross Sea sector displayed the strongest and most consistent similarity between rotation dynamics, as evidenced by the greatest coefficient mean (0.60) and the smallest spread (±0.12). The Weddell and

Amundsen Bellingshausen sectors were similarly consistent, with wider data spread in the latter, likely due to smaller ice extent. Conversely, the King Haakon and East Antarctica sectors show a progressive similarity increase until plateauing in August-September, with a large data spread in the austral autumn and reduced spread in late winter and spring as the ice extent grew. Notably, a surge occurred in October and November across all sectors due to reliance on the wind-driven free-drift model for sea-ice displacement estimates.

A timeseries of correlation coefficient anomalies were computed as the difference between each month and its respective seasonal baseline mean, thus removing the seasonal signal. These timeseries are displayed in Figure 4.5, panels b – f. October and November are not shown here, as the same free-drift model is used to estimate ice displacement in these summer months throughout the 30-year period, and so only negligible changes are observed in the anomalies. Results show that winter months (April – September) exhibit a statistically significant increasing correlation ($p$-value $< 0.05$) in monthly anomalies between 1991 – 2020 in all five sectors. This is illustrated in Figure 4.5b-f as mostly negative anomalies (blue) transitioned into mostly positive anomalies (red). Anomalies primarily ranged between -0.1 and 0.1 (Figure 4.5b-e), except for the Amundsen-Bellingshausen sector, which exhibited higher variability, typically between -0.15 and 0.15 (Figure 4.5f). This indicates an approximately 0.2 increase in the atmosphere-ice vorticity correlation coefficient in the Weddell Sea, King Haakon, East Antarctica, and Ross Sea sectors over the past three decades, and a 0.3 increase in the Amundsen-Bellingshausen sector. It is therefore shown that the similarity of the rotation dynamics quantified in the sea-ice field have become more similar to that of the surface atmosphere since 1991.

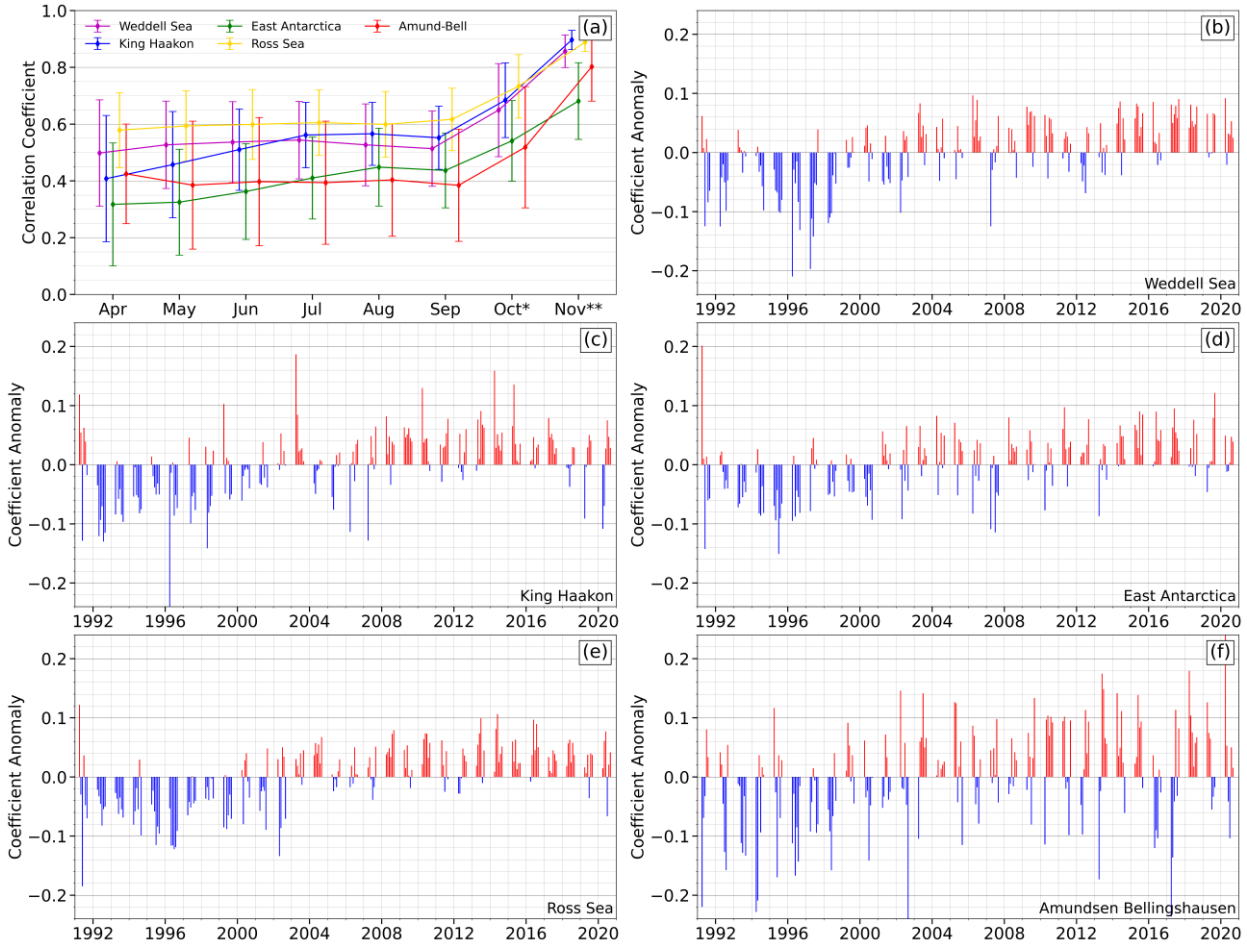


**Figure 4.5: (a) Seasonality in atmosphere-ice linear correlation coefficient, with the 1991-2020 mean and standard deviation for each sector indicated with the marker and bars respectively (symbols have been staggered to visualize the bars). Panels b-f illustrate the monthly anomalies in the coefficient with respect to the presented seasonality for the (b) Weddell Sea, (c) King Haakon, (d) East Antarctica, (e) Ross Sea and (f) Amundsen-Bellingshausen sectors.**

### 4.3.4 Weddell Weakening: Diminishing Rotational Intensity in Weddell Sea Sea Ice

In the Weddell Sea sector, a unique phenomenon emerged upon isolating the sea-ice vorticity field into its anticyclonic and cyclonic components. This involved computing the mean vorticity for negatively and positively rotating cells independently. Monthly climatologies were generated and subsequent anomaly

timeseries were derived. These timeseries are displayed in Figure 4.6, indicating that the Weddell Sea experienced a discernible reduction in rotational magnitude in both components from 2001 to 2002 (dashed line). In instances of cyclonic rotation (Figure 4.6a), earlier years displayed mostly negative anomalies, indicating a heightened intensity of cyclonic rotation compared to the climatological mean. Post-2001, a regime shift occurred with monthly anomalies adopting a positive sign. This shift implies a diminishing magnitude of cyclonic rotation, as the cyclonic vorticity tended toward zero. A similar trend is observed in anticyclonic rotation (Figure 4.6b), but with opposite signs, and again indicating a diminishing magnitude of rotation. The amalgamation of these scenarios suggests an overall reduction in the intensity of rotation in the Weddell Sea ice over time, a feature observed only in this sector and concealed by the mean vorticity metric due to the opposing signs of rotation diminishing at comparable magnitudes. Following this, a sensor or drift product processing change was hypothesized to explain of this abrupt shift. The OSI-455 drift dataset utilizes passive microwave data from a series of satellite-mounted sensors over the 30-year record (including SSMI-F10, SSMI-F11, SSMI-F13, SSMI-F14, SSMI-F15, SSMIS-F16, SSMIS-F17, SSMIS-F18, AMSR-AQ, and AMSR2-GW1). To combine data from multiple sensors, the product applies a weighting function inversely proportional to the error associated with each sensor, thereby giving greater weight to better-performing instruments. This approach ensures continuity across the 30-year record, as each sensor only partially contributes to the final output and newer sensors are calibrated against multiple predecessors. Consequently, no obvious discontinuities are evident during sensor transition periods. Specifically, during the 2000-02-28 to 2006-07-31 interval – which encompasses the abrupt change observed between 2001 and 2002 – there were no changes in sensor constituents (SSMI-F13, SSMI-F14, and SSMI-F15) or their relative weighting (Lavergne & Down, 2023). Considering these points, it is therefore unlikely that sensor changes explain the abrupt weakening observed in the Weddell Sea rotation dynamics.

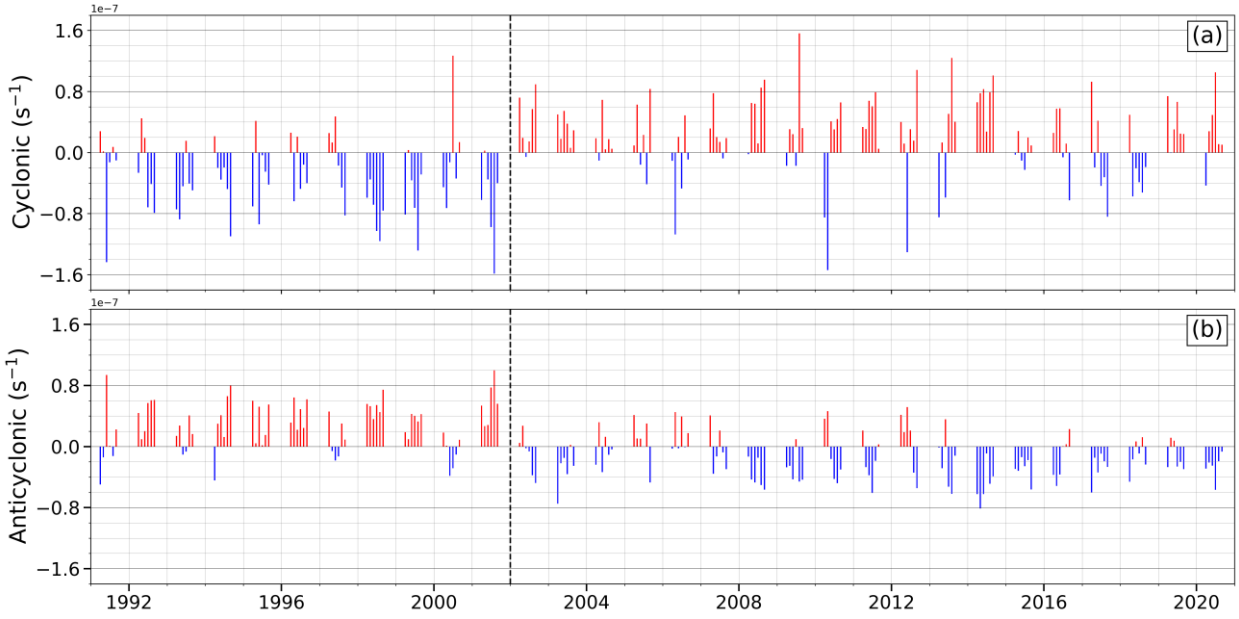


**Figure 4.6: Anomaly in the mean vorticity for (a) cyclonic and (b) anticyclonic rotating cells in the Weddell Sea sector for months April – September, with respect to the 1991-2020 climatological mean.**

## 4.4 Discussion

This study marks the first attempt to describe and quantify the interplay between rotational dynamics within Antarctic sea ice and the overarching atmospheric conditions. Targeting daily timescales, our methodology aims to capture the influence of synoptic-scale events, including large polar storms and high-pressure systems, on sea-ice motion. Utilizing hourly atmospheric reanalysis data and daily satellite-derived ice drift estimates, we examine the cumulative contributions of these weather features to longer-term dynamical trends over the past 30 years. This choice is justified by the case study presented in Section 4.3.1 whereby results substantiate that sea-ice drift response to atmospheric forcing occurs at sub-daily timescales, thus establishing a foundation for employing a spatial similarity correlation method to assess air-ice coupling at 24-hour intervals. In the following, we discuss the net dominance of clockwise rotation observed in the sea ice, which is generally attributed to atmospheric storms imparting cyclonic rotation into the underlying ice field (Turner et al., 2017; Z. Wang et al., 2019). Despite the absence of overt trends in mean atmospheric

or sea-ice vorticity, our findings demonstrate a discernible increasing correlation between atmospheric and ice rotation. This strengthened coupling over the past three decades suggests a growing susceptibility of ice drift to atmospheric forcing. Notably, our investigation identifies a distinctive scenario in the Weddell Sea, where rotational intensity diminishes despite a strengthening relationship to atmospheric rotation over the same period. Since this increased coupling is observed over a period of more frequently positive Southern Annular Mode (SAM) phases (Fogt & Marshall, 2020), our discussion will also address its influence.

### 4.4.1 Atmospheric and Ocean Drivers of Rotational Drift in Sea Ice

Our results further evidence the atmosphere's role as a primary driver of rotation in Antarctic sea ice. Section 4.3.1 provides a qualitative description of the similarities between the sea-ice and atmospheric vorticity fields, demonstrating that sea-ice mimics the general patterns of the overlying atmosphere at the daily scales (Figure 4.2c, g). The sub-daily product is not yet routinely available and so we could not extrapolate our methodology into a climatological analysis using the higher temporal resolution estimates, however, we recommend its development since the analysis of sub-daily scales will likely bring more insights into the relationship between dynamics and thermodynamics, contributing to increasing our knowledge for better model parameterizations. The timeseries of monthly anomalies presented in Section 4.3.2 demonstrates a clear dependence between atmosphere and ice rotation over the 30-year time scale (Figure 4.3c, d), informing that any deviation in atmospheric vorticity from its climatological mean resulted in a similar deviation in the sea ice in both sign and relative magnitude. The 100:1 order-of-magnitude ratio between the atmosphere and ice is a consistent theme throughout our analysis (i.e. $10^{-5}$ m $s^{-1}$ in the atmosphere and $10^{-7}$ m $s^{-1}$ in the ice), displayed by the case study maps (Figure 4.2) and the monthly mean and anomaly analysis (Figure 4.3). This order-of-magnitude ratio is typically associated with the wind-to-ice momentum exchange in compact ice (Leppäranta, 2005), and implies that the scales of vorticity tied to synoptic features are maintained when averaging over a longer period.

Our results indicate a dominance of cyclonic rotation (clockwise in the Southern Hemisphere) in both the atmosphere (Figure 4.3a) and sea ice (Figure 4.3b) as first indicated in Chapter 3 and extended here over a

larger study period and using a higher temporal resolution ice drift product. It is therefore necessary to consider that the subsequent results described here – specifically in the cases of monthly anomalies – are occurring within a sea-ice field that is primarily rotating in a clockwise direction. While these findings evidence the atmosphere's participation in driving the ice rotation dynamics, it still leaves room for other considerations, such as sea-ice rheology, ocean influences and the accuracy of the daily-averaged sea-ice drift retrieval method. Thus, distinguishing the drivers of this cyclonic dominance is complex. The role of the under-ice ocean currents must also be considered, although there are no available robust estimates besides ocean reanalyses which can be used as broad references (Womack et al., 2022). Large-scale dynamical systems such as the Weddell and Ross Sea Gyres are obvious ocean-forcing candidates but likely make negligible contributions to the daily variability observed in the sea ice. Instead, southward propagating mesoscale eddies spinning off from the Antarctic Circumpolar Current (ACC) are likely more influential to sea-ice variability (e.g. S. Swart et al., 2020). Models and observations indicate that variability in local wind forcing primarily drives changes in the ocean surface eddy kinetic energy (EKE), rather than changes to the ACC transport (Hughes, 2005; Munday et al., 2013; Tansley & Marshall, 2001). EKE is the primary source of turbulence in the region's surface ocean dynamics (Gille & Kelly, 1996; Mazloff et al., 2010), which not only affects sea-surface vorticity dynamics at scales comparable to that of sea ice (i.e. at the order of magnitude $10^{-6}$ $s^{-1}$), but also has implications for the Southern Ocean overturning circulation (Hallberg & Gnanadesikan, 2006; Morrison & Hogg, 2013). Over longer time scales, it is argued that surface vorticity is typically balanced by changes to the vertical transport, and it can take years for wind perturbations to affect EKE along the ACC (Meredith et al., 2012; Rintoul & Naveira Garabato, 2013, and references therein). Thus, while the ACC turbulence is likely a factor in sea-ice rotational dynamics, it does not directly explain this disproportionately intense cyclonic rotation observed in the sea-ice field. This suggests that atmospheric contributions are likely to be more substantial, although dedicated modelling experiments should be performed to better quantify the role of cyclones in shaping the vorticity of sea ice.

### 4.4.2 Multidecadal Atmospheric and Sea-Ice Vorticity Trends

To our knowledge, the contributions of synoptic-scale features on the long-term trends in sea-ice rotation dynamics have previously remained unexplored. Antecedent studies have demonstrated regional variability

of sea-ice dynamics over the decades of the satellite records, but with focus given to general circulation patterns at monthly timeframes, rather than the daily response of the sea ice to local weather (P. Holland & Kwok, 2012; Kwok et al., 2017; Sun & Eisenman, 2021; Z. Wang et al., 2019). de Jager & Vichi (2022) examined weather-induced rotation more directly, but the data coverage of just seven years limited any comment on potential drift trends. We therefore present the first look at multidecadal trends in Antarctic sea-ice rotation. Our results show that the similarity of spatial features between the atmospheric and sea-ice vorticity increased over time, thus suggesting that the rotation dynamics in the ice have become more aligned to that of the overlying surface atmosphere from 1991 to 2020 (Figure 4.5b-f). This is true for each of the five sectors in the Southern Ocean described in Figure 4.1. 30-year timeseries of spatial pattern correlations show a ~0.2 increase in the Weddell Sea, King Haakon, East Antarctica, and Ross Sea sectors, and a ~0.3 increase in the Amundsen-Bellingshausen sector. These findings suggest that synoptic weather patterns have played an increasingly influential role in sea-ice rotation dynamics since 1991, prompting questions about the longer-term climate processes driving this closer alignment between sea ice and the overlying atmosphere. While our results reaffirm the atmosphere as the primary driver of sea-ice rotation dynamics, no clear trend in atmospheric baroclinic vorticity is evident (Figure 4.3a). Although recent decades have shown a positive trend in the summer SAM, no corresponding winter trend is observed (Figure 4.4a), a finding consistent with previous studies (Abram et al., 2014; Fogt & Marshall, 2020). This conclusion is further supported by surface EKE composites, which reveal that positive-phase SAM conditions enhance atmospheric turbulence during summer but not during winter when EKE attains its maximum and directly transfers momentum to a growing sea-ice cover (Figure 4.4b). Notably, ice rotation intensity correlates to the positive SAM phase as shown in Figure 4.4c, suggesting that sea ice responds to the SAM index within a month, but the absence of a winter SAM trend or explicit mechanism for a lagged response provides some evidence that the increased coupling is not directly explained the summer SAM trend. Factors such as ice rheology, ocean dynamics, and high-frequency atmospheric eddy saturation may also play a role.

While our results do not directly demonstrate increased ice mobility, they do reveal a stronger correlation between sea ice and overlying wind vorticity, implying either enhanced mobility or increased sensitivity to wind forcing. Enhanced mobility is typically associated with thinner, unconsolidated floes or pancake

ice rather than the consolidated pack-ice inferred from satellite-derived sea-ice concentration products in the ice interior (Alberello et al., 2020; Kwok et al., 2017). Thinner ice is inherently weaker and more susceptible to deformation (Leppäranta, 2005; Wilchinsky & Feltham, 2004), while dispersed ice floes are less prone to rafting, a critical process for ice thickening (Auclair et al., 2022; Lange & Eicken, 1991; Worby et al., 2013). It is therefore worth considering how ocean and atmosphere conditions may be mobilizing the consolidated pack-ice by modifying the mechanical properties of the sea-ice that determine its rheology. Between 1992 and 2010, wind-driven advection dispersed ice equatorward, contributing to a positive trend in sea ice extent (SIE) during that period (P. Holland & Kwok, 2012). This dispersion likely slowed thermodynamic thickening, reduced rafting in divergent zones, and encouraged the formation of thinner, younger ice. Despite the increased SIE trend over this period, this process would result in overall thinning of the ice cover. From 2014 onwards, an abrupt decline in SIE has been linked to increased upper ocean temperatures and northerly winds that impeded ice advance (Eayrs et al., 2021; Meehl et al., 2019; Purich & Doddridge, 2023; Zhang et al., 2022). Warmer ocean conditions would further inhibit thermodynamic thickening and reduce the cementing of rafted floes, exacerbating ice thinning. Interpreting the Antarctic sea-ice landscape as a complex mosaic of heterogenous and intermittent ice types, we speculate that conditions favouring the formation of thinner, more mobile ice floes persisted, and perhaps intensified, throughout the 1991–2020 period. Break-up into smaller floes, which melt more rapidly (Christopher Horvat et al., 2016), may have triggered a positive feedback mechanism: (i) increased melting leads to thinning and enhanced mobility; (ii) enhanced mobility increases deformation and breakup of pack-ice into smaller, unconsolidated floes which melt faster. This feedback may have resulted in a higher proportion of the ice cover being composed of thinner, mobile floes, free from the internal stresses of consolidated pack-ice, thus making the ice field more responsive to atmospheric forcing and leading to the increased coupling observed. This change of sea-ice characteristics towards more MIZ-like conditions has been observed in the Southern Ocean Atlantic (Germishuizen et al., 2024), because it correlated with ecosystem changes that affected the population of southern right whales since 2009. Remote sensing observations currently provide limited evidence for a definitive long-term trend in Antarctic sea ice thickness – and by extension, sea ice volume – primarily due to substantial uncertainties in satellite retrievals and the pronounced spatial and regional heterogeneity in ice thickness changes (Kurtz & Markus,

2012; Mangatane & Vichi, 2025). Lastly, the role of possible changes in the ice-ocean momentum transfer must also be considered. Both the roughness of sea ice, which is also loosely related to rheology, and the intensity of under-ice ocean currents. However, significant knowledge gaps exist in under-ice upper ocean trends, which complicate the disentangling of its contributions from thermodynamically driven rheological changes.

Interestingly, the unique case of the Weddell Sea adds further complexity, whereby concurrently weakening cyclonic and anticyclonic components imply a diminishing of the rotational intensity. This took place over a period in which the sea ice had become more prone to atmospheric forcing (Figure 4.5b), meaning that the sea ice is simultaneously rotating slower and mimicking the atmosphere more closely. However, this 'weakening' phenomenon was not evident in the atmosphere, raising further questions about how the ocean or sea-ice rheology components may be affecting the response of sea ice to a seemingly unchanged atmospheric forcing. Hence the reason is to be found in the coupling process. Possible explanations could include a reduction in northeasterly export of ice from the southwestern Weddell Sea during summer months, leading to a modified pack-ice in the subsequent winter (Turner et al., 2020). Other studies have shown that high surface air temperature anomalies in the region act to reduce storm track activity by maintaining anticyclonic systems (Morioka et al., 2019), however we did not find evidence of this phenomenon in atmospheric vorticity. We note that this shift occurred exclusively in the Weddell Sea, the region with the weakest atmospheric vorticity (Figure 4.3a). This is unsurprising given that cyclogenesis generally occurs here, and so these synoptic systems are still in their infancy, resulting in a low density of well-developed cyclones traversing the region (Grieger et al., 2018; Wei & Qin, 2016). It was described in Section 4.3.2.1 that the Weddell Sea is characterized by low intensity but high variability in atmospheric vorticity. This contrasts with the King Hakon and East Antarctica sectors, whereby the frequent and relatively consistent passage of mature cyclones introduces high-intensity cyclonic rotation but low variability. This is corroborated by Hepworth et al. (2022), who further demonstrate a strong association between weak cyclones and extreme changes in the Weddell Sea sea-ice concentration. Thus, in conjunction with results presented here, this suggests that large synoptic systems are not the primary driver of ice rotation in the Weddell Sea. Instead, changes in the characteristics of smaller mesoscale

atmospheric features which are not resolved by the drift product may need to be investigated to appropriately attribute cause.

In conclusion, our analysis contributes to a deeper understanding of the intricate relationship between Antarctic sea ice and the overlying atmosphere. The findings highlight the complexity of synoptic-scale atmospheric forcing on sea-ice dynamics, regional variations in coupling patterns, and the emergence of unique phenomena in specific sectors. This study lays the groundwork for continued research into the evolving dynamics of Southern Ocean sea ice.

---

# Chapter 5 : Dynamic and Thermodynamic Contributions to SIC Changes using Single Swaths

## 5.1 Introduction

Satellite remote sensing data is provided by various institutions in the form of operational products (Section 2.1), whereby raw data measurements from spaceborne sensors are processed in a specific and consistent manner before distributing the dataset to the userbase. It is intended that these products have many potential uses, providing data to the scientific community, government agencies, commercial sector, etc. However, because these products are intended to satisfy a wide range of applications, the implemented design choices are often generalized, meaning that the processed data are useful in many applications but not optimized for specific ones. Consequently, datasets distributed to the scientific community forcibly reduce the possibility to extract maximum information from the raw sensor measurements, thus limiting their effectiveness in specific studies. In the context of brightness temperature derived sea-ice properties, a considerable limitation is caused by the aggregation of multiple swaths into a singular map – typically daily, whereby all measurements over a 24 hour are binned and averaged by location. This serves two benefits, namely, to (a) achieve full spatial coverage of the polar oceans and (b) to discretize the continuous scanning of the spaceborne sensor into datasets of regular time intervals. However, this design choice comes with drawbacks:

I. It reduces the temporal resolution of the datasets, meaning that data cannot be used to resolve sub-daily processes.
II. It leads to a blurring effect as we are typically observing different regions of the moving ice field with each scanning instance, which in turn can degrade the quality of the temporal mean at a given location.
III. Swath boundaries add further complexity, as neighbouring locations may fall on different sides of the swath boundary and thus adjacent observations in the dataset may be derived from scans performed 0-24 hours apart. This often results in a spatial artefact whereby the swath boundary is visible in the dataset.

IV. Discretizing the continuous scanning of the sensor into regular, daily intervals creates temporal ambiguity as to when the scan was performed. More specifically, while the timestamp of a swath measurement is precise, the timestamp of an assimilated daily dataset can only be attributed to a range of timestamps within the 24 hour observation window. Operational products typically assign a single, imprecise timestamp arbitrarily within this range for user convenience.

In practice, a combination of these limiting factors leads to an overall degradation of product and its associated metadata. This degradation is exacerbated in conditions of a fast-flowing ice field, or the observation period lengthens. Thus, a consequence of these product design choices is that daily averaged maps are less useful for studying sub-daily variability, or changes associated to rapidly moving features over a few days, particularly considering the highly dynamic Antarctic weather. This prompts the need to explore whether brightness temperature observations from spaceborne sensors can be exploited to gather sub-daily information.

Variability in the sea-ice landscape can be driven by any combination of atmospheric and ocean phenomenon, as discussed in Section 1.3. Broadly speaking, the ice variability can be categorized into two primary processes:

1. Dynamic processes, whereby sea-ice is mechanically advected to or from a given location.
2. Thermodynamic processes, whereby air and ocean temperatures and precipitation cause localized sea-ice growth or melt.

In practice, remote sensing methods can only scan discrete instances of sea-ice concentration, and thus any variability observed across multiple instances represents the accumulated effect of the dynamic and thermodynamic processes acting on the sea-ice. Sea-ice models typically simulate both thermodynamic growth/melt and dynamic redistribution processes, but their ability to accurately separate these contributions is challenging to validate due to a lack of coherent observational datasets at sub-daily and global scales. The proposed framework creates a benchmark dataset to diagnose model skill in reproducing observed dynamic versus thermodynamic processes, and to improve rheological parameterizations in coupled ice-ocean models used in sea-ice forecasting and weather prediction. Understanding the mechanisms leading to dynamic and thermodynamic driven changes in the ice concentration is a significant

challenge (e.g Serreze & Stroeve, 2015; Wayand et al., 2019), particularly when describing the effects of intense events such as atmospheric cyclones. Several studies, primarily in the Arctic, have attempted to quantify the relative dynamic and thermodynamic contributions of a cyclone to the observed sea-ice concentration variability. This includes studies utilizing climate models (Cai et al., 2020), observation-based approaches (Clancy et al., 2022; Schreiber & Serreze, 2020), or both (Aue et al., 2023), all of which demonstrate mixed results and comment on the limitations of the satellite derived sea-ice concentration and motion estimates at sub-daily timescales. It is therefore reasoned that incorporating higher resolution satellite observations would provide valuable sub-daily information for studies like these. A swath-based approach would provide multiple observations each day at precise timestamps, removing the temporal ambiguity of satellite data and enabling our ability to test sub-daily processes, while the incomplete coverage is less consequential when investigating localized processes. We therefore investigate the viability of utilising a swath-based retrieval approach to quantify Antarctic sea ice properties by exploring how ice concentration and drift retrieval algorithms applied directly onto brightness temperature swaths can help disentangle the dynamic and thermodynamic contributions to sub-daily sea-ice concentration changes.

More specifically, we aim to (a) estimate sub-daily ice variability and (b) quantify its advection, melt and formation constituents. This disentanglement is theoretically possible because both the sea-ice concentration and drift estimates can be derived from the same brightness temperature scans, thus no other data source is required, and the spatial and temporal coverage of the observations overlap entirely. A key consideration of this approach is that it requires minimal resources to implement because the necessary brightness temperatures swaths are already recorded and archived, meaning implementation would only require the reprocessing of historical datasets rather than any new instrumentation or satellite infrastructure. The main benefit of this approach is to quantify SIC variability between any two brightness temperature swaths that overlap in space – notably at sub-daily timescales. The analysis presented here makes use of brightness temperature measurements from the Advanced Microwave Scanning Radiometer 2 (AMSR-2), a passive-microwave sensor attached to JAXA's G-COM W1 satellite. While the AMSR-2 captures a wide range of frequencies (6.9 - 89.0 GHz), we will primarily utilize both horizonal ($h$) and vertical ($v$) polarizations of the 18.7 and 36.5 GHz channels. These frequency channels are chosen since they represent

a balance between spatial resolution, weather sensitivity, and effectiveness at distinguishing sea ice from water (Comiso, 1983; Comiso et al., 1984; Comiso & Zwally, 1984), a sensitivity that is commonly exploited to derived sea-ice concentration estimates and to apply a feature tracking technique for drift vector retrieval.

## 5.2 Materials and Methods

Sea-ice concentration ($C$) is a common metric used to quantify sea-ice change as a function of time ($t$). Detectable change in the ice concentration can be attributed to a combination of advection, and melt or growth processes, and so the rate of change in the concentration can be expanded as the summation of these individual dynamic ($D$) and thermodynamic ($TD$) components:

$$\frac{C(t)}{dt} = \left(\frac{\delta C}{\delta t}\right)_D + \left(\frac{\delta C}{\delta t}\right)_{TD} \tag{5.1}$$

In remote sensing applications, we can only measure the ice when satellites orbit overhead. Therefore, we assume a consistent rate of change between the initial and final concentration over the period of the observation window ($\Delta t$). While only a single swath is necessary to derive the instantaneous concentration ($C$), two overlapping swath pairs are required to estimate the difference ($\Delta C$), and so coverage is limited to the region of overlap between swath pairs. Footprint scans are discretised and interpolated onto a 2D-Cartesian grid $C(x,y)$:

$$\left(\frac{\Delta C_{x,y}}{\Delta t}\right)_{obs} \cong \left(\frac{\Delta C_{x,y}}{\Delta t}\right)_D + \left(\frac{\Delta C_{x,y}}{\Delta t}\right)_{TD} \tag{5.2}$$

Equation 5.2 thus informs that the change in ice concentration between two observations at location $xy$ can be described as the summation of its dynamic and thermodynamic components. The analysis presented here works to use swath-based observations to estimate each term of Equation 5.2.

### 5.2.1 Sub-daily Sea-Ice Concentration Retrieval

A variety of sea-ice concentration retrieval algorithms have been developed and operationally distributed, with the variations in design choices attributed to its intended use in research and inherent technological limitations (see Section 2.1.2). Here, we applied a modified version of the Environment Canada's Ice Concentration Extractor (ECICE) algorithm (Shokr et al., 2008) onto brightness temperature observations from the Advanced Microwave Scanning Radiometer 2 (AMSR-2). The ECICE algorithm utilizes a linear radiometric mixing-model to minimize differences between observed and estimated brightness temperature. This method can be applied using *n*-number of input parameters, meaning that the algorithm can theoretically distinguish between *n-1* surface types such as MY or FY ice, hence its usefulness in sea-ice type retrieval applications. The ECICE algorithm does not use individual tie point values like traditional ice concentration retrieval products but instead considers a distribution of possible brightness temperature values for each surface type. These distributions are derived by a cluster analysis of the scattered data points, demonstrated by Figure 5.1, which illustrates the clustering analysis methodology that underpins Antarctic sea-ice type retrieval, specifically using the $Tb_{19V}$ and $Tb_{37V}$ brightness temperature channels employed here, where the statistical distribution between ice and open ocean is clearly delineated in their clustering output. In this case, Figure 5.1 presents satellite-derived ice-type classifications tested against in situ observations by Ivanova et al. (2015). An alternative validation by Melsheimer et al. (2023) employed SAR imagery and Stage of Development charts to assess classification accuracy, while Shokr et al. (2008) also utilized the ECICE algorithm, but their study is confined to the Arctic Ocean and relies heavily on the $Tb_{85V}$ channel, which produces a markedly different cluster distribution from the $Tb_{19V}$ and $Tb_{37V}$ channels.

The distribution of $Tb_{19V,}$ $Tb_{37V}$ and $Tb_{37H}$ values can be described by a probability curve, with each cluster generating a unique curve with each input channel. Figure 5.2 displays the probability distribution of brightness temperature values associated with each surface type, whereby the curves represent the radiometric appearance of YI, FYI, MYI and open water (OW). Here it is shown that each surface type demonstrates a probability spread (y-axis) at different brightness temperature intensities (x-axis). These peaks are further distinguishable using different frequency channels, polarization filters and gradient ratios (panels a – d). Therefore, the extent to which these curves are distinguishable from one another across

multiple input parameters determines the robustness of surface identification from brightness temperature observations.

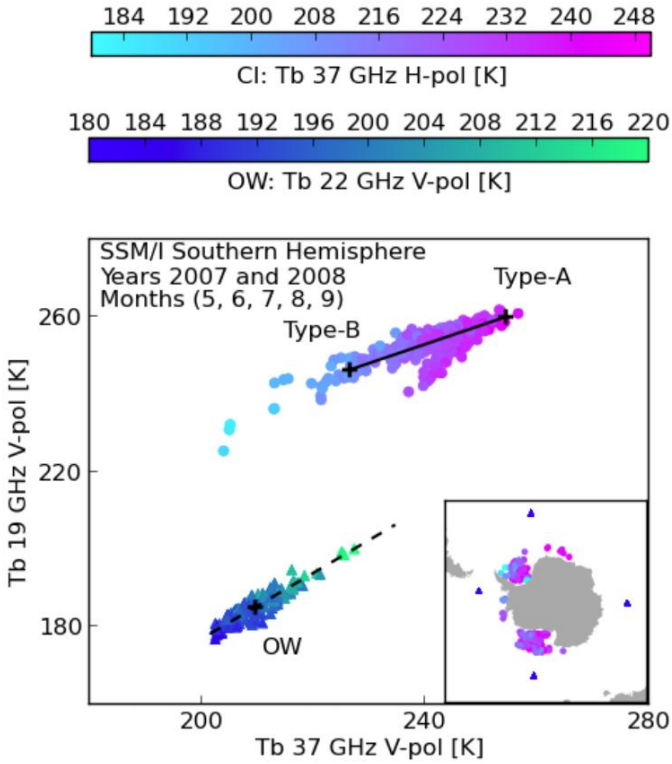


**Figure 5.1: Coverage graphs for the SSM/I subset of the Southern Hemisphere's round robin data package (RRDP) in winters 2007 and 2008. Both brightness temperature (Tb) and spatial coverage are displayed. Open water (OW) and closed ice (CI) locations are shown by triangle and circle symbols, respectively. In the Tb diagram, the OW symbols are coloured according to $Tb_{22V}$ colour scale, while the CI symbols are coloured according to $Tb_{37H}$ colour scale. Solid and dashed lines show ice and OW lines, respectively. Source: Ivanova et al. (2015).**

Once the distribution of expected emissivity for each surface type has been established, disentangling their relative contributions to the total observed brightness temperature is necessary. ECICE thus decomposes each observation into a linear combination of each surface type, whereby the relative area coverage (i.e. concentration) of each surface type can be considered as a weighting coefficient. The algorithm then solves an optimization problem by minimising the difference between the observation and the estimate that is

weighted against the concentration coefficients. Mathematically, Shokr & Agnew (2013) describe this as the summation of the squared differences between the simulated ($Tb_i$) and the observed ($Tb_{obs}$) brightness temperature values:

$$f(\vec{C}) = \sum_{j=1}^{j=n} \left[ \left[ \sum_{i=1}^{i=n-1} C_i Tb_{i,j} \right] - Tb_{obs,j} \right]^2 + \left[ \sum_{i=1}^{i=n-1} c_i - 1 \right]^2 \quad where \quad 0 \leq C_i \leq 1 \qquad (5.3)$$

Where $f(\vec{C})$ is the cost function we aim to minimise for every surface type ($i$) and normalized input parameter ($j$); $C_i$ is the ice concentration weighting coefficient; and $Tb_{i,j}$ and $Tb_{obs,j}$ are the expected and observed brightness temperatures by input parameter.

Equation 5.3 is a generic optimization technique and so can theoretically be applied to any choice of input parameters. Previous studies like Shokr et al. (2008) originally used the 37 and 85 GHz channels in the Arctic, enabling high spatial resolution and ice-type sensitivities but also resulted in a strong sensitivity to weather conditions. Shokr & Agnew (2013) later addressed this by replacing the 85 GHz input parameter with backscattering data, ultimately balancing its sensitivity to weather and multiyear ice. In the Southern Hemisphere, Melsheimer et al. (2023) selected radiometric and backscattering YI, FYI, and MYI probability distributions from samples of known ice types to calibrate the ECICE algorithm against Antarctic sea ice. Additional motion and temperature corrections were also applied, yielding improved ice type concentration estimates.

In our application, however, the use of backscattering data means another satellite sensor is required, making its use incompatible with a swath-based retrieval approach. Instead, we consider the $Tb_{37V}$, $Tb_{37H}$, $Tb_{19H}$ and $GR_{37V,19V}$ channels as input parameters ($j$) in our investigation, all of which are observed by the AMSR-2. To estimate the relative concentration of YI, FYI, MYI and open water (OW) at each location, we perform 1000 Monte Carlo simulations to minimise the cost function (Equation 5.3) using the probability distribution of each surface type according to Melsheimer et al. (2023), who themselves present results using $Tb_{37V}$, $Tb_{37H}$, $GR_{37V,19V}$ and $\sigma^0$ (backscatter observations), but has made the probability distributions for all AMSR-2 channels available to me, including the $Tb_{19H}$ used here. The combination of concentration values ($C_i$) used in the cost function which yielded the smallest difference to the observed

brightness temperature was selected. This algorithm was directly applied onto the AMSR-2 Level-1B product, meaning that the observed brightness temperatures have been geo-located and calibrated but without any form of spatial interpolation or masking. We accessed the Level-1B swath data from the Japan Aerospace Exploration Agency (JAXA) Global Portal System (https://gportal.jaxa.jp/gpr/, last access: 10 August 2024).

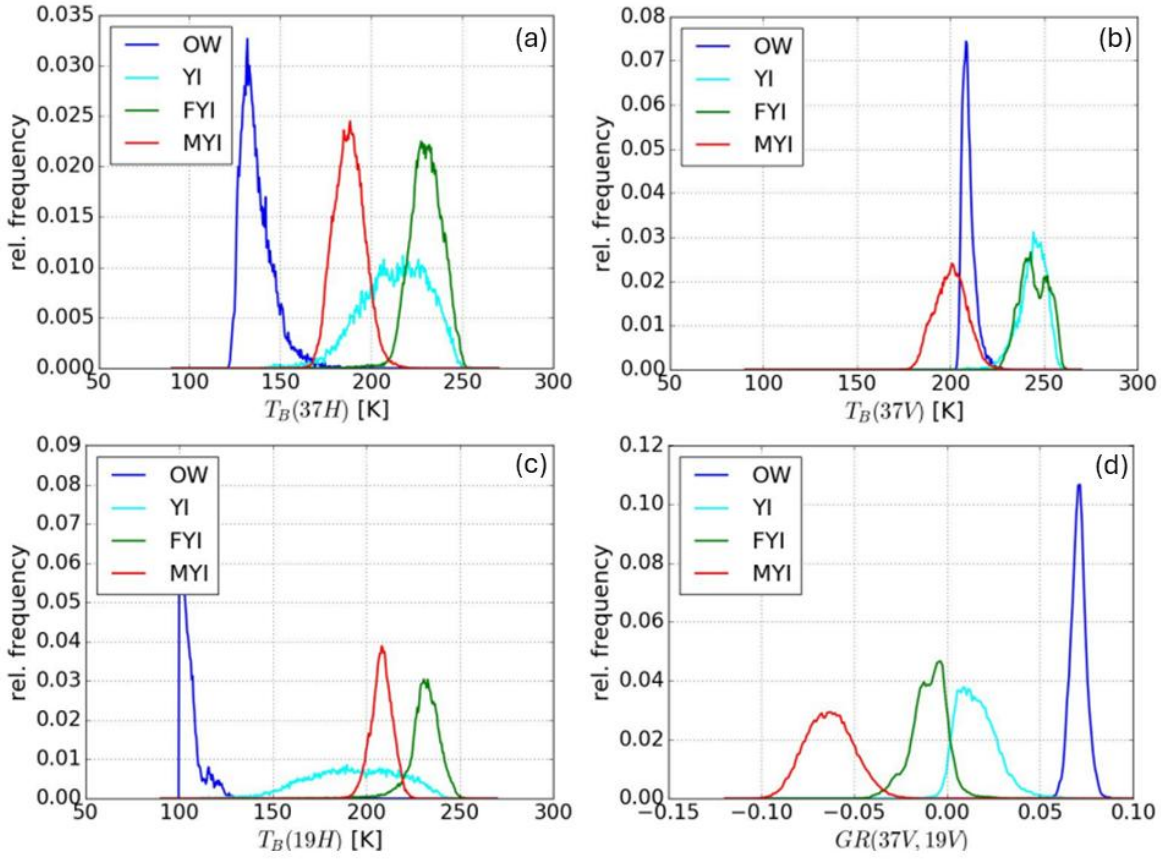


**Figure 5.2: Probability distribution curves of Arctic YI, FYI, MYI and open water surface types according to radiometric parameters (a) Tb37H, (b) Tb37V, (c) Tb19H, and (d) GR37V,19V. Brightness temperatures were obtained from AMSR-2. Source: Scarlat et al. (2019).**

### 5.2.2 Swath-based Sea-Ice Motion Vectors

Sea-ice drift products are typically derived from satellite observations and provide information on the movement of sea ice. As extensively discussed in Section 2.1.1, most satellite-derived drift products utilize a feature tracking technique, whereby patterns are defined in an initial image and then identified in sequential images, yielding the displacement of the pattern over time. Traditionally, daily averaged images of brightness temperature are used, however this method can be applied to any sequence of images in which the pattern can be repeatedly located. Therefore, Lavergne et al. (2021) show that swath-based brightness temperature observations can be used to compute displacement vectors in the region of overlap between two swaths, provided that the identified pattern does not drift outside of either swath's boundary. We therefore supplement the swath-derived ice concentration estimates (described above in Section 5.2.1) with the swath-derived ice displacement product – named *S2S* – provided by the Arctic Data Centre (Lavergne, 2020; last accessed: 10 July 2024). The S2S product utilizes pairs of AMSR-2 brightness temperature swaths between 13$^{th}$ – 31$^{st}$ July 2019 using the CMCC retrieval technique (explained in Section 2.1.1) with permutations of pairs ranging from 1.6 – 72 hours apart and projected onto a 62.5 km resolution NSIDC South Polar Stereographic grid. Analysis of sea-ice motion was supplemented with *in situ* GPS data from an ice tethered velocity profiler buoy. The buoy, named ISVP2 in de Vos et al. (2023), provided geolocation updates at an hourly frequency following its deployment from the SA Agulhas II during pancake ice conditions (1–5 m floes and ~40 cm thick) and tethered directly onto a large pancake ice floe (Skatulla et al., 2022).

### 5.2.3 Advection-Driven Changes in Sea-Ice Concentration at Sub-daily Timescales

A case study was conducted to examine how combining swath-derived ice concentration and motion fields can disentangle the dynamic and thermodynamic contributions to observed changes in ice concentration on sub-daily timescales. Continuing from Equation 5.2, it is evident that using daily-averaged ice concentration and motion products introduces significant uncertainty into each contribution through the $\Delta t$ term due to temporal ambiguity. This ambiguity arises because averaging multiple swaths into a single dataset yields a temporal range rather than a precise timestamp. This issue is addressed using a swath-based

approach, where Δt is precisely known. In the selected case presented in Section 5.3.1, two swaths from AMSR-2 were manually selected: an ascending swath at 17:09 UTC on 2019-07-26 ($t_0$) and a descending swath at 02:13 UTC on 2019-07-27 ($t_1$), providing brightness temperature observations 9.07 hours apart ($\Delta t = t_1 - t_0 = 9.07$ hrs). These swaths were chosen for their considerable spatial overlap and the suitability of the 9.07-hour difference, which is sufficient to detect changes in the ice landscape and short enough to capture sub-daily processes. Consequently, Equation 5.2 simplifies to:

$$\Delta C_{obs} \cong \Delta C_D + \Delta C_{TD} \tag{5.4}$$

which considers the observed sea-ice concentration change over a 9.07-hour period as the sum of its dynamic and thermodynamic components. By applying the ECICE algorithm and utilizing the S2S product, we can estimate two terms in Equation 5.4: the observed change ($\Delta C_{obs}$) and the dynamic component ($\Delta C_D$), respectively The observed change ($\Delta C_{obs}$) between swaths was computed using the ECICE algorithm at timestamps $t_0$ and $t_1$. The dynamic component ($\Delta C_D$) was estimated using a Lagrangian vector transform, which involved advecting the gridded ice concentration field at $t_0$ by distances derived from the S2S ice motion product. The process, illustrated in Figure 5.3, begins with an empty grid projection defined using the NSIDC South Polar Stereographic grid at a 6.25 km resolution, referred to as *G* (panel a). *G* is then populated with ice concentration observations at time $t_0$, derived from an interpolated ECICE swath scan, and yields $C_{t0}$ (panel b). Next, S2S-derived motion vectors are upscaled onto *G* (panel c), creating spatially and temporally coherent fields of ice concentration and motion. A Lagrangian particle tracking simulation, conducted using the Ocean Parcels software (M. Lange & Sebille, 2017), is then performed for 9.07 hours, with each grid cell in *G* displaced by a distance corresponding to its motion vector, resulting in a spatially warped grid, termed *G*' (panel d). This grid represents the expected ice concentration positions at time $t_1$ under advective forcing alone. The main assumption is that during advection the ice parcel is isolated and there are no further transformations occurring to the sea ice. Finally, the warped grid (*G*') is spatially interpolated back onto *G* to produce $C'_{t1}$. Thus, the $\Delta C_D$ term can be computed as the difference between $C'_{t1}$ and $C_{t0}$:

$$\Delta C_D \cong C'_{t1} - C_{t0} \tag{5.5}$$

Following a simple rearrangement of Equation 5.4 and substitution of Equation 5.5, the unknown $\Delta C_{TD}$ term is isolated as a function of the known $\Delta C_{obs}$ and $\Delta C_D$ terms:

$$\Delta C_{TD} \cong \Delta C_{obs} - \Delta C_D \cong (C_{t1} - C_{t0}) - (C'_{t1} - C_{t0}) = C_{t1} - C'_{t1} \quad (5.6)$$

This methodology theoretically approximates a separation of dynamic and thermodynamic contributions to observed sea-ice concentration changes at global scales, enabling further analyses. The thermodynamically driven change in observed sea-ice concentration can, in theory, be estimated using brightness temperature-derived concentration and motion data from any pair of overlapping swath observations at $t_0$ and $t_1$, assuming that the SIC field is conserved during the advection process.

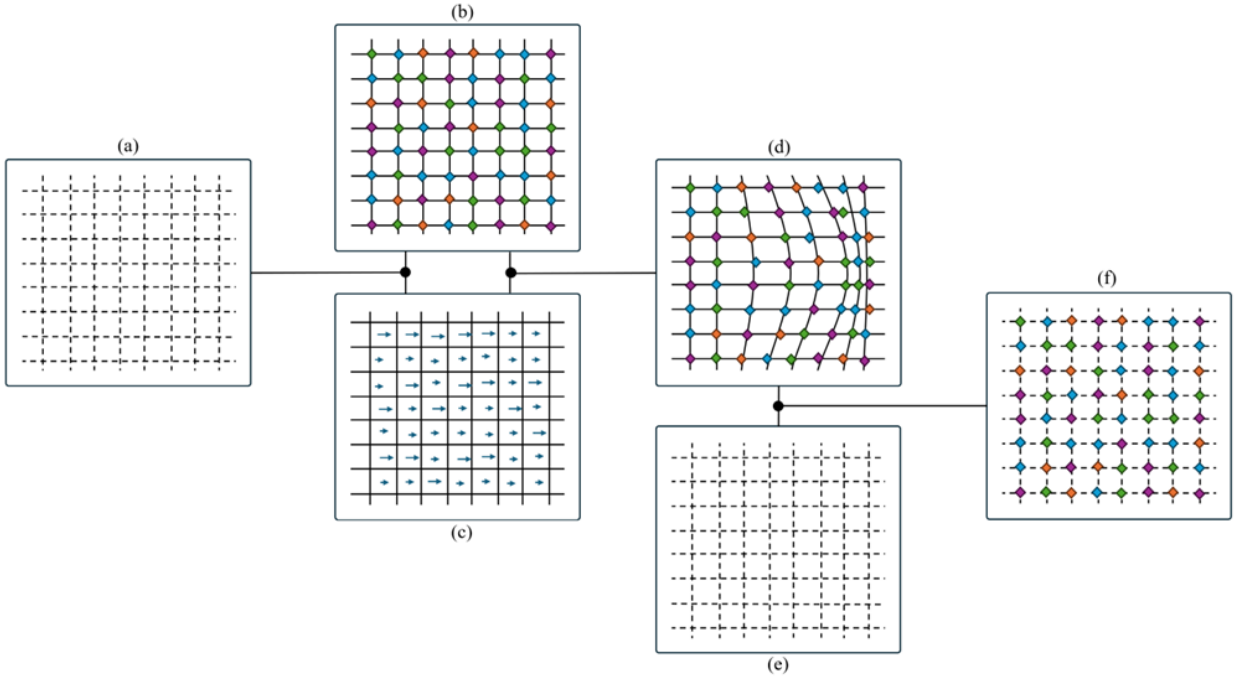


**Figure 5.3: A flow diagram describing the processes in which a Lagrangian vector transform is applied to an ice concentration field. A standardized grid (a) is populated with concentration values (b). A Lagrangian vector transform using sea-ice motion vectors (c) is performed on the concentration field. The resulting concentration field is spatially warped (d) and thus interpolated back onto the standardized grid (f).**

## 5.3 Results and Discussions

### 5.3.1 Swath-based Sea-Ice Type Retrieval

Figure 5.4 illustrates the resulting sea-ice concentration of each ice type – where total ice (Figure 5.4a) displays the summation of all three ice types (Figure 5.4b–d) according to the ECICE algorithm of an individual ascending swath at 17:09 UTC on 2019-07-26 (time $t_0$) at a spatial resolution of 6.25 kilometres. The ECICE derived sea-ice concentrations suggest a distribution of ice types that qualitatively align with the sea-ice stage of development (SoD) chart in Figure 5.5, namely that YI is usually found at the ice-ocean interface, FYI forms the bulk of the ice interior, and MYI is sparsely distributed in the western Weddell Sea near the Antarctic peninsula. This process was repeated using a descending swath at 02:13 UTC on 2019-07-27 (time $t_1$), which is approximately 9.07 hours later than the ascending swath at $t_0$. Although, this method is not limited to this chosen pair, and can be applied onto any two swaths, but with a temporal resolution limit of 1.6 hours due to the orbital frequency of the JAXA G-COM W1 satellite platform.

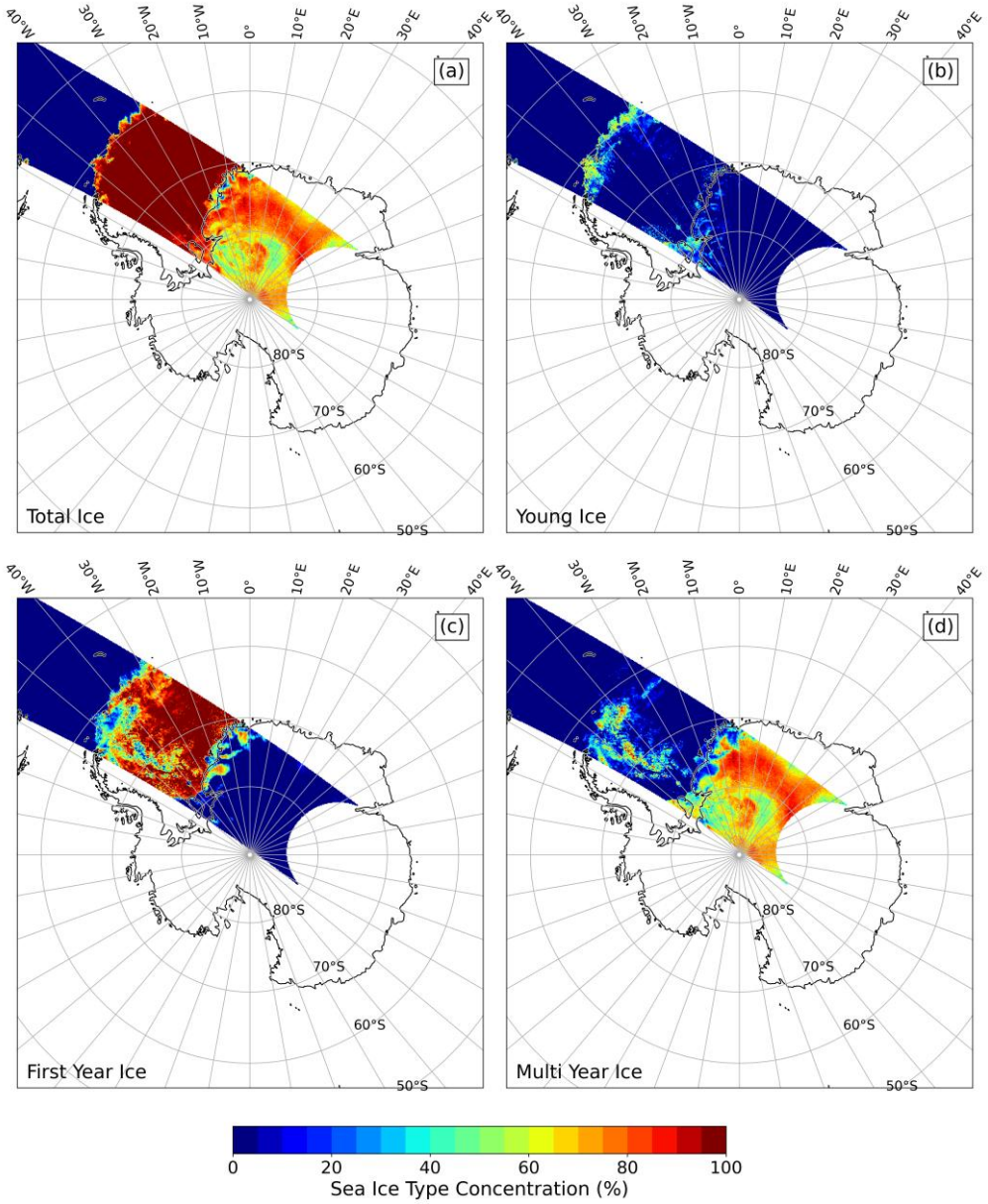


**Figure 5.4: The estimated Antarctic sea-ice type concentrations at 17:09 UTC on 26 July 2019 according to the ECICE ice-type algorithm. ECICE applied directly onto the AMSR-2 swath-derived input parameters $Tb_{37V}$, $Tb_{37H}$, $Tb_{19H}$ and $GR_{37V,19V}$. The (a) total ice, (b) young ice, (c) first year ice and (d) multiyear ice surface types are displayed, where total ice represents the summation of young, first year and multiyear ice concentrations.**

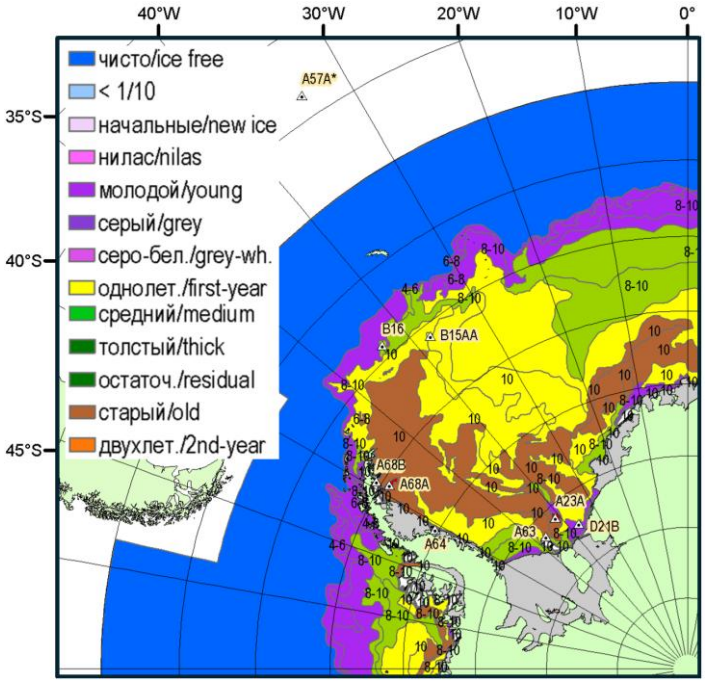


**Figure 5.5: Weekly Antarctic sea ice stage of development (SoD) charts for the week ending on 26 July 2019, produced through the AARI-NIC-NMI pilot project – a collaboration between the US National Ice Center (NIC) and the Russian Arctic and Antarctic Research Institute (AARI) (source: http://ice.aari.aq/antice/, last accessed 17 December 2024). These charts are derived from analyses of visible/infrared and microwave satellite imagery, along with temperature and wind data (detailed procedures available at https://usicecenter.gov/Resources/AnalystProcedures, last accessed 17 December 2024).**

Figure 5.6 illustrates the total ice concentration at time $t_0$ (Figure 5.6a) and $t_1$ (Figure 5.6b) according to the ECICE. As this algorithm was applied directly onto the AMSR-2 Level-1B footprint data, the output concentration coefficients needed to be spatially interpolated onto a common projection such that they can be directly compared, the 6.25 km NSIDC South Polar Stereographic in this case. The change in the concentration of each respective ice type was then computed as the difference between $t_0$ and $t_1$ conditions within the region of overlap between swaths. Figure 5.6c illustrates this region, demonstrating that our choice of swaths enables us to quantify the change in the ice concentration ($\Delta C_i$) over a large portion of the Weddell Sea. Figure 5.6d is equivalent to Figure 5.6c, but for demonstrative purposes is zoomed in further, indicated by the red box in Figure 5.6c.

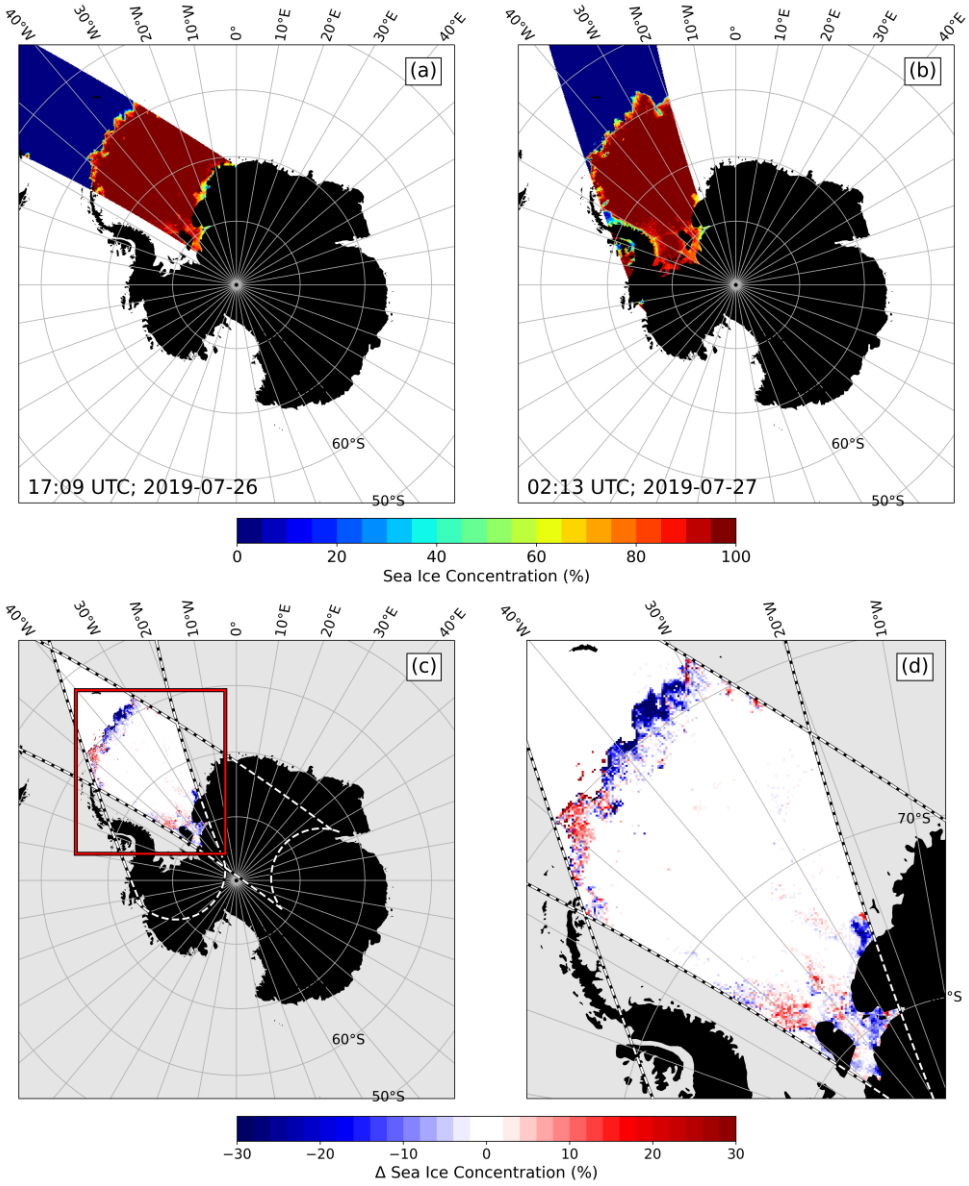


**Figure 5.6: The total sea-ice concentration according to the ECICE algorithm applied to AMSR-2 swaths at (a) 17:09 UTC on 26 July 2019 and at (b) 02:13 UTC on 27 July 2019. (c) The change in ice concentration, where the detected decrease (blue) or increase (red) over the 9.07 hour period is shown. Swath boundaries are indicated with the dashed lines, outlining the region of overlap between the two swaths. (d) Same as panel c, but zoomed in for demonstrative purposes, where the domain of panel d is illustrated by the red rectangle in panel c.**

The change in concentration detected in each surface type – now referred to $\Delta C_{total}$, $\Delta C_{YI}$, $\Delta C_{FYI}$ and $\Delta C_{MYI}$ – are shown in Figure 5.7. According to the ECICE, most of the $\Delta C_{total}$ is detected in the MIZ and nearer to the coastline (Figure 5.7a). The change is mostly characterized by a sharp loss of ice (as high as 100% in some locations) in the MIZ between 30-45°W, implying a 1-2° latitudinal retreat of the ice-edge in some locations. Conversely, the ice interior demonstrates little change from a $\Delta C_{total}$ perspective.

However, with consideration of each respective ice type, the ECICE detects substantial change in the ice interior in the $\Delta C_{YI}$, $\Delta C_{FYI}$ and $\Delta C_{MYI}$. Young ice demonstrates high variability in the MIZ which extends far into the ice interior (Figure 5.7b), with the bulk of this variability detected north of 65°S. FYI is shown to change substantially throughout the sea-ice landscape, both in the MIZ and deep into the ice interior towards the coastline (Figure 5.7c), while variability in MYI suggests decreased concentration in the central Weddell Sea while increasing in the western Weddell Sea adjacent to the peninsula.

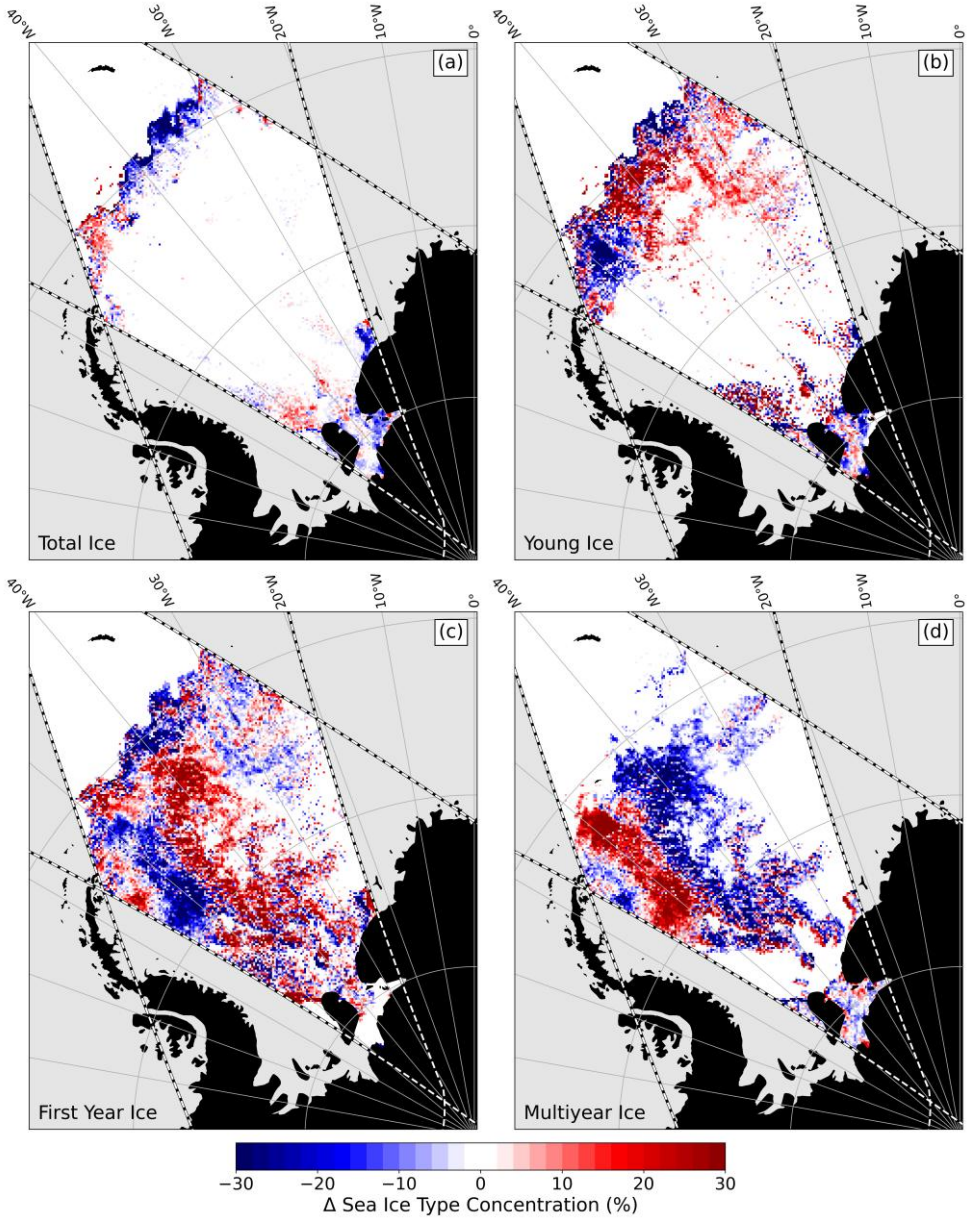


**Figure 5.7: The change in ice-type concentration according to the ECICE algorithm in the 9.07 hours between AMSR-2 swaths at 17:09 UTC on 26 July 2019 and 02:13 UTC on 27 July 2019. The change in ice concentration in the (a) total, (b) YI, (c) FYI and (d) MYI concentrations are visualized by the colormap. Swath boundaries are indicated with the dashed lines, outlining the region of overlap between the two swaths.**

Assessing the accuracy of the ECICE-determined ice type concentrations is a significant challenge, especially at the spatial and temporal scales presented here. Ground-based or *in-situ* sampling is not feasible at these scales, leaving a reliance on indirect methods for comparison. Stage of development (SoD) charts are useful tools, but these are produced weekly and so provide a more generalized distribution of ice types rather than quantified variability at sub-daily scales. Previous studies compare the ECICE's performance in the Southern Ocean against high-resolution SAR images (Melsheimer et al., 2023) but focused on the daily classification of the MYI boundary while using backscattering data as an input parameter, ultimately limiting its pertinence in a swath-based analysis context. While the ECICE algorithm suggests significant variability in all ice types over the 9.07 hour period, such rapid changes are unlikely. This is particularly true for MYI, where its inherent stability and resilience to short-term environmental forces makes the ECICE-derived $\Delta C_{MYI}$ appear unrealistic. Furthermore, increases in MYI at sub-daily timescales is, by definition, impossible.

These discrepancies point to potential challenges in distinguishing ice types using the algorithm, particularly in areas where radiometric distributions overlap between ice types. Misclassification errors between swaths may therefore explain the extreme changes observed, suggesting that slight shifts in the radiometric appearance of the ice are responsible for the derived changes, rather than a substantial increase or decrease in their respective concentrations. While a modification of the radiometric appearance of the ice may hint at environmental conditions – such as surface melting, precipitation, etc – it cannot be conclusively attribute to concentration changes. A possible reason for the erroneous ice-type classification could be related to the use of the $Tb_{19H}$ input parameter instead of the $Tb_{85V}$ or backscattering data used in previous reports (Melsheimer et al., 2023; Shokr et al., 2008; Shokr & Agnew, 2013). It can be noted in Figure 5.2c that the distribution of YI overlaps considerably with that of FYI and MYI at the $Tb_{19H}$ frequency, making its detection less certain. Furthermore, a less certain YI classification results in degraded FYI and MYI concentration coefficients, as is the consequence of using a linear combination optimizing function (Equation 5.3). Furthermore, brightness temperature observations are subject to several intertwined sources of error and noise that can introduce both bias and spatial inconsistencies in the derived SIC and drift data. A central issue is retrieval bias, particularly prevalent in the marginal ice zone (MIZ), where sub-pixel heterogeneity – such as mixed ice and open water – can lead to misclassification of

partially ice-covered pixels as fully ice-covered (Kern et al., 2022). Another major source of uncertainty is spatial interpolation during the satellite footprint scan, which smooths natural sharp transitions between ice and water. This results in a smearing effect that artificially dampens ice variability and distributes retrieval errors unevenly across the region (Wernecke et al., 2024). Additionally, weather-induced aliases exacerbate retrieval uncertainty, particularly over thin or slushy ice. These aliases primarily arise from atmospheric contributions such as water vapor, cloud liquid water, surface wind roughness, and snow cover (Spreen & Kern, 2017).

However, there is benefit to the $Tb_{19H}$ parameter inclusion, specifically that this frequency channel is particularly reliable for distinguishing ice from open water, evidenced by the distinct OW curve displayed in Figure 5.2c with minimal overlap between signals. Thus, while the ECICE algorithm's difficulty in distinguishing between surface types limits our ability to analyse sub-daily changes for individual ice types, the reliable separation of ice and water ensures that the total ice concentration estimates remain robust. Moving forward, this analysis will focus exclusively on total sea-ice concentration, as our choice of input parameters are reliable for quantifying total with the swath-based approach.

### 5.3.2 Swath-based Sea-Ice Motion

Figure 5.8 demonstrates the performance of the swath-derived ice motion estimates provided by the S2S product. Here we compare the drift of an ice-tethered buoy (blue) – detailed in Section 5.2.2 – against simulated parcel trajectories using a 24 hr drift product (yellow) and the S2S product (green). Parcel trajectories were computed with Ocean Parcels (M. Lange & Sebille, 2017), initiating from 57.91°S and 0.01°W, which was the location of the buoy at 20:00 UTC on 20 July 2019. The x-symbol indicates their respective locations after 72 hours. The OSI-455 product provided the daily averaged motion estimates, with an arbitrarily assigned centred-in-time timestamp scheme at noon. For swath-derived motion estimates, we manually selected eight S2S datasets whose swath-pairs covered the buoy location and where their associated $\Delta t$ was 9-15 hours apart. These datasets were computed from sequential swaths, meaning they have complete temporal coverage, no temporal overlap, and each pair of $t_n$ and $t_{n+1}$ timestamps are known precisely. The red rectangle in Figure 5.8a outlines the domain considered in Figure 5.8b, giving

locational context to the proceeding analysis. Simulation results indicate that both the 24-hour and swath-based approaches approximate general drifting direction of the buoy, initially showing a north-eastward motion which soon deflects into an eastward zonal drift (Figure 5.8b). However, the simulation using swath-derived motion vectors (green) demonstrates a markedly improved ability to capture the detailed movements of the buoy trajectory compared to the 24-hour resolution simulation (yellow). This higher resolution allows for more precise representation of short-term variations in sea-ice motion, resulting in trajectories that align more closely with the observed buoy trajectory. More specifically, the swath-based simulation better portrays the extent of the southward deflection between 0.2-0.9°E. Neither simulation captures the loop exhibited by the buoy at approximately 1.17°E, however we note a slight deflection in the swath trajectory near loop's location. Conversely, the 24-hour simulation exhibits a smoother trajectory that failed to resolve finer-scale movements evident in the GPS data. Furthermore, the accumulation of error at each iteration with lower frequency drift data unsurprisingly resulted in a divergence of the simulated trajectories from the buoy, specifically that the northward advancement of the buoy is overestimated.

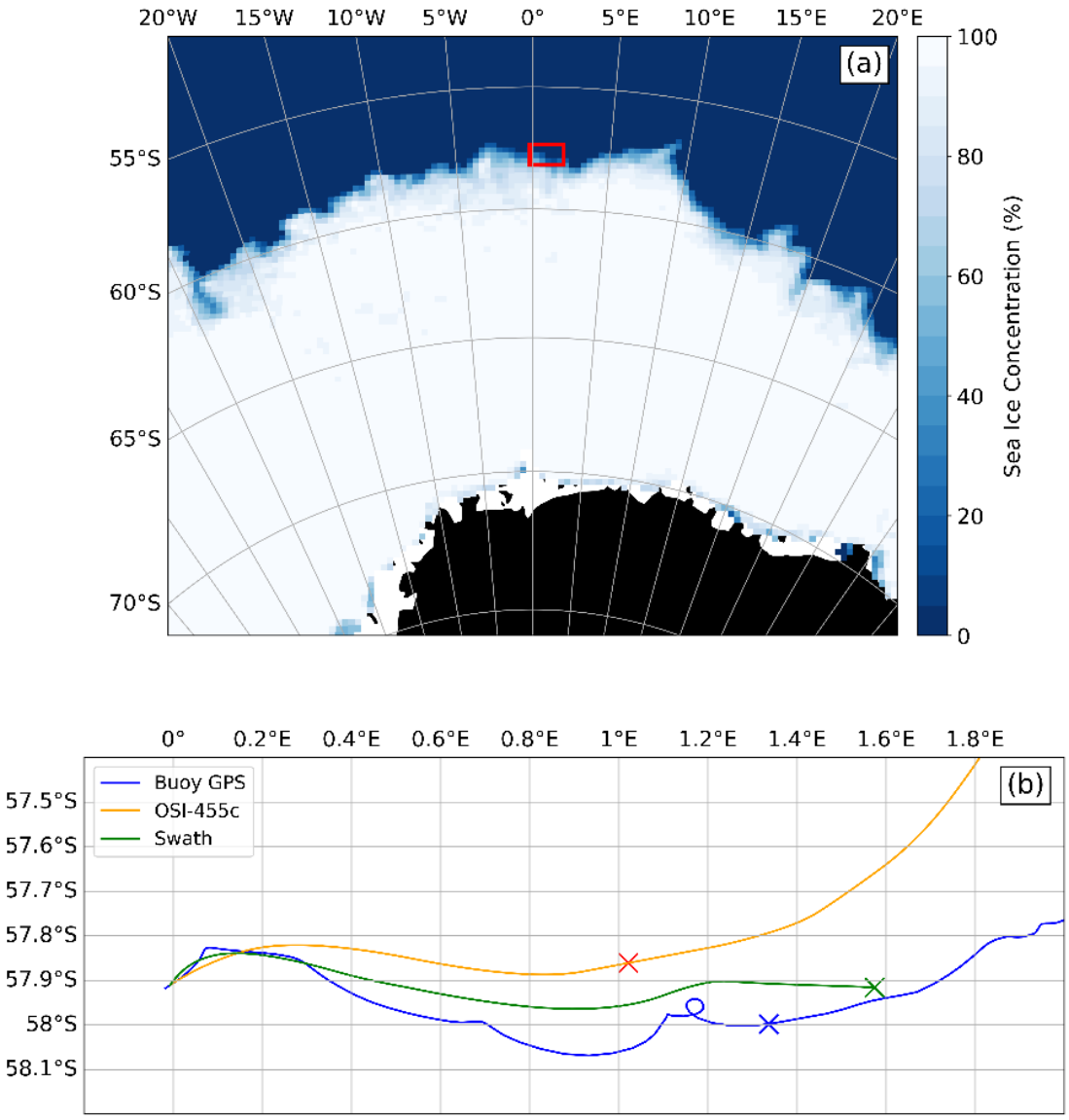


**Figure 5.8: (a) The location of the ice-tethered buoy deployed the Antarctic marginal ice zone, with the colourmap illustrating the sea-ice concentration on 20 July 2019. The red rectangle in panel a indicates the domain of coverage in panel b. (b) The GPS location of the buoy as it drifted eastwards (blue), with the simulated trajectories of a parcel using 24-hr average motion vectors (yellow) and swath-derived motion vectors (green). The simulation was initialized from 20:00 UTC on 20 July 2019, and x-symbol represents the location of the buoy/parcel after 72 hrs.**

This exploration of the S2S product's performance in Antarctic sea-ice (Figure 5.8) gave us confidence in its further use in our case study, whereby we used the ice motion vectors derived from the aforementioned AMSR-2 swaths (Section 5.2.1) at 17:09 UTC on 2019-07-26 (time $t_0$) and 02:13 UTC on 2019-07-27 (time $t_1$). This dataset is visualized in Figure 5.9, where crossing swath boundaries illustrate the region of overlap, and the density of arrows represents the 62.5 km resolution of the S2S product. However, we note that the product failed to compute valid estimates at locations near the ice edge, coastline and adjacent to the swath-boundaries. This is a consequence of the feature-tracking method of the ice drift retrieval, which requires that a distinct pattern in the ice at any given location persists between observations $t_0$ and $t_1$. As discussed in Section 2.1.1, ice conditions are highly dynamic in the MIZ and at the coastline, often yielding unreliable drift estimates that are removed in post-processing quality control. At the swath-boundaries, the selected pattern may drift outside of the region of overlap and thus cannot be identified in proceeding datasets. Consequently, motion vectors could not be estimated in these regions. Nevertheless, the product provides good data coverage over the ice interior.

The maximum displacement observed in the 9.07 hour period was 19.28 km – which implies an average speed of 0.59 m $s^{-1}$. This datapoint was located in the ice interior in an area of 100% SIC, a region typically assumed to consist primarily of thick, consolidated pack-ice with small drift (Figure 5.9a). These large drift speeds have been revealed previously by Alberello et al. (2020) who reported that a pancake ice floe reached a maximum drift speed of 0.75 m $s^{-1}$ in the Eastern Weddell Sea MIZ, and substantial drift observed even deep within the ice interior. Vihma et al. (1996) and Ackley et al. (2015) also observed comparable drift speeds in the central Weddell and Amundsen Seas, respectively. While a comparison of the S2S drift product against *in situ* data is not made in my analysis, a comprehensive validation report indicates a relatively small root mean square errors (RMSEs) for Antarctic sea-ice drift of approximately 3 to 4 km over the 9.07 hour period (Lavergne et al., 2021). The ice field demonstrated a mostly southward flow, especially in the central Weddell Sea. Additionally, we note a cyclonic (clockwise) rotation in the eastern half adjacent to the peninsula. The presence of this cyclonic system was explored extensively in the case study presented in Section 4.3.1, whereby we emphasize the similarities between the sea-ice and atmospheric rotation patterns displayed in Figure 4.2. Here it is discussed that the polar cyclone persists over the 9.07 hour period near the peninsula, imparting cyclonic rotation into the underlying sea-ice at sub-

daily timescales. Figure 5.9 thus further supplements the vorticity metric shown in Figure 4.2 with ice motion vector arrows. Additionally, Figure 5.9b depicts the corresponding sea-ice divergence field, quantifying the local rate of areal expansion (divergence) or contraction (convergence) of the ice cover. Positive values denote regions of divergence (net outflow of ice; red) while negative values indicate convergence (net inflow; blue). The southward drift of sea ice is associated with weak convergence within the ice interior (blue shading), flanked by divergent zones to the west and east of the primary flow. However, the interior convergence is modest in magnitude – typically between −1 and 1 $x10^{-6}$ $s^{-1}$ at a spatial resolution of 62.5 km – and is unlikely to result in appreciable ice accumulation over the 9 hr analysis period. In contrast, more pronounced convergence is evident in the marginal ice zone (MIZ), consistent with rapid ice-edge retreat driven by strong northerly winds. A similar event was documented by Vichi et al. (2019), who reported a large-scale clockwise rotation of the ice edge induced by a polar cyclone, marked by pronounced retreat and advance of the ice margin on the leading and trailing flanks of the system, respectively.

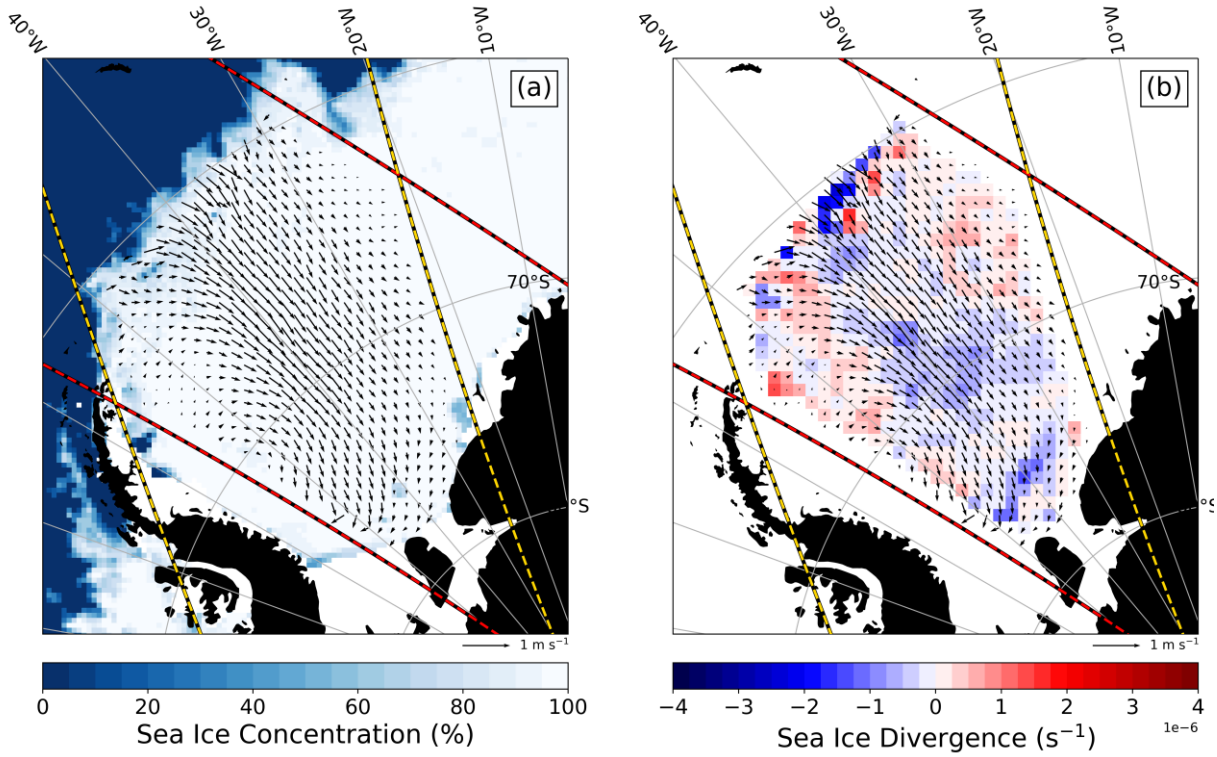


**Figure 5.9: Black arrows depict the average sea-ice drift speeds according to the S2S product over the 9.07 hour period between two overlapping AMSR-2 swaths. The swath boundaries of the ascending swath at 17:09 UTC on 26 July 2019 (dashed red outline) and descending swath at 02:13 UTC on 27 July 2019 (dashed yellow outline). (a) The daily averaged sea-ice concentration field on 26 July 2019 according to the ECICE retrieval algorithm provided by Melsheimer et al. (2023). (b) The sea-ice divergence field computed from S2S drift vectors in the region of swath overlap, where negative (blue) values indicate convergence, and positive (red) values indicate divergence.**

### 5.3.3 Isolating Thermodynamic Contributions to Changes in Sea-Ice Concentration

We separated the dynamic and thermodynamic contributions to the total change in sea-ice concentration between two swaths through the method described in Section 5.2.3. Figure 5.10 displays the change in concentration associated with each term in Equation 5.4. Figure 5.10a represents the change in total sea-ice concentration according to the ECICE algorithm, as discussed previously in Section 5.3.1. Following application of the Lagrangian vector transform method (Section 5.2.3), Figure 5.10b shows the difference

between the observed concentration at $t_0$ and the concentration at $t_1$ that would be expected in hypothetical conditions where the ice field is only subject to advective forcing. This can be described in simpler terms as the redistribution of $C_{t0}$ according to the S2S motion product. Importantly, we note that limitations of the drift product at the MIZ, coastlines and swath-boundaries mean that motion vectors were not available at these locations (panel b). Consequently, this reduces the domain in which the $\Delta C_D$ and $\Delta C_{TD}$ terms can be computed, which is visualized by the expanded grey-shading in Figure 5.10b and c, respectively. Figure 5.10b indicates that a relatively small portion of the total observed change is driven by advection ($\Delta C_D$), with most of this variability located along the MIZ, and near the Filchner-Ronne Ice Shelf at about 75°S and 40°W. The relative change ranged from -41% to +31% over the 9.07 hour period, but the bulk of values changed between -10% and +10%, and so the colour bar was scaled accordingly for demonstrative purposes.

Despite its relatively fast and expansive drift field (Figure 5.9a), almost no advection-driven change is detected in the ice interior (Figure 5.10b). This does not mean that ice pack did not move at larger scales; most likely, the overall drift did not engender any local SIC changes. The divergence field in Figure 5.9b further implies this, as a heterogeneous mosaic of small divergence values (of the order $10^{-6}$ $s^{-1}$) demonstrates widespread motion but would yield no overall larger scale changes to the interior SIC. In particular, the convergence observed at the centre of the study region is associated with SIC values already at 100% that would yield no change, although the change in ice type indicated by the ECICE algorithm revealed alterations of the ice cover (Figure 5.7). However, it is necessary to note that this analysis does not directly consider any specific thermodynamic processes but rather theorizes that any observable change not attributed to advective processes must therefore be thermodynamically driven. Following this reasoning, Figure 5.10c shows this thermodynamic component, where negative and positive $\Delta C_{TD}$ imply melting (blue) and growth (red), respectively, over the 9.07 hour period in locations where a S2S data was available. The largest decrease (increase) in the $\Delta C_{TD}$ was -71% (+55%), with most variability falling between -20% and +20%. Much like the $\Delta C_D$ component, $\Delta C_{TD}$ is similarly distributed along the MIZ with no apparent change in the ice interior, but it does make up most of the variability observed nearer the continent.

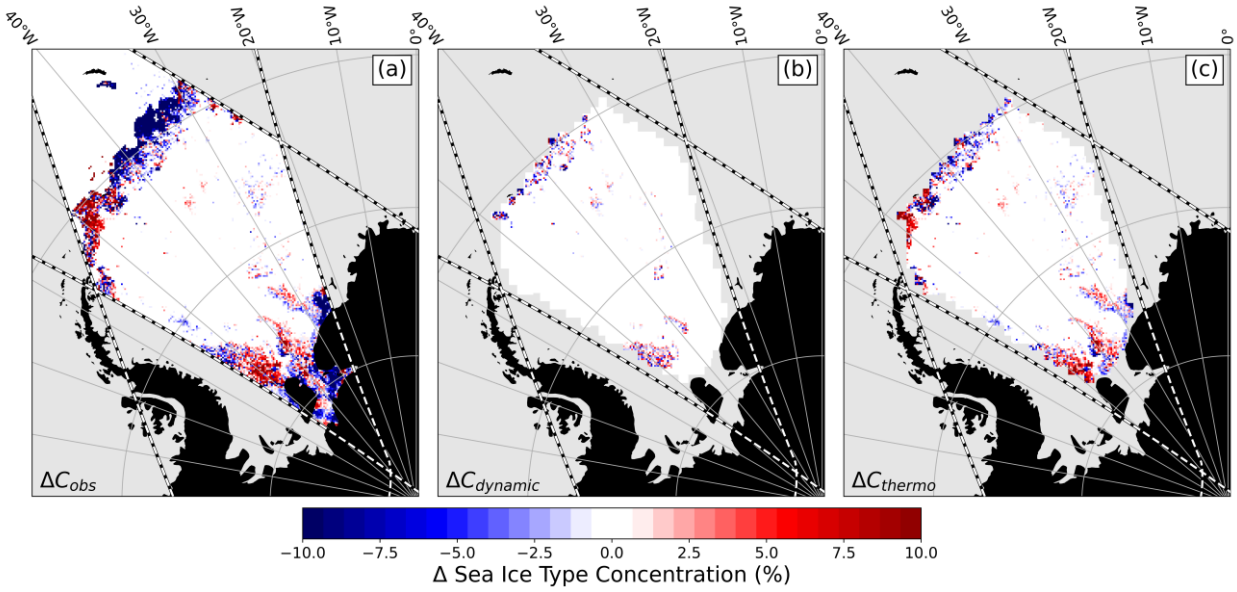


**Figure 5.10: (a) The change in total ice concentration according between two overlapping AMSR-2 swaths according to the ECICE algorithm. Swaths at 17:09 UTC on 26 July 2019 and 02:13 UTC on 27 July 2019 are outlined with dashed lines, demonstrating the region of overlap between two brightness temperature observations 9.07 hours apart. (b) The estimated variability in ice concentration driven by advection, whereby the grey-shaded area represents the domain in which swath-derived ice motion vectors are available. (c) The change in ice concentration attributed to melting (blue) and freezing (red), representing the difference between panels a and b.**

## 5.4 Summary and Concluding Remarks

This study demonstrates the potential of a swath-based approach for retrieving sea-ice concentration and motion, especially at sub-daily timescales where traditional daily-averaged products cannot resolve variability. By applying the ECICE algorithm directly to AMSR-2 Level-1B footprint data, we derived sub-daily sea-ice concentration observations. When combined with motion vectors from the same data, this method offers the possibility of quantifying the contributions of advection, melt, and formation to sea-ice concentration changes at these shorter timescales. Nevertheless, several challenges associated with ice-type classification and motion retrieval techniques emerged that require further investigation before widespread swath-based retrieval techniques can be systematically implemented.

The application of the ECICE algorithm allowed for a detailed analysis of sea-ice type distribution and variability over short periods. While the derived ice types aligned broadly with the stage of development (SoD) chart, the observed incoherence in ice type – particularly in multi-year ice (MYI) – within a 9.07-hour window suggests that some variability is likely due to misclassification rather than physical processes. These misclassifications stem from the overlapping radiometric signatures of ice types, particularly young ice (YI) at the $Tb_{19H}$ frequency. The reliance on a linear combination of weighting coefficients exacerbates this issue, making YI, first-year ice (FYI), and MYI estimates interdependent. This means that a less reliable YI estimate subsequently yields less reliable FYI and MYI estimates. Ice type misclassifications are a recognized issue in both Arctic and Antarctic conditions, and alternative input parameters such as the $Tb_{85GHz}$ frequency or backscatter data have been presented previously (Melsheimer et al., 2023; Shokr et al., 2008; Shokr & Agnew, 2013). However, in the context of this study, the use of backscatter data is less feasible due to the limitations associated with relying on a single satellite platform. Additionally, although previous studies have recommended the application of weather filters or correction schemes to reduce atmospheric noise in the 85 GHz brightness temperature observations (Andersen et al., 2006; Lu et al., 2022; Shokr et al., 2008; Spreen et al., 2008), these approaches entail additional processing steps and access to numerical weather prediction model (NWP) data that may not be readily compatible within a swath-based framework. At present, our understanding of Antarctic ice-type retrieval from space remains limited, as existing algorithms have been developed primarily for Arctic sea ice and subsequently recalibrated for Antarctic conditions using sparse validation datasets. Consequently, the use of the 19 and 37 GHz frequency channels in this analysis represents an initial exploration of the swath-based framework at a foundational level, offering a baseline for future methodological refinements.

In the Arctic, improved MYI distributions have been achieved using temperature and drift corrections (Ye, Heygster, et al., 2016; Ye, Shokr, et al., 2016). However, MYI constitutes a relatively small portion of the total Antarctic sea-ice coverage, with the bulk of its area comprising of non-MYI (which the ECICE algorithm defines as either FYI or YI). Our results demonstrate considerable interchange between FYI and YI over short timescales, likely indicative that small radiometric variations in the ice are being interpreted as a different ice-type. This issue arises from the discretization of continuous emissivity distributions into predefined surface categories, raising questions about the appropriateness of the FYI and YI classifications

in an Antarctic context. Unlike MYI, which exhibits distinct and well-documented physical characteristics, the categories of FYI and YI are primarily defined by thresholds in emissivity that is indirectly related to thickness and so may hold limited physical significance in the Antarctic context. Although operationally classified according to thickness criteria (WMO, 2014), the Antarctic sea-ice cover generally spans a much narrower thickness range than its Arctic counterpart. Moreover, a substantial portion of the Antarctic ice pack consists of pancake ice, whose radiometric properties do not correspond well to thickness-based classifications. Consequently, the use of discrete ice-type categories such as FYI and YI may be of limited practical value in this region. Future work should critically evaluate these categories and explore more context-appropriate classifications. Despite challenges in ice-type classification, the swath-based approach proved consistent in retrieving total ice concentration distribution. The clear distinction between ice and water theoretically implies reliable total concentration estimates, even on short timescales, although the analysis presented here does not explicitly validate this. This capability is particularly important for understanding the highly dynamic marginal ice zone (MIZ), which is conventionally characterized by its extreme sea-ice variability (Vichi, 2022). For instance, our results revealed a significant loss of ice concentration in the MIZ, particularly between 30°W and 45°W, over just ~9 hours. Combining these findings with motion vector data, we attribute the ice retreat to strong advective forces driving the ice edge southward. This observation aligns with earlier studies, such as Vichi et al. (2019), which describe ice-edge retreat caused by cyclonic wind forcing. However, while Vichi et al. relied on daily averaged sea-ice concentration products, our results demonstrate similar dynamics occurring at sub-daily timescales, demonstrating the advantages of higher temporal resolution observations.

Disentangling the dynamic and thermodynamic contributions to observed ice retreat proved challenging, particularly in the MIZ, where motion vector coverage was limited. While we show effective retrieval of swath-based ice concentration, the S2S product cannot reliably estimate ice motion in these regions as it depends on persistent ice patterns between successive observations, a condition that is often unmet in the MIZ. This limitation restricted our ability to attribute the advection rates in this region. This is a significant obstacle in our approach to disentangle the two constituents because the high frequency swath observations justify its usage in the MIZ but is also simultaneously limited there because of the poor S2S coverage. However, in the ice interior, where drift patterns were more stable, thermodynamic processes emerged as

the dominant drivers of observed variability. This finding is surprising given the substantial ice drift detected throughout the ice interior (Figure 5.9) – supporting previous studies which report fast, unconsolidated ice floes far into the ice interior moving in free drift conditions (Alberello et al., 2020; de Jager & Vichi, 2022; Vichi et al., 2019) – and the unrealistically large volumes of melt and formation implied by thermodynamic variability over such short periods. The coarse 62.5 km resolution of the S2S product – downscaled to 6.25 km for analysis – further complicates the interpretation of results by assuming that finer-scale features move homogeneously in broader clusters. Consequently, temporal variability within clusters was attributed to thermodynamics rather than advection. While the swath-based trajectory aligned more closely with ice-tethered buoy deployed in FYI conditions than daily averaged products, neither approach resolved localized features, such as loops in the drift trajectory. This suggests that even the spatial and temporal resolution of the swath product may be insufficient to fully capture the heterogeneity of Antarctic sea-ice dynamics. However, the swath-observed cyclonic rotation in the eastern Weddell Sea provides further evidence of the interaction between atmospheric forcing and sea-ice dynamics at sub-daily timescales. This finding aligns with the analysis presented in Section 4.3.1. and further exemplifies the advantages of incorporating high-resolution drift data to elucidate more comprehensive understanding of coupled atmosphere-ice dynamic.

To our knowledge, this study represents the first attempt to quantify sea-ice concentration and drift variability using swath-derived satellite data. The ability to quantify changes at the sub-daily scale provides a supplement to sea-ice modelling efforts, which often lack observational data at these timescales. Although limitations in motion vector coverage at the ice margins persist, they are not exclusive to the swath drift and daily averaged drift is also similarly limited. In fact, we reason that the shorter observational window associated with the swath drift product means the ice patterns are more likely to persist between subsequent observations, theoretically improving its performance in the MIZ. This, however, was not directly assessed in our study, and while Lavergne (2020) demonstrated improved performance of swath drift products compared to its 24-hour counterpart, this analysis considers the entire sea-ice extent rather than the MIZ specifically. Furthermore, the concentration retrievals at maximum values (e.g., 100% SIC) reduces sensitivity to variability in the ice interior, where the retrieval algorithm assumes consolidated pack-ice. This limitation underscores the need for improved algorithms capable of distinguishing unconsolidated ice

floes from consolidated pack ice in high SIC regions. Addressing these challenges requires a multi-faceted approach, such as the integration of higher-resolution sensors such as SAR or optical imagery for improved calibration, and the development of algorithms capable of detecting and correcting mixed-pixel bias. We reiterate the importance of continued investment in satellite missions capable of delivering high-resolution swath data, but also the importance of optimizing information from existing datasets.

---

# Chapter 6 : Synthesis

Antarctic sea-ice coverage is a linchpin of Earth's climate system, with cascading impacts on ocean circulation, carbon cycling, and polar ecosystems. Understanding its perpetually changing distribution is thus a key requirement for improving predictions of future climate scenarios. Synoptic-scale whether systems are the dominant drivers of sea-ice variability at short-term timescales (sub-daily to daily), with it is still unknown whether their accumulated effects may steer longer-term distribution trends. Despite its significance, the mechanisms driving short-term sea-ice variability – particularly the influence of weather systems like polar and extra-tropical cyclones – remain poorly understood. This knowledge gap stems from two intertwined challenges: (1) sparse and infrequent data acquisition at sub-daily timescales, including the logistical impracticality of extensive *in situ* sampling and the limitations associated with satellite-derived observations, and (2) inadequate representation of some sub-daily air-sea-ice interactions in climate models. This thesis broadens our understanding of Antarctic sea-ice dynamics while critically evaluating the observational tools that underpin this knowledge. The findings hold significance for climate science, Earth observation, and efforts to reconcile model-observation discrepancies in polar regions.

## 6.1 Linking the Thesis Findings to the Research Objectives

In this section, the key findings of the thesis are used to address the research aims that are outlined in Section 1.7.1:

### 6.1.1 Satellite Sea-Ice Motion Products for Detecting Rotational Dynamics (Research Aim I)

The capability of satellite-derived products to detect rotational sea-ice features is demonstrated in Chapter 3 through the application of a novel vorticity quantification method. These features occur at spatial scales comparable to atmospheric cyclones and high-pressure systems, making them useful for assessing the influence of atmospheric forcing on sea-ice dynamics. While all the analysed drift products successfully capture rotational features, their performance varies in terms of spatial coverage and retrieval uncertainty.

Four satellite-derived drift products were evaluated: three single-sensor products (AMSR-2, SSMI/S, and ASCAT) and a merged product that integrates drift estimates from these sources. These products represent the average drift over a 48-hour period, as the 24-hour equivalent was unavailable at the time of analysis. Since synoptic weather systems drive substantial sea-ice advection, the ability of each product to capture rotation under such conditions determines its effectiveness for studying weather-induced sea-ice dynamics. The merged product offers superior spatial coverage, resulting in a more complete vorticity field. Chapter 1 shows that it consistently detects a larger proportion of rotational features compared to single-sensor products. This makes the merged product well-suited for synoptic-scale vorticity analysis. However, the merging process may artificially enhance rotation intensity, a consideration discussed further in Section 6.1.2. Of the single-sensors, the AMSR-2 performed the best with superior coverage and retrieval uncertainty. In contrast, ASCAT exhibits significantly poorer coverage and higher retrieval uncertainty. The AMSR-2 performed best of the selected sensors – in terms of coverage and drift uncertainty – and was used again for the swath-based analysis in the subsequent Chapter 5. Notably, the merged product was not compatible with this methodological approach because it relies on data sourced from multiple satellite sensors. Chapter 4 utilizes AMSR-2-derived drift vectors to demonstrate that sub-daily sea-ice vorticity closely follows overlying wind patterns, confirming that atmospheric forcing drives sea-ice rotation at these timescales. Additionally, in Chapter 5, AMSR-2 swath-based drift and concentration observations are combined to decompose sub-daily sea-ice variability into its dynamic (advection) and thermodynamic (melt/formation) components, providing deeper insights into short-term sea-ice changes.

### 6.1.2 Intensity and Uncertainty of Sea-Ice Rotation by Low- and High-Pressure Systems (Research Aim II)

Chapter 1 demonstrates that cyclonic features in Antarctic sea ice are generally more intense and frequent than their anticyclonic counterparts. On average, the rotational intensity of major cyclonic events is approximately 1.5 to 2 times greater than that of anticyclonic events, and satellite-derived sea-ice drift products detect a higher proportion of intense cyclonic features compared to anticyclonic ones. This suggests that low-pressure systems (LP) inject more rotational momentum into the sea ice than high-

pressure (HP) systems, consistent with previous studies (e.g. P. Uotila et al., 2011; Vichi et al., 2019; Z. Wang et al., 2014). The dominance of cyclonic rotation in the atmosphere, as presented in Chapter 2, corresponds with the prevalence of cyclonic vorticity in the sea ice. However, the observed asymmetry between cyclonic and anticyclonic rotation may also be influenced by retrieval biases in feature-tracking methods. A key source of uncertainty arises from discrepancies between satellite-derived products in estimating the intensity of rotational features, with greater variability noted for LP events. Case studies indicate that storms can alter sea-ice radiometric properties, affecting drift estimation quality and leading to inconsistencies across products. In contrast, HP systems are typically associated with calmer conditions, resulting in more stable and accurate drift retrievals. Consequently, the stronger response of sea ice to LP compared to HP systems is superimposed with the increased retrieval uncertainty associated with these events. Among the evaluated products, the merged product consistently exhibits the most intense cyclonic rotation estimates and the greatest spatial variability. This suggests that the merging process produces a more heterogeneous drift field, leading to sharper gradients between adjacent drift vectors. Such extreme gradients can artificially enhance cyclonic vorticity estimates. Additionally, the merged product has higher retrieval uncertainty due to error propagation from its single-sensor constituents, exemplified by the larger drift uncertainty associated with LP systems. However, in the absence of independent observational validation, it remains unclear whether this effect is an artifact of the merging process or a genuine representation of heterogeneous sea-ice dynamics. All products perform significantly worse in the marginal ice zone (MIZ) compared to the pack ice, primarily due to their reliance on persistent ice features between consecutive images. As a result, drift retrievals in the MIZ are sparse, limiting the ability to quantify dynamic contributions to sea-ice concentration changes in this region. This was an inherent limitation of the analysis presented in Chapters 3 and 4, as the dynamic component of sea-ice variability could not be estimated in the MIZ due to inadequate drift coverage.

### 6.1.3 Multidecadal Trends and Variability in Sea-Ice and Atmospheric Rotation (Research Aims III & IV)

An analysis of interannual trends in Antarctic sea-ice rotation dynamics reveals the cumulative influence of daily weather conditions on long-term dynamical trends. These trends are shaped by a combination of atmospheric and oceanic forcings, and it is speculated to be modulated by an evolving sea-ice rheology. The case studies presented in Chapters 3 and 4 demonstrate that sea-ice drift responds to atmospheric forcing at sub-daily timescales, justifying a systematic extrapolation across the full satellite drift record. Chapter 3 provided an initial assessment of interannual variability in sea-ice rotation trends within the Atlantic Sector of the Southern Ocean; however, data constraints limited the analysis to 2013–2020, a period too short for detecting climatic signals. Results indicated that the intensity of anticyclonic features in the ice remained relatively stable over this period, while a significant increase in cyclonic rotation was observed from 2014 to 2017. This trend, robust to retrieval uncertainties, coincides with the record decline in Antarctic sea-ice extent (SIE) from late winter 2015 onward. This decline marks a shift from the extreme SIE variability observed in the satellite record, with recent studies suggesting a sea-ice *regime shift* – a term describing a transition from the high variability that characterized the Antarctic SIE before 2014 to a more sustained decline proceeding it (Fogt et al., 2022; Hobbs et al., 2024; Purich & Doddridge, 2023). Following the release of a 24-hour satellite drift product extending back to 1991, a comprehensive long-term analysis of daily sea-ice rotation and its relationship to surface winds was conducted across the entire Southern Ocean, divided into five sectors. Chapter 4 demonstrated that over the past three decades (1991–2020), sea-ice vorticity has become increasingly aligned with atmospheric vorticity, indicating a strengthened coupling between the two. A key finding of this chapter is the absence of a significant trend in the mean rotational intensity of both the sea ice and atmosphere, despite the increased correlation between them. Furthermore, this strengthened coupling is not directly explained by trends in the Southern Annular Mode. While these findings do not directly indicate increased sea-ice mobility, the stronger correlation suggests either enhanced mobility or heightened sensitivity to wind forcing. Enhanced mobility is typically associated with thinner, smaller floes or pancake ice, rather than a more homogeneous and rigid pack ice. This could imply a 30 year evolution of the ice interior towards a more fragmented, thinner ice

field, consisting of smaller floes or pancakes that are tightly-packed but mechanically independent – a distinction not detectable by satellite-derived sea-ice concentration products. Given the heterogeneity of Antarctic sea ice, this trend may reflect fundamental changes in ice rheology, potentially linked to oceanic influences that promote increased sea-ice deformation, including thinning, break-up and an expanded marginal ice zone (MIZ).

Interannual variability in sea-ice rotation further highlights the complex interplay of regional drivers. The Amundsen-Bellingshausen sector exhibits the most pronounced increase in ice-atmosphere vorticity correlation (~0.3 over 30 years), while the other four sectors show a comparable but slightly lower increase (~0.2). The King Haakon and East Antarctica sectors display high ice rotational intensity but relatively low variability, a result consistent with the regular passage of mature cyclones over the sectors. This suggests that while atmospheric forcing strongly modulates daily ice motion in these regions, its influence remains relatively stable over time, yielding less interannual variability. In contrast, the Weddell Sea – where cyclogenesis is prevalent and cyclonic systems are still in their infancy – experiences a lower density of well-developed cyclones, resulting in weaker but more variable sea-ice rotation. Notably, in the Weddell Sea, both cyclonic and anticyclonic rotational intensities have weakened over time, even as the correlation with atmospheric vorticity has strengthened, a finding yet to be explained. A key challenge in assessing regional differences in sea-ice rotation dynamics stems from the limitations of deriving drift in the MIZ, as discussed in Section 6.1.2. Satellite retrievals struggle to capture ice dynamics in this region due to lower ice concentration and increased deformation, meaning that reported trends are restricted to the ice interior, where drift estimates are more reliable. Overall, these findings reinforce the dominant role of atmospheric forcing in shaping sea-ice rotation and regional variability. However, changes in ice rheology, potentially driven by oceanic influences, introduce additional complexity. Inferring these rheological changes from satellite observations is challenging, necessitating future research integrating high-resolution satellite observations in sea-ice models. Chapter 5 explores this by presenting a new framework with which to acquire high-resolution satellite observations, where swath-based sea-ice concentration and drift estimates are used to decompose the dynamic and thermodynamic contributions to sub-daily sea-ice changes.

### 6.1.4 A Swath-Based Satellite Retrieval Approach (Research Aim V)

Deriving sea-ice concentration (SIC) and drift from swath-based satellite observations has been demonstrated to be a reliable means to obtain high-resolution observations at sub-daily timescales using passive microwave data. This approach supplements modelling efforts aimed at capturing short-term variability in sea ice that is often unresolved by traditional daily-averaged observations. Chapter 5 explores the feasibility and limitations of a swath-based sea-ice retrieval framework. The framework's primary advantage lies in its ability to analyse rapid changes in the ice, although this comes at the expense of reduced spatial coverage. Notably, the framework can be retroactively applied to historical passive microwave datasets, thereby gaining additional scientific value of existing archives for climatological studies without necessitating improvements in sensor technology or satellite infrastructure.

The publicly available AMSR-2 swath-based sea-ice drift dataset (S2S) enabled the detection of sub-daily variability that more accurately reflects the impact of short-lived, transient weather systems and avoids the temporal blurring inherent in daily-averaged datasets. This method allows for precise timestamp assignment in regions where swaths overlap, in contrast to the ambiguous range of timestamps associated with daily-averaged products. Both the swath-based and daily-average products derive drift vectors through feature-tracking techniques that match patterns between sequential swaths. While this method can be compromised in highly dynamic regions – where rapid deformation of ice patterns diminishes the efficacy of pattern recognition – the shorter time intervals between observations in the swath-based approach increase the likelihood that the ice pattern persists sufficiently to be tracked, particularly in the marginal ice zone (MIZ), although a detailed performance comparison in the MIZ was beyond the scope of this thesis. The S2S data analysis in Chapter 5 indicates substantial ice drift throughout the ice landscape and yields improved particle trajectory simulations compared to daily-averaged data when referenced against an ice-tethered buoy. In Chapter 4, the case studies reveal that displacement estimates over a 9-hour window indicate that sea-ice rotation aligns closely with overlying isobars, implying that sea ice can respond to surface winds and mobilize within just 9 hours. Moreover, significant drift observed deep within the pack-ice challenges previous assumptions that interior regions consist of consolidated, relatively immobile ice, and suggests instead a far more dynamic ice interior. However, limited availability of *in situ*

buoy data in these central regions hampers the validation of satellite-derived ice motion products, and so the potential influence of atmospheric artefacts – such as wind or air temperature-induced surface aliases – must be considered, as they may lead to an overestimation of actual ice motion. Although episodes of similarly rapid drift in the Weddell Sea's interior have been reported (e.g. Ackley et al., 2015; Alberello et al., 2020; Vihma et al., 1996), and so the S2S-derived speeds are not unprecedented.

Sea-ice concentration (SIC) from swaths was derived using the ECICE algorithm, which applies a radiometric mixing model to brightness temperature data from AMSR-2. The algorithm estimates the fractional contributions of various ice types – including young ice (YI), first-year ice (FYI), and multiyear ice (MYI) – within each satellite footprint scan. By preserving the native resolution of the swath data, this approach minimizes interpolation errors and blurring that are typically introduced when merging multiple swaths onto a common grid in daily-averaged products. Although ECICE-derived sea-ice type distributions roughly align with the stage-of-development chart, inconsistencies – notably in the classification of YI – remain problematic. The algorithm struggles to reliably classify YI over short timescales due its overlapping radiometric signatures with FYI and MYI, particularly at the $Tb_{19H}$ frequency. This issue is compounded by the interdependence of ice-type estimates, where errors in YI classification propagate into FYI and MYI estimates. While daily-average Arctic ice-type retrievals have benefited from temperature and drift corrections (Ye, Heygster, et al., 2016; Ye, Shokr, et al., 2016), implementing analogous corrections in a swath-based framework is a challenge. Additionally, the conventional ice-type classifications – originally developed for Arctic conditions – lack the physical significance needed to characterize Antarctic sea ice. In Antarctic regions, where MYI coverage is limited and ice is generally thinner, the thickness thresholds used to distinguish FYI from YI based on brightness temperature distributions may be less relevant. These issues highlight the necessity for developing classification schemes tailored specifically to Antarctic conditions.

Despite these challenges in ice-type classification, the swath-based approach provides reliable estimates of total SIC due to the well-defined radiometric contrast between ice and open water. This capability is particularly valuable for monitoring rapid changes in the MIZ. Chapter 5, for instance, documents a significant SIC decrease in the MIZ over a 9-hour period. The observed retreat suggests strong poleward

advection, consistent with the overall dynamics implied by the S2S product over the same 9-hour period. Although previous studies have documented similar processes using daily-averaged data (e.g. Vichi et al., 2019), the swath-based approach – with its finer temporal resolution and precise timestamping – provides high resolution observations into the effects of transient weather events on sea-ice dynamics.

### 6.1.6 Disentangling Sub-Daily Dynamic and Thermodynamic Contributions to SIC Variability (Research Aim VI)

The feasibility of disentangling the dynamic and thermodynamic contributions to sea-ice concentration (SIC) variability using swath-based concentration and drift estimates is both promising and challenging. As detailed in Chapter 5, this approach leverages the high temporal resolution provided by sub-daily brightness temperature data. By utilizing AMSR-2 sensor data and applying the ECICE algorithm directly to Level-1B footprint data, the method captures rapid SIC changes that traditional daily-averaged observations cannot resolve.

Another potential application of the swath-based approach is its ability to combine SIC measurements with drift vectors derived from the same brightness temperature dataset. This pairing theoretically enables the separation of the dynamic component (advection) from the thermodynamic component (melt and growth) in the area of overlap between two swaths. The dynamic contribution is quantified by redistributing the initial SIC field according to observed ice motion using a Lagrangian vector transform method. In theory, this process isolates the portion of SIC change directly attributable to the advection of ice masses. The results indicate that, although widespread drift is observed throughout the ice interior, the advective contribution to SIC change is relatively small because SIC is already at the 100% value. In practice, however, several limitations complicate this separation. One notable issue is the occurrence of unrealistic volumes of ice melt and formation inferred from the thermodynamic component over a short period – just over 9 hours in the presented case study. This approach assumes that any SIC change not directly linked to advection must therefore be thermodynamically driven, a simplification that may not hold universally. In regions where motion vectors were unavailable – particularly in the marginal ice zone (MIZ), near coastlines, and along swath boundaries – the inability to compute dynamic contributions led to the

attribution of all observed SIC changes to thermodynamic processes. Moreover, despite the finer temporal resolution of the swath-based drift product, it remains challenged by the inherent difficulty of accurately tracking rapidly deforming ice patterns. This limitation diminishes the method's effectiveness in the MIZ and calls into question the plausibility of the extreme thermodynamic changes implied by the analysis, as substantial melting or growth over mere hours is unlikely. Although the short observational window should, in theory, reduce the likelihood of significant radiometric changes between successive observations which aids the pattern recognition algorithm, the S2S failed to capture the full complexity of ice motion in the MIZ, leading to ambiguities in interpreting whether observed SIC changes are due to advection or thermodynamic processes. This is a significant obstacle in our approach to disentangle the two constituents because the high frequency swath observations justify its usage in the MIZ but is also simultaneously limited there because of the high S2S retrieval uncertainty.

In the ice interior, where drift vectors are more reliably detected, thermodynamic processes emerged as the dominant drivers of observed variability. Minimal advection-driven change was detected despite the extensive drift field. This does not mean that pack-ice did not move at larger scales, but more likely that the overall drift did not engender any local SIC changes because the saturated SIC field in the interior mitigates the translation of drift into measurable SIC variations. The process of downscaling the spatially coarse drift field to match the finer SIC field further complicates interpretation by assuming that finer-scale features move uniformly within broader clusters, thereby attributing the homogeneous SIC variability within these clusters entirely to thermodynamics. Ultimately, while swath-based concentration and drift estimates offer a novel and promising route for disentangling the dynamic and thermodynamic drivers of sea-ice variability, limitations – primarily incomplete motion vector coverage and a saturated SIC field in the ice interior – pose significant challenges.

## 6.2 Limitations and Future Work

This thesis provides valuable insights into the rotational dynamics of Antarctic sea ice; however, several limitations must be acknowledged. The analysis of multidecadal dynamic trends reveals challenges in accurately representing oceanic influences on sea-ice variability. While atmospheric forcing is well captured in the observed rotational dynamics, the role of ocean currents, sea surface temperatures (SSTs), eddies, and wave-ice interactions remains poorly understood due to the inherent limitations of remote sensing techniques. The scarcity of high-resolution oceanic datasets, particularly beneath the ice, complicates efforts to quantify the exact contributions of oceanic processes to sea-ice motion and rheological changes. Furthermore, while this thesis identifies trends in sea-ice rotation and its correlation with cyclones and high-pressure systems, the physical mechanisms governing these interactions require further exploration. The focus on large-scale rotational dynamics may overlook mesoscale and sub-mesoscale processes, such as ice deformation, fracturing, and localized divergence/convergence patterns, which influence local heat and momentum exchanges. A more detailed understanding of the mechanisms by which local weather conditions engender ice rotation across different spatial and temporal scales could improve our ability to explain dynamical trends and further benefit coupled atmosphere-ice-ocean modelling efforts.

A core objective of this thesis is to address the temporal resolution limitations associated with daily-averaged sea-ice concentration and drift datasets. While these limitations are extensively addressed in Chapter 5, swath-based datasets still share some methodological constraints with their daily-averaged counterparts. The detection and quantification of rotational dynamics depend on the accuracy of satellite-derived ice motion vectors, which are subject to uncertainties arising from PM retrieval algorithms, spatial resolution constraints, and blurring associated with merging multiple swath observations of a dynamic field. Passive microwave sensors infer sea-ice information indirectly from brightness temperature measurements, meaning the accuracy of derived properties depends on the distinctiveness of their radiometric signatures. This limitation is evident in Chapter 5, where ice-type classification was challenging due to the relatively indistinct radiometric signatures of young and first-year ice, prompting the need to reassess ice-type classification thresholds in Antarctic conditions. For sea-ice drift products,

the feature-tracking algorithm applied to brightness temperature observations is susceptible to PM retrieval errors, which propagate through to the drift datasets, increasing overall uncertainty. Additionally, the algorithm relies on the persistence of radiometric patterns in sequential images, a methodological constraint that is not well-suited for analysing highly dynamic sea-ice regions. Consequently, this thesis primarily excludes the marginal ice zone, despite its critical role in air-sea-ice interactions and its substantial contribution to overall sea-ice variability. A shorter observational window, as facilitated by swath-based retrievals, should theoretically improve pattern recognition algorithms, improving its performance in the MIZ. However, a dedicated assessment of swath-based retrieval performance in such regions is necessary to validate this hypothesis. A shorter observational window also limits the total distance travelled by the ice, reducing the search domain for feature-tracking algorithms, thereby lowering computational costs.

While this thesis establishes that a swath-based approach enables high-frequency observations at the cost of spatial coverage, swath-derived drift datasets are further constrained by the requirement for overlapping swaths. The systematic implementation of this approach introduces additional complexities, particularly in selecting appropriate swath pairs for deriving ΔSIC and drift. The numerous potential pair permutations, each with unique start ($t_0$) and end ($t_1$) timestamps and varying observation windows ($\Delta t$), create ambiguity in defining optimal datasets for specific research objectives. Future studies should investigate the most appropriate swath-pairing strategies based on different scientific aims. For example, determining the response time of sea ice to extreme rotational wind forcing could benefit from an optimized selection of swath pairs. Although case studies in Chapter 4 demonstrate that sea ice responds to atmospheric forcing within approximately nine hours, a dedicated experiment could refine this timescale further. In conclusion, while this thesis advances the understanding of Antarctic sea-ice rotation and its driving forces, limitations in satellite data and the representation of oceanic processes highlight the need for improved data acquisition or assimilation methods. Future efforts should focus on improving observational capabilities, integrating multi-source datasets, and refining process-based models. Although this work demonstrates a means to extract sub-daily information from historical satellite records, satellite observations alone cannot fully explain air-sea-ice interactions. Instead, they should serve as a supplementary dataset to inform coupled modelling studies, ultimately improving our ability to predict sea-ice variability in response to changing climate conditions.

## 6.3 Broader Implications and Concluding remarks

Understanding sea-ice variability is necessary for unravelling the complexities of global climate systems, and this thesis makes a significant contribution to this by focusing on the short-term dynamics of Antarctic sea ice. By investigating sub-daily rotational patterns, the work demonstrates how atmospheric forcing – operating at spatial and temporal scales comparable to weather systems – drives rapid changes in sea-ice motion. This refined understanding is important because sea ice plays a key role in regulating ocean circulation, carbon cycling, and the exchange of energy between the ocean and atmosphere. Such dynamic interactions provide additional information to current modelling efforts aimed at deciphering the mechanisms governing air-sea-ice exchanges. The timeliness of this thesis is emphasised by the rapid shifts observed in both polar regions due to climate change. While most attention has concentrated on long-term trends, this work emphasizes the accumulated contribution of short-term drift variability to these observed trends. The rapid response of sea ice to transient weather events can trigger cascading impacts on ocean circulation and regional climate anomalies, mechanisms that are important for refining climate models. Moreover, the findings offer valuable analogues for the Arctic, which is transitioning toward a more seasonal ice regime characterized by thinner, more transient ice cover that is increasingly sensitive to atmospheric and oceanic forcing. The analysis of Antarctic sea-ice dynamics in this thesis may serve as a proxy for predicting future sea-ice scenarios in the Arctic, and by extension, the Northern Hemisphere ocean and climate systems. A key innovation of this work lies in its advancement of sea-ice retrieval frameworks using swath-based satellite observations. Unlike traditional daily-averaged products, these methods provide higher temporal resolution, enabling the capture rapid sea-ice variability. Enhanced retrieval techniques not only expand our current understanding of sea-ice dynamics but also facilitate more effective integration of satellite data into coupled atmosphere-ice-ocean models. The proposed framework establishes a benchmark dataset to support the refinement of high-frequency rheological parameterizations in coupled ice–ocean models, and to specifically diagnose model skill in reproducing observed dynamic versus thermodynamic sea-ice processes, thereby bolstering the reliability of climate predictions

In summary, this thesis bridges gaps in our understanding of sea-ice variability on short timescales by integrating novel methodologies with advanced satellite remote sensing. The work advances our

knowledge of Antarctic sea-ice dynamics while evaluating the observational tools that underpin these insights. The findings hold broad significance for climate science and Earth observation, offering new perspectives on the dynamic processes that govern polar environments and their responses to global climate change.

---

# References


Abram, N. J., Mulvaney, R., Vimeux, F., Phipps, S. J., Turner, J., & England, M. H. (2014). Evolution of the Southern Annular Mode during the past millennium. *Nature Climate Change*, *4*(7). https://doi.org/10.1038/nclimate2235

Ackley, S. F., Xie, H., & Tichenor, E. A. (2015). Ocean heat flux under Antarctic sea ice in the Bellingshausen and Amundsen Seas: Two case studies. *Annals of Glaciology*, *56*(69). https://doi.org/10.3189/2015AoG69A890

Alberello, A., Onorato, M., Bennetts, L., Vichi, M., Eayrs, C., Machutchon, K., & Toffoli, A. (2019). Brief communication: Pancake ice floe size distribution during the winter expansion of the Antarctic marginal ice zone. *Cryosphere*, *13*(1). https://doi.org/10.5194/tc-13-41-2019

Alberello, A., Bennetts, L., Heil, P., Eayrs, C., Vichi, M., MacHutchon, K., et al. (2020). Drift of Pancake Ice Floes in the Winter Antarctic Marginal Ice Zone During Polar Cyclones. *Journal of Geophysical Research: Oceans*, *125*(3). https://doi.org/10.1029/2019JC015418

Alberello, A., Dolatshah, A., Bennetts, L. G., Onorato, M., Nelli, F., & Toffoli, A. (2021). A physical model of wave attenuation in pancake ice. *International Journal of Offshore and Polar Engineering*, *31*(3). https://doi.org/10.17736/ijope.2021.ik08

Andersen, S., Tonboe, R., Kern, S., & Schyberg, H. (2006). Improved retrieval of sea ice total concentration from spaceborne passive microwave observations using numerical weather prediction model fields: An intercomparison of nine algorithms. *Remote Sensing of Environment*, *104*(4). https://doi.org/10.1016/j.rse.2006.05.013

Ardhuin, F., Stopa, J., Chapron, B., Collard, F., Smith, M., Thomson, J., et al. (2017). Measuring ocean waves in sea ice using SAR imagery: A quasi-deterministic approach evaluated with Sentinel-1 and in situ data. *Remote Sensing of Environment*, *189*. https://doi.org/10.1016/j.rse.2016.11.024

Arrigo, K. R., Dieckmann, G., Gosselin, M., Robinson, D. H., Fritsen, C. H., & Sullivan, C. W. (1995). High resolution study of the platelet ice ecosystem in McMurdo Sound, Antarctica: biomass, nutrient,

and production profiles within a dense microalgal bloom. *Marine Ecology Progress Series*, *127*(1–3). https://doi.org/10.3354/meps127255

Auclair, J. P., Dumont, D., Lemieux, J. F., & Ritchie, H. (2022). A model study of convergent dynamics in the marginal ice zone. *Philosophical Transactions of the Royal Society A: Mathematical, Physical and Engineering Sciences*, *380*(2235). https://doi.org/10.1098/rsta.2021.0261

Audh, R. R., Fawcett, S. E., Johnson, S., Rampai, T., & Vichi, M. (2023). Rafting of Growing Antarctic Sea Ice Enhances In-Ice Biogeochemical Activity in Winter. *Journal of Geophysical Research: Oceans*, *128*(12). https://doi.org/10.1029/2023JC019925

Aue, L., & Rinke, A. (2023). Cyclone Impacts on Sea Ice Concentration in the Atlantic Arctic Ocean: Annual Cycle and Recent Changes. *Geophysical Research Letters*, *50*(17). https://doi.org/10.1029/2023GL104657

Aue, L., Röntgen, L., Dorn, W., Uotila, P., Vihma, T., Spreen, G., & Rinke, A. (2023). Impact of three intense winter cyclones on the sea ice cover in the Barents Sea: A case study with a coupled regional climate model. *Frontiers in Earth Science*, *11*. https://doi.org/10.3389/feart.2023.1112467

Baldwin, M. P. (2001). Annular modes in global daily surface pressure. *Geophysical Research Letters*, *28*(21). https://doi.org/10.1029/2001GL013564

Baldwin, M. P., & Dunkerton, T. J. (2001). Stratospheric harbingers of anomalous weather regimes. *Science*, *294*(5542). https://doi.org/10.1126/science.1063315

Blanchard-Wrigglesworth, E., Roach, L. A., Donohoe, A., & Ding, Q. (2021). Impact of Winds and Southern Ocean SSTs on Antarctic Sea Ice Trends and Variability. *Journal of Climate*, *34*(3). https://doi.org/10.1175/JCLI-D-20-0386.1

Bouillon, S., & Rampal, P. (2015). Presentation of the dynamical core of neXtSIM, a new sea ice model. *Ocean Modelling*, *91*. https://doi.org/10.1016/j.ocemod.2015.04.005

Bracegirdle, T. J., Stephenson, D. B., Turner, J., & Phillips, T. (2015). The importance of sea ice area biases in 21st century multimodel projections of Antarctic temperature and precipitation. *Geophysical Research Letters*, *42*(24). https://doi.org/10.1002/2015GL067055

Brouwer, J., Fraser, A. D., Murphy, D. J., Wongpan, P., Alberello, A., Kohout, A., et al. (2022). Altimetric observation of wave attenuation through the Antarctic marginal ice zone using ICESat-2. *Cryosphere*, *16*(6). https://doi.org/10.5194/tc-16-2325-2022

Budikova, D. (2009). Role of Arctic sea ice in global atmospheric circulation: A review. *Global and Planetary Change*. https://doi.org/10.1016/j.gloplacha.2009.04.001

Cai, L., Alexeev, V. A., & Walsh, J. E. (2020). Arctic Sea Ice Growth in Response to Synoptic-And Large-Scale Atmospheric Forcing from CMIP5 Models. *Journal of Climate*, *33*(14). https://doi.org/10.1175/JCLI-D-19-0326.1

Callahan, J. E. (1972). The structure and circulation of deep water in the Antarctic. *Deep-Sea Research and Oceanographic Abstracts*, *19*(8). https://doi.org/10.1016/0011-7471(72)90040-X

Carter, L., McCave, I. N., & Williams, M. J. M. (2008). Chapter 4 Circulation and Water Masses of the Southern Ocean: A Review (pp. 85–114). https://doi.org/10.1016/S1571-9197(08)00004-9

Cavalieri, D. J. (1991). Aircraft active and passive microwave validation of sea ice concentration from the Defense Meteorological Satellite Program special sensor microwave imager. *Journal of Geophysical Research*, *96*(C12). https://doi.org/10.1029/91jc02335

Cavalieri, D. J., & Parkinson, C. L. (2008). Antarctic sea ice variability and trends, 1979–2006. *Journal of Geophysical Research: Oceans*, *113*(C7). https://doi.org/10.1029/2007jc004564

Cavalieri, D. J., Gloersen, P., & Campbell, W. J. (1984). Determination of sea ice parameters with the Nimbus 7 SMMR. *Journal of Geophysical Research*, *89*(D4). https://doi.org/10.1029/JD089iD04p05355

Chang, E. K. M. (2017). Projected Significant Increase in the Number of Extreme Extratropical Cyclones in the Southern Hemisphere. *Journal of Climate*, *30*(13). https://doi.org/10.1175/JCLI-D-16-0553.1

Clancy, R., Bitz, C. M., Edward, B. W., McGraw, M. C., & Cavallo, S. M. (2022). A Cyclone-Centered Perspective on the Drivers of Asymmetric Patterns in the Atmosphere and Sea Ice during Arctic Cyclones. *Journal of Climate*, *35*(1). https://doi.org/10.1175/JCLI-D-21-0093.1

Clark, P. U., Pisias, N. G., Stocker, T. F., & Weaver, A. J. (2002). The role of the thermohaline circulation in abrupt climate change. *Nature*. https://doi.org/10.1038/415863a

Clem, K. R., Renwick, J. A., McGregor, J., & Fogt, R. L. (2016). The relative influence of ENSO and SAM on antarctic Peninsula climate. *Journal of Geophysical Research*, *121*(16). https://doi.org/10.1002/2016JD025305

Clem, K. R., Renwick, J. A., & Mcgregor, J. (2017). Large-scale forcing of the Amundsen Sea low and its influence on sea ice and west antarctic temperature. *Journal of Climate*, *30*(20). https://doi.org/10.1175/JCLI-D-16-0891.1

Coggins, J. H. J., & McDonald, A. J. (2015). The influence of the Amundsen Sea Low on the winds in the Ross Sea and surroundings: Insights from a synoptic climatology. *Journal of Geophysical Research*, *120*(6). https://doi.org/10.1002/2014JD022830

Comiso, J. (1983). Sea ice effective microwave emissivities from satellite passive microwave and infrared observations. *Journal of Geophysical Research*, *88*(C12). https://doi.org/10.1029/JC088iC12p07686

Comiso, J. (1986). Characteristics of Arctic winter sea ice from satellite multispectral microwave observations. *Journal of Geophysical Research*, *91*(C1). https://doi.org/10.1029/JC091iC01p00975

Comiso, J. (2012). Large decadal decline of the arctic multiyear ice cover. *Journal of Climate*, *25*(4). https://doi.org/10.1175/JCLI-D-11-00113.1

Comiso, J., & Steffen, K. (2001). Studies of Antarctic sea ice concentrations from satellite data and their applications. *Journal of Geophysical Research: Oceans*, *106*(C12). https://doi.org/10.1029/2001jc000823

Comiso, J., & Zwally, H. J. (1984). Concentration gradients and growth/decay characteristics of the seasonal sea ice cover. *Journal of Geophysical Research*, *89*(C5). https://doi.org/10.1029/JC089iC05p08081

Comiso, J., Ackley, S. F., & Gordon, A. L. (1984). Antarctic sea ice microwave signatures and their correlation with in situ ice observations ( Weddell Sea). *Journal of Geophysical Research*, *89*(C1). https://doi.org/10.1029/JC089iC01p00662

Comiso, J., Parkinson, C. L., Gersten, R., & Stock, L. (2008). Accelerated decline in the Arctic sea ice cover. *Geophysical Research Letters*, *35*(1). https://doi.org/10.1029/2007GL031972

Comiso, J., Grenfell, T. C., Lange, M., Lohanick, A. W., Moore, R. K., & Wadhams, P. (2011). Microwave remote sensing of the Southern Ocean ice cover. https://doi.org/10.1029/gm068p0243

Crewell, S., Prigent, C., & Mech, M. (2021). Spaceborne Microwave Radiometry. In T. Foken (Ed.), *Springer Handbook of Atmospheric Measurements* (pp. 1151–1170). Springer, Cham. https://doi.org/10.1007/978-3-030-52171-4_41

Damsgaard, A., Sergienko, O., & Adcroft, A. (2021). The Effects of Ice Floe-Floe Interactions on Pressure Ridging in Sea Ice. *Journal of Advances in Modeling Earth Systems*, *13*(7). https://doi.org/10.1029/2020MS002336

Dierking, W., Stern, H. L., & Hutchings, J. K. (2020). Estimating statistical errors in retrievals of ice velocity and deformation parameters from satellite images and buoy arrays. *Cryosphere*, *14*(9). https://doi.org/10.5194/tc-14-2999-2020

Doble, M. J., & Wadhams, P. (2006). Dynamical contrasts between pancake and pack ice, investigated with a drifting buoy array. *Journal of Geophysical Research: Oceans*, *111*(11). https://doi.org/10.1029/2005JC003320

Doble, M. J., Coon, M. D., & Wadhams, P. (2003). Pancake ice formation in the Weddell Sea. *Journal of Geophysical Research: Oceans*, *108*(7). https://doi.org/10.1029/2002jc001373

Doddridge, E. W., & Marshall, J. (2017). Modulation of the Seasonal Cycle of Antarctic Sea Ice Extent Related to the Southern Annular Mode. *Geophysical Research Letters*, *44*(19). https://doi.org/10.1002/2017GL074319

Drinkwater, M. R., & Liu, X. (1999). Active and passive microwave determination of the circulation and characteristics of Weddell and Ross sea ice. In *International Geoscience and Remote Sensing Symposium (IGARSS)* (Vol. 1). https://doi.org/10.1109/igarss.1999.773482

Dumont, D. (2022). Marginal ice zone dynamics: History, definitions and research perspectives. *Philosophical Transactions of the Royal Society A: Mathematical, Physical and Engineering Sciences*, *380*(2235). https://doi.org/10.1098/rsta.2021.0253

Eayrs, C., Li, X., Raphael, M., & Holland, D. (2021). Rapid decline in Antarctic sea ice in recent years hints at future change. *Nature Geoscience*. https://doi.org/10.1038/s41561-021-00768-3

Ekman, W. (1905). On the influence of the earth's rotation on ocean currents. *Arkiv. Mat. Astronomi. Fys.*, 1–52.

Emery, W. J., Thomas, A. C., Collins, M. J., Crawford, W. R., & Mackas, D. L. (1986). An objective method for computing advective surface velocities from sequential infrared satellite images. *Journal of Geophysical Research: Oceans*, *91*(C11). https://doi.org/10.1029/jc091ic11p12865

Feltham, D. L. (2008). Sea Ice Rheology. *Annual Review of Fluid Mechanics*, *40*(1), 91–112. https://doi.org/10.1146/annurev.fluid.40.111406.102151

Fogt, R. L., & Marshall, G. (2020). The Southern Annular Mode: Variability, trends, and climate impacts across the Southern Hemisphere. *Wiley Interdisciplinary Reviews: Climate Change*. https://doi.org/10.1002/wcc.652

Fogt, R. L., Sleinkofer, A. M., Raphael, M., & Handcock, M. S. (2022). A regime shift in seasonal total Antarctic sea ice extent in the twentieth century. *Nature Climate Change*, *12*(1). https://doi.org/10.1038/s41558-021-01254-9

Fukamachi, Y., Ohshima, K. I., Mukai, Y., Mizuta, G., & Wakatsuchi, M. (2011). Sea-ice drift characteristics revealed by measurement of acoustic Doppler current profiler and ice-profiling sonar off Hokkaido in the Sea of Okhotsk. *Annals of Glaciology*, *52*(57 PART 1). https://doi.org/10.3189/172756411795931507

Fyfe, J. C., Saenko, O. A., Zickfeld, K., Eby, M., & Weaver, A. J. (2007). The role of poleward-intensifying winds on Southern Ocean warming. *Journal of Climate*, *20*(21). https://doi.org/10.1175/2007JCLI1764.1

Germishuizen, M., Vichi, M., & Vermeulen, E. (2024). Population changes in a Southern Ocean krill predator point towards regional Antarctic sea ice declines. *Scientific Reports*, *14*(1), 25820. https://doi.org/10.1038/s41598-024-74007-1

Gilbert, E., & Holmes, C. (2024). 2023's Antarctic sea ice extent is the lowest on record. *Weather*, *79*(2). https://doi.org/10.1002/wea.4518

Giles, A. B., Massom, R. A., Heil, P., & Hyland, G. (2011). Semi-automated feature-tracking of East Antarctic sea ice from Envisat ASAR imagery. *Remote Sensing of Environment*, *115*(9). https://doi.org/10.1016/j.rse.2011.04.027

Gille, S. T., & Kelly, K. A. (1996). Scales of spatial and temporal variability in the Southern Ocean. *Journal of Geophysical Research: Oceans*, *101*(C4). https://doi.org/10.1029/96JC00203

Gimbert, F., Marsan, D., Weiss, J., Jourdain, N. C., & Barnier, B. (2012). Sea ice inertial oscillations in the Arctic Basin. *Cryosphere*, *6*(5). https://doi.org/10.5194/tc-6-1187-2012

Girard, L., Weiss, J., Molines, J. M., Barnier, B., & Bouillon, S. (2009). Evaluation of high-resolution sea ice models on the basis of statistical and scaling properties of Arctic sea ice drift and deformation. *Journal of Geophysical Research: Oceans*, *114*(C8). https://doi.org/10.1029/2008jc005182

Golden, K. M., Bennetts, L. G., Cherkaev, E., Eisenman, I., Feltham, D., Horvat, C., et al. (2020). Modeling Sea Ice. *Notices of the American Mathematical Society*, *67*(10), 1. https://doi.org/10.1090/noti2171

Gonzalez, S., Vasallo, F., Recio-Blitz, C., Guijarro, J. A., & Riesco, J. (2018). Atmospheric patterns over the Antarctic Peninsula. *Journal of Climate*, *31*(9). https://doi.org/10.1175/JCLI-D-17-0598.1

Goosse, H., Lefebvre, W., de Montety, A., Crespin, E., & Orsi, A. H. (2009). Consistent past half-century trends in the atmosphere, the sea ice and the ocean at high southern latitudes. *Climate Dynamics*, *33*(7–8). https://doi.org/10.1007/s00382-008-0500-9

Greene, C. A., Blankenship, D. D., Gwyther, D. E., Silvano, A., & Van Wijk, E. (2017). Wind causes Totten Ice Shelf melt and acceleration. *Science Advances*, *3*(11). https://doi.org/10.1126/sciadv.1701681

Grieger, J., Leckebusch, G. C., Raible, C. C., Rudeva, I., & Simmonds, I. (2018). Subantarctic cyclones identified by 14 tracking methods, and their role for moisture transports into the continent. *Tellus, Series A: Dynamic Meteorology and Oceanography*, *70*(1). https://doi.org/10.1080/16000870.2018.1454808

Hahn, L. C., Armour, K. C., Zelinka, M. D., Bitz, C. M., & Donohoe, A. (2021). Contributions to Polar Amplification in CMIP5 and CMIP6 Models. *Frontiers in Earth Science*, *9*. https://doi.org/10.3389/feart.2021.710036

Hall, A., & Visbeck, M. (2002). Synchronous variability in the Southern Hemisphere atmosphere, sea ice, and ocean resulting from the annular mode. *Journal of Climate*, *15*(21). https://doi.org/10.1175/1520-0442(2002)015<3043:SVITSH>2.0.CO;2

Hallberg, R., & Gnanadesikan, A. (2006). The role of Eddies in determining the structure and response of the wind-driven Southern hemisphere overturning: Results from the Modeling Eddies in the Southern Ocean (MESO) project. *Journal of Physical Oceanography*, *36*(12). https://doi.org/10.1175/JPO2980.1

Hausmann, U., Sallée, J. B., Jourdain, N. C., Mathiot, P., Rousset, C., Madec, G., et al. (2020). The Role of Tides in Ocean-Ice Shelf Interactions in the Southwestern Weddell Sea. *Journal of Geophysical Research: Oceans*, *125*(6). https://doi.org/10.1029/2019JC015847

Heil, P., Massom, R. A., Allison, I., Worby, A. P., & Lytle, V. I. (2009). Role of off-shelf to on-shelf transitions for East Antarctic sea ice dynamics during spring 2003. *Journal of Geophysical Research: Oceans*, *114*(9). https://doi.org/10.1029/2008JC004873

Heil, P., Massom, R. A., Allison, I., & Worby, A. P. (2011). Physical attributes of sea-ice kinematics during spring 2007 off East Antarctica. *Deep-Sea Research Part II: Topical Studies in Oceanography*, *58*(9–10). https://doi.org/10.1016/j.dsr2.2010.12.004

Hellmer, H. H. (2004). Impact of Antarctic ice shelf basal melting on sea ice and deep ocean properties. *Geophysical Research Letters*, *31*(10). https://doi.org/10.1029/2004GL019506

Heorton, H., Radia, N., & Feltham, D. (2017). A model of sea ice formation in leads and polynyas. *Journal of Physical Oceanography*, *47*(7). https://doi.org/10.1175/JPO-D-16-0224.1

Heorton, H., Feltham, D., & Tsamados, M. (2018). Stress and deformation characteristics of sea ice in a high-resolution, anisotropic sea ice model. *Philosophical Transactions of the Royal Society A: Mathematical, Physical and Engineering Sciences*, *376*(2129). https://doi.org/10.1098/rsta.2017.0349

Hepworth, E., Messori, G., & Vichi, M. (2022). Association Between Extreme Atmospheric Anomalies Over Antarctic Sea Ice, Southern Ocean Polar Cyclones and Atmospheric Rivers. *Journal of Geophysical Research: Atmospheres*, *127*(7). https://doi.org/10.1029/2021JD036121

Hibler, W. D., & Bryan, K. (1987). A Diagnostic Ice–Ocean Model. *Journal of Physical Oceanography*, *17*(7). https://doi.org/10.1175/1520-0485(1987)017<0987:adim>2.0.co;2

Hobbs, W., Massom, R., Stammerjohn, S., Reid, P., Williams, G., & Meier, W. N. (2016). A review of recent changes in Southern Ocean sea ice, their drivers and forcings. *Global and Planetary Change*. https://doi.org/10.1016/j.gloplacha.2016.06.008

Hobbs, W., Klekociuk, A., & Pan, Y. (2020). Validation of reanalysis Southern Ocean atmosphere trends using sea ice data. *Atmospheric Chemistry and Physics*, *20*(23). https://doi.org/10.5194/acp-20-14757-2020

Hobbs, W., Spence, P., Meyer, A., Schroeter, S., Fraser, A. D., Reid, P., et al. (2024). Observational Evidence for a Regime Shift in Summer Antarctic Sea Ice. *Journal of Climate*, *37*(7). https://doi.org/10.1175/JCLI-D-23-0479.1

Holland, M., & Bitz, C. M. (2003). Polar amplification of climate change in coupled models. *Climate Dynamics*, *21*(3–4). https://doi.org/10.1007/s00382-003-0332-6

Holland, M., Landrum, L., Kostov, Y., & Marshall, J. (2017). Sensitivity of Antarctic sea ice to the Southern Annular Mode in coupled climate models. *Climate Dynamics*, *49*(5–6). https://doi.org/10.1007/s00382-016-3424-9

Holland, P., & Kwok, R. (2012). Wind-driven trends in Antarctic sea-ice drift. *Nature Geoscience*, *5*(12). https://doi.org/10.1038/ngeo1627

Holland, P., Jenkins, A., & Holland, D. (2010). Ice and ocean processes in the Bellingshausen sea, Antarctica. *Journal of Geophysical Research: Oceans*, *115*(5). https://doi.org/10.1029/2008JC005219

Holmes, C. R., Bracegirdle, T. J., & Holland, P. (2022). Antarctic Sea Ice Projections Constrained by Historical Ice Cover and Future Global Temperature Change. *Geophysical Research Letters*, *49*(10). https://doi.org/10.1029/2021GL097413

Hori, M., Aoki, Te., Stamnes, K., & Kokhanovsky, A. (2010). Cryosphere products in the first generation of the Global Change Observation Mission-Climate (GCOM-C1). In *International Archives of the Photogrammetry, Remote Sensing and Spatial Information Sciences - ISPRS Archives* (Vol. 38).

Horvat, C., Blanchard-Wrigglesworth, E., & Petty, A. (2020). Observing Waves in Sea Ice With ICESat-2. *Geophysical Research Letters*, *47*(10). https://doi.org/10.1029/2020GL087629

Horvat, Christopher, Tziperman, E., & Campin, J. M. (2016). Interaction of sea ice floe size, ocean eddies, and sea ice melting. *Geophysical Research Letters*, *43*(15). https://doi.org/10.1002/2016GL069742

Hughes, C. W. (2005). Nonlinear vorticity balance of the Antarctic Circumpolar Current. *Journal of Geophysical Research: Oceans*, *110*(11). https://doi.org/10.1029/2004JC002753

Hunke, E. C., Lipscomb, W. H., & Turner, A. K. (2011). Sea-ice models for climate study: Retrospective and new directions. *Journal of Glaciology*. https://doi.org/10.3189/002214311796406095

Hutchings, J. K., Roberts, A., Geiger, C. A., & Richter-Menge, J. (2011). Spatial and temporal characterization of sea-ice deformation. *Annals of Glaciology*, *52*(57 PART 2). https://doi.org/10.3189/172756411795931769

Imaoka, K., Kachi, M., Fujii, H., Murakami, H., Hori, M., Ono, A., et al. (2010). Global change observation mission (GCOM) for monitoring carbon, water cycles, and climate change. *Proceedings of the IEEE*, *98*(5). https://doi.org/10.1109/JPROC.2009.2036869

IPCC. (2023). *Intergovernmental Panel on Climate Change 2021 – The Physical Science Basis*. Cambridge University Press. https://doi.org/10.1017/9781009157896

Itkin, P., Spreen, G., Cheng, B., Doble, M., Girard-Ardhuin, F., Haapala, J., et al. (2017). Thin ice and storms: Sea ice deformation from buoy arrays deployed during N-ICE2015. *Journal of Geophysical Research: Oceans*, *122*(6). https://doi.org/10.1002/2016JC012403

Ivanova, N., Pedersen, L. T., Tonboe, R. T., Kern, S., Heygster, G., Lavergne, T., et al. (2015). Inter-comparison and evaluation of sea ice algorithms: Towards further identification of challenges and optimal approach using passive microwave observations. *Cryosphere*, *9*(5). https://doi.org/10.5194/tc-9-1797-2015

de Jager, W. (2022). Vorticity feature detection in Antarctic sea ice using OSI SAF low resolution global sea ice drift products. (Version 1.0) [Software]. Zenodo. https://doi.org/10.5281/zenodo.6340140.

de Jager, W. (2024). SeaIce_and_Atmosphere_Vorticity_Coupling. (Version 1.0) [Software]. Zenodo. https://doi.org/10.5281/zenodo.10817259.

de Jager, W., & Vichi, M. (2022). Rotational drift in Antarctic sea ice: Pronounced cyclonic features and differences between data products. *Cryosphere*, *16*(3). https://doi.org/10.5194/tc-16-925-2022

JAXA. (2012). GCOM-W/AMSR2 L1B Brightness Temperature. Japan Aerospace Exploration Agency.

Jena, B., Kshitija, S., Bajish, C. C., Turner, J., Holmes, C., Wilkinson, J., et al. (2024). Evolution of Antarctic Sea Ice Ahead of the Record Low Annual Maximum Extent in September 2023. *Geophysical Research Letters*, *51*(7). https://doi.org/10.1029/2023GL107561

Kacimi, S., & Kwok, R. (2022). Arctic Snow Depth, Ice Thickness, and Volume From ICESat-2 and CryoSat-2: 2018–2021. *Geophysical Research Letters*, *49*(5). https://doi.org/10.1029/2021GL097448

Kaleschke, L., Tian-Kunze, X., Maaß, N., Mäkynen, M., & Drusch, M. (2012). Sea ice thickness retrieval from SMOS brightness temperatures during the Arctic freeze-up period. *Geophysical Research Letters*, *39*(5). https://doi.org/10.1029/2012GL050916

Kawanishi, T., Sezai, T., Ito, Y., Imaoka, K., Takeshima, T., Ishido, Y., et al. (2003). The Advanced Microwave Scanning Radiometer for the Earth Observing System (AMSR-E), NASDA's contribution to the EOS for global energy and water cycle studies. *IEEE Transactions on Geoscience and Remote Sensing*. https://doi.org/10.1109/TGRS.2002.808331

Kern, S., Lavergne, T., Notz, D., Toudal Pedersen, L., & Tonboe, R. (2020). Satellite passive microwave sea-ice concentration data set inter-comparison for Arctic summer conditions. *Cryosphere*, *14*(7). https://doi.org/10.5194/tc-14-2469-2020

Kern, S., Lavergne, T., Pedersen, L. T., Tonboe, R. T., Bell, L., Meyer, M., & Zeigermann, L. (2022). Satellite passive microwave sea-ice concentration data set intercomparison using Landsat data. *Cryosphere*, *16*(1). https://doi.org/10.5194/tc-16-349-2022

Kidson, J. W. (1999). Principal modes of Southern Hemisphere low-frequency variability obtained from NCEP-NCAR reanalyses. *Journal of Climate*, *12*(9). https://doi.org/10.1175/1520-0442(1999)012<2808:PMOSHL>2.0.CO;2

Kimmritz, M., Counillon, F., Bitz, C. M., Massonnet, F., Bethke, I., & Gao, Y. (2018). Optimising assimilation of sea ice concentration in an Earth system model with a multicategory sea ice model. *Tellus, Series A: Dynamic Meteorology and Oceanography*, *70*(1). https://doi.org/10.1080/16000870.2018.1435945

King, J., Anchukaitis, K. J., Allen, K., Vance, T., & Hessl, A. (2023). Trends and variability in the Southern Annular Mode over the Common Era. *Nature Communications*, *14*(1). https://doi.org/10.1038/s41467-023-37643-1

Kohout, A., Williams, M. J. M., Dean, S. M., & Meylan, M. H. (2014). Storm-induced sea-ice breakup and the implications for ice extent. *Nature*, *509*(7502). https://doi.org/10.1038/nature13262

Kohout, A., Smith, M., Roach, L. A., Williams, G., Montiel, F., & Williams, M. J. M. (2020). Observations of exponential wave attenuation in Antarctic sea ice during the PIPERS campaign. *Annals of Glaciology*, *61*(82). https://doi.org/10.1017/aog.2020.36

Kohyama, T., & Hartmann, D. L. (2016). Antarctic sea ice response to weather and climate modes of variability. *Journal of Climate*, *29*(2). https://doi.org/10.1175/JCLI-D-15-0301.1

Kotamarthi, R., Hayhoe, K., Mearns, L., Wuebbles, D., Jacobs, J., & Jurado, J. (2021). Global Climate Models. In *Downscaling Techniques for High-Resolution Climate Projections* (pp. 19–39). Cambridge University Press. https://doi.org/10.1017/9781108601269.003

Kottmeier, C., & Sellmann, L. (1996). Atmospheric and oceanic forcing of Weddell Sea ice motion. *Journal of Geophysical Research: Oceans*, *101*(C9). https://doi.org/10.1029/96JC01293

Kottmeier, C., Olf, J., Frieden, W., & Roth, R. (1992). Wind forcing and ice motion in the Weddell Sea region. *Journal of Geophysical Research*, *97*(D18). https://doi.org/10.1029/92jd02171

Koyama, T., Stroeve, J., Cassano, J., & Crawford, A. (2017). Sea ice loss and arctic cyclone activity from 1979 to 2014. *Journal of Climate*, *30*(12). https://doi.org/10.1175/JCLI-D-16-0542.1

Kumar, A., Yadav, J., & Mohan, R. (2021). Seasonal sea-ice variability and its trend in the Weddell Sea sector of West Antarctica. *Environmental Research Letters*, *16*(2). https://doi.org/10.1088/1748-9326/abdc88

Kurtz, N. T., & Markus, T. (2012). Satellite observations of Antarctic sea ice thickness and volume. *Journal of Geophysical Research: Oceans*, *117*(8). https://doi.org/10.1029/2012JC008141

Kwok, R. (2015). Sea ice convergence along the Arctic coasts of Greenland and the Canadian Arctic Archipelago: Variability and extremes (1992-2014). *Geophysical Research Letters*, *42*(18). https://doi.org/10.1002/2015GL065462

Kwok, R. (2018). Arctic sea ice thickness, volume, and multiyear ice coverage: Losses and coupled variability (1958-2018). *Environmental Research Letters*. https://doi.org/10.1088/1748-9326/aae3ec

Kwok, R., & Comiso, J. (2002). Spatial patterns of variability in Antarctic surface temperature: Connections to the Southern Hemisphere Annular Mode and the Southern Oscillation. *Geophysical Research Letters*, *29*(14). https://doi.org/10.1029/2002GL015415

Kwok, R., & Cunningham, G. F. (2012). Deformation of the Arctic Ocean ice cover after the 2007 record minimum in summer ice extent. *Cold Regions Science and Technology*, *76–77*. https://doi.org/10.1016/j.coldregions.2011.04.003

Kwok, R., Curlander, J. C., Pang, S. S., & Mcconnell, R. (1990). An Ice-Motion Tracking System at the Alaska SAR Facility. *IEEE Journal of Oceanic Engineering*, *15*(1). https://doi.org/10.1109/48.46835

Kwok, R., Schweiger, A., Rothrock, D. A., Pang, S., & Kottmeier, C. (1998). Sea ice motion from satellite passive microwave imagery assessed with ERS SAR and buoy motions. *Journal of Geophysical Research: Oceans*, *103*(3334). https://doi.org/10.1029/97jc03334

Kwok, R., Cunningham, G. F., Wensnahan, M., Rigor, I., Zwally, H. J., & Yi, D. (2009). Thinning and volume loss of the Arctic Ocean sea ice cover: 2003-2008. *Journal of Geophysical Research: Oceans*, *114*(7). https://doi.org/10.1029/2009JC005312

Kwok, R., Comiso, J., Lee, T., & Holland, P. (2016). Linked trends in the South Pacific sea ice edge and Southern Oscillation Index. *Geophysical Research Letters*, *43*(19). https://doi.org/10.1002/2016GL070655

Kwok, R., Pang, S. S., & Kacimi, S. (2017). Sea ice drift in the Southern Ocean: Regional patterns, variability, and trends. *Elementa*, *5*. https://doi.org/10.1525/elementa.226

Lange, M., & Eicken, H. (1991). Textural characteristics of sea ice and the major mechanisms of ice growth in the Weddell Sea. *Annals of Glaciology*, *15*. https://doi.org/10.3189/1991aog15-1-210-215

Lange, M., & Sebille, E. Van. (2017). Parcels v0.9: Prototyping a Lagrangian ocean analysis framework for the petascale age. *Geoscientific Model Development*, *10*(11). https://doi.org/10.5194/gmd-10-4175-2017

Lange, M., Ackley, S. F., Wadhams, P., Dieckmann, G. S., & Eicken, H. (1989). Development of sea ice in the Weddell Sea. *Annals of Glaciology*, *12*. https://doi.org/10.1017/s0260305500007023

Lavergne, T. (2020). Antarctic sea-ice drift vectors using a S2S (swath-to-swath) approach. Norwegian Meteorological Institute. https://doi.org/https://doi.org/10.21343/0asd-6t60

Lavergne, T., & Down, E. (2023). A climate data record of year-round global sea-ice drift from the EUMETSAT Ocean and Sea Ice Satellite Application Facility (OSI SAF). *Earth System Science Data*, *15*(12), 5807–5834. https://doi.org/10.5194/essd-15-5807-2023

Lavergne, T., Eastwood, S., Teffah, Z., Schyberg, H., & Breivik, L. A. (2010). Sea ice motion from low-resolution satellite sensors: An alternative method and its validation in the Arctic. *Journal of Geophysical Research: Oceans*, *115*(10). https://doi.org/10.1029/2009JC005958

Lavergne, T., Piñol Solé, M., Down, E., & Donlon, C. (2021). Towards a swath-to-swath sea-ice drift product for the Copernicus Imaging Microwave Radiometer mission. *Cryosphere*, *15*(8). https://doi.org/10.5194/tc-15-3681-2021

Lavergne, T., Kern, S., Aaboe, S., Derby, L., Dybkjaer, G., Garric, G., et al. (2022). A New Structure for the Sea Ice Essential Climate Variables of the Global Climate Observing System. *Bulletin of the American Meteorological Society*, *103*(6). https://doi.org/10.1175/BAMS-D-21-0227.1

Lefebvre, W., Goosse, H., Timmermann, R., & Fichefet, T. (2004). Influence of the Southern Annular Mode on the sea ice - Ocean system. *Journal of Geophysical Research: Oceans*, *109*(9). https://doi.org/10.1029/2004JC002403

Leppäranta, M. (2005). The drift of sea ice. Berlin and Heidelberg, Springer-Verlag. 266pp. ISBN 3–540-40881-9, hardback. *Journal of Glaciology*, *51*(174). https://doi.org/10.3189/s0022143000209581

Li, D., DeConto, R. M., & Pollard, D. (2023). Climate model differences contribute deep uncertainty in future Antarctic ice loss. *Science Advances*, *9*(7). https://doi.org/10.1126/sciadv.add7082

Lu, J., Scarlat, R., Heygster, G., & Spreen, G. (2022). Reducing Weather Influences on an 89 GHz Sea Ice Concentration Algorithm in the Arctic Using Retrievals From an Optimal Estimation Method. *Journal of Geophysical Research: Oceans*, *127*(9). https://doi.org/10.1029/2019JC015912

Lynas, M., Houlton, B. Z., & Perry, S. (2021). Greater than 99% consensus on human caused climate change in the peer-reviewed scientific literature. *Environmental Research Letters*. https://doi.org/10.1088/1748-9326/ac2966

Maksym, T. (2019). Arctic and antarctic sea ice change: Contrasts, commonalities, and causes. *Annual Review of Marine Science*. https://doi.org/10.1146/annurev-marine-010816-060610

Mangatane, M. J., & Vichi, M. (2025). Intercomparison of Antarctic Sea-Ice Thickness Estimates from Satellite Altimetry and Assessment over the 2019 Data-Rich Year. *Remote Sensing*, *17*(7), 1180. https://doi.org/10.3390/rs17071180

Marshall, G. (2003). Trends in the Southern Annular Mode from observations and reanalyses. *Journal of Climate*, *16*(24). https://doi.org/10.1175/1520-0442(2003)016<4134:TITSAM>2.0.CO;2

Martinson, D. G., & Iannuzzi, R. A. (2013). Antarctic Ocean-Ice Interaction: Implications from Ocean Bulk Property Distributions in the Weddell Gyre. https://doi.org/10.1029/ar074p0243

Martinson, D. G., & Wamser, C. (1990). Ice drift and momentum exchange in winter Antarctic pack ice. *Journal of Geophysical Research: Oceans*, *95*(C2). https://doi.org/10.1029/jc095ic02p01741

Maslanik, J., & Stroeve, J. (1999). Near-Real-Time DMSP SSM/I-SSMIS Daily Polar Gridded Brightness Temperatures. (NSIDC-0080, Version 1). [Data Set]. Boulder, Colorado, USA: NASA National Snow and Ice Data Center Distributed Active Archive Center. https://doi.org/https://doi.org/10.5067/AKQDND71ZDLF

Massom, R. A., & Stammerjohn, S. E. (2010). Antarctic sea ice change and variability - Physical and ecological implications. *Polar Science*, *4*(2). https://doi.org/10.1016/j.polar.2010.05.001

Massom, R. A., Scambos, T. A., Bennetts, L. G., Reid, P., Squire, V. A., & Stammerjohn, S. E. (2018). Antarctic ice shelf disintegration triggered by sea ice loss and ocean swell. *Nature*, *558*(7710), 383–389. https://doi.org/10.1038/s41586-018-0212-1

Masson-Delmotte, V., Kageyama, M., Braconnot, P., Charbit, S., Krinner, G., Ritz, C., et al. (2006). Past and future polar amplification of climate change: Climate model intercomparisons and ice-core constraints. *Climate Dynamics*, *26*(5). https://doi.org/10.1007/s00382-005-0081-9

Massonnet, F., Fichefet, T., Goosse, H., Vancoppenolle, M., Mathiot, P., & König Beatty, C. (2011). On the influence of model physics on simulations of Arctic and Antarctic sea ice. *Cryosphere*, *5*(3). https://doi.org/10.5194/tc-5-687-2011

Massonnet, F., Fichefet, T., Goosse, H., Bitz, C. M., Philippon-Berthier, G., Holland, M., & Barriat, P. Y. (2012). Constraining projections of summer Arctic sea ice. *Cryosphere*, *6*(6). https://doi.org/10.5194/tc-6-1383-2012

Matear, R. J., O'Kane, T. J., Risbey, J. S., & Chamberlain, M. (2015). Sources of heterogeneous variability and trends in Antarctic sea-ice. *Nature Communications*, *6*. https://doi.org/10.1038/ncomms9656

Mayewski, P. A., Meredith, M. P., Summerhayes, C. P., Turner, J., Worby, A., Barrett, P. J., et al. (2009). State of the antarctic and southern ocean climate system. *Reviews of Geophysics*. https://doi.org/10.1029/2007RG000231

Mazloff, M. R., Heimbach, P., & Wunsch, C. (2010). An eddy-permitting Southern Ocean state estimate. *Journal of Physical Oceanography*, *40*(5). https://doi.org/10.1175/2009JPO4236.1

McPhee, M. G. (1988). Analysis and Prediction of Short-Term Ice Drift. *Journal of Offshore Mechanics and Arctic Engineering*, *110*(1). https://doi.org/10.1115/1.3257130

McPhee, M. G. (2016). The sea ice-ocean boundary layer. In *Sea Ice: Third Edition*. https://doi.org/10.1002/9781118778371.ch5

Meehl, G. A., Arblaster, J. M., Chung, C. T. Y., Holland, M., DuVivier, A., Thompson, L. A., et al. (2019). Sustained ocean changes contributed to sudden Antarctic sea ice retreat in late 2016. *Nature Communications*, *10*(1). https://doi.org/10.1038/s41467-018-07865-9

Meier, W. N. (2019). Satellite Passive Microwave Observations of Sea Ice. In *Encyclopedia of Ocean Sciences, Third Edition: Volume 1-5* (Vol. 1–5). https://doi.org/10.1016/B978-0-12-409548-9.11461-7

Meier, W. N., & Stewart, J. S. (2019). Assessing uncertainties in sea ice extent climate indicators. *Environmental Research Letters*, *14*(3). https://doi.org/10.1088/1748-9326/aaf52c

Melsheimer, C., Spreen, G., Ye, Y., & Shokr, M. (2023). First results of Antarctic sea ice type retrieval from active and passive microwave remote sensing data. *Cryosphere*, *17*(1). https://doi.org/10.5194/tc-17-105-2023

Meredith, M. P., Naveira Garabato, A. C., Hogg, A. M., & Farneti, R. (2012). Sensitivity of the overturning circulation in the Southern Ocean to decadal changes in wind forcing. *Journal of Climate*, *25*(1). https://doi.org/10.1175/2011JCLI4204.1

Mongwe, P., Gregor, L., Tjiputra, J., Hauck, J., Ito, T., Danek, C., et al. (2024). Projected poleward migration of the Southern Ocean CO2 sink region under high emissions. *Communications Earth & Environment*, *5*(1), 232. https://doi.org/10.1038/s43247-024-01382-y

Morioka, Y., Doi, T., Iovino, D., Masina, S., & Behera, S. K. (2019). Role of sea-ice initialization in climate predictability over the Weddell Sea. *Scientific Reports*, *9*(1). https://doi.org/10.1038/s41598-019-39421-w

Morrison, A., & Hogg, A. M. C. (2013). On the relationship between southern ocean overturning and ACC transport. *Journal of Physical Oceanography*, *43*(1). https://doi.org/10.1175/JPO-D-12-057.1

Morrison, A., McC. Hogg, A., England, M. H., & Spence, P. (2020). Warm Circumpolar Deep Water transport toward Antarctica driven by local dense water export in canyons. *Science Advances*, *6*(18). https://doi.org/10.1126/sciadv.aav2516

Munday, D. R., Johnson, H. L., & Marshall, D. (2013). Eddy saturation of equilibrated circumpolar currents. *Journal of Physical Oceanography*, *43*(3). https://doi.org/10.1175/JPO-D-12-095.1

Naughten, K. A., Holland, P., Dutrieux, P., Kimura, S., Bett, D. T., & Jenkins, A. (2022). Simulated Twentieth-Century Ocean Warming in the Amundsen Sea, West Antarctica. *Geophysical Research Letters*, *49*(5). https://doi.org/10.1029/2021GL094566

Neme, J., England, M. H., & Hogg, A. M. C. (2021). Seasonal and Interannual Variability of the Weddell Gyre From a High-Resolution Global Ocean-Sea Ice Simulation During 1958–2018. *Journal of Geophysical Research: Oceans*, *126*(11). https://doi.org/10.1029/2021JC017662

Nese, J., & Grenci, L. (2020). *A World of Weather: Fundamentals of Meteorology*. (D. Babb, Ed.) (6th ed.). Dubuque, IO, United States: Kendall/Hunt Publishing Co.

Notz, D. (2014). Sea-ice extent and its trend provide limited metrics of model performance. *Cryosphere*, *8*(1). https://doi.org/10.5194/tc-8-229-2014

Notz, D. (2015). How well must climate models agree with observations? *Philosophical Transactions of the Royal Society A: Mathematical, Physical and Engineering Sciences*, *373*(2052). https://doi.org/10.1098/rsta.2014.0164

Notz, D. (2020). Arctic Sea Ice in CMIP6. *Geophysical Research Letters*, *47*(10). https://doi.org/10.1029/2019GL086749

Notz, D., Jahn, A., Holland, M., Hunke, E., Massonnet, F., Stroeve, J., et al. (2016). The CMIP6 Sea-Ice Model Intercomparison Project (SIMIP): Understanding sea ice through climate-model simulations. In *Geoscientific Model Development* (Vol. 9). https://doi.org/10.5194/gmd-9-3427-2016

Orsi, A. H., Whitworth, T., & Nowlin, W. D. (1995). On the meridional extent and fronts of the Antarctic Circumpolar Current. *Deep-Sea Research Part I*, *42*(5). https://doi.org/10.1016/0967-0637(95)00021-W

Padman, L., Siegfried, M. R., & Fricker, H. A. (2018). Ocean Tide Influences on the Antarctic and Greenland Ice Sheets. *Reviews of Geophysics*, *56*(1). https://doi.org/10.1002/2016RG000546

Parkinson, C. L. (2019). A 40-y record reveals gradual Antarctic sea ice increases followed by decreases at rates far exceeding the rates seen in the Arctic. *Proceedings of the National Academy of Sciences of the United States of America*, *116*(29). https://doi.org/10.1073/pnas.1906556116

Parkinson, C. L. (2022). Arctic sea ice coverage from 43 years of satellite passive-microwave observations. *Frontiers in Remote Sensing*, *3*. https://doi.org/10.3389/frsen.2022.1021781

Parkinson, C. L., & Cavalieri, D. J. (2008). Arctic sea ice variability and trends, 1979-2006. *Journal of Geophysical Research: Oceans*, *113*(7). https://doi.org/10.1029/2007JC004558

Parkinson, C. L., & Comiso, J. (2013). On the 2012 record low Arctic sea ice cover: Combined impact of preconditioning and an August storm. *Geophysical Research Letters*, *40*(7). https://doi.org/10.1002/grl.50349

Parkinson, C. L., Comiso, J., & Zwally, H. (1999). Nimbus-5 ESMR Daily Polar Gridded Brightness Temperatures. USA, CO, Boulder: National Snow and Ice Data Center.

Partington, K. C. (2000). A data fusion algorithm for mapping sea-ice concentrations from special sensor microwave/imager data. *IEEE Transactions on Geoscience and Remote Sensing*, *38*(4 II). https://doi.org/10.1109/36.851776

Passerotti, G., Bennetts, L. G., Polach, F. V. B. U., Alberello, A., Puolakka, O., Dolatshah, A., et al. (2022). Interactions between Irregular Wave Fields and Sea Ice: A Physical Model for Wave Attenuation and Ice Breakup in an Ice Tank. *Journal of Physical Oceanography*, *52*(7). https://doi.org/10.1175/JPO-D-21-0238.1

Paul, F., Mielke, T., Schwarz, C., Schröder, J., Rampai, T., Skatulla, S., et al. (2021). Frazil ice in the antarctic marginal ice zone. *Journal of Marine Science and Engineering*, *9*(6). https://doi.org/10.3390/jmse9060647

Paul, F., Schwarz, C., Audh, R. R., Bluhm, J., Johnson, S., MacHutchon, K., et al. (2023). Sea ice mechanics. *Computer Methods in Material Science*, *23*(3). https://doi.org/10.7494/cmms.2023.3.0816

Pellichero, V., Sallée, J. B., Schmidtko, S., Roquet, F., & Charrassin, J. B. (2017). The ocean mixed layer under Southern Ocean sea-ice: Seasonal cycle and forcing. *Journal of Geophysical Research: Oceans*, *122*(2). https://doi.org/10.1002/2016JC011970

Perovich, D. K., Jones, K. F., Light, B., Eicken, H., Markus, T., Stroeve, J., & Lindsay, R. (2011). Solar partitioning in a changing Arctic sea-ice cover. *Annals of Glaciology*, *52*(57 PART 2). https://doi.org/10.3189/172756411795931543

Pezza, A. B., Rashid, H. A., & Simmonds, I. (2012). Climate links and recent extremes in antarctic sea ice, high-latitude cyclones, Southern Annular Mode and ENSO. *Climate Dynamics*, *38*(1–2). https://doi.org/10.1007/s00382-011-1044-y

Polvani, L. M., Banerjee, A., Chemke, R., Doddridge, E. W., Ferreira, D., Gnanadesikan, A., et al. (2021). Interannual SAM Modulation of Antarctic Sea Ice Extent Does Not Account for Its Long-Term Trends, Pointing to a Limited Role for Ozone Depletion. *Geophysical Research Letters*, *48*(21). https://doi.org/10.1029/2021GL094871

Purich, A., & Doddridge, E. W. (2023). Record low Antarctic sea ice coverage indicates a new sea ice state. *Communications Earth and Environment*, *4*(1). https://doi.org/10.1038/s43247-023-00961-9

Rabault, J., Sutherland, G., Gundersen, O., Jensen, A., Marchenko, A., & Breivik, Ø. (2020). An open source, versatile, affordable waves in ice instrument for scientific measurements in the Polar Regions. *Cold Regions Science and Technology*, *170*. https://doi.org/10.1016/j.coldregions.2019.102955

Rabault, J., Müller, M., Voermans, J., Brazhnikov, D., Turnbull, I., Marchenko, A., et al. (2023). A dataset of direct observations of sea ice drift and waves in ice. *Scientific Data*, *10*(1). https://doi.org/10.1038/s41597-023-02160-9

Rampal, P., Weiss, J., Marsan, D., Lindsay, R., & Stern, H. (2008). Scaling properties of sea ice deformation from buoy dispersion analysis. *Journal of Geophysical Research: Oceans*, *113*(3). https://doi.org/10.1029/2007JC004143

Rampal, P., Weiss, J., & Marsan, D. (2009). Positive trend in the mean speed and deformation rate of Arctic sea ice, 1979-2007. *Journal of Geophysical Research: Oceans*, *114*(5). https://doi.org/10.1029/2008JC005066

Raphael, M., Marshall, G., Turner, J., Fogt, R. L., Schneider, D., Dixon, D. A., et al. (2016). The Amundsen sea low: Variability, change, and impact on Antarctic climate. *Bulletin of the American Meteorological Society*, *97*(1). https://doi.org/10.1175/BAMS-D-14-00018.1

Raphael, M., & Hobbs, W. (2014). The influence of the large-scale atmospheric circulation on Antarctic sea ice during ice advance and retreat seasons. *Geophysical Research Letters*, *41*(14). https://doi.org/10.1002/2014GL060365

Rintoul, S. R., & Naveira Garabato, A. C. (2013). Dynamics of the southern ocean circulation. In *International Geophysics* (Vol. 103). https://doi.org/10.1016/B978-0-12-391851-2.00018-0

Roach, L. A., Horvat, C., Dean, S. M., & Bitz, C. M. (2018). An Emergent Sea Ice Floe Size Distribution in a Global Coupled Ocean-Sea Ice Model. *Journal of Geophysical Research: Oceans*, *123*(6). https://doi.org/10.1029/2017JC013692

Roach, L. A., Dörr, J., Holmes, C. R., Massonnet, F., Blockley, E. W., Notz, D., et al. (2020). Antarctic Sea Ice Area in CMIP6. *Geophysical Research Letters*, *47*(9). https://doi.org/10.1029/2019GL086729

Sandven, S., Spreen, G., Heygster, G., Girard-Ardhuin, F., Farrell, S. L., Dierking, W., & Allard, R. A. (2023). Sea Ice Remote Sensing—Recent Developments in Methods and Climate Data Sets. *Surveys in Geophysics*. https://doi.org/10.1007/s10712-023-09781-0

Scarlat, R., Melsheimer, C., Spreen, G., & Heygster, G. (2019). CIMR Mission Requirement Consolidation study (Version 3). European Space Agency.

Schreiber, E. A. P., & Serreze, M. C. (2020). Impacts of synoptic-scale cyclones on Arctic sea-ice concentration: A systematic analysis. *Annals of Glaciology*, *61*(82). https://doi.org/10.1017/aog.2020.23

Schroeter, S., Hobbs, W., & Bindoff, N. L. (2017). Interactions between Antarctic sea ice and large-scale atmospheric modes in CMIP5 models. *The Cryosphere*, *11*(2). https://doi.org/10.5194/tc-11-789-2017

Schroeter, S., Hobbs, W., Bindoff, N. L., Massom, R., & Matear, R. (2018). Drivers of Antarctic Sea Ice Volume Change in CMIP5 Models. *Journal of Geophysical Research: Oceans*, *123*(11). https://doi.org/10.1029/2018JC014177

Serreze, M. C., & Meier, W. N. (2019). The Arctic's sea ice cover: trends, variability, predictability, and comparisons to the Antarctic. *Annals of the New York Academy of Sciences*. https://doi.org/10.1111/nyas.13856

Serreze, M. C., & Stroeve, J. (2015). Arctic sea ice trends, variability and implications for seasonal ice forecasting. *Philosophical Transactions of the Royal Society A: Mathematical, Physical and Engineering Sciences*, *373*(2045). https://doi.org/10.1098/rsta.2014.0159

Shen, Z., Zhou, W., Li, J., & Chan, J. C. L. (2023). A frequent ice-free Arctic is likely to occur before the mid-21st century. *Npj Climate and Atmospheric Science*, *6*(1). https://doi.org/10.1038/s41612-023-00431-1

Shokr, M., & Agnew, T. A. (2013). Validation and potential applications of Environment Canada Ice Concentration Extractor (ECICE) algorithm to Arctic ice by combining AMSR-E and QuikSCAT observations. *Remote Sensing of Environment*, *128*. https://doi.org/10.1016/j.rse.2012.10.016

Shokr, M., & Sinha, N. (2015). *Sea Ice: Physics and Remote Sensing*. Wiley. https://doi.org/10.1002/9781119028000

Shokr, M., Lambe, A., & Agnew, T. (2008). A new algorithm (ECICE) to estimate ice concentration from remote sensing observations: An application to 85-GHz passive microwave data. *IEEE Transactions on Geoscience and Remote Sensing*, *46*(12). https://doi.org/10.1109/TGRS.2008.2000624

Simmonds, I., Keay, K., & Lim, E. P. (2003). Synoptic activity in the seas around Antarctica. *Monthly Weather Review*, *131*(2). https://doi.org/10.1175/1520-0493(2003)131<0272:SAITSA>2.0.CO;2

Skatulla, S., Audh, R. R., Cook, A., Hepworth, E., Johnson, S., Lupascu, D. C., et al. (2022). Physical and mechanical properties of winter first-year ice in the Antarctic marginal ice zone along the Good Hope Line. *Cryosphere*, *16*(7). https://doi.org/10.5194/tc-16-2899-2022

Smith, D. M., Screen, J. A., Deser, C., Cohen, J., Fyfe, J. C., García-Serrano, J., et al. (2019). The Polar Amplification Model Intercomparison Project (PAMIP) contribution to CMIP6: Investigating the causes and consequences of polar amplification. *Geoscientific Model Development*, *12*(3). https://doi.org/10.5194/gmd-12-1139-2019

Spreen, G., & Kern, S. (2017). Methods of satellite remote sensing of sea ice. In *Sea Ice* (pp. 239–260). Wiley. https://doi.org/10.1002/9781118778371.ch9

Spreen, G., Kaleschke, L., & Heygster, G. (2008). Sea ice remote sensing using AMSR-E 89-GHz channels. *Journal of Geophysical Research: Oceans*, *113*(2). https://doi.org/10.1029/2005JC003384

Spreen, G., Kwok, R., & Menemenlis, D. (2011). Trends in Arctic sea ice drift and role of wind forcing: 1992-2009. *Geophysical Research Letters*. https://doi.org/10.1029/2011GL048970

Stammerjohn, S. E., Martinson, D. G., Smith, R. C., Yuan, X., & Rind, D. (2008). Trends in Antarctic annual sea ice retreat and advance and their relation to El Niño-Southern Oscillation and Southern Annular Mode variability. *Journal of Geophysical Research: Oceans*, *113*(3). https://doi.org/10.1029/2007jc004269

Stark, J. D., Ridley, J., Martin, M., & Hines, A. (2008). Sea ice concentration and motion assimilation in a sea ice-ocean model. *Journal of Geophysical Research: Oceans*, *113*(5). https://doi.org/10.1029/2007JC004224

Steele, M., & Boyd, T. (1998). Retreat of the cold halocline layer in the Arctic Ocean. *Journal of Geophysical Research: Oceans*, *103*(C5). https://doi.org/10.1029/98jc00580

Stevens, R. P., & Heil, P. (2011). The interplay of dynamic and thermodynamic processes in driving the ice-edge location in the Southern Ocean. *Annals of Glaciology*, *52*(57 PART 1). https://doi.org/10.3189/172756411795931642

Stopa, J. E., Sutherland, P., & Ardhuin, F. (2018). Strong and highly variable push of ocean waves on Southern Ocean sea ice. *Proceedings of the National Academy of Sciences of the United States of America*, *115*(23). https://doi.org/10.1073/pnas.1802011115

Storto, A., Alvera-Azcárate, A., Balmaseda, M. A., Barth, A., Chevallier, M., Counillon, F., et al. (2019). Ocean reanalyses: Recent advances and unsolved challenges. *Frontiers in Marine Science*. https://doi.org/10.3389/fmars.2019.00418

Stössel, A., von Storch, J. S., Notz, D., Haak, H., & Gerdes, R. (2018). High-frequency and meso-scale winter sea-ice variability in the Southern Ocean in a high-resolution global ocean model. *Ocean Dynamics*, *68*(3). https://doi.org/10.1007/s10236-018-1135-y

Stroeve, J., & Notz, D. (2018). Changing state of Arctic sea ice across all seasons. *Environmental Research Letters*. https://doi.org/10.1088/1748-9326/aade56

Stuecker, M. F., Bitz, C. M., & Armour, K. C. (2017). Conditions leading to the unprecedented low Antarctic sea ice extent during the 2016 austral spring season. *Geophysical Research Letters*, *44*(17). https://doi.org/10.1002/2017GL074691

Sumata, H., Kwok, R., Gerdes, R., Kauker, F., & Karcher, M. (2015). Uncertainty of Arctic summer ice drift assessed by high-resolution SAR data. *Journal of Geophysical Research: Oceans*, *120*(8). https://doi.org/10.1002/2015JC010810

Sun, S., & Eisenman, I. (2021). Observed Antarctic sea ice expansion reproduced in a climate model after correcting biases in sea ice drift velocity. *Nature Communications*, *12*(1). https://doi.org/10.1038/s41467-021-21412-z

Swart, N., & Fyfe, J. (2012). Observed and simulated changes in the Southern Hemisphere surface westerly wind-stress. *Geophysical Research Letters*, *39*(16). https://doi.org/10.1029/2012GL052810

Swart, S., du Plessis, M. D., Thompson, A. F., Biddle, L. C., Giddy, I., Linders, T., et al. (2020). Submesoscale Fronts in the Antarctic Marginal Ice Zone and Their Response to Wind Forcing. *Geophysical Research Letters*, *47*(6). https://doi.org/10.1029/2019GL086649

Swift, C. T., & Cavalieri, D. J. (1985). Passive microwave remote sensing for sea ice research. *Eos, Transactions American Geophysical Union*, *66*(49). https://doi.org/10.1029/EO066i049p01210

Tamarin-Brodsky, T., & Kaspi, Y. (2017). Enhanced poleward propagation of storms under climate change. *Nature Geoscience*, *10*(12). https://doi.org/10.1038/s41561-017-0001-8

Tansley, C. E., & Marshall, D. (2001). On the dynamics of wind-driven circumpolar currents. *Journal of Physical Oceanography*, *31*(11). https://doi.org/10.1175/1520-0485(2001)031<3258:OTDOWD>2.0.CO;2

Tavakolifar, H., Shahghasemi, E., & Nazif, S. (2017). Evaluation of climate change impacts on extreme rainfall events characteristics using a synoptic weather typing-based daily precipitation downscaling model. *Journal of Water and Climate Change*, *8*(3). https://doi.org/10.2166/wcc.2017.107

Teresa, M., Espinosa, M., Giuliani, G., & Ray, N. (2019). Essential Climate Variables. *International Journal of Digital Earth*, *13*(2).

Teske, V., Timmermann, R., & Semmler, T. (2024). Subsurface warming in the Antarctica's Weddell Sea can be avoided by reaching the 2∘C warming target. *Communications Earth and Environment*, *5*(1). https://doi.org/10.1038/s43247-024-01238-5

Thompson, D. W. J., & Solomon, S. (2002). Interpretation of recent Southern Hemisphere climate change. *Science*, *296*(5569). https://doi.org/10.1126/science.1069270

Thompson, D. W. J., Solomon, S., Kushner, P. J., England, M. H., Grise, K. M., & Karoly, D. J. (2011). Signatures of the Antarctic ozone hole in Southern Hemisphere surface climate change. *Nature Geoscience*. https://doi.org/10.1038/ngeo1296

Thorndike, A. S., & Colony, R. (1982). Sea ice motion in response to geostrophic winds. *Journal of Geophysical Research: Oceans*, *87*(C8). https://doi.org/10.1029/jc087ic08p05845

Toggweiler, J. R., & Key, R. M. (2003). OCEAN CIRCULATION | Thermohaline Circulation. In *Encyclopedia of Atmospheric Sciences*. https://doi.org/10.1016/b0-12-227090-8/00281-5

Turner, J. (2004). The El Niño-Southern Oscillation and Antarctica. *International Journal of Climatology*, *24*(1). https://doi.org/10.1002/joc.965

Turner, J., Phillips, T., Marshall, G., Hosking, J. S., Pope, J. O., Bracegirdle, T. J., & Deb, P. (2017). Unprecedented springtime retreat of Antarctic sea ice in 2016. *Geophysical Research Letters*, *44*(13). https://doi.org/10.1002/2017GL073656

Turner, J., Guarino, M. V., Arnatt, J., Jena, B., Marshall, G., Phillips, T., et al. (2020). Recent Decrease of Summer Sea Ice in the Weddell Sea, Antarctica. *Geophysical Research Letters*, *47*(11). https://doi.org/10.1029/2020GL087127

Uotila, J., Vihma, T., & Launiainen, J. (2000). Response of the Weddell Sea pack ice to wind forcing. *Journal of Geophysical Research: Oceans*, *105*(C1). https://doi.org/10.1029/1999jc900265

Uotila, P., Vihma, T., Pezza, A. B., Simmonds, I., Keay, K., & Lynch, A. H. (2011). Relationships between Antarctic cyclones and surface conditions as derived from high-resolution numerical weather prediction data. *Journal of Geophysical Research Atmospheres*, *116*(7). https://doi.org/10.1029/2010JD015358

Uotila, P., Goosse, H., Haines, K., Chevallier, M., Barthélemy, A., Bricaud, C., et al. (2019). An assessment of ten ocean reanalyses in the polar regions. *Climate Dynamics*, *52*(3–4). https://doi.org/10.1007/s00382-018-4242-z

Vancoppenolle, M., Meiners, K. M., Michel, C., Bopp, L., Brabant, F., Carnat, G., et al. (2013). Role of sea ice in global biogeochemical cycles: Emerging views and challenges. *Quaternary Science Reviews*, *79*. https://doi.org/10.1016/j.quascirev.2013.04.011

Vernet, M., Geibert, W., Hoppema, M., Brown, P. J., Haas, C., Hellmer, H. H., et al. (2019). The Weddell Gyre, Southern Ocean: Present Knowledge and Future Challenges. *Reviews of Geophysics*. https://doi.org/10.1029/2018RG000604

Vichi, M. (2022). An indicator of sea ice variability for the Antarctic marginal ice zone. *Cryosphere*, *16*(10). https://doi.org/10.5194/tc-16-4087-2022

Vichi, M., Eayrs, C., Alberello, A., Bekker, A., Bennetts, L., Holland, D., et al. (2019). Effects of an Explosive Polar Cyclone Crossing the Antarctic Marginal Ice Zone. *Geophysical Research Letters*, *46*(11). https://doi.org/10.1029/2019GL082457

Vihma, T. (2014). Effects of Arctic Sea Ice Decline on Weather and Climate: A Review. *Surveys in Geophysics*, *35*(5). https://doi.org/10.1007/s10712-014-9284-0

Vihma, T., Launiainen, J., & Uotila, J. (1996). Weddell Sea ice drift: Kinematics and wind forcing. *Journal of Geophysical Research: Oceans*, *101*(C8). https://doi.org/10.1029/96JC01441

de Vos, M., Ramjukadh, C., de Villiers, M., Lyttle, C., Womack, A., & Vichi, M. (2023). Polar Iridium Surface Velocity Profilers (p-iSVP), and standard Iridium Surface Velocity Profilers (iSVP) during SCALE 2019 Winter and Spring Cruises. Zenodo [data set].

Wadhams, P., Aulicino, G., Parmiggiani, F., Persson, P. O. G., & Holt, B. (2018). Pancake Ice Thickness Mapping in the Beaufort Sea From Wave Dispersion Observed in SAR Imagery. *Journal of Geophysical Research: Oceans*, *123*(3). https://doi.org/10.1002/2017JC013003

Wang, G., Hendon, H. H., Arblaster, J. M., Lim, E. P., Abhik, S., & van Rensch, P. (2019). Compounding tropical and stratospheric forcing of the record low Antarctic sea-ice in 2016. *Nature Communications*, *10*(1). https://doi.org/10.1038/s41467-018-07689-7

Wang, J., Luo, H., Yu, L., Li, X., Holland, P., & Yang, Q. (2023). The Impacts of Combined SAM and ENSO on Seasonal Antarctic Sea Ice Changes. *Journal of Climate*, *36*(11). https://doi.org/10.1175/JCLI-D-22-0679.1

Wang, Z., Turner, J., Sun, B., Li, B., & Liu, C. (2014). Cyclone-induced rapid creation of extreme Antarctic sea ice conditions. *Scientific Reports*, *4*. https://doi.org/10.1038/srep05317

Wang, Z., Turner, J., Wu, Y., & Liu, C. (2019). Rapid decline of total Antarctic sea ice extent during 2014–16 controlled by wind-driven sea ice drift. *Journal of Climate*, *32*(17). https://doi.org/10.1175/JCLI-D-18-0635.1

Watanabe, E., Wang, J., Sumi, A., & Hasumi, H. (2006). Arctic dipole anomaly and its contribution to sea ice export from the Arctic Ocean in the 20th century. *Geophysical Research Letters*, *33*(23). https://doi.org/10.1029/2006GL028112

Wayand, N. E., Bitz, C. M., & Blanchard-Wrigglesworth, E. (2019). A Year-Round Subseasonal-to-Seasonal Sea Ice Prediction Portal. *Geophysical Research Letters*, *46*(6). https://doi.org/10.1029/2018GL081565

Wei, L., & Qin, T. (2016). Characteristics of cyclone climatology and variability in the Southern Ocean. *Acta Oceanologica Sinica*, *35*(7). https://doi.org/10.1007/s13131-016-0913-y

Wernecke, A., Notz, D., Kern, S., & Lavergne, T. (2024). Estimating the uncertainty of sea-ice area and sea-ice extent from satellite retrievals. *The Cryosphere*, *18*(5), 2473–2486. https://doi.org/10.5194/tc-18-2473-2024

Wilchinsky, A. V., & Feltham, D. L. (2004). Dependence of sea ice yield-curve shape on ice thickness. *Journal of Physical Oceanography*, *34*(12). https://doi.org/10.1175/JPO2667.1

Wilheit, T. (1972). The electrically scanning microwave radiometer(ESMR) experiment. In *Nimbus 5 User's Guide*. NASA.

Williams, T. D., Bennetts, L. G., Squire, V. A., Dumont, D., & Bertino, L. (2013). Wave-ice interactions in the marginal ice zone. Part 1: Theoretical foundations. *Ocean Modelling*, *71*. https://doi.org/10.1016/j.ocemod.2013.05.010

Willmes, S., Heinemann, G., & Schnaase, F. (2023). Patterns of wintertime Arctic sea-ice leads and their relation to winds and ocean currents. *Cryosphere*, *17*(8). https://doi.org/10.5194/tc-17-3291-2023

Wilson, E. A., Riser, S. C., Campbell, E. C., & Wong, A. P. S. (2019). Winter upper-ocean stability and ice-ocean feedbacks in the sea ice-covered Southern Ocean. *Journal of Physical Oceanography*, *49*(4). https://doi.org/10.1175/JPO-D-18-0184.1

WMO. (2014). Sea-Ice Nomenclature (no. 259). Geneva: World Meteorological Organization. Retrieved from https://library.wmo.int/idurl/4/41953

Womack, A., Vichi, M., Alberello, A., & Toffoli, A. (2022). Atmospheric drivers of a winter-to-spring Lagrangian sea-ice drift in the Eastern Antarctic marginal ice zone. *Journal of Glaciology*, *68*(271). https://doi.org/10.1017/jog.2022.14

Womack, A., Alberello, A., de Vos, M., Toffoli, A., Verrinder, R., & Vichi, M. (2024). A contrast in sea ice drift and deformation between winter and spring of 2019 in the Antarctic marginal ice zone. *The Cryosphere*, *18*(1), 205–229. https://doi.org/10.5194/tc-18-205-2024

Womack, A., Alberello, A., De Vos, M., Toffoli, A., Verrinder, R., & Vichi, M. (2024a). A contrast in sea ice drift and deformation between winter and spring of 2019 in the Antarctic marginal ice zone. *Cryosphere*, *18*(1). https://doi.org/10.5194/tc-18-205-2024

Womack, A., Alberello, A., De Vos, M., Toffoli, A., Verrinder, R., & Vichi, M. (2024b). Atmospheric drivers of a winter-to-spring Lagrangian sea-ice drift in the Eastern Antarctic marginal ice. *Cryosphere*, *18*(1). https://doi.org/10.5194/tc-18-205-2024

Worby, A. P., Jeffries, M. O., Weeks, W. F., Morris, K., & Jaña, R. (1996). The thickness distribution of sea ice and snow cover during late winter in the Bellingshausen and Amundsen Seas, Antarctica. *Journal of Geophysical Research: Oceans*, *101*(C12). https://doi.org/10.1029/96JC02737

Worby, A. P., Massom, R. A., Allison, I., Lytle, V. I., & Heil, P. (2013). East Antarctic Sea Ice: A Review of Its Structure, Properties and Drift. https://doi.org/10.1029/ar074p0041

Yang, J., & Neelin, J. D. (1993). Sea-ice interaction with the thermohaline circulation. *Geophysical Research Letters*, *20*(3). https://doi.org/10.1029/92GL02920

Yang, J., & Neelin, J. D. (1997). Decadal variability in coupled sea-ice-thermohaline circulation systems. *Journal of Climate*, *10*(12). https://doi.org/10.1175/1520-0442(1997)010<3059:DVICSI>2.0.CO;2

Ye, Y., Heygster, G., & Shokr, M. (2016). Improving Multiyear Ice Concentration Estimates with Reanalysis Air Temperatures. *IEEE Transactions on Geoscience and Remote Sensing*, *54*(5). https://doi.org/10.1109/TGRS.2015.2503884

Ye, Y., Shokr, M., Heygster, G., & Spreen, G. (2016). Improving multiyear sea ice concentration estimates with sea ice drift. *Remote Sensing*, *8*(5). https://doi.org/10.3390/rs8050397

Yeung, Y., Yiu, S., & Maycock, A. C. (2019). On the seasonality of the El Niño teleconnection to the Amundsen sea region. *Journal of Climate*, *32*(15). https://doi.org/10.1175/JCLI-D-18-0813.1

Yuan, X. (2004). ENSO-related impacts on Antarctic sea ice: A synthesis of phenomenon and mechanisms. *Antarctic Science*, *16*(4). https://doi.org/10.1017/S0954102004002238

Yuan, X., & Li, C. (2008). Climate modes in southern high latitudes and their impacts on Antarctic sea ice. *Journal of Geophysical Research: Oceans*, *113*(6). https://doi.org/10.1029/2006JC004067

Zhang, L., Delworth, T. L., Yang, X., Zeng, F., Lu, F., Morioka, Y., & Bushuk, M. (2022). The relative role of the subsurface Southern Ocean in driving negative Antarctic Sea ice extent anomalies in 2016–2021. *Communications Earth and Environment*, *3*(1). https://doi.org/10.1038/s43247-022-00624-1

Zwally, H. J., Yi, D., Kwok, R., & Zhao, Y. (2008). ICESat measurements of sea ice freeboard and estimates of sea ice thickness in the Weddell Sea. *Journal of Geophysical Research: Oceans*, *113*(2). https://doi.org/10.1029/2007JC004284